

**Quantum Glass, Spin liquids, Fragmentation, Fractional Orbitals,
and Flat Band Physics in Classical and Quantum Spin Models**

A THESIS

SUBMITTED FOR THE DEGREE OF

Doctor of Philosophy

IN THE FACULTY OF SCIENCE

by

Kale Balayogendra Babu



Department of Physics
Indian Institute of Science
Bangalore – 560 012, INDIA

August 2024

© Kale Balayogendra Babu
August 2024
All rights reserved

Declaration

I hereby declare that the work reported in this thesis is original. It was carried out by me during my tenure as a regular Ph.D. student at the Department of Physics, Indian Institute of Science, Bangalore. This thesis has not formed the basis for the award of any degree, diploma, associateship, membership, or similar title of any university or institution. Wherever contributions from others are involved, every effort is made to indicate this clearly, with due reference to the literature and acknowledgment of collaborative research. The work is done under the supervision of Prof. Tanmoy Das.

Date: 19 August, 2024
Bangalore, India

Kale Balayogendra Babu
Department of Physics
Indian Institute of Science

Dedicated to my late grand mother,
Eeshwaramma

Acknowledgements

Ever since I encountered quantum physics in my first year of engineering studies in Electronics and Communication, I have developed a deep passion for reading, discussing, and working in the field of physics. My journey through my bachelor's degree was relatively smooth, and I was successful in everything I undertook. However, the PhD journey has not been easy, and I do not think I could have completed it without the help of certain individuals. I would like to take this opportunity to express my heartfelt thanks to everyone who has supported me along the way.

First and foremost, I would like to express my heartfelt gratitude to my supervisor, Prof. Tanmoy Das, for giving me a chance to be part of his group and for his invaluable guidance and support throughout my PhD journey. I greatly admire his approach to research and his openness to exploring new areas of research. Coming from a B.Tech background, I entered PhD with so many ambitious thoughts but with limited practical knowledge of research. I believe I have grown in my ability to be practical in doing research during this time. I am especially thankful to him for giving me the freedom throughout my PhD. He never imposed restrictions on me and allowed me to make mistakes and learn from them. As many people in academics say, a PhD serves as a form of 'training' to become a researcher. I believe my experience over the past few years has focused on fostering independence in research and developing a genuine understanding of the research process rather than merely following instructions. I credit him entirely for any good things that have happened during this tenure and owe him my gratitude for this opportunity. I hope that he will continue to be my mentor and a source of support in my future endeavors as well.

Another fortunate aspect of my time as a PhD student has been the opportunity to work with Prof. Baskaran and spend time with him. I would like to express my gratitude for his invaluable support and for sharing his wisdom throughout this period. I admire his enthusiasm for physics and his willingness to engage in discussions about topics of current research. Even after retirement, his patience and eagerness to participate in active discussions, as well as his excitement for new ideas, are truly inspiring. I feel fortunate to have spent time with him

and to have witnessed his passion for physics. From him, I have certainly learned to be more optimistic and joyful in my approach to research.

I would like to extend my heartfelt gratitude to all the faculty in the Physics department for their dedication to teaching. I have gained all my physics knowledge from their classes. I want to especially mention Prof. Subroto Mukherjee's course on 'Quantum Statistical Field Theory,' which I found immensely enjoyable and educational; it is truly the best course I have ever attended. Additionally, I am grateful for Prof. Sumilan's course on 'Advanced Condensed Matter Physics,' as it was through his course and the accompanying project that I learned about the Kitaev model and was able to continue my research in that direction. I would also like to mention Prof. Manish for his encouraging and optimistic support during his course period and during our regular general encounters in the department corridors.

I thoroughly enjoyed all the courses taught by the faculty of the physics department, including my supervisor, Prof. Tanmoy Das, as well as those by Prof. Vijay, Prof. Manish, Prof. Rahul Pandit, Prof. Sriram Ramaswamy, Prof. Deeptiman Sen, Prof. Ananth, and Prof. Prasad. The effort these faculty members put into developing advanced courses aligned with current research significantly eased my path in conducting research.

I would also like to highlight the discussions I had with Prof. Vijay Shenoy, particularly related to my first project and during my time as a teaching assistant in his course. I thoroughly enjoyed our discussions and admire his ability to pinpoint the most relevant points in our discussions.

Also, I would like to thank all the chairpersons of the department during this tenure. Let me start by mentioning the chairperson of the department, the late Prof. Venkataraman. He is the nicest researcher I have ever come across. When I got the PhD position at IISc and had to choose faculty supervisors, I faced considerable difficulty in finding faculty in condensed matter theory. He was so kind that, without hesitation, he allowed me into his office and listened to my story. I still remember the statements I made during our discussions: "I started my journey in physics with so much interest in strongly correlated electrons, and I will be the best of all the students in the department after the coursework." It was so generous of him to make me feel comfortable during that time, and I owe him for the chance he gave me. I would also like to mention Prof. Prabal for his supportive and encouraging comments throughout my journey and Prof. Ramesh Mallik for remembering me since my interview and for always wishing me well whenever I see him.

I have many friends I wish to thank, especially Sibaram and Animesh from the Physics department. We have been together from the beginning, and they have supported me in every possible way throughout this rollercoaster ride. I have truly enjoyed the discussions we've had over the years. Whenever I got stuck, they were always there to talk it through and help me out.

Whenever I needed to understand physics or sought any professional advice, they were there to assist me.

Another person I hold immense gratitude for is Harsha. He is more than a friend; he is like an elder brother and mentor. Whenever I face setbacks at work or struggle to understand people, he is always there to guide me and offer support, even when I don't ask for it.

I have also shared many memorable moments over the years with my batchmates Sanath, Partha, Surobhi, and Jayetha, as well as with seniors like Sudeb, Jagannath, Subham, and others. I wish to thank Dr. Rajesh Sharma, with whom I have spent a significant amount of time in the later stages, and for the support he has shown me during this period.

Non-academically, I have created lifetime memories throughout my PhD. This journey has been the most memorable one, thanks to my "Jathiratnalu" friends Mallikharjuna and Ramesh Jay. Despite the many failures along the way in research, my mental strength and the happy ending to this journey are largely due to the time I spent with them. I would also like to mention my dear friend Malleswararao. We share a similar vibe, and he has always inspired me with his commitment and sincerity in everything he does. Additionally, I want to highlight Balanna from the Chemistry department. His journey as a researcher and the commitment he has shown over the years are truly inspiring. I had so much fun being around all of them. I wish to mention Venky and Mallikharjuna for introducing me to Osho, Jiddu Krishnamurthi, and Sadguru and for all the overnight discussions on life and for making me realize a whole new way of looking at it. A special mention to Sharmi for being so affectionate, and I thank her for all the uncountable experiences and for keeping my hope alive. I also want to mention my friends from other departments, especially Sreejha, for all the fun and joyful chats we shared, as well as the 'pan India community' group from C-mess and TSS community. I wish to mention many seniors from the ECE department, mainly Naresh Sir, Anji Anna, KK Anna, and Chethan Anna. When I joined, I spent quality time with them in the mess, and I thank them for their well wishes.

Additionally, I am grateful to have met my friends from B.Tech: Pittu, Balu, Ashok, Samba, Subbareddy, Reesa, and others. They inspired me and taught me many lessons, for which I cannot thank them enough. I also want to acknowledge my many other friends from RGUKT Nuzvid. I am particularly thankful to the faculty from my B. Tech, especially the physics faculty, Siddireddy Srinivas and Dr. Satish, for their invaluable support and encouragement while I was studying physics independently. Importantly, I would like to mention my school teachers, Lakshmi Ma'am and Raju Sir, for nurturing my academic and non-academic skills during the crucial stages of my life, as well as Pichchi Reddy Sir for his continuous support throughout my journey. I acknowledge my dear childhood friends Shiva and Raju for their love and their wonderful support whenever I needed it.

Last but not least, I want to acknowledge my family. I cannot thank them enough, nor do I feel the need to; I always feel blessed to have been born into my family. My parents, Yogaiah and Tirupatamma, are "uneducated" scholars who are naturally skillful, hard-working, and wonderful supporters of mine. They are my role models for whatever I do. My brother, Yogendra, is my inspiration, along with my supportive and loving sister and brother-in-law, their daughter Srihitha. I also want to thank my other family members—my aunts, uncles, brothers, and sisters—for their love and support over the years.

The most important person in my life is my late grandmother, Eeshwaramma. She is the strongest and most independent woman I have ever known, and I am also grateful to my other grandmother, Laxmi, for her immense love, care, and support. She is the sweetest person I have known from my childhood.

I am fortunate and blessed to have them all in my life. As Osho said, '*Life is not a problem to be solved; it's a mystery to be lived.*' I thank God for all the wonderful mysteries/coincidences I have encountered and for all the adventures that continue to unfold.

Preface

The world of many-body physics, encompassing both classical and quantum systems, is a breeding ground for novel phases of matter. Recent attention revolves around exotic phases characterized by fractionalized particles, emergent gauge fields, and long-range entanglement that hold immense potential for applications in quantum computing, information processing, and advanced sensing. Spin liquids (SLs) are a prime example, where the local spins exhibit neither a long-range order nor a complete disorder but rather a unique correlation structure with long-range entanglement. In the quantum SLs, gauge fields emerge at low energies, potentially interacting with the (fractional) particle-like excitations. Despite extensive research, numerous puzzles remain unsolved across quantum and classical SLs (Q/CSLs), such as understanding the dynamics of different gauge degrees of freedom, their influence on the dynamics of particle-like excitations, and their unique statistical properties. The present thesis delves into the study of the QSLs and CSLs in corresponding frustrated systems.

In the first project, I investigated the 2D Kitaev SL model via the Density-Matrix Renormalization Group (DMRG) study. The Kitaev model, one of the very few exactly solvable lattice models in 2D, predicts an interplay between Majorana fermions and Z_2 gauge fields. The ground state consists of uniform zero fluxes with gapped or gapless Majorana dispersions depending on parameters. A magnetic field along the $[111]$ direction disrupts this uniformity, and the model becomes not exactly solvable. Within DMRG calculations, I identify five phases with distinct gauge sectors. The phases are uniform zero-flux, π -flux gas, amorphous π -flux crystal, a novel quantum glass, and a ferromagnet. Intriguingly, the origin of this glassiness arises from the restricted dynamics of excitations such as Majorana-flux or flux-flux pairs connected by finite-length strings, but not from conventional disorder or conserved quantities.

In the next project, I explore periodic arrangements of π -fluxes in the Kitaev model and their impact on the low-energy Majorana dispersions. By tuning the π -flux pair length and the coupling constants, I observe nearly flat-band Majorana dispersions with gaps and gap-less linearly dispersing Dirac points and tunable bandwidth and gaps. These gapped bands possess

non-trivial Chern numbers and quantum metrics, meeting the criteria for ideal fractional Chern insulators. In the presence of interactions, these bands give the fractional Chern insulator phase for the Majorana fermions. I study the fractional Chern insulator phase with the mean-field theory involving density-wave orders. I systematically construct a low-energy tight-binding model via the Wannierization technique to describe the Majorana fermions in the presence of Z_2 gauge fields. This model introduces a gauge potential through a superexchange-like interaction.

In the third project, I explore CSLs. CSLs are cooperative paramagnets that have extensive degeneracy and finite zero-temperature entropy, in contrast to QSLs with zero entropy. Gauge theories also emerge here, but for different reasons. In recent years, significant interest in CSLs has been spurred by the emergence of higher-rank gauge theories and fragmentation properties. Traditionally, CSLs are studied using models like the spin-ice rule or the Luttinger-Tisza approximation. I developed a group theoretical method based on forming a vector space representation for spins within a plaquette of the lattice. The key to this method involves the decomposition of the spin vector into irreducible representations of point-group symmetry. The on-site unit-length spin constraint and frustration play pivotal roles in the emergence of CSLs. This method has been verified with the experimentally relevant XXZ model with Dzyaloshinskii-Moriya (DM) interaction. Among various interesting findings, I observe AFM-vortex/Anti-AFM-vortex-like structures in the ordered phases, a fragmented phase due to the coexistence of ordered phase and disordered CSLs. The group theoretical method helps unify all these phases into a single picture. Notably, the method allows us to quantify the exact ratio of order to disordered components in the case of classical continuous spins.

List of Publications/Preprints

- Fractional Wannier Orbitals and Tight Binding Gauge Fields for Kitaev Honeycomb superlattices with Flat Majorana Bands
K. B. Yogendra, G. Baskaran, and Tanmoy Das
([arXiv:2407.12559](https://arxiv.org/abs/2407.12559))
- Symmetry, Superposition and Fragmentation in Classical Spin Liquids: A General Framework and Applications to Square Kagome Magnets
K.B.Yogendra, S. Karmakar, and Tanmoy Das
([Phys. Rev. B 110, L060401 \(2024\)](https://arxiv.org/abs/2407.12559))
- Emergent glassiness in the disorder-free Kitaev model: Density matrix renormalization group study on a one-dimensional ladder setting
K.B.Yogendra, Tanmoy Das, and G. Baskaran
([Phys. Rev. B 108, 165118 \(2023\)](https://arxiv.org/abs/2407.12559))

Table of contents

1	Introduction: Spin liquids	1
1.1	Quantum Spin Liquids	2
1.1.1	Early mechanisms of Spin Liquids: Resonating Valence Bond theory	3
1.1.2	Parton Mean Field theory: Emergent Gauge fields, Fractionalization .	5
1.1.2.1	Schwinger Fermion Mean-field Theory	6
1.1.2.2	Schwinger Boson Mean-field Theory	8
1.1.2.3	Projective Symmetry Group	9
1.1.2.4	Topological Order	10
1.1.3	Experimental signatures of QSLs	12
1.1.4	Experimental survey of QSLs	13
1.2	Algebraic spin liquids	14
1.3	Kitaev Model: Z_2 -spin liquids	14
1.3.1	The Model	15
1.3.2	Exact Solution in Majorana Representation	15
1.3.3	External Perturbations: Small Magnetic field	18
1.3.4	Material realization- Kitaev Materials	20
A	Appendix	23
A.1	Topological Degeneracy	23
A.2	Ultra short-range spin-spin Correlations in Kitaev Model	24
A.2.1	Static Spin Correlations	26
2	Introduction: Classical Spin liquids	37
2.1	Spin Ice Models and the Coloumb Phase	38
2.2	Magnetic Fragmentation	45
2.2.1	Helmholtz Decomposition	45

2.3	Luttinger-Tisza Approximation and Classification	46
2.4	Order by Disorder	48
2.5	Material realization	49
B	Appendix	51
B.1	Dumbbell Approximation to Dipolar Spin Ice (DSI) Model	51
3	Emergent Glassiness in Disorder-free Kitaev model	61
3.1	Introduction	62
3.2	Method	64
3.3	Results	66
3.3.1	Uniform and Crystalline phases of fluxes	68
3.3.2	Emergent Glassiness	70
3.3.3	Robustness of results with other Lattice Settings	71
3.4	Phase transitions and Fidelity	72
3.5	Discussion	73
3.6	Towards 2D: Results on 4 Leg model	75
3.7	Topological Overprotection, Non-local String Operators and Emergent glassiness at finite temperature in Disorder free Kitaev model	76
3.8	Exact diagonalization calculations	78
3.9	Conclusions	78
C	Appendix	81
C.1	Estimation of Gaps	81
C.2	Phases for Different Couplings	82
4	Fractional Wannier Orbitals and Tight-Binding Gauge Fields in Kitaev Honeycomb Superlattices with Flat Majorana Bands	89
4.1	Introduction	90
4.2	The Kitaev model with staggered fluxes	91
4.3	Tight-binding Gauge-field model for Majorana orbitals	94
4.3.1	Gauge fixing and topological invariants	99
4.3.2	Examples of two Majorana bands in a honeycomb lattice	100
4.4	Results	102
4.4.1	Majorana band structure of the full supercell Hamiltonian	102
4.4.2	Effective model and Majorana Wannier centers	104
4.4.3	Chern number and Quantum metric	105

4.4.4	Gauge invariant Mean-field theory for Fractional Chern insulator . . .	107
4.5	Summary and outlook	110
D		113
D.1	Matrix Elements of the Supercell Hamiltonian	113
D.2	Matrix-Elements of the Tight-Binding Model	114
D.3	Numerical fitting procedure	116
D.3.1	Gauge Obstruction and spread function of Wannier Majorana states .	116
D.3.2	Completeness of the Wannier Majorana states	118
D.3.3	Choosing the trial wavefunction	118
D.3.4	Values of tight-binding parameters	120
5	Symmetry, Superposition, and Fragmentation in Classical Spin Models	131
5.1	Introduction	132
5.2	Mathematical foundation:	134
5.2.1	Realizations in a square-Kagome lattice	136
5.2.2	Irreps in square-Kagome lattice	136
5.2.3	Eigen energies:	137
5.3	Phase diagrams and correlation functions	138
5.4	Conclusions and outlook	141
E	Appendix	143
E.1	Detailed derivation of the Symmetry properties	143
E.1.1	Symmetry of the Hamiltonian	145
E.1.2	Irreducible spin configurations	146
E.1.3	XXZ and DM interactions	147
E.2	Details of Classical Monte Carlo	150
E.3	Structure Factor Plots	151
E.4	Soft-spin Approximation	154
E.5	Finite Magnetic field	155
6	Summary	161

List of figures

- 1.1 A honeycomb lattice with two sublattices denoted by A and B. A unit cell consisting of two sublattice sites with basis vectors $\mathbf{n}_1 = (\sqrt{3}, 0)$ and $\mathbf{n}_2 = (\frac{\sqrt{3}}{2}, \frac{3}{2})$ is shown. Corresponding reciprocal lattice vectors are $\mathbf{G}_1 = 2\pi(\frac{1}{\sqrt{3}}, \frac{-1}{3})$ and $\mathbf{G}_2 = 2\pi(0, \frac{2}{3})$. The nearest neighbor distance, a , is taken to be a unit. W_p corresponds to a loop operator in each plaquette. 16
- 2.1 (Top left) The pyrochlore lattice with corner-sharing tetrahedron of spin ice embedded in a cube. (Top right) The diamond lattice (thick lines) is formed by the centers of the tetrahedral lattice (thin lines). The spins, site variables on the tetrahedral lattice, become link variables (arrows) on the bonds of the diamond. (Bottom left) The ground state configuration of spins with '2-in-2-out' condition. (Bottom center) shows as link variables on the diamond lattice, the spins can be thought of as a lattice flux B (brown arrows of the top right figure). (Bottom right) a set of spins on a green line arranged on a head-to-tail on a loop may be inverted to produce another ground state configuration. Such a loop has zero net magnetization. The term, which strength g , produces a liquid ground state, which is a quantum spin liquid as discussed in the text. The figure is taken from Ref. [39] with permission from the springer nature. . . . 41
- 2.2 (left) 3-in-1-out monopole configuration in a tetrahedron, (middle) respective dumbbell representation of 3-in-1-out tetrahedron, (right) their Helmholtz decomposition into divergence-full and divergence-free elements with the size of the arrows indicating their magnitude discussed in the texts. The figure is taken from Ref. [65] with permission from the Springer Nature. 45

- 3.1 A Kitaev ladder setup that we study here. At each site, we have three nearest neighbor bonds with exchange interactions, $J_{x,y,z}$, between $S^{x,y,z}$, respectively, as in a honeycomb analog. The J_z interactions (J_3, J_4) are kept to be the same as well as different for comparison. \mathbf{a} denotes the lattice constant, while W, T_i are flux operators defined in the text. 64
- 3.2 (a) The spatial average value of the magnetization along the magnetic field direction is plotted as a function of field strength. (b) Corresponding values of the uniform spin susceptibility (χ) are plotted here. Three different colors denote the same calculated values but for three different system sizes $N = 400, 300, 200$. The vertical dashed lines mark the phase boundaries, which are located at $h \simeq 0.24, 0.28, 0.3$, and 0.43 . (The plots are magnified between $h = 0.2 - 0.5$ values for visualization.) 66
- 3.3 Computed values of the spatial average of the three flux operators W, T_i are plotted as a function of field strength. The results are shown for a DMRG run on a 400 site lattice. The vertical dashed lines indicate the same phase boundaries as in Fig. 3.2. The horizontal dashed line marks the $\langle W \rangle = 0$ line. 67
- 3.4 The computed value of $\langle W_p \rangle$ are shown for each plaquette p for two different fields (a) $h = 0.2$ (b) $h = 0.275$, which correspond to Phase I and Phase II. (c),(d) The values of $\langle T_{\beta p} \rangle$ are shown in the corresponding bottom panel. The $T_{2p} > T_{1p}$ at a p corresponds to T_{1p} flux sitting at the boundaries, and vice versa 68
- 3.5 Similar to Fig. 3.4, but here the results are shown at two representative fields of Phase III ($h = 0.2975$) and Phase IV ($h = 0.365$). In the middle panel ((c),(d)), we plot the real part of the Fourier transformation of $\langle W_p \rangle$ with wave vector k . 69
- 3.6 We plot the correlation function of the flux operator ΔW_p with $p = 50$ for (a) $h = 0.295$, and (b) $h = 0.365$ 70
- 3.7 I plot the quantum Fidelity (defined in the text) with magnetic field for $N = 400$ lattice sites. The vertical dashed lines indicate all five phase transition points, which coincides with Figs. 3.2 and 3.3. 72
- 3.8 The spatial average values of $\langle W_p \rangle$ as a function of the magnetic field for the four-leg Honeycomb lattice with system size $N = 52$ sites. The vertical dashed lines are pointing the fields of phase transitions identified from the magnetic susceptibility. 75
- 3.9 $\langle W_p \rangle$ at (a) $h = 0.18$ and (b) $h = 0.26$, the emergence of periodic ordering in flux configurations is observed at this field. The color bar indicates the strength of the flux in a given plaquette. The shaded plaquettes are connected for the periodic boundary in the cylinder geometry. 76

- 3.10 (a) $E - E_0$ at the magnetic fields: $h = 0.1$ (Phase-I), 0.26 (Phase-II), 0.29 (Phase-III), 0.36 (Phase-IV) and 0.6 (Phase-V) for system sizes $N = 6, 10, \text{ and } 14$ are plotted. E_0 is the corresponding ground state energy. (b) The gap between the first excited state from the ground state at the above-mentioned magnetic fields is plotted as a function of system size (N). 78
- C.1 (a) Average of $\langle W_p \rangle$ for $N = 400$ as a function of magnetic field for the coupling $J_4 = 0$ with $J_x = J_y = J_3 = 1$. The phase boundary is indicated with a vertical dashed line. (b) $\langle W_p \rangle$ as function of plaquette number, p at field $h = 0.165$ 82
- 4.1 \mathbb{Z}_2 flux crystal structure and the supercell formation in the Kitaev model. (a) We show a 2×2 supercell of honeycomb lattice containing a π -flux ($W_p = -1$) pair (orange plaquette) separated by two vertical bonds having $u_{ij} = -1$, while the rest of the plaquettes (white) have zero flux and bond have $u_{ij} = +1$. $\mathbf{a}_1 = (4a\sqrt{3}, 0)$ and $\mathbf{a}_2 = a(\sqrt{3}, 3)$, where a is the nearest neighbor distance in the honeycomb lattice. *Inset*: Three different exchange interactions J along the three nearest neighbors at each site are highlighted in different colors. (b) The chosen gauge convention for the u operators in the Kitaev model is shown as $u_{ij} = +1$ if an arrow points from site i to j , or -1 otherwise. The same is shown for the next nearest neighbors by dashed lines where two u operators for the intervening nearest neighbor bonds are multiplied. For example, the bond from the site, i to k term has $u_{ij}u_{jk}$ is -1 . This convention is for the uniform flux sector, where each plaquette has zero flux. 92
- 4.2 (a) Schematic plots of the superexchange mechanism of gauge potential H^I in the low-energy spectrum (blue lines) due to virtual hopping to the eliminated high-energy states (red lines). Note that the virtual hopping potential V is a fitting parameter in the TB model. (b) The gauge fields in the effective theory in a honeycomb lattice. The sets of first and second nearest neighbor sites are denoted by $\mathbf{R}^{(1)} = \{\mathbf{R}_{1-3}\}$ and $\mathbf{R}^{(2)} = \{\mathbf{R}_{1-6}\}$. The gauge field for the second nearest neighbor across diagonally opposite directions must be opposite in sign to commence odd-parity hopping (superconducting term in Eq. (D.6), i.e., $\mathcal{U}_{\mathbf{R}, \mathbf{R}_2^{(2)}} = -\mathcal{U}_{\mathbf{R}, \mathbf{R}_1^{(2)}}$ 95

- 4.3 The dispersions of the Majorana fermions for two representative flux configurations. (a) The dispersions for the 3×3 are shown here along the \mathbf{k} - directions as given in the inset. Here, we set $K/J = 0$, which shows a gapped dispersion. (b–c) The Majorana dispersions for 4×4 supercell are shown for $K/J = 0.0$ in (b) and $K/J = 0.01$ in (c). $K/J > 0$ opens a band gap across the zero energy. The adjacent right-hand panel shows the density of states for all three cases. 102
- 4.4 (a) The locations of the Wannier centers (magenta color) are shown to be adjacent to the π flux plaquettes for the 4×4 supercell. (bottom) (b) The band structures from the original band structure and the effective Hamiltonian are shown for $K/J = 0.01$ on 4×4 configuration. 104
- 4.5 (a) Band gap (Δ), bandwidth (δ), and the fitness ratio (δ/Δ) are plotted as a function of K (from Eq. (4.2) for the 4×4 supercell. (b) Computed values of the quantum metric invariant (G) and Chern number (C) are plotted as a function of K , and compared with zero-flux configuration. Two topological phase transitions are located here: at $K=0$, we have a topological phase transition from trivial to non-trivial phase with Dirac cone degeneracy, and another one at $K \approx 0.175J$ between two non-trivial topologies with a flat-band degeneracy. 106
- 4.6 We plot (a) the Berry curvature $G(\mathbf{k})$ and (b) the difference $G(\mathbf{k}) - U(\mathbf{k})$ from the trace condition (ii) in the first Brillouin zone. The plots in each column correspond to different K values of 0.035, 0.12, and 0.22, from left to right. 108
- D.1 We plot the orbital weight of the two lowest energy ($p = 1$) particle-hole states $\sum_{\mathbf{k}} \chi_{p,i}(\mathbf{k})$ at different sites i , defined in Eq. D.13. The results are shown for the 4×4 - flux configuration. The size of the open circles denotes the orbital weight strength. We notice that the weight is largest around the π - fluxes. 119
- 5.1 (a) A plaquette of a 2D square-Kagome lattice, belonging to the D_4 group, is shown with sublattices enumerated as $i = 0 - 7$. (b) Among five irreps with different multiplets, we show a few representative irreps here, while others are shown in SM[51]. Each irrep consists of either S_i^\perp (horizontal arrow) or S_i^z (open and filled dots for up and down spins) components, with the sizes of the arrows or dots dictate their magnitudes. 134

- 5.2 Computed phase diagrams within the MC simulation (also group theory analysis) are shown for (a) for AFM ($J = +1$) and (b) for the FM ($J = -1$) couplings. We highlight spin textures in a randomly chosen four-plaquette setting for representative phases (upper panel) and respective ensembles of irreps in four plaquettes (lower panel). (c) CSL at $(J, \Delta, D) = (1, 1, 0)$ showing disordered values of m_v from both in-plane and out-of-plane ensembles. (d) AO at $(1, 0, -3)$ with degenerate irreps $B_{1,2}^{(a)}$ are staggered. (e) FAA phase at $(1, 4, -1)$ where $B_{1,2}^{(a)}$ being ordered but $B_1^{(c)}$ is disordered. (f) FFM phase at $(-1, -2.5, 0)$ where 2D irrep $E^{(a)}$ is ferromagnetically ordered in-plane, but out-of-plane irreps are disordered. Note that all disordered values take random numbers between different plaquettes, while we display only four representative plaquettes here. 137
- 5.3 Simulated $\chi(\mathbf{k})$ is plotted in the momentum space for the four phases discussed in Fig. 2. (a) CSL at $(J, \Delta, D) = (1, 1, 0)$, where red dots are plotted separately to signify additional strong magnetic Bragg-like peaks that overwhelm the spectral density of the disordered pattern. (b-c) FFA at $(1, 4, -1)$ where the plots for the ordered S_i^\perp and disordered S_i^z components are separated in (b) and (c), respectively. (d) AO at $(1, 0, -3)$ showing Bragg peaks similar to S_i^\perp components in (b). (e-f) FFM phase at $(-1, -2.5, 0)$ with FM ordered S_i^\perp and disorder S_i^z are separated in (e) and (f). Panels (a) and (f) host pinch-points around $(\pi, 3\pi)$ and its equivalent points. 140
- E.1 We plot all the irreps' basis functions. The vertical dashed line demarcates the out-of-plane irreps m_z on the right-hand side, among which only the top row satisfies the local constraint while the others do not. The horizontal arrows give the spin direction for S_i^\perp , while the filled and open dots correspond to S_i^z . The size of the dots corresponds to $|S_i^z|$. For $A_2^{(c,d)}$, the size of the dots is adjusted for $|S_i^z| = 1$, while for $B_{1,2}^{(c)}$, sites with symbols give $|S_i^z| = \sqrt{2}$, while sites without symbols have $|S_i^z| = 1$. Similar consideration is used for the E irreps that do not meet the local constraint. 148

- E.2 The real spin configurations (left panel) and the corresponding structure factor (middle panel) are plotted for various phases for the AFM coupling $J = +1$. The ensemble of order parameters, which are mentioned in the main text, for each phase is presented in the right panel. (a) Order phase (red region in the phase diagram) with staggered anti-vortices between the neighboring sites, showing Bragg-like peaks at a finite but preferential wavevector. (b) Mixed or fragmented phase where the inner anti-vortices turn into an AFM-anti-vortex with opposite S_i^z components, while $S_i^z = 0$ for the outer anti-vortex. The S_i^z values, however, take random values and show disorder features in the corresponding structure factor without any pinch-point correlation. This is expected as the inner vortices become decoupled from each other, lacking any significant correlation between them. (c) A CSL phase (close to the Z_2 CSL phase) showing larger spectral weight the S_i^z correlation function with pinch-points. (d) The mixed or fragmented phase for $D < 0$ is similar to the mixed phase for $D > 0$, except here, vortices replace the anti-vortices. (e) Orderd phase for $D < 0$, similar to the $D > 0$ case in (a), with vortices replacing anti-vortices. (f) A collinear out-of-plane FM phase arising in the limit of strong our-of-plane anisotropy term $\Delta \rightarrow -\infty$ 152
- E.3 Similar to Fig. S2, but for the FM interaction $J = -1$. All three phases shown here are the fragmented phases at different values of D and Δ , showing pinch-point in the S_i^z correlation function, but FM ordering in the in-plane component. 153
- E.4 Energy dispersion of the Hamiltonian $\mathcal{H}(\mathbf{q})$ at four with re)spective degeneracy of flat bands d, for (a) $\Delta = 1.0, D = 0.0$ (CSL), (b) $\Delta = 4.0, D = 1.0$ (Mixed phase) for $J = +1$ and (c) $\Delta = -2.5, D = 0.0$ (d) $\Delta = 4.0, D = 1.0$ (Mixed phases) for $J = -1$ 155
- E.5 Phase diagram at $D=0$, as a function of h and Δ . For $\Delta < 1$, the phase is a mixed phase and spin liquid for another case. The mixed phase here is unstable for any finite value of D ; the phase becomes ordered in and out-of-plane for non-zero D value. 155

List of tables

- 5.1 We tabulate all the phases and the contributing irreps obtained consistently with the MC simulation and the group theory analysis. The irrep with a bar in the third column reflects it to be ordered; otherwise, it's a disorder irrep. 138
- E.1 Character table of the group D_4 . The last row corresponds to the characters of the reducible representation \mathcal{S}_p for each class. $N_k C_k$ notion is used in the first row. N_k is the number of elements in each conjugacy class, C_k 146

1

Introduction: Spin liquids

In the realm of condensed matter physics, from the microscopic world of atoms and molecules to the macroscopic scale, many-body physics provides invaluable insights into the complexities of nature. Studying many-body systems is a cornerstone for understanding collective behaviors arising from interactions between an Avogadro number of particles. These interacting systems at zero temperatures exhibit properties and behaviors that cannot be understood with individual constituents; this is the concept of emergence coined by P.W Anderson [1]. Despite the simplicity of their individual constituents, many-body systems exhibit remarkably diverse emergent properties. These range from the intricate phenomena of quantum entanglement at the microscopic scale to behaviors reminiscent of the physics governing massive black holes on galaxy scales.

The exotic phases in the quantum many-body systems include simple metals to instances where the metals defy the single particle picture, termed as 'non-fermi liquids.' In the strong interaction limit at half-filling, insulators with significant charge gaps show intriguing phenomena, for example, 'spin liquids.' [2] In these instances, the spin degrees of freedom govern the low-energy physics. One seminal example that catalyzed the exploration of these concepts and paved the way for modern research topics is the study of Mott insulators. The Mott insulators initially emerged as the parent state for the high T_c superconductor compounds like La_2CuO_4

[3]. The Hamiltonian that describes these materials is typically the Hubbard model on a square lattice with strong on-site interaction U :

$$H = -t \sum_{\langle ij \rangle, \sigma = \uparrow, \downarrow} c_{i, \sigma}^\dagger c_{j, \sigma} + \text{h.c.} + U n_{i\uparrow} n_{i\downarrow} \quad (1.1)$$

Here, t is the nearest neighbor hopping strength, $c_{i\sigma}$ is the electron annihilation operator with spin σ , and their corresponding number operator $n_{i\sigma} = c_{i\sigma}^\dagger c_{i\sigma}$. At half-filling, for $U = 0$, the ground state is a simple metal, while for $U = \infty$, the ground state is an ordered anti-ferromagnet. The double occupancy is restricted at $U = \infty$, leading to a scenario where spins dominate physics. The half-filled states at finite but large U limit are described by an effective spin-exchange Heisenberg model [4]:

$$H = J \sum_{\langle ij \rangle} \mathbf{S}_i \cdot \mathbf{S}_j, \quad (1.2)$$

where $J \sim 4t^2/U$. When frustration, like the next-nearest neighbor hopping in a square lattice, is present, the ordered state is no longer the ground state. The state is given by a 'spin liquid' where the spins neither do order nor completely disordered but have a non-trivial correlation with entanglement.

In this chapter, I aim to elucidate the intricacies of spin liquids in the quantum regime. Since quantum spin liquids have been in active research for the past few decades, my discussion will be concise, primarily focusing on theoretical advancements. Additionally, in Chapter 2, I discuss the classical analogs of spin liquids, also known as cooperative magnets [5], exploring various theoretical perspectives.

1.1 Quantum Spin Liquids

Quantum spin liquid (QSL) is a non-magnetic phase where spins do not order even at zero temperature. QSLs naturally occur in low-dimensional systems like in 1D and 2D (also 3D in a few materials) where quantum fluctuations due to frustration are predominant, making the spins not ordered. In general, the paramagnetic phase is also not ordered. However, it is a trivial state, meaning the ground state and the excitations are deterministically unique- where the spins at different sites are uncorrelated. On the other hand, the QSL state is a superposition of all possible spin configurations and hence has finite entanglement and correlations with topologically non-trivial excitations (both abelian and non-abelian). QSLs may look featureless

if we look at individual spins like a paramagnet. However, differences lie in features like ground-state degeneracy, exotic fractional excitations, and entanglement [6].

Frustration plays a crucial role in realizing QSLs. A simple model showcasing frustration is the antiferromagnetic Heisenberg spin-1/2 model on a triangular lattice [7]. In any given triangle, there's always at least one site that fails to align antiferromagnetically with its neighboring sites—a phenomenon termed frustration. Consequently, the probable scenario for the ground state involves superpositioning all possible spin configurations across all sites.

A contemporary definition of QSLs is that it is a phase with long-range entanglement and emergent excitations with fractional statistics- a topological ordered phase [6, 8]. The gauge symmetry emerges in QSLs, and the type of emergent gauge theory present in the QSLs is used for their nomenclature, i.e., for example, a phase with emerging U(1) gauge theory¹ is called U(1)-spin liquid. Wen et al. [9] proposed the concept of topological order for phases that do not have Landau local order parameters. A topological order is defined by a state with ground state degeneracy (which is D^2) that depends on the number of quasiparticle types present in theory (D). For example, $D = 2$ in Z_2 spin liquids corresponding to two types of quasiparticles, which are called 'e' and 'm' excitations. This degeneracy leads to an intrinsic entropy that is independent of the system size and manifests as a universal long wavelength correction in bipartite-entanglement entropy called the topological entanglement entropy (TEE). The corresponding details are discussed in the following sections.

The structure of this chapter is as follows. The early mechanisms of QSLs based on RVB states by Anderson for understanding the phase diagram of high-Tc superconductor La_2CuO_4 is discussed in Sec. 1.1.1. Sec. 1.1.2 discusses the extension of RVB ideas of QSLs to effective field theory descriptions using parton mean-field theories and emergent gauge fields and fractionalization. In Sec. 1.1.4 and Sec. 1.1.3 I summarize existing materials proposed to exhibit QSLs and their experimental signatures, respectively.

1.1.1 Early mechanisms of Spin Liquids: Resonating Valence Bond theory

RVB theory is one of the early mechanisms of QSLs and was introduced by P.W. Anderson [10] as a proposal to explain the unconventional superconductivity in copper oxide compounds [11]. The idea of resonating valence bonds (RVB) was originally proposed to describe the quantum mechanical resonance of covalent bonds in unsaturated benzene molecules. Then, Pauling generalized this idea to 2D graphite and metals [12]. Later, Anderson applied the RVB concept to the family of spin-half Mott insulators, particularly in situations where the anticipated long-

¹Precisely, the invariant gauge group of the projective symmetry group

range antiferromagnetic order was absent due to frustration [13]. The variational analysis done in Ref. [13] on a 2D triangular lattice of spin-1/2 Heisenberg antiferromagnet demonstrated that a state characterized by coherent superposition of spin-singlets formed between nearest neighbor sites yielded a ground state more favorable than the long-range ordered antiferromagnet. The stability of the RVB state was attributed to the movement or resonance of singlet pairs. The RVB trial wavefunction, as commonly depicted, following discussion from Ref. [14], is

$$\Psi_{\text{RVB}} = P_d \left(\sum_{ij} \phi_{ij} b_{ij}^\dagger \right)^{N/2} |0\rangle,$$

where $P_d = \prod_i (1 - n_{i\uparrow} n_{i\downarrow})$ is the Gutzwiller projection operator restricts the double occupancy on each lattice site of the Mott insulator, and $b_{ij}^\dagger = \frac{1}{\sqrt{2}} (c_{i\uparrow}^\dagger c_{j\downarrow}^\dagger - c_{i\downarrow}^\dagger c_{j\uparrow}^\dagger)$ creates a singlet pair on sites i and j . The factor ϕ_{ij} characterizes the RVB state, which depends on the lattice and the kind of spin liquid of interest. On a square lattice, only the nearest neighbor pair has non-zero contributions.

The Gutzwiller projection operator P_d constrains the allowed Hilbert space to single occupancy at each site. In general, a projection operator on wavefunctions allows correlations between the constituent particles, even if the particles are non-interacting before the projection. This is a complex problem to implement analytically. Various Monte Carlo techniques are often used. The essence of the projection becomes evident in capturing the topological excitations, as demonstrated in Ref. [15–17] for the RVB states. Subsequently, the topological entanglement entropy is calculated using the variational Monte Carlo method [18–20] in the triangular lattice. The U(1) gauge field emerges in the theory on triangular lattice [21, 22], which reduces into the Z_2 theory under the relevant spinon pairing. An elaborate discussion on this is presented in the next section.

Furthermore, the excitations in the system exhibit fractional statistics. One notable excitation is the spinon, a neutral spin-1/2 particle. Creating a pair of spinons involves breaking a singlet bond. Additionally, a single spinon can move through the lattice by breaking nearby singlet bonds and rearranging others, leaving behind an unpaired spinon. This movement results in the formation of a string connecting the two unpaired spinons. [23, 24] The other gapped excitations, known as visons in Z_2 -spin liquids, correspond to the creation of fluxes. When a spinon is braided around a vison, the wavefunction acquires sign change (-1) [25, 26], leading to Semion statistics. The statistics of these excitations are equivalent to those of the bosonic fractional quantum hall state, as demonstrated in Ref. [27].

In further developments, the dimer models were introduced [28, 29] to better describe RVB states and illustrate how the RVB state is a true ground state of a local Hamiltonian. Each configuration of the dimer coverings is orthogonal to each other, which is not the case in the

general RVB state, and this made the dimer models easy to tackle. This feature of dimer models made it possible to create a variational tensor product state for RVB states [30–32]. These RVB-states as variational wavefunctions ansatz, prove to be successful in simulating topological ordered phases via most of the modern numerical techniques like tensor networks [33–36]. It remains an active research topic, see for example Ref. [37].

The RVB state and that obtained from an effective theory (to be discussed below), are equivalent in case if the visons and spinons are gaped in the Z_2 spin liquid state² [38, 39]. This state is a short-range RVB state [40, 41]. On the other hand, the long-range RVB states³ [44] have spinons with gapless nodal points and small Vison gap [45]. This state is created by using Gutzwiller projection on d -wave BCS wavefunctions on a square lattice and also on the other bipartite lattices where the Marshall sign rule plays a significant role [46]. Later, this construction generalized to non-bipartite lattices. In such scenarios, the RVB states do not correspond to the ground state obtained from mean-field analysis. Usually, these states are unstable and are called algebraic spin liquids. A brief summary of the intricacies of algebraic spin liquids is presented in Sec. 1.2.

1.1.2 Parton Mean Field theory: Emergent Gauge fields, Fractionalization

In this section, I discuss the effective field theory approach for studying QSLs. This method offers a clearer analytical framework than the variational approach. Here, the emergence of gauge theory as a low-energy description of QSLs and the fractional statistics exhibited by excitations become transparent.

The key idea behind this formalism, mainly developed by Baskaran [21, 47], Sachdev [38] and Wen [9], is that spin-1/2 degrees of freedom are decomposed into some fractional particles with up and down spins, called *Partons*. The partons can be fermions or bosons. This increases the Hilbert space dimension. The physical Hilbert space spanning spins is recovered by imposing a local constraint on the enlarged Hilbert space.⁴ The extra dimensions of the enlarged Hilbert space do not affect the physical observables. Hence, those extra degrees of freedom behave like a gauge sector, just like the gauge freedom in Maxwell's theory. Surprisingly, these extra gauge degrees of freedom turn out to be low-energy excitations in a

²Which is discussed above in the triangular lattice, or in the square lattice by introducing hopping onto next nearest neighbor bonds[38], and also Toric code introduced by Kitaev [39])

³These RVB states have the singlet dimer coverings covering over the whole lattice with uniform weights for all configurations [42, 43]. Contrast to the short-range RVB states where the dimer coverings are within the nearest or next nearest neighbor distances [40, 41], like in the dimer models.

⁴In the case of global ones, chemical potential-like terms can take care of that constraint.

few cases (gapped QSLs) and impact the low-energy physics to different 'emerging' phases (in gapless QSLs). This enhanced symmetry in the low-energy gives freedom to create different QSLs satisfying the physical symmetries- this construction is called the *Projective Symmetry Group* (PSG) analysis developed by Wen [9]. The discussion on these ideas is presented below by taking an example for each representation.

1.1.2.1 Schwinger Fermion Mean-field Theory

This theory was developed by Baskaran [21, 47] and later used by Wen [9] for spin liquids. For this discussion, I mainly follow Refs. [9, 48, 49]. In this approach, the spin is written into fermionic parton operators $f_{i\alpha}$, $\alpha = \uparrow, \downarrow$ carries spin-1/2 with no charge. The spin operator \mathbf{S}_i is represented as

$$\mathbf{S}_i = \frac{1}{2} f_{i\alpha}^\dagger \boldsymbol{\sigma}_{\alpha\beta} f_{i\beta}, \quad (1.3)$$

with $S_i^+ = S_i^x + iS_i^y = f_{i\uparrow}^\dagger f_{i\downarrow}$ and $S_i^- = S_i^x - iS_i^y$. The partons have SU(2) invariance. By this representation, the Hilbert space dimension, which is two at each site for spin-1/2 particles (called '*physical Hilbert space*'), increased to 4 (called '*extended Hilbert space*'). The Hamiltonian considered here is the Heisenberg Hamiltonian for a half-filled Mott insulator given in Eq. 1. The constraints for half-filling at each site are

$$\sum_{\alpha=\uparrow,\downarrow} f_{i\alpha}^\dagger f_{i\alpha} = 1, \quad \sum_{\alpha,\beta} f_{i\alpha} f_{i\beta} \varepsilon_{\alpha\beta} = 0, \quad (1.4)$$

where $\varepsilon_{\alpha\beta}$ is the Levi-Civita matrix. The second constraint is redundant from the first one, annihilating double occupancy. These constraints are difficult to implement exactly because the Hamiltonian is quartic in these operators; rather, impose these constraints at the mean-field level on the ground state as

$$\left\langle \sum_{\alpha=\uparrow,\downarrow} f_{i\alpha}^\dagger f_{i\alpha} \right\rangle = 1, \quad \left\langle \sum_{\alpha,\beta} f_{i\alpha} f_{i\beta} \varepsilon_{\alpha\beta} \right\rangle = 0. \quad (1.5)$$

Since these constraints are local, these can be implemented in the Hamiltonian by including a site-dependent Lagrangian multiplier, $a_0^l(i)$, $l = 1, 2, 3$, where a_0^1 for the first constraint and a_0^2 , a_0^3 corresponds to the imaginary and real parts of the second one. In the zeroth order approximation, we ignore the time dependence of the a_0^l , i.e., its fluctuations. By including the fluctuations, the constraint in Eq. 1.5 becomes the original constraint, Eq. 1.4. The Heisenberg

Hamiltonian, eq. 1:

$$\begin{aligned} H &= \frac{J}{4} \sum_{\langle ij \rangle} (2S_i^+ S_j^- + h.c. + (n_{i\uparrow} - n_{i\downarrow})(n_{j\uparrow} - n_{j\downarrow})), \\ &= \frac{J}{4} \sum_{\langle ij \rangle} (2f_{i\uparrow}^\dagger f_{i\downarrow}^\dagger f_{j\downarrow}^\dagger f_{j\uparrow} + h.c. + (n_{i\uparrow} - n_{i\downarrow})(n_{j\uparrow} - n_{j\downarrow})) \end{aligned} \quad (1.6)$$

with $\sum_{i,\alpha=\uparrow,\downarrow} f_{i\alpha}^\dagger f_{i\alpha} = 1$ and subtracting the constant term $\sum_{\langle ij \rangle, \alpha \neq \beta = \uparrow, \downarrow} n_{i\alpha} n_{j\beta}$,

$$H = -\frac{J}{2} \sum_{\langle ij \rangle, \alpha \neq \beta = \uparrow, \downarrow} (f_{i\alpha}^\dagger f_{j\alpha} f_{j\beta}^\dagger f_{i\beta} + \frac{1}{2} f_{i\alpha}^\dagger f_{i\alpha} f_{j\beta}^\dagger f_{j\beta}). \quad (1.7)$$

Since the above Hamiltonian is quartic in fermionic operators, we decompose the terms into quadratic fermionic operators by considering the mean field parameters

$$\begin{aligned} \eta_{ij} &= -2\varepsilon_{\alpha\beta} \langle f_{i\alpha} f_{j\beta} \rangle, \quad \text{with } \eta_{ij} = \eta_{ji}, \text{ and} \\ \chi_{ij} &= \delta_{\alpha\beta} \langle f_{i\alpha}^\dagger f_{j\beta} \rangle, \quad \text{with } \chi_{ij} = \chi_{ji}^\dagger. \end{aligned} \quad (1.8)$$

η_{ij} is a singlet pair creation term, and χ_{ij} is a single spin hopping term. These mean field equations are calculated self consistently. Using these terms, the mean-field Hamiltonian is

$$H_{mean} = \frac{-3J}{8} \sum_{ij} [\chi_{ij} f_{i\alpha}^\dagger f_{i\alpha} + \eta_{ij} f_{i\alpha}^\dagger f_{j\beta}^\dagger \varepsilon_{\alpha\beta} + H.c. - |\chi_{ij}|^2 - |\eta_{ij}|^2] \quad (1.9)$$

$$+ \sum_i [(a_0^3 (f_{i\alpha}^\dagger f_{i\alpha} - 1) + (a_0^1 + i a_0^2) f_{i\alpha} f_{i\beta} \varepsilon_{\alpha\beta} + h.c.)]. \quad (1.10)$$

This Hamiltonian has local SU(2) gauge symmetry which can be seen by defining,

$$\psi = \begin{pmatrix} f_\uparrow \\ f_\downarrow \end{pmatrix}, \quad U_{ij} = \begin{pmatrix} \chi_{ij}^\dagger & \eta_{ij} \\ \eta_{ij}^\dagger & -\chi_{ij} \end{pmatrix} = U_{ji}^\dagger. \quad (1.11)$$

Where ψ is a spinor and U_{ij} act as SU(2) gauge field. As a result, Eq. 1.5 and Eq. 1.9 are written as

$$\langle \psi_i^\dagger \tau^l \psi_i \rangle = 0, \quad (1.12)$$

$$H_{mean} = \frac{-3J}{8} \sum_{ij} \left[\frac{1}{2} Tr(U_{ij}^\dagger U_{ij}) - (\psi_i^\dagger U_{ij} \psi_j + H.c.) \right] + \sum_i a_0^l \psi_i^\dagger \tau^l \psi_i. \quad (1.13)$$

The first term is from the mean field, corresponds to the gauge fluctuation and the gauge-matter coupling in a lattice. The second term is from the constraints, implements the Peierls phase of the emergent gauge fields for the f_i in the lattice. The gauge fields in the above Hamiltonian *emerges* as follows. This Hamiltonian is invariant under local $SU(2)$ transform $W(i)$: $\psi_i \rightarrow W(i)\psi_i$ and $U_{ij} \rightarrow W(i)U_{ij}W^\dagger(j)$. The physical wave function for spins is obtained from the mean-field answer from the self-consistency method by projecting the mean field state into a single occupancy constraint at each site. The physical observables do not affect by this local $SU(2)$ transform. The states may transform but not observables. So, this transformation is not a symmetry but a redundancy.

A mean-field ansatz is chosen depending on the lattice of interest and internal symmetries, like time reversal and parity. In addition to these physical symmetries, the ansatz has a local gauge redundancy or gauge symmetry, $SU(2)$ symmetry here (precisely invariant gauge group of the projective symmetry group, which will be discussed in the next section). For any chosen ansatz, the Hamiltonian in Eq. 1.13 is quadratic, and solve the Hamiltonian is solved self-consistently for order parameter. Hence, the spectrum and the nature of excitations are studied efficiently. The excitations include the phase excitations of mean field parameters. The magnitude fluctuations are generally gapped, in some cases, the phase fluctuations can be gapless which makes the phase is unstable. But Z_2 spin liquids in triangular lattices and Kagome lattices [50] have gapped phase fluctuations and stable. Likewise, the ansatz may break $SU(2)$ local symmetry into $U(1)$ or Z_2 . In the case of a square lattice, the phase fluctuations make $U(1)$ spin liquids unstable. Hence, by introducing the next nearest neighbor hoppings in the model, the gauge group breaks into subgroup Z_2 [48, 49], which has massive phase fluctuations. So, Z_2 spin liquids can be stable.⁵

In such stable phases, the gapped spinon excitations (created by breaking a singlet in the RVB picture) can be integrated out to obtain a low-energy effective field theory in terms of the order parameter fluctuations- which turns out to a gauge theory. The universal long-wavelength properties like topological degeneracy, entanglement entropy, and the nature of fractional statistics can be studied from the resulting gauge theory.

1.1.2.2 Schwinger Boson Mean-field Theory

I will follow the discussions from Refs. [38, 52]. In this approach, the spins are written in terms of bosonic partons $\mathbf{S}_i = \frac{1}{2}b_{i\alpha}^\dagger \boldsymbol{\sigma}_{\alpha,\beta} b_{i\beta}$, with constraint $\sum_\alpha b_{i\alpha}^\dagger b_{i\alpha} = 1$. Just like in the above case, the Hamiltonian is written in terms of these bosonic partons, and then the quartic terms are decomposed in terms of singlet pair creation/annihilation term (\hat{A}_{ij}) and single spinon hopping

⁵Intruding various terms into unstable $U(1)$ spin liquid phase, stabilizes different phases either ordered or spin liquids [51].

term (\hat{B}_{ij})

$$\mathbf{S}_i \cdot \mathbf{S}_j =: \hat{B}_{ij}^\dagger \hat{B}_{ij} : - \hat{A}_{ij}^\dagger \hat{A}_{ij}, \quad (1.14)$$

with

$$\hat{B}_{ij} = \frac{1}{2} \sum_{\alpha} b_{i\alpha}^\dagger b_{j\alpha} \text{ and } \hat{A}_{ij} = \frac{1}{2} \sum_{\alpha, \beta} \varepsilon_{\alpha\beta} b_{i\alpha} b_{j\beta}, \quad (1.15)$$

where $: :$ denotes the normal ordering in terms of $b_{i\alpha}^\dagger$ operators. The mean-field equations are

$$A_{ij} = \langle \hat{A}_{ij} \rangle, \quad B_{ij} = \langle \hat{B}_{ij} \rangle,$$

and the constraint is implemented on average: $\langle \sum_{\alpha} b_{i\alpha}^\dagger b_{i\alpha} \rangle = 1$. This representation has the U(1) local symmetry not the SU(2) symmetry we obtain for the fermionic case: $b_{i\alpha}^\dagger \rightarrow e^{i\phi(i)} b_{i\alpha}^\dagger$, and $\hat{A}_{ij} \rightarrow e^{-i\phi(i)-i\phi(j)} \hat{A}_{ij}$, $\hat{B}_{ij} \rightarrow e^{i\phi(i)-i\phi(j)} \hat{B}_{ij}$. So, by exploiting this local U(1) local symmetry, this physical symmetry can be implemented differently for different mean-field ansatz, resulting in different spin liquid phases. As discussed in the previous section, the physical state is constructed by imposing the constraint on the mean-field wave function. The mean field ansatz may vary between bosonic and fermionic parton constructions for the same state, but the resultant physical states must remain the same state. As discussed in the fermionic parton scenario, various ansatz can be formulated to assess state stability further. Depending on the energetics of the excitations of the resulting state from the ansatz, a low-energy field theory can be constructed, giving rise to different gauge theories.

1.1.2.3 Projective Symmetry Group

As discussed in the previous sections, the same physical symmetry can be implemented differently due to the emergence of local symmetry in the mean-field ansatz. The set of all transformations (including physical symmetries and local symmetries) that keep the mean field ansatz invariant is called the '*projective symmetry group*' (PSG). In PSG, if the transformations are completely local without involving physical symmetries, they also form a group called the '*invariant gauge group*.' The different mean-field ansatz, which is related by only IGG transformations, gives the same physical state. This is used in the literature as a nomenclature for spin liquids, for example, Z_2 -spin liquids for IGG= Z_2 or similarly for U(1) or SU(2) spin liquids. PSG of any QSLs is the index of mean field ansatz with IGG of the group indicating the spin liquid type, i.e., with $Z_2(U_{ij}, a_0^l \tau^l)$ for the fermion case discussed in the previous section

[9]. For example, different mean-field Ansatz have different PSGs even though they all have the same physical symmetry, giving different spin liquids. So, the PSG provides a way to implement different symmetry-allowed background flux configurations for the partons. Not all the PSG ansatz can give stable physical spin liquids [49]. In the absence of any local order parameters for QSLs, the PSG of QSLs is used to classify the phase. For example, 196 types of Z_2 PSGs in the square lattice can give physical Z_2 -spin liquids, which can be used to identify them. Similarly, see for triangular [52, 53], and Kagome [54]. In addition to the symmetric spin liquids, there are spin liquids that do not obey all the symmetries; for example, the Z_2 spin liquid constructed in Ref. [38]. Those can not be classified with PSGs.

1.1.2.4 Topological Order

The concept of 'topological order' is used for the gapped states and can lack the local ordered parameters as in the Landau paradigm. In addition to QSLs, fractional quantum hall states are another famous example of topological ordered phases. The definitive signature of the topological ordered phase is the long-order entanglement and topological degeneracy. Both depend on the number of distinct quasiparticle types present in the model. The measure of long-range entanglement is the topological entanglement entropy (TEE) [55], which is the universal term in the bipartite entanglement entropy. Bipartite entanglement entropy of a pure state ⁶ is calculated by dividing the system into two subsystems (A, B) with a boundary of length L in a 2D lattice and by defining the reduced density matrix ρ for subsystem A or subsystem B. Entanglement entropy is the von Neumann entropy $[S_\rho = -tr(\rho \log(\rho))]$ of the sub-system density matrix ρ . For the topological ordered phase, S_ρ is

$$S_\rho = \alpha L - \gamma + \dots, \quad (1.16)$$

where α is the non-universal, ultraviolet divergent constant and γ non-negative universal constant depends on the global entanglement on the boundary ⁷. γ is system length independent, so this can be calculated using effective topological field theories. γ behaves as

$$\gamma = \log(\mathcal{D}), \quad \text{with } \mathcal{D} = \sqrt{\sum_a d_a^2}, \quad (1.17)$$

where $\mathcal{D} \geq 1$ is the total quantum dimension of the medium and d_a is the quantum dimension of the quasiparticle with charge a . For any abelian quasiparticle, the quantum dimension is 1. \mathcal{D} counts the total number of superselection sectors present: for example, the toric code, which is

⁶For mixed states, bipartite entanglement entropy is not a good measure.

⁷Some subtleties of the universality of TEE are discussed recently in Ref.[56].

an abelian Z_2 gapped spin liquid, has four superselection sectors: vacuum, fermion $\varepsilon = e \times m$, and vortices e, m . each having quantum dimensions to be one, which is the case for all abelian particles. So, $\gamma = \log(2)$. For the non-abelian case, the quantum dimension is the dimension of a fusion vector space spanned by all the distinguishable ways of fusing n types of quasiparticles into the trivial ones, see Appendix. E of Ref. [57]⁸. The total quantum dimension for the non-abelian phase in the Kitaev honeycomb model (which is also a Z_2 spin liquid) is 4 (where each superselection sector: vacuum (represented by 1, $d_1=1$), fermion (represented by $\varepsilon, d_\varepsilon = 1$), and vortex (represented by $\sigma, d_\sigma = \sqrt{2}$). So, the entanglement entropy is the same as in the abelian case. There is recent interest in calculating multi-partite entanglement entropy of the states in distinguishing the abelian and non-abelian spin liquids [59]. Since the bipartite entanglement has the extra non-universal term, which depends on the boundary area, different procedures were proposed to extract the universal term- known as Kitaev Preskill construction [55] or the Levin-Wen construction [60]. Here, one divides the system into four sub-regions and calculates the tripartite mutual information of the regions to extract the TEE. Recently, an interesting proposal from Feng et al. [61] to calculate TEE from correlation functions of spins. Also, there are interesting proposals for measuring TEE in experimental settings [62].

Another signature of topological order is the degeneracy of the ground state. This degeneracy is also equivalent to $\mathcal{D}^2 = \sum_a d_a^2$, and depends on the genus of the manifold. This can be seen in short-range RVB states as follows⁹: Consider nearest neighbor singlet bonds covered RVB state on the square lattice with periodic boundary conditions. If we draw a line along the boundary of one of the holes in the torus (which is along x - or y - directions in the lattice.) and count the number of singlet bonds crossing the line, which is even always. Then, breaking a single singlet bond that crosses the line into individual spinons creates an odd number of singlets crossing the line, where the individual spinons can be paired by moving the spinon to the other side without crossing the line. By this procedure, the states with even and odd numbers of singlets are not distinguishable, i.e., degenerate. Likewise, the complete degeneracy is calculated by the genus number of the manifold.

The above procedure for computing the topological degeneracy of a state utilizes quasiparticle statistics, as detailed in Ref. [63–65]. This demonstrates the direct connection between fractional statistics and topological order. This calculation assumes that the state is gapped and the excitations placed on the ground state do not change the state when they move around, keeping the state in the ground state manifold. The detailed derivation of the topological degeneracy for the torus with genus $g = 2$, for example, with fractional charges $1/q$, is presented in appendix A.1. In the case of toric code, the exact operators corresponding to these degenerate

⁸See Preskill notes on 'Quantum Information and Computation' [58].

⁹This discussion is taken from Ref. [2].

states are discussed explicitly in Sec. 1.3.3. This degeneracy of the states depends on the fractional statistics of the quasiparticles, so it also survives in the long-wavelength effective field theory calculations. This degeneracy is only valid with gapped systems. Whether the corresponding degeneracy is relevant or not for gap-less quasiparticles where topological order (called 'quantum order') is also present is still an open question.

1.1.3 Experimental signatures of QSLs

Note that there are no direct smoking-gun experimental probes that can give the unambiguous signature of the QSL phase. There exist a few indirect probes, which, with proper analysis, can indicate the presence of a QSL phase. The discussion below is taken from [66–68].¹⁰

The foremost criterion for a QSL is the lack of magnetic order down to temperatures well below the magnetic exchange constant. In this regard, the first step is to estimate the exchange constant from magnetic susceptibility via the Curie-Weiss temperature fitting. The second signature is the specific heat measurement. The absence of the typical λ – line peak in C_v is another evidence of no order. $C_v \sim T$ is another prediction of spinon in QSL, than phonons etc. One of the ways to rule out this possibility is to check the excitation spectrum- which is fractional spin-1/2 excitations with fractional statistics in QSLs. Probing fractional statistics of the quasiparticles is not an easy task. There are theoretical proposals [71–74] and experimental verification of fractional statistics using interferometer experiments in fractional quantum Hall edges [75, 76] which have both abelian and non-abelian but not in the QSL materials. However, the experiments probing the fractional excitations have successfully identified the candidate materials. The experiments that are sensitive to magnetic excitations are used, such as inelastic neutron scattering (INS), thermal conductivity and thermal Hall conductivity, nuclear magnetic resonance, electron-spin resonance, specific heat, and Raman and terahertz (THz) spectroscopies, can be utilized to identify the type of fractional excitations and further classify the QSLs.

Particle-hole continuum of spinons, which are broad. This should be contrasted with the magnon spectrum for an ordered state [66, 77, 78]. In the case of ordered magnets, the excitation spectrum has magnons. The magnons dispersion is calculated, had sharp peaks at the ordering vectors in high-Tc compound La_2CuO_4 [77], confirming the antiferromagnetic nature of high-

¹⁰While finishing this thesis, I have come across an interesting proposal by Patrick Lee et al. Ref. [69] to probe the Meissner effect of emergent gauge fields. The core idea of the proposal is to use Nitrogen-Vacancy (NV) Centers in the diamond placed from a distance z_0 from the crystal hosting the U(1) spin liquid to probe the Meissner effect of spinons, which is the signature of emergent gauge fields. The current fluctuations in the spinon fermi surface of U(1) spin liquids generate magnetic fluctuations in the NV centers [70]. Extending this idea further, the relaxation rate of the NV centers falls rapidly during the spinon pairing transition from U(1) spin liquid to Z_2 .

Tc parent compound. On the other hand, there is a continuum observed on top of the sharp outer background in triangular compound $\text{Ba}_3\text{CoSb}_2\text{O}_9$ [78], signifying there are excitations present other than magnons- which are spinon pairs or multi-spinon excitations, see References there in Ref. [66]. The continuum in the energy spectrum is the indication of disordered structures in the underlying spins and Fractionalization. Inelastic neutron scattering experiment is used to probe the these excitation spectrum. Further, measuring thermal conductivity can probe the gap or gapless nature of QSLs, which is used in Kitaev candidate materials, $\alpha\text{-RuCl}_3$.

1.1.4 Experimental survey of QSLs

This section comprises a list of materials that realize QSL phases. [66–68] The main ingredient for having QSLs is frustration (either by exchange interactions in the lattice or by geometry due to specific Hamiltonian structure) and quantum fluctuations. Although the quantum fluctuations are prominent in 1D and a spin-1/2 chain is the 1D analog of QSLs with spinon excitations, the phase is not a QSL. Because there is no braiding in 1D, and the statistics are not fractional. The fluctuations in 3D may not be as eminent as in 2D, but 3D materials like pyrochlores and hyperkagome are still good candidates for QSLs. Spin-1/2 materials are favorable since spin-1/2 (either from spin or from the effective total angular momentum J) has stronger quantum fluctuations. But spin-1 [79], spin-3/2 [80] and for spin-S cases [81–83] materials also show spin liquid phase. Recently, there has been tremendous interest in materials with multipole- interactions (mainly dipolar-dipolar and octopolar-octopolar exchange interactions) with $J > 1/2$, which has a phase called *multipolar spin liquids* having fractionalization of higher magnetic multiples, see Ref. [84] and references therein.

Following Ref. [68], the candidate materials having spin or angular momentum 1/2 are mainly with triangular lattice (such as 2D organic salts, for example $\kappa\text{-(ET)}_2\text{Cu}_2(\text{CN})_3$ and $\text{EtMe}_3\text{Sb}[\text{Pd}(\text{dmit})_2]_2$), Kagome lattice (such as herbertsmithite and Zn-Barlowite), and Kitaev materials with Honeycomb lattice (such as strong-spin-orbit coupled materials, $\alpha\text{-RuCl}_3$)¹¹.

In addition to the real materials, synthetic materials based on Rydberg atoms are used to prepare spin liquid phases [85, 86]. The 2D arrangement of neutral atoms with excitations, i.e., to a Rydberg state: a two-level system analogous to the qubit, having controlled interactions, can be used as a programmable quantum simulator [87, 88] and references therein.

¹¹ See Sec. 1.3.4 for detailed discussion on Kitaev materials

1.2 Algebraic spin liquids

As discussed in the previous sections, the spinons in the spin liquids can have a gapped or gapless spectrum. For the gapped spectrum, the spin liquids are stable phases. But there are cases when the spinon spectrum possesses gapless Dirac-like linear dispersion, such as staggered flux (sF) and π -flux (π F) phases. These are called the 'Dirac spin liquids' or 'algebraic spin liquids' [89]. These states have enhanced stability in non-bipartite lattices compared to bipartite lattices [45, 51].

Let us consider the π F phase, a prototypical example of one of the algebraic spin liquids. The mean field Hamiltonian is

$$H_{\text{MF}} = -t \sum_{\langle rr' \rangle} f_{r\alpha}^\dagger e^{-ia_{rr'}} f_{r'\alpha} + \text{h.c.}, \quad (1.18)$$

where $a_{rr'}$ are $U(1)$ gauge fields living on the bonds of the lattice. $a_{rr'}$ are chosen such that each plaquette gives π -flux state in a lattice. The π F state in different lattices corresponds to different configurations of fluxes- $0, \pi$ on the lattice; see [51]. To assess the stability of the phase, a low energy theory is considered, which is quantum electrodynamics in 2+1 dimensions (QED_3) with $\alpha = 4$ -flavors. The four flavors are two spins and the other two valley points in the Dirac spectrum. Any bilinear operators that produce mass for any of the 4-flavor fermions are irrelevant and stabilize the phase. However, monopoles (which change the flux by 2π) are local operators that can be written as the polynomial of the fermionic operators. These monopole operators are trivial under physical symmetries in the bipartite lattices, so they can be included in the action and make the spin liquid unstable. However, in the case of non-bipartite lattices, the monopole operators are not trivial, and the spin liquid is stable. One can include different symmetry-allowed monopole operators in the action that are relevant and drive the phase away from spin liquids to the particular ordered phase; see Ref. [45, 51, 90] also Ref. [91] for recent study on $SU(8)$ -Dirac systems. Hence, the algebraic spin liquids are treated as the parent state for many symmetry-allowed ordered states of the Hamiltonian.

1.3 Kitaev Model: Z_2 -spin liquids

The Kitaev Honeycomb model [57] is one of the few exactly solvable models in 2D. The features of QSLs, like fractionalization, emergent gauge fields, and topological excitations, discussed via mean field analysis in Sec. 1.1.2 are relatively easily understood in this model. Later, many spin-orbital coupling models depicting the Kitaev model were discussed, called the '*compass models*,' which are also exactly solvable.

1.3.1 The Model

The Hamiltonian is

$$H_{\text{Kitaev}} = -J_x \sum_{\langle ij \rangle_x} \sigma_i^x \sigma_j^x - J_y \sum_{\langle ij \rangle_y} \sigma_i^y \sigma_j^y - J_z \sum_{\langle ij \rangle_z} \sigma_i^z \sigma_j^z. \quad (1.19)$$

Here i, j label the sites of a hexagonal lattice, $\langle ij \rangle_\alpha$ with $\alpha = x, y, z$ denotes the nearest neighbor bonds along the α direction, shown in Fig. 1.1. Exchange interactions are different in each nonequivalent bond, resulting in a geometrical exchange frustration in the model. This means fixing spin polarisation along one direction, say z -direction for minimizing the zz term, will not satisfy the xx - and yy - terms in other neighbors. The xx - and yy - terms give quantum fluctuations to the z -polarised phase and destroy the ordered phase. So, this does not show any order even at $T=0$. However, the existence of an extensive number of conserved quantities makes this model solvable exactly. The conserved quantities are plaquette operators in each plaquette p , shown in Figure. 1.1, defined as.

$$W_p = \sigma_1^{\alpha_{1,2}} \sigma_2^{\alpha_{1,2}} \sigma_2^{\alpha_{2,3}} \sigma_3^{\alpha_{2,3}} \sigma_3^{\alpha_{3,4}} \sigma_4^{\alpha_{3,4}} \sigma_4^{\alpha_{4,5}} \sigma_5^{\alpha_{4,5}} \sigma_5^{\alpha_{5,6}} \sigma_6^{\alpha_{5,6}} \sigma_6^{\alpha_{6,1}} \sigma_1^{\alpha_{6,1}}, \quad (1.20)$$

where, $\alpha_{i,j} = x, y, z$ bonds connecting bonds i and j . Using $\sigma^x \sigma^y = i\sigma^z$, the W_p operator is a product of the out-going spin component at each site of 6 sites of the plaquette, defined as

$$W_p = \sigma_1^x \sigma_2^y \sigma_3^z \sigma_4^x \sigma_5^y \sigma_6^z. \quad (1.21)$$

Eigenvalues of W_p are ± 1 as $W_p^2 = \mathbf{1}$, a Z_2 operator. These loop operators commute with Hamiltonian, $[H_{\text{Kitaev}}, W_p] = 0$, and with each other $[W_p, W_{p'}] = 0$. The exact solution for H_{Kitaev} for each invariant subspace of different $\{W_1, W_2, W_3, \dots, W_N\}$ with N being the total number of plaquettes. The spectrum is solved in terms of fractionalized quasiparticles. Kitaev solved this model by writing the spin at each site in terms of four Majorana fermions [57].

1.3.2 Exact Solution in Majorana Representation

In general, Majorana fermions (c_1, c_2) do not have any physical significance and can be viewed as the real and imaginary parts of a complex fermion (a) as

$$c_1 = (a^\dagger + ia), \quad c_2 = i(a^\dagger - ia).$$

Notionally, with Hilbert space dimension of Majorana fermion is $\sqrt{2}$. At each site, one can define four Majorana fermions c, c^α , $\alpha = x, y, z$ with $c^{\alpha^\dagger} = c^\alpha$ hence $(c^\alpha)^2 = 1$ and obey the

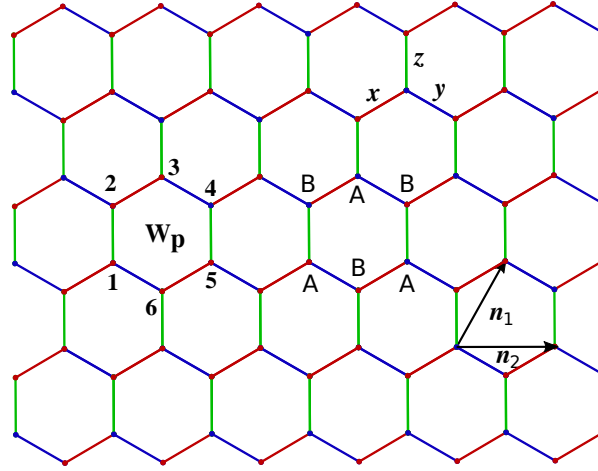


Fig. 1.1 A honeycomb lattice with two sublattices denoted by A and B. A unit cell consisting of two sublattice sites with basis vectors $\mathbf{n}_1 = (\sqrt{3}, 0)$ and $\mathbf{n}_2 = (\frac{\sqrt{3}}{2}, \frac{3}{2})$ is shown. Corresponding reciprocal lattice vectors are $\mathbf{G}_1 = 2\pi(\frac{1}{\sqrt{3}}, \frac{-1}{3})$ and $\mathbf{G}_2 = 2\pi(0, \frac{2}{3})$. The nearest neighbor distance, a , is taken to be a unit. W_p corresponds to a loop operator in each plaquette.

usual fermionic anti-commutational relations $\{c^\alpha, c^\beta\} = 2\delta_{\alpha\beta}$. In writing complex fermions into Majorana fermions, the Hilbert space dimension increases from 2^{2N} to 4^{2N} with N unit cells consisting of two spins (two sublattice sites in the Honeycomb unit cell). A representation of Pauli spin operators $\sigma_x, \sigma_y, \sigma_z$ into these Majorana fermions is given by

$$\sigma^x = ic^x c, \quad \sigma^y = ic^y c, \quad \sigma^z = ic^z c,$$

In the extended space with a constraint $(\sigma^\alpha)^\dagger = \sigma^\alpha, (\sigma^\alpha)^2 = 1$,

$$\sigma_x \sigma_y \sigma_z = i$$

with $cc^x c^y c^z = 1$ ¹². There is one more Majorana representation, where spins are represented by three Majorana fermions, c^x, c^y , and c^z , without any physical constraint. Still, the Hilbert space dimension has to be chosen properly for exact mapping [93, 94]. This is also studied in terms of Schwinger fermions discussed in the first section, and it is exactly solvable- which is a p -wave pairing term of spinons [95, 96]. By denoting $c_j c_j^x c_j^y c_j^z$ at each site j as D_j , impose a condition on states on extended Hilbert space to get physical states

¹²This model is also exactly solvable by doing a Jordan-Wigner (JW) transformation [92]. JW transformation is not usually suitable for 2D models because there will be a non-local string of spin operators that lies with the local fermion operators, making the JW transformation not useful. But in the Kitaev model, the local string gets canceled out because of the special structure of the Hamiltonian.

$$(D_j - 1)|\psi\rangle_{phys} = 0.$$

The above constraint is similar to the constraint of single-site occupancy in the Heisenberg model. As mentioned before, these constraints are significant and have physical implications. In general, implementing this constraint in calculations is quite tricky, and the Gutzwiller projection method of imposing is one among them. Here, the imposition of this constraint is easy for the ground state, where the constraint is taken care of automatically when working with the invariant flux subspace. The Hamiltonian will result into

$$H_{\text{Kitaev}} = - \sum_{a=x,y,z} J_a \sum_{\langle ij \rangle_a} i c_i u_{\langle ij \rangle_a} c_j, \quad (1.22)$$

where $u_{\langle ij \rangle_a} = i c_i^a c_j^a$ is the operator at the link between i and j sites with the bond represented by a . $u_{\langle ij \rangle_a}$ is hermitian and

$$u_{\langle ij \rangle_a}^2 = 1.$$

with eigen values $u_{\langle ij \rangle_a} = \pm 1$ and it commutes with Hamiltonian (1.22), $[H, u_{\langle ij \rangle_a}] = 0$. Since $u_{\langle ij \rangle_a} = -u_{\langle ji \rangle_a}$, use the convention that i belongs to sublattice A with j corresponding to B sublattice. The above Hamiltonian has Z_2 gauge redundancy, where the Hamiltonian is invariant by transformations: $u_{\langle ij \rangle_a} \rightarrow \eta_i u_{\langle ij \rangle_a} \eta_j$ with $c_i \rightarrow \eta_i c_i$. Since this invariance is not present in the parent Hamiltonian in Eq. 1.19, hence is called 'emergent.' The above Hamiltonian is invariant under transformation from $J_\alpha = +1$ to $J_\alpha = -1$, $\forall \alpha$, in which the sign can be absorbed into the corresponding u_{ij}^α without changing the model. The physics of the model is the same for both ferromagnetic and antiferromagnetic interactions J , which is no longer the case if the external magnetic field is applied. The $u_{\langle ij \rangle_a}$ are interpreted as Z_2 gauge fields on each bond. In terms of these link operators, the plaquette operators (1.21) become

$$W_p = -u_{\langle 12 \rangle_z} u_{\langle 23 \rangle_x} u_{\langle 34 \rangle_y} u_{\langle 45 \rangle_z} u_{\langle 56 \rangle_x} u_{\langle 61 \rangle_y}. \quad (1.23)$$

This measures the flux passing through the plaquette p . This is similar to Wilson loop operators in gauge theories. The particle that traverses over the plaquette acquires a phase corresponding to Aharonov-Bohm-like flux of either 0 or π , i.e., gauge invariant Z_2 vortex charges ± 1 , respectively. $W_p = +1$ at the plaquette is termed flux-free, and π -flux in the other case.

The Hamiltonian (Eq. 1.22) is a simple, non-interacting Majorana fermion coupled with static Z_2 gauge fields. For lattice of N unit cells with two spins in each unit cell, all the eigenstates can be written as a product of 2^N dimensional Fock space of c_i Majorana fermions (*matter sector* denoted as M_G) and 2^{3N} dimensional space of Z_2 link variables (*gauge field sector* is denoted with G). The extended Hamiltonian of dimension 4^N is the direct product of

these two subspaces.

$$|\psi\rangle = |M_G; G\rangle = |M_G\rangle |G\rangle.$$

This perfect decoupling of the gauge and matter sectors makes them treated independently and, hence, exactly solvable. This is no longer the case in the presence of perturbations. Coupling these sectors has important implications, as found in our work [97] shows rich phases like glass and amorphous crystal phases (See Chapter 3 for details). As Lieb's theorem dictates, the gauge sector is flux-free in the low-energy ground state. Hence, the ground state has $W_p = +1$ at each plaquette. This is achieved by fixing the bond operators in each bond $u_{ij}^\alpha = +1$. Since the Hamiltonian is invariant under Z_2 -gauge transformations, fixing the gauge is necessary. Therefore, $u_{ij}^\alpha = +1, \forall \alpha$, for $i(j) \in \text{sub-lattice A (B)}$, or otherwise $u_{ij}^\alpha = -1$. This simplifies the model, Eq. 1.22 into only the matter sector, the free hopping matter Majorana fermions (c) in the Honeycomb lattice. The spectrum consists of gapped and gapless bands depending on the parameters, J_α . For $J_\alpha \geq J_\beta + J_\gamma$, the bands are gapped. The low-energy gauge field model is equivalent to the Toric code [39], another toy model introduced by Kitaev. The excitations are abelian. In the other case, $J_\alpha \leq J_\beta + J_\gamma$, there exists gapless linearly dispersive gapless points at $\pm \mathbf{K} = \pm \frac{4\pi}{3\sqrt{3}a}(1, 0)$ in the spectrum. This is exactly like the dispersion relation for electrons in graphene. For Majorana fermions, the Brillouin zone is half of the electron counterpart because $c_i^{\alpha\dagger} = c_i$ implies $c_{\mathbf{k}}^{\alpha\dagger} = c_{-\mathbf{k}}$. So one considers only half of the BZ for the Majorana fermion case. The energy to create a single π -flux in a plaquette is finite, called vison gap in the literature, and it is approximately $E_{\text{vison}} \approx 0.15J$ at $J_x = J_y = J_z = J$ [57]. The visons are always gapped. That means the visons are frozen and massively heavy particles. The gap to create a pair of visons in the nearest neighbor plaquettes ($E_{\text{vison-pair}} \approx -0.04$, see Appendix. A of Ref. [57]) is much less than the gap to create a single vison.

The low-energy excitations of the model are matter fermions (c) and visons/ π -flux excitations. A single spin-flip is fractionalized into a matter Majorana excitations and a pair of visons. This Fractionalization differs from the one mentioned in the Sec. 1.1.2. Another characteristic of spin liquids is the short-range correlations of the spins. In the Kitaev model, the spin-spin correlations are ultra-short-range [98], meaning the correlations are zero if the spins belong to sites beyond the nearest neighbors; see Appendix. A.2 for detailed results.

1.3.3 External Perturbations: Small Magnetic field

The exact solvability of the model, Eq. 1.19, is not present once any external magnetic field is applied. Also, the model for $J_\alpha = +1$ and $J_\alpha = -1$ is no longer equivalent to the applied magnetic field. Since external perturbations give dynamics to the visons, the matter sector and gauge section intermix, and the problem becomes non-trivial. In the presence of the time

reversal breaking term like an applied magnetic field, another interesting aspect of the model is related to the gapless region. We focus on $J_x = J_y = J_z = J$ region throughout here unless otherwise mentioned. If the magnetic field is applied along [111], the spins couple to the external field via Zeeman term. The Hamiltonian is

$$H = H_{\text{Kitaev}} - \sum_i h_x \sigma_i^x + h_y \sigma_i^y + h_z \sigma_i^z. \quad (1.24)$$

As mentioned, the plaquette operators are no longer conserved $[H, W_p] \neq 0$. This Hamiltonian can be solvable perturbatively exactly in the limit of small magnetic fields, $h_x, h_y, h_z \ll J$, i.e., by preserving in the flux-free sector. So, this approximation is valid for the region where $h_x, h_y, h_z \ll E_{\text{vortex}}$. The leading correction to the H_{Kitaev} is the third-order interaction between spins. The first-order term is zero, and the second-order term preserves the time-reversal symmetry and does not change the physics of the Kitaev model. So, the effective Hamiltonian is

$$H_{\text{pert}} = H_{\text{Kitaev}} - \frac{h_x h_y h_z}{J^2} \sum_{\langle\langle i,j,k \rangle\rangle} \sigma_i^\alpha \sigma_j^\beta \sigma_k^\gamma, \quad \alpha \neq \beta \neq \gamma, \quad (1.25)$$

where i, j , and k are the three nearest neighbor sites, α, β, γ are chosen such that the ending site spin component points inwards to the middle. Another interesting aspect of the model is the gap opening in the Majorana dispersion with time-reversal symmetry, i.e., with applied magnetic field. Using Majorana fermionic representation, the Hamiltonian results into

$$H_{\text{pert}} = - \sum_{a=x,y,z} J_a \sum_{\langle ij \rangle_a} i c_i u_{\langle ij \rangle_a} c_j - iK \sum_{\langle\langle i,j,k \rangle\rangle} u_{\langle ij \rangle_a} u_{\langle jk \rangle_\gamma} c_i c_k. \quad (1.26)$$

In the flux-free sector, the perturbation term introduces the next nearest neighbor hopping to the matter Majorana fermions. As a result, the gap appears in the band structure, just like the gap in the Haldane model [99]. These gapped bands have non-zero Chern numbers and gapless Majorana zero modes at the edge. Since the Majorana fermions have no charge, neutral particles carry only thermal energy. This is one of the smoking gun signatures used in experiments [100, 101]. Although experiments [100] presented the thermal Hall signature for the existence of Majorana fermionic edges, and the results are sample dependent [102], yielding no conclusions. [103]

Theoretically, the Hamiltonian, Eq. 1.26, and its ground state are equivalent to the $p + ip$ superconductor. This can be seen by combining Majorana fermions from two nearest neighbor sites into a complex fermion (called bond fermions [98]). The excitations of the $p+ip$ superconductor are non-abelian [104]: the fermion, a vortex, and a semion (fermion + vortex). Here, the semion has one unpaired Majorana bound to it. The created vortex in semion provides

an edge from the regular vacuum to the bulk of $p + ip$ SC. Consequently, the gap-less Majorana fermion edge adheres to the vortex [105], so-called Majorana Zero Mode (MZM). In the case of the Kitaev model, a π -flux, if created on top of a uniform flux-free ground state, bound with the unpaired Majorana fermion, forms an MZM. There is an issue: a single π -flux can not be created. They are only created in pairs. By flipping the bond operator, $u_{\langle ij \rangle \alpha}$, the two plaquettes common to the bond accommodate the flux pair. The single π -flux is created by taking one of the fluxes in the pair to infinity. In the finite system, taking these fluxes far enough distances is enough. So, each π -flux accommodates one zero mode, resulting in two modes with zero energy. When the fluxes are brought closer, the two Majorana combine and give one complex fermion, and the zero modes will be gaped.

Another key ingredient of QSLs is the presence of long-range entanglement measured using entanglement entropy. As discussed in previous sections, the phase (both Abelian and non-Abelian phases) also has the entanglement entropy obeying the area law. It has a universal term, topological entanglement entropy, $S_{\text{topo}} = -\log 2$ [106]. The topological degeneracy is very easy to see in the case of Abelian case [107]- which is equivalent to the toric code model¹³. Consider, for example, a torus; there exist four Z_2 global operators that are products of σ^z on two closed strings, denote them by C_x, C_y for along x -string and y -string, and similarly, two operators from the product of σ^x on the same two closed strings, denote them by D_x, D_y ¹⁴. These four operators commute with the Hamiltonian. They have commutation relations as $\{C_x, D_y\} = 0$ and $\{C_y, D_x\} = 0$, and all remaining operators commute with each other. The four states labeled by C_x, C_y states have differed by different D_x, D_y values and have the same energy- degenerate. This argument is similar to any genus- g manifold [39]. As mentioned in the previous sections, this topological degeneracy is global and depends on the manifold.

1.3.4 Material realization- Kitaev Materials

The exchange interactions of the Kitaev model, Eq. 1.19, are peculiar and proposed as a toy model for realizing exotic excitations with fractional statistics for topological computation. Jackeli and G. Khaliullin [108] showed that there are few materials whose effective Hamiltonian has Kitaev exchange interactions in addition to other exchange terms. Transition metal ions such as Ir, Ru, Os, and Rh have strong spin-orbit coupling exceeding intersite interactions; the spin and orbitals interlock. When a single hole in the triply degenerate t_{2g} orbitals is present, the interplay of spin-orbit coupling and tetragonal splitting gives effective spin-1/2

¹³The Hamiltonian is $H_{\text{toric-code}} = -J \sum_s A_s + \sum_p B_p$, where $A_s = \prod_{i \in s} \sigma_i^x$ at each vortex, s and $B_p = \prod_{i \in p} \sigma_i^z$ at each plaquette p .

¹⁴These operators are the ones which move fractional excitations e and m in the toric code along the path of strings. The commutations indicate the statistics of the particles involved.

isospin to bond-dependent compass models. When the transition metal is combined with alkali metals into layered compounds A_2BO_3 , the Kitaev model can be realized [109]. One of the popular and recent materials of interest is in the ruthenium compound, α - $RuCl_3$ [110–112]. In addition to Kitaev interactions, exchange interactions like Heisenberg and exotic exchanges like Γ -exchanges also appear. The insulating materials have zig-zag spin ordering, and when applied in-plane magnetic field along the $[11 - 2]$ direction, the Kitaev exchange dominates at the intermediate field strength approximately from 7 Tesla to 11 Tesla, and the Kitaev spin liquid with Majorana edges is proposed to exist [100]. The Majorana edge modes can be identified by half quantization of thermal hall conductivity [100]. This proposal has been under debate, claiming that the intermediate field region shows oscillatory behavior in in-plane thermal conductivity with no $1/2$ quantization in thermal hall conductivity [103]. Other experiments supporting the Majorana edges, [101, 102] and gave a possible explanation for the oscillations in the thermal conductivity: these are due to multiple phase transitions implied by considering phonons are not completely oscillations. In addition to that puzzle, another experiment [113] claimed that the intermediate field region has large zero-temperature non-linear susceptibilities, and their behavior as a function of temperature does not match any of the known ordered/disordered phases, such as ferro/anti-ferro magnet or spin glass phase. In our work [97], we found that the higher non-linear susceptibilities are due to the glassiness of the excitations present in the Kitaev model. Which is presented in Chapter 3.

More recently, there has been a lot of interest in higher spin generalization of the Kitaev model [82, 83, 114, 115] with few experimental proposals [80, 82, 116] in materials. Even with spin- S Kitaev model, theoretically the exact solution exists like in spin- $1/2$ case by extending the Majorana fermion representation into general spin- S case [117], especially with spin $3/2$ in CrI_3 [80, 116] and spin-1 in NiI_2 [114].

A

Appendices for chapter 1

A.1 Topological Degeneracy

In this section, I discuss the details of the topological degeneracy of the ground state with topological order. Consider a torus with genus $g = 2$ as a manifold for example. Denote the translational operator, T_x , for traversing fractionally charged quasiparticles, with a charge of $1/q$ along the x -axis and, similarly, T_y along the y -axis. If Aharonov-Bohm flux quanta are threaded along the x -axis, denoted with \mathcal{F}_x , the quasiparticle acquires a phase $e^{2\pi i/q}$ after its return to the same position. This is written as

$$\mathcal{T}_x \mathcal{F}_x = e^{2\pi i/q} \mathcal{F}_x \mathcal{T}_x. \quad (\text{A.1})$$

Similarly, for \mathcal{T}_y and \mathcal{F}_y . But, quasiparticles traversing along the x -direction do not have any effect from flux passing through the y -direction, i.e., $\mathcal{T}_x \mathcal{F}_y = \mathcal{F}_y \mathcal{T}_x$, and the same for $\mathcal{T}_y, \mathcal{F}_x$. So, the operators $\mathcal{T}_\S, \mathcal{F}_\dagger$ have eigenstates simultaneously, i.e. $|t_x, f_y\rangle$. \mathcal{T}_x changes the eigenvalue of \mathcal{F}_x to $f_x e^{-2i\pi/q}$ - give q degenerate states which are $\left[f_y e^{-2i\pi/q} (\mathcal{T}_x |t_x, f_y\rangle) \right]$. Similarly, $\mathcal{T}_y, \mathcal{F}_y$ give q more of degenerate states: $\left[f_y e^{-2i\pi/q} (\mathcal{T}_y |t_y, f_y\rangle) \right]$. But, all these states are independent of each other. This we can see by calculating the commutation relations between $\mathcal{T}_x, \mathcal{T}_y$

and $\mathcal{F}_x, \mathcal{F}_\dagger$. They have non-trivial commutations depending on the statistics of the particles. Consider exchanging two particles to acquire a phase $e^{i\theta}$, θ depending on the statistics of the quasiparticles, which is $e^{\pi i/q}$. This process creates a linked knot between the worldlines of the two quasiparticles, denoted as follows:

$$\begin{aligned}\mathcal{T}_x^{-1}\mathcal{T}_y^{-1}\mathcal{T}_x\mathcal{T}_y &= e^{2i\pi/q}, \\ \mathcal{T}_x\mathcal{T}_y &= e^{2i\pi/q}\mathcal{T}_y\mathcal{T}_x,\end{aligned}\tag{A.2}$$

Using this relation,

$$\mathcal{T}_x\mathcal{T}_y|t_x, f_y\rangle = t_x e^{2i\pi/q}(\mathcal{T}_y|t_x, f_y\rangle).\tag{A.3}$$

The repeated action of \mathcal{T}_y can change eigenvalues of $\mathcal{F}_y, \mathcal{T}_x$ operators to $(f_y e^{-2i\pi/q}, t_x e^{2i\pi/q})$ - give q states and using commutation relations $\mathcal{F}_x, \mathcal{F}_y$ give rise to the same set of q degeneracy states¹. As a result, only q -states are independent. This argument can be generalized to number of punching holes, giving rise to q^g , for genus, g , manifold.

A.2 Ultra short-range spin-spin Correlations in Kitaev Model

This section give the detailed derivation of the ultra-short range spin correlations of the Kitaev model. Forming complex fermions in terms of Majorana fermions in matter and gauge sector subspaces as matter fermions (denote f_i) and bond fermions (denote $\chi_{\langle ij \rangle a}$) respectively

$$f_i = \frac{1}{2}(c_i + ic_i),\tag{A.4}$$

$$\chi_{\langle ij \rangle a} = \frac{1}{2}(c_i^a + ic_j^a).\tag{A.5}$$

The link variables defined in the main text 1.3 can be related to bond fermions as $u_{\langle ij \rangle a} = ic_i c_j^a = 2\chi_{\langle ij \rangle a}^\dagger \chi_{\langle ij \rangle a} - 1$ and

$$\chi_{\langle ij \rangle a}^\dagger \chi_{\langle ij \rangle a} |G\rangle = n_{ij} |G\rangle\tag{A.6}$$

with $n_{\langle ij \rangle a} = \frac{u_{\langle ij \rangle a} + 1}{2}$. In terms of these bond fermions, the spin operators become

¹ $\mathcal{T}_{x,y}$ are equivalent to $\mathcal{F}_{y,x}$. As a result, only one independent magnetic algebra arises in the ground state manifold

$$\begin{aligned}
c_i^a &= (\chi_{\langle ij \rangle a} + \chi_{\langle ij \rangle a}^\dagger), \\
c_j^a &= (\chi_{\langle ij \rangle a} - \chi_{\langle ij \rangle a}^\dagger), \\
\sigma_i^a &= ic_i(\chi_{\langle ij \rangle a} + \chi_{\langle ij \rangle a}^\dagger), \\
\sigma_j^a &= ic_j(\chi_{\langle ij \rangle a} - \chi_{\langle ij \rangle a}^\dagger).
\end{aligned} \tag{A.7}$$

These bond fermions change the link operators corresponding to that bond. Hence, the fluxes in the plaquettes adjacent to that bond will change from 1 to -1 or vice versa and denote these symbolically as

$$\sigma_i^a = ic_i(\chi_{\langle ij \rangle a} + \chi_{\langle ij \rangle a}^\dagger) \rightarrow ic_i\pi_{\langle ij \rangle a}\pi_{\langle ij \rangle a}, \tag{A.8}$$

where $\pi_{\langle ij \rangle a}$ will add the fluxes in the plaquettes adjacent to bond $\langle ij \rangle_a$. From these results, the dynamical spin-spin correlation function in the ground state becomes

$$\begin{aligned}
S_{ij}^{ab}(t) &= \langle M_G | \langle G | \sigma_i^a(t) \sigma_j^b(0) | G \rangle | M_G \rangle, \\
&= \langle M_G | \langle G | (e^{iHt} ic_i(\chi_{\langle ij' \rangle a} + \chi_{\langle ij' \rangle a}^\dagger) e^{-iHt})(ic_j(\chi_{\langle i'j \rangle b} - \chi_{\langle i'j \rangle b}^\dagger)) | G \rangle | M_G \rangle,
\end{aligned} \tag{A.9}$$

where i' and j' fixed by the bond $\langle ij' \rangle$ and $\langle i'j \rangle$ respectively. In the Kitaev honeycomb model, the ground state corresponds to a flux-free case, so consider $u_{\langle ij \rangle a} = +1$. As a result, $\chi_{\langle ij \rangle a}^\dagger \chi_{\langle ij \rangle a} | G \rangle = 1$ from equ. (A.6) and hence $\chi_{\langle ij \rangle a}^\dagger | G \rangle = 0$. Using quantum mechanical identity for any operators A, B

$$Be^A = e^{A-D}B \text{ if } [A, B] = DB, \text{ and } [D, B] = 0, \tag{A.10}$$

and $[\chi_{\langle ij \rangle a}^\dagger \chi_{\langle ij \rangle a}, \chi_{\langle ij \rangle b}] = \chi_{\langle ij \rangle a} \delta_{ab}$, simplifying equ. (A.9)

$$S_{ij}^{ab}(t) = \langle M_G | \langle G | (e^{iHt} ic_i e^{-i(H-V_{\langle ij \rangle a})t} (\chi_{\langle ij' \rangle a}^\dagger)) (ic_j \chi_{\langle i'j \rangle b}) | G \rangle | M_G \rangle \text{ where } V_{\langle ij \rangle} = -2jc_i c_j, \tag{A.11}$$

In the interaction representation, this becomes

$$S_{ij}^{ab}(t) = \langle M_G | \langle G | (ic_i(t) T(e^{-2J_a \int_0^t c_i(\tau) c_j(\tau) d\tau}) (-1) c_j (\chi_{\langle ij' \rangle a}^\dagger \chi_{\langle i'j \rangle b})) | G \rangle | M_G \rangle, \tag{A.12}$$

with in the ground state: $\langle G | \chi_{\langle ij' \rangle a}^\dagger \chi_{\langle i'j \rangle b} | G \rangle = \delta_{i,i'} \delta_{j,j'} \delta_{a,b} \delta_{\langle ij \rangle} = \delta_{a,b} \delta_{\langle ij \rangle a}$

$$S_{ij}^{ab}(t) = \langle M_G | (ic_i(t) T(e^{-2J_a \int_0^t c_i(\tau) c_j(\tau) d\tau}) (-1) c_j | M_G \rangle \delta_{\langle ij \rangle a}. \quad (\text{A.13})$$

As $\delta_{\langle ij \rangle a}$ indicates, the spin correlations are only limited to nearest neighbor distances, ultra-short range. This is because of the static nature of the fluxes.

A.2.1 Static Spin Correlations

From dynamic spin correlation expression equ. (A.13), static spin correlations become

$$S_{ij}^{ab}(t=0) = -i \langle M_G | c_i c_j | M_G \rangle. \quad (\text{A.14})$$

These are exact results, and to solve equ. (A.14), use matter fermions as defined in equ. (A.4), $c_{A,i} = f_i + f_i^\dagger$ and $c_{B,i} = -i(f_i - f_i^\dagger)$. The spin correlation function in equ. A.14 become

$$S_{ij}^{ab}(t=0) = -i \langle M_G | (f_i + f_i^\dagger) i (f_i^\dagger - f_i) | M_G \rangle, \quad (\text{A.15})$$

operators can be transformed into momentum space as

$$f_{\mathbf{q}} = \frac{1}{\sqrt{2N}} \sum_{\mathbf{r}_i} e^{i\mathbf{q} \cdot \mathbf{r}_i} f_i, \quad (\text{A.16})$$

equ. A.14 becomes

$$S_{ij}^{ab}(t=0) = \frac{1}{2N} \langle M_G | \left(\sum_{\delta_i, \mathbf{q}} (f_{\mathbf{q}}^\dagger f_{-\mathbf{q}}^\dagger + f_{\mathbf{q}} f_{\mathbf{q}}^\dagger) e^{i\mathbf{q} \cdot \delta_i} - (f_{\mathbf{q}}^\dagger f_{\mathbf{q}} + f_{\mathbf{q}} f_{-\mathbf{q}}) e^{-i\mathbf{q} \cdot \delta_i} \right) | M_G \rangle. \quad (\text{A.17})$$

with simple Bogoliubov transform solves problem with $\theta_{\mathbf{q}} = -\frac{\text{Im}(S(\mathbf{q}))}{\text{Re}(S(\mathbf{q}))}$,

$$\begin{pmatrix} f_{\mathbf{q}} \\ f_{-\mathbf{q}}^\dagger \end{pmatrix} = \begin{pmatrix} \cos(\theta_{\mathbf{q}}) & i \sin(\theta_{\mathbf{q}}) \\ i \sin(\theta_{\mathbf{q}}) & \cos(\theta_{\mathbf{q}}) \end{pmatrix} \begin{pmatrix} a_{\mathbf{q}} \\ a_{-\mathbf{q}}^\dagger \end{pmatrix},$$

Denote $\sum_{\delta_i} J_{a(\delta_i)} e^{\mathbf{q} \cdot \delta_i}$ by $S(\mathbf{q})$, with δ_i are vectors along the bonds denoted with i , $\delta_x = (\frac{1}{2}, \frac{\sqrt{3}}{2})$, $\delta_y = (\frac{1}{2}, -\frac{\sqrt{3}}{2})$ and $\delta_z = (0, 0)$. equ. (A.17) gives

$$S_{ij}^{ab} = \frac{1}{2N} \sum_{\mathbf{q}} \cos(2\theta_{\mathbf{q}}), \quad (\text{A.18})$$

where $\cos(2\theta_{\mathbf{q}}) = \frac{\text{Im}(S(\mathbf{q}))}{S(\mathbf{q})}$. By converting sum into integral over Brillouin zone and transforming integral in $\mathbf{q}_x, \mathbf{q}_y$ into $\mathbf{q}_1 = \mathbf{q} \cdot \delta_x$ and $\mathbf{q}_2 = \mathbf{q} \cdot \delta_y$ with Jacobian $\frac{\sqrt{3}}{2}$, will give

$$S_{ij}^{ab}(t=0) = \frac{\sqrt{3}}{16\pi^2} \int_{BZ} \cos(2\theta_{\mathbf{q}}) d\mathbf{q}_1 d\mathbf{q}_2, \quad (\text{A.19})$$

values at $J_x = J_y = J_z = 1$ is 0.47, the points in J's space at $J_x = 1, J_y = 0.1, J_z = 0.2 \rightarrow S_{ij}^{ab} = 0.098$ and $J_x = 0.1, J_y = 0.1, J_z = 0.7 \rightarrow S_{ij}^{ab} = 0.99$ at $J_x = 0.1, J_y = 0.7, J_z = 0.1 \rightarrow S_{ij}^{ab} = 0.069$. To see fractionalization, consider the time evolution of a single spin operation on ground state, "spin-flip", operation using (A.13) and (A.8)

$$\sigma_i^a = i c_i(t) T \left(e^{2u_{\langle ij \rangle a} J_a \int_0^t c_i(\tau) c_j(\tau) d\tau} \right) \pi_{\langle ij \rangle a} \pi_{\langle ij \rangle a}^\dagger |\psi\rangle, \quad (\text{A.20})$$

This shows freely propagating Majorana fermions as a function of time with band perturbing term, $2u_{\langle ij \rangle a} J_a c_i(t) c_j(t)$. This spin flip operation consists of Majorana fermion with π -flux pair. Spin flip operation adds fluxes to plaquettes adjacent to a-bond $\langle ij \rangle a$. As these fluxes are static and bond fermions are conserved quantities under time evaluation, the other spin flip operation in dynamical spin correlations has to remove these fluxes to have a non-zero value. By this selection rule, the other spin adds π -fluxes to adjacent site j with having bond a . This gives spin correlations to be short-ranged.

References

- [1] P. W. Anderson, [Science](#) **177**, 393 (1972).
- [2] S. Sachdev, *Quantum phases of matter* (Cambridge University Press, 2023).
- [3] C. M. Varma, [Rev. Mod. Phys.](#) **92**, 031001 (2020).
- [4] G. Giuliani and G. Vignale, *Quantum Theory of the Electron Liquid* (Cambridge University Press, 2005).
- [5] J. T. Chalker, in *Topological Aspects of Condensed Matter Physics: Lecture Notes of the Les Houches Summer School: Volume 103, August 2014* (Oxford University Press, 2017).
- [6] L. Savary and L. Balents, *Reports on Progress in Physics* **80**, 016502 (2016).
- [7] C. Lacroix, P. Mendels, and F. Mila, *Introduction to Frustrated Magnetism*, Vol. 164 (Springer Series in Solid-State Sciences, 2011).
- [8] Y. Zhou, K. Kanoda, and T.-K. Ng, [Rev. Mod. Phys.](#) **89**, 025003 (2017).
- [9] X.-G. Wen, [Phys. Rev. B](#) **65**, 165113 (2002).
- [10] P. W. Anderson, [Science](#) **235**, 1196 (1987).
- [11] J. G. Bednorz and K. A. Müller, [Zeitschrift für Physik B Condensed Matter](#) **64**, 189 (1986).
- [12] L. Pauling, *The nature of the chemical bond and the structure of molecules and crystals: an introduction to modern structural chemistry*, Vol. 18 (Cornell university press, 1960).
- [13] P. Anderson, [Materials Research Bulletin](#) **8**, 153 (1973).

-
- [14] G. Baskaran, [Ind.Journal of Phys.](#) **89**, 583 (2006).
- [15] S. A. Kivelson, D. S. Rokhsar, and J. P. Sethna, [Phys. Rev. B](#) **35**, 8865 (1987).
- [16] D. A. Ivanov and T. Senthil, [Phys. Rev. B](#) **66**, 115111 (2002).
- [17] A. Paramekanti, M. Randeria, and N. Trivedi, [Phys. Rev. B](#) **71**, 094421 (2005).
- [18] Y. Zhang, T. Grover, and A. Vishwanath, [Phys. Rev. B](#) **84**, 075128 (2011).
- [19] J. Pei, S. Han, H. Liao, and T. Li, [Phys. Rev. B](#) **88**, 125135 (2013).
- [20] J. Wildeboer, A. Seidel, and R. G. Melko, [Phys. Rev. B](#) **95**, 100402 (2017).
- [21] G. Baskaran and R. Shankar, [Mod. Phys. Lett. B](#) **2**, 1211 (1988).
- [22] E. Fradkin and S. Kivelson, [Modern Physics Letters B](#) **4**, 225 (1990).
- [23] T. Senthil and M. P. A. Fisher, [Phys. Rev. B](#) **63**, 134521 (2001).
- [24] G. Baskaran and R. Shankar, [Modern Physics Letters B; \(USA\)](#) **2** (1988).
- [25] N. Read and B. Chakraborty, [Phys. Rev. B](#) **40**, 7133 (1989).
- [26] Y. Zhang, T. Grover, A. Turner, M. Oshikawa, and A. Vishwanath, [Phys. Rev. B](#) **85**, 235151 (2012).
- [27] V. Kalmeyer and R. B. Laughlin, [Phys. Rev. Lett.](#) **59**, 2095 (1987).
- [28] D. S. Rokhsar and S. A. Kivelson, [Phys. Rev. Lett.](#) **61**, 2376 (1988).
- [29] R. Moessner, S. L. Sondhi, and E. Fradkin, [Phys. Rev. B](#) **65**, 024504 (2001).
- [30] F. Verstraete, M. M. Wolf, D. Perez-Garcia, and J. I. Cirac, [Phys. Rev. Lett.](#) **96**, 220601 (2006).
- [31] N. Schuch, D. Poilblanc, J. I. Cirac, and D. Pérez-García, [Phys. Rev. B](#) **86**, 115108 (2012).
- [32] D. Poilblanc, N. Schuch, D. Pérez-García, and J. I. Cirac, [Phys. Rev. B](#) **86**, 014404 (2012).
- [33] J. I. Cirac, D. Pérez-García, N. Schuch, and F. Verstraete, [Rev. Mod. Phys.](#) **93**, 045003 (2021).

- [34] M. C. Bañuls, [Annual Review of Condensed Matter Physics](#) **14**, 173 (2023).
- [35] P. C. G. Vlaar and P. Corboz, [SciPost Phys.](#) **15**, 126 (2023).
- [36] R. T. Ponnaganti, M. Mambrini, and D. Poilblanc, [Phys. Rev. B](#) **106**, 195132 (2022).
- [37] R. Moessner and K. S. Raman, in *Introduction to frustrated magnetism: materials, experiments, theory* (Springer, 2010) pp. 437–479.
- [38] N. Read and S. Sachdev, [Phys. Rev. Lett.](#) **66**, 1773 (1991).
- [39] A. Kitaev, [Annals of Physics](#) **303**, 2 (2003).
- [40] E. Fradkin and S. Kivelson, [Modern Physics Letters B](#) **4**, 225 (1990).
- [41] R. Moessner, S. L. Sondhi, and E. Fradkin, [Phys. Rev. B](#) **65**, 024504 (2001).
- [42] G. Baskaran, Z. Zou, and P. Anderson, [Solid State Communications](#) **88**, 853 (1993), special Issue A Celebratory Issue to Commemorate 30 Years of Solid State Communications.
- [43] S. Liang, B. Doucot, and P. W. Anderson, [Phys. Rev. Lett.](#) **61**, 365 (1988).
- [44] T. Dombre and G. Kotliar, [Phys. Rev. B](#) **39**, 855 (1989).
- [45] M. Hermele, T. Senthil, and M. P. A. Fisher, [Phys. Rev. B](#) **72**, 104404 (2005).
- [46] T. Li and H.-Y. Yang, [Phys. Rev. B](#) **75**, 172502 (2007).
- [47] G. Baskaran, Z. Zou, and P. Anderson, [Solid State Communications](#) **63**, 973 (1987).
- [48] X. G. Wen, [Phys. Rev. B](#) **44**, 2664 (1991).
- [49] C. Mudry and E. Fradkin, [Phys. Rev. B](#) **49**, 5200 (1994).
- [50] Y. Huh, M. Punk, and S. Sachdev, [Phys. Rev. B](#) **84**, 094419 (2011).
- [51] X.-Y. Song, C. Wang, A. Vishwanath, and Y.-C. He, [Nature Communications](#) **10**, [10.1038/s41467-019-11727-3](https://doi.org/10.1038/s41467-019-11727-3) (2019).
- [52] F. Wang and A. Vishwanath, [Phys. Rev. B](#) **74**, 174423 (2006).
- [53] Y. Zhou and X.-G. Wen, Quantum orders and spin liquids in Cs_2CuCl_4 (2003), [arXiv:cond-mat/0210662](https://arxiv.org/abs/cond-mat/0210662) [cond-mat.str-el] .

- [54] Y. Huh, M. Punk, and S. Sachdev, *Phys. Rev. B* **84**, 094419 (2011).
- [55] A. Kitaev and J. Preskill, *Phys. Rev. Lett.* **96**, 110404 (2006).
- [56] I. H. Kim, M. Levin, T.-C. Lin, D. Ranard, and B. Shi, *Phys. Rev. Lett.* **131**, 166601 (2023).
- [57] A. Kitaev, *Annals of Physics* **321**, 2 (2006).
- [58] J. Preskill, *California institute of technology* **16**, 1 (1998).
- [59] R. Sohal and S. Ryu, *Phys. Rev. B* **108**, 045104 (2023).
- [60] M. Levin and X.-G. Wen, *Phys. Rev. B* **67**, 245316 (2003).
- [61] S. Feng, Y. He, and N. Trivedi, *Phys. Rev. A* **106**, 042417 (2022).
- [62] S. Feng, Y. He, and N. Trivedi, *Phys. Rev. A* **106**, 042417 (2022).
- [63] M. Oshikawa and T. Senthil, *Phys. Rev. Lett.* **96**, 060601 (2006).
- [64] X. G. Wen and Q. Niu, *Phys. Rev. B* **41**, 9377 (1990).
- [65] N. Read and D. Green, *Phys. Rev. B* **61**, 10267 (2000).
- [66] J. Wen, S.-L. Yu, S. Li, W. Yu, and J.-X. Li, *npj Quantum Materials* **4**, 12 (2019).
- [67] L. Clark and A. H. Abdeldaim, *Annual Review of Materials Research* **51**, 495 (2021).
- [68] C. Broholm, R. J. Cava, S. A. Kivelson, D. G. Nocera, M. R. Norman, and T. Senthil, *Science* **367**, eaay0668 (2020).
- [69] P. A. Lee and S. Morampudi, *Phys. Rev. B* **107**, 195102 (2023).
- [70] J. Y. Khoo, F. Pientka, P. A. Lee, and I. S. Villadiego, *Phys. Rev. B* **106**, 115108 (2022).
- [71] C. de C. Chamon, D. E. Freed, S. A. Kivelson, S. L. Sondhi, and X. G. Wen, *Phys. Rev. B* **55**, 2331 (1997).
- [72] S. Das Sarma, M. Freedman, and C. Nayak, *Phys. Rev. Lett.* **94**, 166802 (2005).
- [73] A. Stern and B. I. Halperin, *Phys. Rev. Lett.* **96**, 016802 (2006).
- [74] E.-A. Kim, *Phys. Rev. Lett.* **97**, 216404 (2006).
- [75] F. S. S. H. e. a. Nakamura, J., *Nature Physics* **15**, 563 (2019).

- [76] J. Nakamura, S. Liang, G. C. Gardner, and M. J. Manfra, *Nature Physics* **16**, 931 (2020).
- [77] R. Coldea, S. M. Hayden, G. Aeppli, T. G. Perring, C. D. Frost, T. E. Mason, S.-W. Cheong, and Z. Fisk, *Phys. Rev. Lett.* **86**, 5377 (2001).
- [78] H. D. Zhou, C. Xu, A. M. Hallas, H. J. Silverstein, C. R. Wiebe, I. Umegaki, J. Q. Yan, T. P. Murphy, J.-H. Park, Y. Qiu, J. R. D. Copley, J. S. Gardner, and Y. Takano, *Phys. Rev. Lett.* **109**, 267206 (2012).
- [79] S. Kumar, S. K. Panda, M. M. Patidar, S. K. Ojha, P. Mandal, G. Das, J. W. Freeland, V. Ganesan, P. J. Baker, and S. Middey, *Phys. Rev. B* **103**, 184405 (2021).
- [80] C. Xu, J. Feng, M. Kawamura, Y. Yamaji, Y. Nahas, S. Prokhorenko, Y. Qi, H. Xiang, and L. Bellaïche, *Phys. Rev. Lett.* **124**, 087205 (2020).
- [81] W. Witczak-Krempa, G. Chen, Y. B. Kim, and L. Balents, *Annual Review of Condensed Matter Physics* **5**, 57 (2014).
- [82] T. Takayama, J. Chaloupka, A. Smerald, G. Khaliullin, and H. Takagi, *Journal of the Physical Society of Japan* **90**, 062001 (2021).
- [83] G. Baskaran, D. Sen, and R. Shankar, *Phys. Rev. B* **78**, 115116 (2008).
- [84] V. S. de Carvalho, H. Freire, and R. G. Pereira, *Phys. Rev. B* **108**, 094418 (2023).
- [85] S. Ebadi, T. T. Wang, H. Levine, A. Keesling, G. Semeghini, A. Omran, D. Bluvstein, R. Samajdar, H. Pichler, W. W. Ho, S. Choi, S. Sachdev, M. Greiner, V. Vuletić, and M. D. Lukin, *Nature* **595**, 227–232 (2021).
- [86] P. Scholl, M. Schuler, H. J. Williams, A. A. Eberharter, D. Barredo, K.-N. Schymik, V. Lienhard, L.-P. Henry, T. C. Lang, T. Lahaye, A. M. Läuchli, and A. Browaeys, *Nature* **595**, 233–238 (2021).
- [87] D. Jaksch, J. I. Cirac, P. Zoller, S. L. Rolston, R. Côté, and M. D. Lukin, *Phys. Rev. Lett.* **85**, 2208 (2000).
- [88] G. Giudici, M. D. Lukin, and H. Pichler, *Phys. Rev. Lett.* **129**, 090401 (2022).
- [89] W. Rantner and X.-G. Wen, *Physical Review Letters* **86**, 3871–3874 (2001).
- [90] J. Alicea, *Phys. Rev. B* **78**, 035126 (2008).
- [91] B. Mondal, V. B. Shenoy, and S. Bhattacharjee, *Phys. Rev. B* **108**, 245106 (2023).

- [92] M. Thakurathi, K. Sengupta, and D. Sen, *Phys. Rev. B* **89**, 235434 (2014).
- [93] R. R. Biswas, L. Fu, C. R. Laumann, and S. Sachdev, *Phys. Rev. B* **83**, 245131 (2011).
- [94] P. Coleman, A. Panigrahi, and A. Tsvelik, *Phys. Rev. Lett.* **129**, 177601 (2022).
- [95] F. J. Burnell and C. Nayak, *Phys. Rev. B* **84**, 125125 (2011).
- [96] Y.-Z. You, I. Kimchi, and A. Vishwanath, *Phys. Rev. B* **86**, 085145 (2012).
- [97] K. B. Yogendra, T. Das, and G. Baskaran, *Phys. Rev. B* **108**, 165118 (2023).
- [98] G. Baskaran, S. Mandal, and R. Shankar, *Phys. Rev. Lett.* **98**, 247201 (2007).
- [99] F. D. M. Haldane, *Phys. Rev. Lett.* **61**, 2015 (1988).
- [100] Y. Kasahara, T. Ohnishi, Y. Mizukami, O. Tanaka, S. Ma, K. Sugii, N. Kurita, H. Tanaka, J. Nasu, Y. Motome, *et al.*, *Nature* **559**, 227 (2018).
- [101] T. Yokoi, S. Ma, Y. Kasahara, S. Kasahara, T. Shibauchi, N. Kurita, H. Tanaka, J. Nasu, Y. Motome, C. Hickey, S. Trebst, and Y. Matsuda, *Science* **373**, 568 (2021).
- [102] J. A. N. Bruin, R. R. Claus, Y. Matsumoto, N. Kurita, H. Tanaka, and H. Takagi, *Nat. Phys.* **18**, 401 (2022).
- [103] P. Czajka, T. Gao, M. Hirschberger, P. Lampen-Kelley, A. Banerjee, J. Yan, D. G. Mandrus, S. E. Nagler, and N. P. Ong, *Nat. Phys.* **17**, 915 (2021).
- [104] D. A. Ivanov, *Phys. Rev. Lett.* **86**, 268 (2001).
- [105] C. Nayak, S. H. Simon, A. Stern, M. Freedman, and S. Das Sarma, *Rev. Mod. Phys.* **80**, 1083 (2008).
- [106] H. Yao and X.-L. Qi, *Phys. Rev. Lett.* **105**, 080501 (2010).
- [107] A. Kitaev and C. Laumann, Topological phases and quantum computation (2009), [arXiv:0904.2771 \[cond-mat.mes-hall\]](https://arxiv.org/abs/0904.2771) .
- [108] G. Jackeli and G. Khaliullin, *Phys. Rev. Lett.* **102**, 017205 (2009).
- [109] H. Takagi, T. Takayama, G. Jackeli, G. Khaliullin, and S. E. Nagler, *Nature Reviews Physics* **1**, 264–280 (2019).
- [110] K. W. Plumb, J. P. Clancy, L. J. Sandilands, V. V. Shankar, Y. F. Hu, K. S. Burch, H.-Y. Kee, and Y.-J. Kim, *Phys. Rev. B* **90**, 041112 (2014).

-
- [111] H. B. Cao, A. Banerjee, J.-Q. Yan, C. A. Bridges, M. D. Lumsden, D. G. Mandrus, D. A. Tennant, B. C. Chakoumakos, and S. E. Nagler, [Phys. Rev. B](#) **93**, 134423 (2016).
- [112] A. Banerjee, C. A. Bridges, J.-Q. Yan, A. A. Aczel, L. Li, M. B. Stone, G. E. Granroth, M. D. Lumsden, Y. Yiu, J. Knolle, S. Bhattacharjee, D. L. Kovrizhin, R. Moessner, D. A. Tennant, D. G. Mandrus, and S. E. Nagler, [Nature Materials](#) **15**, 733–740 (2016).
- [113] L. Holleis, J. C. Prestigiacomo, Z. Fan, S. Nishimoto, M. Osofsky, G.-W. Chern, J. van den Brink, and B. Shivaram, [npj Quantum Mater.](#) **6**, 1 (2021).
- [114] P. P. Stavropoulos, D. Pereira, and H.-Y. Kee, [Phys. Rev. Lett.](#) **123**, 037203 (2019).
- [115] A. M. Samarakoon, A. Banerjee, S.-S. Zhang, Y. Kamiya, S. E. Nagler, D. A. Tennant, S.-H. Lee, and C. D. Batista, [Phys. Rev. B](#) **96**, 134408 (2017).
- [116] W. M. H. Natori, H.-K. Jin, and J. Knolle, [Phys. Rev. B](#) **108**, 075111 (2023).
- [117] H. Ma, [Phys. Rev. Lett.](#) **130**, 156701 (2023).

2

Introduction: Classical Spin liquids

Classical spin liquids (CSLs), as the name suggests, is analogous to the case of quantum spin liquids (QSLs), have no long-range order but have extensive zero temperature entropy, whereas it is zero in QSLs. As discussed in the previous Chapter, quantum fluctuations are vital in getting QSLs over the ordered state. The quantum fluctuations can be enhanced by having lower spin systems, for example, spin-1/2, at low temperatures. However, at high temperatures (compared to the energy scale associated with quantum fluctuations present in the quantum model), the quantum fluctuations play no role compared to thermal fluctuations. In such cases, the physics can be treated in terms of classical spins [1]. So, studying the classical spin models has direct implications in the high-temperature physics of QSLs, and also, CSL models give a good starting point in starting to construct QSL states [2–5]. In addition to that, there exist several materials where the spin physics at low temperature is approximated to classical spin models [6, 7], for example, Ising models for spin-ice materials [8, 9] and the Ashkin-Teller model [10], different variants of $O(N)$ models [11] and Heisenberg models [12], Potts Model [13, 14], \mathbb{Z}_q -clock models [15, 16] and references therein. In such cases, many interesting classical spin phases arise, either ordered phases or disordered phases. There are some scenarios where both the ordered and disordered phases co-exist [17, 18].

The 'Disorder' phase exactly means the phase with no long-range order and has a finite but extensive number of degenerate spin configurations. These phases in classical spin models also possess some non-trivial structures, like in quantum spin liquids. There are a few similarities between them, as QSLs have fractional quasi-particles and emergent low-energy gauge fields. Similarly, CSLs also have fractional excitations and emergent gauge theories [19]. However, the gauge theories in classical spin liquids are physical and appear out of physical spins but not like redundancy in the case of QSLs, and the low-energy excitations correspond to the excitations of the gauge theories. In quantum spin liquids, the emergent gauge field is not directly related to physical spins; instead, only the fractionalized partons can see the gauge fields (see Chapter 3)- their implications only arise in measurable quantities like transport properties. In both cases, the gauge theories govern the low energy physics; even though the origins are different, the primary roots are due to non-trivial local constraints; see, for instance, Ref. [20–22].

There are many aspects still open for investigation in the classical spin liquids. This Chapter briefly overviews classical spin liquids and a few open directions in the field. An essential part of this is understanding classical spin models beyond the spin-ice rule or Luttinger-Tisza approximation, which are relevant to the broad range of materials. In general, the models describing the materials apart from spin-ice pyrochlores do not need to respect spin-ice rules like the models with the Dzyaloshinskii–Moriya (DM) interaction [23]. This raises the demand for analytical methods to study these models. We have developed a unified framework in Ref. [23] to understand the existence of spin liquids and various interesting order, disordered phases in the classical spin model.

2.1 Spin Ice Models and the Coloumb Phase

Spin ice is a group of materials that resembles water ice [24] with the chemical formula $A_2B_2O_7$ [25, 26], where A^{3+} are the magnetic rare-earth ions on the sites of pyrochlore lattice and B^{4+} are non-magnetic ions on an interpenetrating pyrochlore lattice. For example, $\text{Ho}_2\text{Ti}_2\text{O}_7$ ¹ [27], $\text{Dy}_2\text{Ti}_2\text{O}_7$ [28]. The ground state governing these compounds follows an ice rule famously known as '2-in-2-out' configuration [29], as shown in Fig. 2.1, hence the name '*spin ice*'. Since this constraint within the four sites of the pyrochlore lattice can be satisfied by many configurations, consequently, for the whole lattice. This results in extensive degeneracy of the ground state. Hence, these materials have zero temperature entropy, also known as the Pauling entropy. Later, this methodology of constructing models to have ground states that possess the ice rules or its generalization laid a foundation for more studies in classical spin models

¹This is the first material found to have frustrated ferromagnet.

and then to the general class of CSLs. I am going to jointly refer to them as 'spin ice models.' These are a class of models that has the Hamiltonian written in terms of constraints, which are different variants of the simple 'ice rule' of the pyrochlores. Firstly, I discuss the spin ice pyrochlore materials and their related physics of emergent electromagnetic theory, monopole excitations. Further, I present these ideas to the more general class of spin ice models with more general constraints.

The first spin-ice material, $\text{Ho}_2\text{Ti}_2\text{O}_7$, is surprisingly a ferromagnet but has strong frustration due to the combination of ferromagnetic coupling and the easy axis anisotropy [27]. This material was found to have no ordering down to temperatures well below the Curie-Weiss temperature and with the large magnetic moment of Ho^{3+} ions. Hence, this can be treated by classical spin models. This has an easy axis pointing towards the center from each site of the tetrahedral lattice with strong easy-axis anisotropy $D < 0$ (ferromagnetic), which is 50 times higher than the strength of the exchange interactions J (ferromagnetic). Because of this high easy-axis anisotropy, the spins point along the easy-axis. The small perturbative exchange interactions J decide the orientation of the spins, which can be towards or away from the center of the tetrahedron. The lowest energy turns out to be 2 spins pointing inwards and 2 outwards in the given tetrahedron. This exactly gives rise to the antiferromagnetic Ising model in terms of pseudo-spins (σ^z) taken along the easy-axis [30, 31], which is a nearest neighbor spin-ice model [29]. The model is,

$$H_{\text{Ising}} = J \sum_{\langle ij \rangle} \sigma_i^z \sigma_j^z, \quad (2.1)$$

where site i and j are in the corner-sharing tetrahedral lattice. For ferromagnetic $J < 0$, the state is an all-up ferromagnet, which becomes a paramagnet at high temperatures. However, the scenario is different in the antiferromagnetic $J > 0$ coupling. And the effective pseudo spin model $\text{Ho}_2\text{Ti}_2\text{O}_7$ is indeed anti-ferromagnetic with $J > 0$ [30, 31]. Here, since the lattice is corner-sharing, the above Hamiltonian is simplified into up to an additional constant,

$$H_{\text{Ising}} = J \sum_p \left(\sum_{i \in p} \sigma_i^z \right)^2 + \text{const.}, \quad (2.2)$$

where p denotes each tetrahedral plaquette. The re-writing of the Hamiltonian implies that the ground state for $J > 0$ corresponds to spins satisfying $\sum_{i \in p} \sigma_i^z = 0$, known as the ice rule. As mentioned, in a pyrochlore tetrahedral unit cell with four lattice sites, the constraint is satisfied by having two spins pointing inwards and the other two pointing outwards, as shown in Fig. 2.1. This corresponds to a state with spins as '2-in-2-out' configuration. Many configurations can satisfy this condition, resulting in a paramagnet with a non-trivial structure that satisfies this local constraint. This results in a zero-temperature residual entropy. It is also called the

'cooperative paramagnet' because, here, the spins in each of these degenerate states follow a constraint cooperating with each other.

Later, a seminal work by Siddharthan et al. [32] and Bramwell et al. [33] found that the dipole-dipole interactions play a significant role in spin ice materials agreeing with the experimentally measured quantities. This model is also known as the dipolar spin ice model. The Hamiltonian is,

$$H_{\text{DSI}} = -J \sum_{\langle ij \rangle} \vec{S}_i^{z_i} \cdot \vec{S}_j^{z_j} + Dr_{nn} \sum_{i>j} \frac{\vec{S}_i^{z_i} \cdot \vec{S}_j^{z_j}}{|\vec{R}_{ij}|^3} - \frac{3(\vec{S}_i^{z_i} \cdot \vec{R}_{ij})(\vec{S}_j^{z_j} \cdot \vec{R}_{ij})}{|\vec{R}_{ij}|^5}, \quad (2.3)$$

where $\vec{S}_i^{z_i}$ are Ising spin pointing along the easy axis z_i in site i of the corner-sharing tetrahedral lattice, and the $J > 0$ is the strength of exchange interactions. The second term in the dipole-dipole interactions between the spins \vec{S}_i and \vec{S}_j with dipolar strength $D = \mu_0 \mu^2 / 4\pi r_{nn}^3 > 0$, μ is the magnetic moment of the spins, r_{nn} is the nearest neighbor distance and the \vec{R}_{ij} is the distance between the site i and j . Here, the strength of dipolar interaction is 2.5 times less than the exchange interactions [34]. Numerical and mean-field studies [34–36] showed that the long-range dipolar interactions of the DSI model screen out and have degenerate states satisfying the ice rule at temperatures above 0.1K, see Ref. [37] for full phase diagram. In such cases, the physics described by the spin-ice model [38], Eq. 2.2 with effective $J_{\text{eff}} = \frac{5D}{J} + \frac{J}{3}$ [34, 36].

In coarse-graining, the spin-ice state possesses non-trivial features like emergent gauge theory at low energy with the power-law spin correlations. For the coarse-graining, consider the pyrochlore lattice sites (denoted by i, j, \dots) residing in the bonds of its medial lattice, which is a diamond lattice². Denote the diamond lattices by I, J, \dots . On the bonds of diamond lattice, define a bond polarisation t_{IJ} , which is +1 if the spin (σ_i^z) residing on the bond is aligned from even (I) to odd (J) diamond lattice sites, see Fig. 2.1. Since the diamond lattice is a bipartite lattice, this convention gives $t_{JI} = -1$ for the other case [40]. The 2-in-2-out condition of the spin-ice ground state gives this bond polarisation to take +1 on two bonds and -1 for the other two bonds for each site of the diamond lattice. Defining this bond polarization to be the unit flux, \mathbf{B} , residing on the bonds with direction dictated by the sign of polarization. So, the spin ice constraint will give rise to a 'flux-free' condition for each diamond site, i.e.,

$$\nabla \cdot \mathbf{B} = 0. \quad (2.4)$$

This results in gauge fields \mathbf{A} , and it is defined as $\mathbf{B} = \nabla \times \mathbf{A}$. The conservation of flux, here, is a *emergent* phenomenon in low-energy but not of any fundamental reason because it appears

²The diamond lattice is formed by considering its sites as the pyrochlore centers. It is a bipartite lattice.

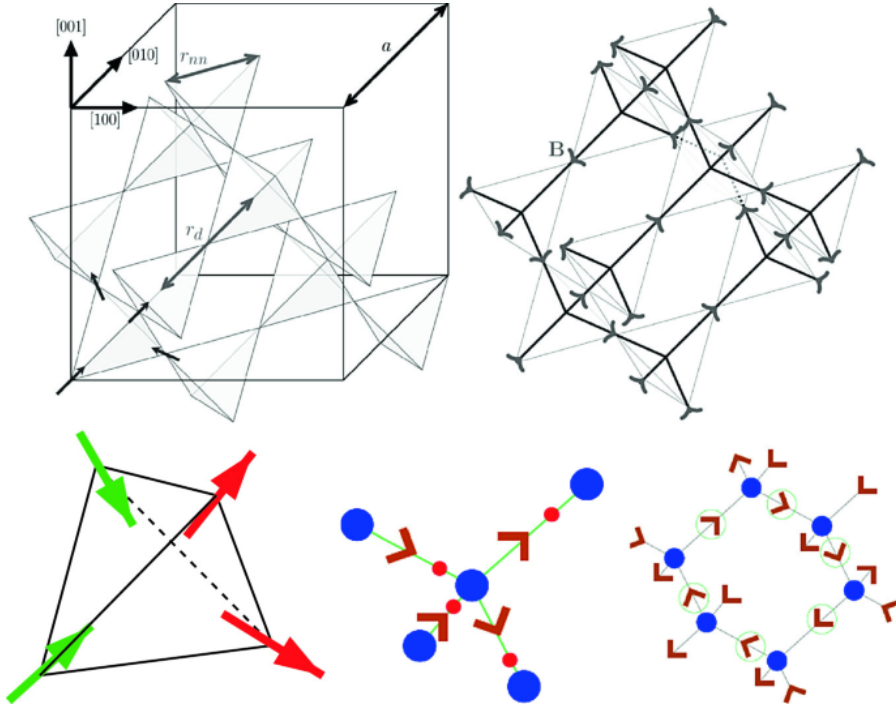


Fig. 2.1 (Top left) The pyrochlore lattice with corner-sharing tetrahedron of spin ice embedded in a cube. (Top right) The diamond lattice (thick lines) is formed by the centers of the tetrahedral lattice (thin lines). The spins, site variables on the tetrahedral lattice, become link variables (arrows) on the bonds of the diamond. (Bottom left) The ground state configuration of spins with '2-in-2-out' condition. (Bottom center) shows as link variables on the diamond lattice, the spins can be thought of as a lattice flux \mathbf{B} (brown arrows of the top right figure). (Bottom right) a set of spins on a green line arranged on a head-to-tail on a loop may be inverted to produce another ground state configuration. Such a loop has zero net magnetization. The term, which strength g , produces a liquid ground state, which is a quantum spin liquid as discussed in the text. The figure is taken from Ref. [39] with permission from the springer nature.

only when the 2-in-2-out condition is enforced. [39] The redefining of the spins in terms of the emergent fluxes gives a handle over the spin-ice state by taking an analogy with Maxwell's theory. The leading order in the action can be written as,

$$S = \frac{\kappa}{2} \int d^d r \mathbf{B}^2, \quad (2.5)$$

where κ is the dimensionless parameter, and it is calculated using Monte Carlo simulations [41]. This coarse-grained model helps in calculating the correlation functions of spins to leading order. The calculation goes as follows, derived from the Ref. [39, 40]. By Fourier transforming

the above Eq. 2.5, give a gaussian theory (quadratic in $\mathbf{B}(\mathbf{q})$) and the correlation becomes,

$$\langle \mathbf{B}_i(-\mathbf{q})\mathbf{B}_j(\mathbf{q}) \rangle \sim \frac{1}{\kappa} \delta_{ij}. \quad (2.6)$$

But, there is the conservation law in Eq. 2.4 that restricts this form. Eq. 2.4 in Fourier space becomes to $\mathbf{q} \cdot \mathbf{B} = 0$, leading to the vanishing longitudinal part. That is $(\hat{q} \cdot \mathbf{B})\hat{q} = 0$, where \hat{q} is the unit vector. Subtracting the longitudinal part of the correlations which is $\sim \frac{q_i q_j}{q^2}$, the correlations in Eq. 2.6 lead to,

$$\langle \mathbf{B}_i(-\mathbf{q})\mathbf{B}_j(\mathbf{q}) \rangle \sim \frac{1}{\kappa} \left(\delta_{ij} - \frac{q_i q_j}{q^2} \right) \sim \langle \sigma_i^z(-\mathbf{q})\sigma_j^z(\vec{q}) \rangle. \quad (2.7)$$

Here, the correlations in \mathbf{B} is equivalent to σ^z since \mathbf{B} are coarse-grained variables from σ^z .

The above momentum space correlations, measurable in neutron scattering experiments, have a quadratic singularity at $\mathbf{q} = 0$, known as 'pinch points.' The pinch points, or variants of the pinch point, are one of the identifiable experimental identities of the spin-ice phase. In real space, this correlation goes like $1/r^3$: dipolar spin correlations. [2, 9, 36, 42, 43] For the concrete derivation of the correlations, see Ref. [3, 41] and for large-N of O(N) model, see Ref. [44].

The excitations of the spin-ice state correspond to flipping one of the spins in the given site in the tetrahedron. As a result, the ice rule is violated to *1-in-3-out* and *3-in-1-out* configuration of two tetrahedra to which the site belongs, and the flux passing through the two tetrahedra has non-zero flux. These defective tetrahedra resemble a source or sink of flux \mathbf{B} . These can be separated by arbitrary distances independently but can only be created pairwise. This is equivalent to the creation of a pair of monopoles. [45] These monopoles can be moved further by flipping the consecutive string of spins, which costs finite bounded energy but does not diverge with the length of the string. These are deconfined excitations because separating them to infinite far distances costs finite energy. Hence, the spin ice state is the deconfined Coloumb phase of the $U(1)$ gauge theory (Maxwell's theory)[22, 39]. These defects/excitations from the spin-ice ground state interact by Coloumb interactions with effective magnetic charges as found in Ref. [45] with the dumbbell approximation to the previously discussed DSI model, Eq. 2.3, of pyrochlores. Hence, this phase is also known as the 'Coloumb' phase.

Using an applied magnetic field, one can tune the density of these monopoles. By tuning the field, the phase transitions occur from a polarized phase at a high field, having these strings confined to a low-field phase with the self-repelling strings with non-zero density. This phase transition is called the 'Kasteleyn transition' - an unusual one. On one side, from the polarised

phase, it looks like a first-order phase transition without any fluctuations, and on the other side, it is like a perfect second-order phase transition. [46, 47]

The above interesting features of pyrochlores are due to the spin configurations satisfying the ice rule present in the ground state. So, irrespective of the origin of the Hamiltonian Eq. 2.2, suppose, if we consider the Hamiltonian is constructed into that form to satisfy the 'ice rule' constraint $\sum_{i \in p} \sigma_i^z = 0$ in the ground state. Then, this procedure can be generalized to construct a class of Hamiltonians. Here, I am referring to them as 'spin-ice' models. For example, a classical anti-ferromagnetic Heisenberg model can also be decomposed into a form with a constraint $\mathcal{C}_p = \sum_{i \in p} \mathbf{S}_i = 0$ for plaquette p up to some constants. Such as

$$H_{\text{Heisenberg}} = J \sum_{\langle ij \rangle} \mathbf{S}_i \cdot \mathbf{S}_j = J \sum_p (\mathcal{C}_p)^2 + \text{constant}.$$

The ground state corresponds to the configurations satisfying the constraint $\mathcal{C}_p = 0$. Similar to the spin-ice pyrochlores, this ground state also has extensive degeneracy in case lattice frustration is present [22]. This recipe of writing different variants of constraints $\mathcal{C}_p = 0$ with spins components and then constructing a Hamiltonian in terms of \mathcal{C}_p to give a ground state satisfying the constraint $\mathcal{C}_p = 0$ produces a low-energy manifold with more generalized gauge theories. [21] The emergent gauge theories in these models have higher-rank gauge theories, which are fractonic in nature. [48] In the Luttinger-Tisza approximation discussed in the next section, the emergence of general gauge theories in these constrained models can be easily seen.

The finite entropy, also known as the Pauling entropy, of the spin-ice at zero temperature is the perfect avenue to host quantum spin liquids in three dimensions. The key to getting a spin liquid is allowing quantum tunneling from one ice configuration to another. That gives a coherent superposition of all the ice configurations, giving zero entropy and keeping the algebraic correlations intact. These are known as 'quantum spin ice' (QSI) models [49]. The resulting spin liquids are also known as 'Coloumb spin liquids.' This idea was proposed by Moessner and Sondhi in the three-dimensional dimer models [50] and Hermele et al. [3] and others in water ice [24]. The term that generates these tunneling events is the product of six spins along the underlying Honeycomb loop of the pyrochlore lattice [3, 50], as shown in Fig. 2.1. This is known as the 'ring-exchange' term. This term flips spins residing on the Honeycomb loop. As a result the flux on the bond changes in time and results in time dependence for the magnetic fields. The time-dependent magnetic field produces the analogous electric field from time-dependent gauge fields \mathbf{A} like in quantum electrodynamics (QED). Those are defined as,

$$\mathbf{B} = \nabla \times \mathbf{A}, \text{ and } \mathbf{E} = -\frac{\partial \mathbf{A}}{\partial t}. \quad (2.8)$$

Where \mathbf{E} is the electric field. The effective low-energy action will be

$$S = \frac{1}{8\pi} \int d^d r (\mathbf{B}^2 + c_{\text{QSI}} \mathbf{E}^2), \quad (2.9)$$

where c_{QSI} is the constant equivalent to the speed of light in 3D QED and is extracted by fitting the low-energy spectrum of the original Hamiltonian with the above coarse-grained model[51].

³ This theory is the lattice analog of electromagnetism with linearly dispersing 'photon' excitations. Quantizing this effective coarse-grained theory with appropriate energy scales and calculating experimentally measurable structure factors due to these photon excitations, see Ref. [49], give the extra power of \mathbf{q} in the spin-spin correlations, $\sim \mathbf{q} \times$ (Eq. 2.7). As a result, the sharp pinch in the spin structure factor gets smeared out to less sharp [49].

In recent times, the QSI model has been generalized to breathing pyrochlore lattice, given the experimental finding of the candidate material $\text{Ba}_3\text{Yb}_2\text{Zn}_5\text{O}_11$ [52–54]. Few theoretical studies [55–58] proposed that the QSI model in this lattice gives rich emergent gauge theories different from simple $U(1)$ gauge theory.

If the magnetic field is applied in the pyrochlores along the crystal direction [111] projects onto one easy axis with a strength three times higher in size than the other three. Then, the spin on that easy axis is pinned along the field. The other three spins are free to fluctuate and form a 2D Kagome lattice. However, in the spin-ice regime of pyrochlores ⁴, the system can lower the energy by taking the next best possible configuration satisfying the ice rule for these three spins in the ground state, which is '2-in-1-out' (a monopole) or '1-in-2-out' (an anti-monopole) depending on the even or odd centers of the triangles in the Kagome lattice. [59, 60] This state is known as the 'Kagome ice.' This occurs slightly before the high-field ordered state ⁵. [61, 62] Since this phase occurs in 2D, the dimensional reduction in resulting gauge theories has correlations different from those in 3D. The correlations are logarithmic as in Maxwell's theory in 2D; see Ref. [62, 63]. Exploring different field directions like applying [001] gives a platform to access the phase transition from spin-ice to Kagome ice [64].

³Tuning the strength of ring exchange term, one can tune the fine structure constant of the QED (which is $\alpha_{\text{QSI}} = e_{\text{QSI}}^2 / \hbar c_{\text{QSI}}$, where e_{QSI} and c_{QSI} are fitting parameters of coarse-graining model, analogous to charge and speed of light in QED). The strength of the ring exchange term is tuned by introducing varying third nearest neighbor interactions. This gives the ability to tune QED from strong coupling to very weak limits. Because of this, emergent QED in the spin-ice materials gives the lattice realization of QED. Hence, spin-ice materials provide a quantum simulator platform for QED with tunable fine structure constants [51].

⁴Reminder to the reader that the DSI model describes the physics of pyrochlores and specific region of phase diagram with temperature is governed by the spin-ice Ising model.

⁵Here, the anti-ferromagnetic ordered state corresponds to 'all-in-all-out' configurations. So, this phase has confined monopoles and anti-monopoles. Hence, this is also regarded as a monopole crystal in the low-energy perspective.

2.2 Magnetic Fragmentation

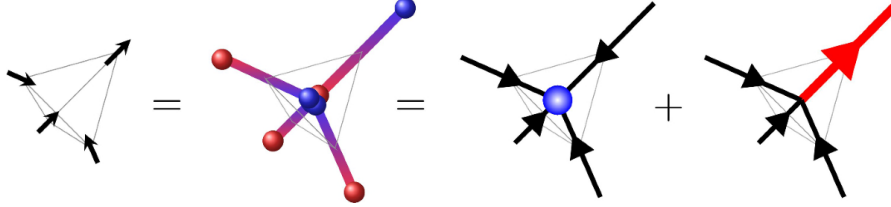


Fig. 2.2 (left) 3-in-1-out monopole configuration in a tetrahedron, (middle) respective dumbbell representation of 3-in-1-out tetrahedron, (right) their Helmholtz decomposition into divergence-full and divergence-free elements with the size of the arrows indicating their magnitude discussed in the texts. The figure is taken from Ref. [65] with permission from the Springer Nature.

This section is derived from the Ref. [65]. As discussed in the previous section, the dipole-dipole interaction plays a significant role in pyrochlores. At a certain part of the temperature regime, above $0.1K$, the spin ice Ising model governs the low-energy physics. But below that temperature [66], the quadrupolar and higher-order interactions between the spins start playing a role and induce finite density of monopoles in the ground state. In that region, the partially ordered phase is found to have spin-ice Coloumb phase co-existing with an ordered phase with ordering vector $\mathbf{q} = (0, 0, 2\pi/a)$, and a is the distance between the centers of corner-sharing tetrahedrons. [37] The structure factor, the Fourier transform of spin-spin correlations, of this phase shows sharp Bragg-peaks at \mathbf{q} along with the usual pinch points corresponding to the Coloumb phase of the pyrochlore spin ice.

In addition, a similar kind of partially ordered phase is also proposed in a specific region of the phase diagram in the Kagome Ice, see Ref. [67–70].

Later, Holdsworth et al. [18] proposed a unified concept known as ‘*magnetic fragmentation*’ to study the co-existence of order and disordered phases in spin ices. This is based on the ‘Helmholtz decomposition’ of the magnetization present in the model. In the case of the pyrochlores, the DSI model is approximated to the problem of magnetic charges using the dumbbell approximation; see Appedix. B. For the Coloumb state, the net magnetization at each center of the tetrahedron is zero.

2.2.1 Helmholtz Decomposition

In the spin ice state, the ice rule dictates the net magnetization to be zero in each site of the diamond lattice, which is $\nabla \cdot \mathbf{M} = 0$ satisfying the Gauss’s law. For the monopole excitations, that becomes $\nabla \cdot \mathbf{M} = -\rho_m$, where ρ_m is the magnetic charge. Using Helmholtz decomposition,

we can estimate how much of the divergence-free of ice rule is broken and estimate the fraction of ordering to disordering contributions in the magnetization. The decomposition of \mathbf{M} is as follows,

$$\mathbf{M} = \mathbf{M}_m + \mathbf{M}_d,$$

where the \mathbf{M}_m is the diverse full part (related to the ordered state) and \mathbf{M}_d is the divergence-less related to the Coloumb phase. In the Coloumb phase, $\mathbf{M}_m = 0$. For the ordered anti-ferromagnetic phase, the ground state configuration is all-in-all-out, which is a monopole with a double charge. That is a divergence-full configuration with $\mathbf{M}_m \neq 0$ and $\mathbf{M}_d = 0$. When the finite density of monopoles is present in the model, both $\mathbf{M}_m, \mathbf{M}_d$ take finite values. The idea of decomposing the magnetisation into different components of the spins is already discussed previously in Ref. [71]. In the spin ice case, this breaking of magnetization is not a coarse-grained phenomenon. The ratios of both contributions are calculated precisely using dumbbell approximation. As discussed in the appendix B, the microscopic magnetization for site I to site J in diamond is $\mathbf{M}_{IJ} = \pm 1$. So, the decomposed magnetization parts, which are denoted by \mathbf{M}_{IJ}^m and \mathbf{M}_{IJ}^d , should satisfy the condition: $\mathbf{M}_{IJ}^m + \mathbf{M}_{IJ}^d = \pm 1$ each bond in the diamond lattice. The orthogonality condition for these parts is $\sum_{I>J} \mathbf{M}_{IJ}^m \mathbf{M}_{IJ}^d = 0$. Using these two conditions, the 3-in-1-out monopole is decomposed into [18],

$$[\mathbf{M}_{\mathbf{I}\mathbf{J}}] \equiv (-1, -1, -1, 1) = \left(-\frac{1}{2}, -\frac{1}{2}, -\frac{1}{2}, -\frac{1}{2}\right) + \left(-\frac{1}{2}, -\frac{1}{2}, -\frac{1}{2}, \frac{3}{2}\right), \quad (2.10)$$

where first part is \mathbf{M}^m and second one is \mathbf{M}^d . This decomposition for one tetrahedron is schematically shown in Fig. 2.2. A similar decomposition procedure is used for the Kagome ice and different ice models to study the partially ordered phase [18].

It is evident that this decomposition works only for discrete spin cases. The partially ordered phase also exists in the classical continuous spin models [23], which are dubbed as fragmented phases. Moreover, the contributions of ordered and disordered parts for the continuous spins are not known previously. The group theoretical method proposed in our work [23] helps in calculating precisely these quantities in the fragmented phase and also in all other ordered, disordered spin liquid phases.

2.3 Luttinger-Tisza Approximation and Classification

As discussed in the above section, the spin-ice models paved a route to construct different CSLs with different emergent low-energy gauge theories. Most of those CSLs have algebraic spin correlations. Not all states with extensive degeneracy in the ground state give rise to algebraic

spin liquids. There exist cases where the state has exponential correlations with non-trivial topological structures in the classical spin models, as discussed in Ref. [19] for the Heisenberg spin-ice model on the ruby lattice and Kagome lattice.

Recently, the Luttinger-Tisza approximation, also known as the soft-spin approximation, has been introduced to study classical spin liquids and construct new and different classical spin liquids. Recently, this approximation has been used to classify the existing CSLs [72–74]. The local unit length constraint, $|\mathbf{S}_i| = 1$ at each site, is sacrificed in this approximation. Instead, the constraint is imposed on the total spin of the lattice with N sites, i.e., $\frac{1}{N} \sum_i |\mathbf{S}_i| = 1$. This simplification effectively makes some progress in classifying the CSLs but has its own pitfalls. The constraint imposed on the whole lattice allows spins to be treated as scalars. This approach is for the set of Hamiltonians which are quadratic in spins such as

$$H = J \sum_p \left(|\mathbf{S}_p|^2 \right). \quad (2.11)$$

where the sum is over the plaquettes denoted by p and The plaquette spin is $\mathbf{S}_p^m = \sum_{i \in p} \eta_i \mathbf{S}_i^\alpha$, where η_i are the real coefficients which are all equal for Heisenberg model with spin components denoted by α , i is for sublattice sites and m index is for the spin component in each sublattice withing the plaquette p . This quadratic Hamiltonian is transformed using Fourier transformation as⁶

$$\mathbf{S}_p = \frac{1}{N} \sum_{i \in p} \mathbf{S}_i^m e^{-i\mathbf{q} \cdot \mathbf{r}_i}. \quad (2.12)$$

Any generic Hamiltonian, such as,

$$H = \sum_{\mathbf{q}} \mathcal{S}^m(-\mathbf{q}) \mathcal{J}_{mn}(\mathbf{q}) \mathcal{S}^n(\mathbf{q}), \quad (2.13)$$

$$= \sum_{\mathbf{q}} \mathcal{S}^m(-\mathbf{q}) T^m(\mathbf{q}) \omega(\mathbf{q}) T^{n*}(-\mathbf{q}) \mathcal{S}^n(\mathbf{q}). \quad (2.14)$$

The interaction matrix $\mathcal{J}(\mathbf{q})$ is the Fourier component of the exchange terms with J for all sublattices sites, which is

$$\mathcal{J}_{mn}(\mathbf{q}) = \sum_{i,j} J e^{-i\mathbf{q} \cdot (\mathbf{r}_i - \mathbf{r}_j)} = T^m(\mathbf{q}) T^{n*}(\mathbf{q}). \quad (2.15)$$

The eigenvectors are denoted by $T(\mathbf{q})^*$ and the eigenspectrum by $\omega(\mathbf{q})$. In the case of the CSL phase, the eigenspectrum consists of flat bands at energy $\omega = 0$, the lowest energy. The flat band is the consequence of the extensive degeneracy of the ground state. All the other

⁶The definition of the Fourier transformation is only feasible under the soft-spin approximation, where spins are treated as scalars.

bands are dispersive with dispersions as $\omega(\mathbf{q}) = |T(\mathbf{q})|^2$. The condition for the ground state manifold for the Hamiltonian mentioned in eq. 2.13 is $\mathbf{S}_{\mathbf{q}} = 0$ (spin 'ice rule'), which results into, in the Fourier space as

$$\sum_m T_m^*(\mathbf{q}) S_m(\mathbf{q}) = 0. \quad (2.16)$$

The conditions for various types of emergent gauge fields in constrained Hamiltonians can be deduced from the kind of dispersions of flat bands represented by $T(\mathbf{q})$. Furthermore, it is also helpful in the classification of classical spin liquids. Apart from the trivial paramagnet, the types of spin liquids deduced from the knowledge of flat band physics are algebraic and fragile spin liquids. The algebraic spin liquids correspond to bands where dispersive bands touch the flat bands at finite points in the Brillouin zone singularly [73]⁷ If not, the points are non-singular. The associated spin liquids are called 'fragile.' These are fragile in the following sense. Suppose the band is gapless with non-singular band touching points or gaped without any band touching; then, the eigenvectors are non-vanishing at any Brillouin zone points without any singular points. The non-vanishing eigenvectors make these bands possess non-zero topological invariant, skyrmion number, from the map of eigenvector from Brillouin to $\mathbb{C}P^{N-1}$; see [73] for more details.

The characteristics of singular band touching points in the Brillouin zone for algebraic spin liquids infer the type of gauge theory that emerges. For example, in the case of the Coloumb phase, the band touching happens at $\mathbf{q} \sim 0$ with leading power in the wave vector $T(\mathbf{q}) \sim \mathbf{q}$. From the constraint condition mentioned above, the constraint gives rise to $\mathbf{q} \cdot \mathbf{S} = 0$, which gives the Gauss law. So, the structure of gapless points directly maps the pinch points or their analogs in the structure factor. See Refs. [72, 73] for more examples of tensor gauge structures and higher-rank gauge theories. This approach can also be employed additionally to construct various classical spin models by developing the model with the required type of dispersions.

2.4 Order by Disorder

So far in this chapter, I discussed that the fluctuations induced by frustration do not allow the system to have ordered phase in the ground state. In contrast, there are scenarios in which the quantum or thermal fluctuations may induce order or close to ordered phase. This concept is known as "order by disorder" introduced by Villain et al. [75] in classical Ising systems.

This key idea of this concept is as follows. [] In classical spin systems, the ground state possess finite degeneracy, for example, symmetry broken phases like ferromagnetic or anti-ferromagnetic phases has degenerate states. The modes, called 'zero modes', which take the

⁷Singular band touching points, say q^* , are defined as where the eigenvector vanishes, i.e., $T(q^*) = 0$.

system from one state to another degenerate state without any further energy cost. The order by disorder works to select the subset of degenerate energy states to the more ordered state. To illustrate this with an example, consider an Heisenberg antiferromagnetic in bcc lattice. The bcc lattice is a cubic lattice with two sub-lattices. Because of the two sublattices, two zero modes exist in this case. One is corresponding to Heisenberg rotation of all the spins together, which is a Goldstone mode. Other is related to out-of-phase rotation of spins between the spins in the two sublattices. This mode is called 'phason'. The introduction of quantum or thermal fluctuations into this phase, break this phason mode of continuous rotations into simple Z_2 Ising symmetry. As a result, the system become more ordered collinear phase, see Ref.[76]. The more the number of zero modes present in the state, the more the system is prone to fluctuations. So, the coplanar and nonplanar phases in Kagome and pyrochlores lattices has more zero modes and has many interesting physics arises, see Ref [77–79]. For the latest activities related this concept, see Ref. [80, 81] and its quantum analogs, see Ref. [82] and references therein.

2.5 Material realization

This section summarises the existing classical spin liquid candidate materials. So far, all the materials possessing CSLs are spin-ice models and related models. One of the foremost experimentally known materials to have classical spin liquids is the 3D pyrochlores [22, 43]. The pyrochlore materials initially investigated to have spin-ice models are rare earth (R) titanates $R_2Ti_2O_7$, $R=Ho, Dy$. The zero point entropy of the pyrochlores was calculated at first to confirm the resemblance of the water ice physics in $Ho_2Ti_2O_7$ [33], $Dy_2Ti_2O_7$ [83]. These dipolar-magnets have surprisingly ferromagnetic frustration with dominating dipolar-dipolar interactions. Later, simplifying models to study these models are proposed but still have many puzzles to address; see Ref. [43] for details. Many spin ices are now known based on the chemical base $A_2B_2X_7$ being extremely large, including spinels rather than pyrochlores [84]. Recently, the classical spin liquid phase has been found in the Heisenberg Kagome compound $Li_9Fe_3(P_2O_7)_3(PO_4)_2$ [85], which has spin $S = \frac{5}{2}$.

In addition to these materials known to have classical spin liquids, few cases in this class of materials had prominent quantum fluctuations. These materials are prime candidates to have quantum spin ice, including $Pr_2Zr_2O_7$ [86], $Pr_2Hf_2O_7$ [87], $Nd_2Zr_2O_7$ [17], and $Ce_2Zn_2O_7$ [88]. Various other materials with triangular [89–91], Kagome [92–94], and square Kagome lattices [95–97] are found, but the spins need not be classical. But, all these are studied theoretically with both classical and quantum spins.

B

Appendices for chapter 2

B.1 Dumbbell Approximation to Dipolar Spin Ice (DSI) Model

The dumbbell approximation to the DSI model goes as follows [45]. The point spin dipoles are considered as infinitesimally thin magnetic needles along the easy axes connecting the centers of adjoining tetrahedra, which give a diamond lattice. These needles carry dumbbells of charges at each end, which touch at the diamond lattice sites, as shown in Fig. 2.2. For each dumbbell at the ends, there is a positive and a negative charge denoted by $\pm Q_I$ at site I , reproducing the magnetic moment of the original point dipole. The spin ice rule is satisfied by taking two ends with $+Q_I$ and two with $-Q_I$. As a result, the ground state has a charge-neutral configuration at each diamond lattice site. Changing the sign of a single dumbbell produces a monopole pair in the tetrahedra connecting the dumbbell. By construction, the magnetic moment at each site of the tetrahedron is given by the magnetic charge $M_{IJ} = \pm 1$ connecting the diamond lattice sites I and J . In the spin-ice state, for spin-ice configuration has $\sum_{I=1}^4 M_{IJ} = 0$ (i.e. $\nabla \cdot \mathbf{M} = 0$ in the coarse-graining), and for '3-in-1-out' monopole has $\sum_{I=1}^4 M_{IJ} = -2$.

References

- [1] S. Sachdev, *Quantum phases of matter* (Cambridge University Press, 2023).
- [2] M. J. Harris, S. T. Bramwell, D. F. McMorrow, T. Zeiske, and K. W. Godfrey, *Phys. Rev. Lett.* **79**, 2554 (1997).
- [3] M. Hermele, M. P. A. Fisher, and L. Balents, *Phys. Rev. B* **69**, 064404 (2004).
- [4] L. Balents, M. P. A. Fisher, and S. M. Girvin, *Phys. Rev. B* **65**, 224412 (2002).
- [5] A. M. Samarakoon, A. Banerjee, S.-S. Zhang, Y. Kamiya, S. E. Nagler, D. A. Tennant, S.-H. Lee, and C. D. Batista, *Phys. Rev. B* **96**, 134408 (2017).
- [6] A. Wipf, Classical spin models: An introduction, in *Statistical Approach to Quantum Field Theory: An Introduction* (Springer Berlin Heidelberg, Berlin, Heidelberg, 2013) pp. 101–118.
- [7] G. D. las Cuevas and T. S. Cubitt, *Science* **351**, 1180 (2016).
- [8] R. J. Baxter, *Exactly solved models in statistical mechanics* (1982).
- [9] J. G. Rau and M. J. Gingras, *Annual Review of Condensed Matter Physics* **10**, 357–386 (2019).
- [10] J. Ashkin and E. Teller, *Phys. Rev.* **64**, 178 (1943).
- [11] P. Blanchard, S. Digal, S. Fortunato, D. Gandolfo, T. Mendes, and H. Satz, *Journal of Physics A: Mathematical and General* **33**, 8603 (2000).
- [12] D. A. Garanin and B. Canals, *Phys. Rev. B* **59**, 443 (1999).
- [13] R. B. Potts, *Mathematical Proceedings of the Cambridge Philosophical Society* **48**, 106–109 (1952).

-
- [14] F. Y. Wu, *Rev. Mod. Phys.* **54**, 235 (1982).
- [15] Z.-Q. Li, L.-P. Yang, Z. Y. Xie, H.-H. Tu, H.-J. Liao, and T. Xiang, *Phys. Rev. E* **101**, 060105 (2020).
- [16] L. Hostetler, J. Zhang, R. Sakai, J. Unmuth-Yockey, A. Bazavov, and Y. Meurice, *Clock model interpolation and symmetry breaking in $o(2)$ models* (2021), [arXiv:2110.05527 \[hep-lat\]](https://arxiv.org/abs/2110.05527) .
- [17] S. Petit, E. Lhotel, B. Canals, M. Ciomaga-Hatnean, J. Ollivier, H. Mutka, E. Ressouche, A. R. Wildes, M. R. Lees, and G. Balakrishnan, Observation of magnetic fragmentation in spin ice (2016), [arXiv:1603.05008 \[cond-mat.str-el\]](https://arxiv.org/abs/1603.05008) .
- [18] M. E. Brooks-Bartlett, S. T. Banks, L. D. C. Jaubert, A. Harman-Clarke, and P. C. W. Holdsworth, *Phys. Rev. X* **4**, 011007 (2014).
- [19] J. Rehn, A. Sen, and R. Moessner, *Phys. Rev. Lett.* **118**, 047201 (2017).
- [20] C. Castelnovo, R. Moessner, and S. Sondhi, *Annual Review of Condensed Matter Physics* **3**, 35–55 (2012).
- [21] O. Benton and R. Moessner, *Phys. Rev. Lett.* **127**, 107202 (2021).
- [22] C. L. Henley, *Annual Review of Condensed Matter Physics* **1**, 179–210 (2010).
- [23] K. B. Yogendra, S. Karmakar, and T. Das, *Phys. Rev. B* **110**, L060401 (2024).
- [24] A. H. Castro Neto, P. Pujol, and E. Fradkin, *Phys. Rev. B* **74**, 024302 (2006).
- [25] A. Bertin, Y. Chapuis, P. D. de Réotier, and A. Yaouanc, *Journal of Physics: Condensed Matter* **24**, 256003 (2012).
- [26] M. J. P. Gingras, P. A. McClarty, and J. G. Rau, Spin ice: Microscopic physics, in *Spin Ice*, edited by M. Udagawa and L. Jaubert (Springer International Publishing, Cham, 2021) pp. 1–18.
- [27] M. J. Harris, S. T. Bramwell, D. F. McMorrow, T. Zeiske, and K. W. Godfrey, *Phys. Rev. Lett.* **79**, 2554 (1997).
- [28] Y. Jana, A. Sengupta, and D. Ghosh, *Journal of Magnetism and Magnetic Materials* **248**, 7 (2002).
- [29] P. W. Anderson, *Phys. Rev.* **102**, 1008 (1956).

-
- [30] S. T. Bramwell and M. J. Harris, [Journal of Physics: Condensed Matter](#) **10**, L215 (1998).
- [31] R. Moessner, [Phys. Rev. B](#) **57**, R5587 (1998).
- [32] R. Siddharthan, B. S. Shastry, A. P. Ramirez, A. Hayashi, R. J. Cava, and S. Rosenkranz, [Phys. Rev. Lett.](#) **83**, 1854 (1999).
- [33] S. T. Bramwell, M. J. Harris, B. C. den Hertog, M. J. P. Gingras, J. S. Gardner, D. F. McMorrow, A. R. Wildes, A. L. Cornelius, J. D. M. Champion, R. G. Melko, and T. Fennell, [Phys. Rev. Lett.](#) **87**, 047205 (2001).
- [34] B. C. den Hertog and M. J. P. Gingras, [Phys. Rev. Lett.](#) **84**, 3430 (2000).
- [35] M. J. Gingras and B. C. den Hertog, [Canadian Journal of Physics](#) **79**, 1339–1351 (2001).
- [36] S. V. Isakov, K. Gregor, R. Moessner, and S. L. Sondhi, [Phys. Rev. Lett.](#) **93**, 167204 (2004).
- [37] R. G. Melko and M. J. P. Gingras, [Journal of Physics: Condensed Matter](#) **16**, R1277 (2004).
- [38] S. V. Isakov, R. Moessner, and S. L. Sondhi, [Phys. Rev. Lett.](#) **95**, 217201 (2005).
- [39] R. Moessner, Spin ice as a coulomb liquid: From emergent gauge fields to magnetic monopoles, in *Spin Ice*, edited by M. Udagawa and L. Jaubert (Springer International Publishing, Cham, 2021) pp. 37–70.
- [40] C. L. Henley, [Phys. Rev. B](#) **71**, 014424 (2005).
- [41] D. A. Huse, W. Krauth, R. Moessner, and S. L. Sondhi, [Phys. Rev. Lett.](#) **91**, 167004 (2003).
- [42] S. T. Bramwell and M. J. P. Gingras, [Science](#) **294**, 1495 (2001).
- [43] S. T. Bramwell and M. J. Harris, [Journal of Physics: Condensed Matter](#) **32**, 374010 (2020).
- [44] S. V. Isakov, K. Gregor, R. Moessner, and S. L. Sondhi, [Phys. Rev. Lett.](#) **93**, 167204 (2004).
- [45] C. Castelnovo, R. Moessner, and S. L. Sondhi, [Nature](#) **451**, 42–45 (2008).
- [46] L. D. C. Jaubert, J. T. Chalker, P. C. W. Holdsworth, and R. Moessner, [Phys. Rev. Lett.](#) **105**, 087201 (2010).

-
- [47] C. S. O. Yokoi, J. F. Nagle, and S. R. Salinas, *Journal of Statistical Physics* **44**, 729 (1986).
- [48] M. Hering, H. Yan, and J. Reuther, *Phys. Rev. B* **104**, 064406 (2021).
- [49] O. Benton, O. Sikora, and N. Shannon, *Phys. Rev. B* **86**, 075154 (2012).
- [50] R. Moessner and S. L. Sondhi, *Phys. Rev. B* **68**, 184512 (2003).
- [51] S. D. Pace, S. C. Morampudi, R. Moessner, and C. R. Laumann, *Phys. Rev. Lett.* **127**, 117205 (2021).
- [52] Y. Okamoto, G. J. Nilsen, J. P. Attfield, and Z. Hiroi, *Phys. Rev. Lett.* **110**, 097203 (2013).
- [53] T. Haku, K. Kimura, Y. Matsumoto, M. Soda, M. Sera, D. Yu, R. A. Mole, T. Takeuchi, S. Nakatsuji, Y. Kono, T. Sakakibara, L.-J. Chang, and T. Masuda, *Phys. Rev. B* **93**, 220407 (2016).
- [54] R. Bag, S. E. Dissanayake, H. Yan, Z. Shi, D. Graf, E. S. Choi, C. Marjerrison, F. Lang, T. Lancaster, Y. Qiu, W. Chen, S. J. Blundell, A. H. Nevidomskyy, and S. Haravifard, *Phys. Rev. B* **107**, L140408 (2023).
- [55] L. Savary, X. Wang, H.-Y. Kee, Y. B. Kim, Y. Yu, and G. Chen, *Phys. Rev. B* **94**, 075146 (2016).
- [56] D. Bulmash and M. Barkeshli, *Phys. Rev. B* **97**, 235112 (2018).
- [57] S. D. Pace, C. Castelnovo, and C. R. Laumann, *Phys. Rev. Lett.* **130**, 076701 (2023).
- [58] A. Sanders and C. Castelnovo, *Phys. Rev. B* **109**, 094426 (2024).
- [59] K. Matsuhira, Z. Hiroi, T. Tayama, S. Takagi, and T. Sakakibara, *Journal of Physics: Condensed Matter* **14**, L559 (2002).
- [60] A. J. Macdonald, P. C. W. Holdsworth, and R. G. Melko, *Journal of Physics: Condensed Matter* **23**, 164208 (2011).
- [61] H. Aoki, T. Sakakibara, K. Matsuhira, and Z. Hiroi, *Journal of the Physical Society of Japan* **73**, 2851 (2004).
- [62] T. Fennell, S. T. Bramwell, D. F. McMorrow, P. Manuel, and A. R. Wildes, *Nature Physics* **3**, 566–572 (2007).
- [63] H. Kadowaki, N. Doi, Y. Aoki, Y. Tabata, T. J. Sato, J. W. Lynn, K. Matsuhira, and Z. Hiroi, *Journal of the Physical Society of Japan* **78**, 103706 (2009).

-
- [64] R. Moessner and S. L. Sondhi, [Phys. Rev. B **68**, 064411 \(2003\)](#).
- [65] E. Lhotel, L. D. C. Jaubert, and P. C. W. Holdsworth, [Journal of Low Temperature Physics **201**, 710–737 \(2020\)](#).
- [66] V. Raban, C. T. Suen, L. Berthier, and P. C. W. Holdsworth, [Phys. Rev. B **99**, 224425 \(2019\)](#).
- [67] G. Möller and R. Moessner, [Phys. Rev. B **80**, 140409 \(2009\)](#).
- [68] G.-W. Chern, P. Mellado, and O. Tchernyshyov, [Phys. Rev. Lett. **106**, 207202 \(2011\)](#).
- [69] O. Cépas and B. Canals, [Phys. Rev. B **86**, 024434 \(2012\)](#).
- [70] G.-W. Chern and O. Tchernyshyov, [Philosophical Transactions of the Royal Society A: Mathematical, Physical and Engineering Sciences **370**, 5718–5737 \(2012\)](#).
- [71] L. Savary and L. Balents, [Phys. Rev. Lett. **108**, 037202 \(2012\)](#).
- [72] N. Davier, F. A. Gómez Albarracín, H. D. Rosales, and P. Pujol, [Phys. Rev. B **108**, 054408 \(2023\)](#).
- [73] H. Yan, O. Benton, A. H. Nevidomskyy, and R. Moessner, Classification of classical spin liquids: Detailed formalism and suite of examples (2023), [arXiv:2305.19189 \[cond-mat.str-el\]](#) .
- [74] Y. Fang, J. Cano, A. H. Nevidomskyy, and H. Yan, Classification of classical spin liquids: Topological quantum chemistry and crystalline symmetry (2023), [arXiv:2309.12652 \[cond-mat.str-el\]](#) .
- [75] Villain, J., Bidaux, R., Carton, J.-P., and Conte, R., [J. Phys. France **41**, 1263 \(1980\)](#).
- [76] E. F. Shender and P. C. W. Holdsworth, Order by disorder and topology in frustrated magnetic systems, in *Fluctuations and Order: The New Synthesis*, edited by M. Millonas (Springer US, New York, NY, 1996) pp. 259–279.
- [77] I. Ritchey, P. Chandra, and P. Coleman, [Phys. Rev. B **47**, 15342 \(1993\)](#).
- [78] E. F. Shender, V. B. Cherepanov, P. C. W. Holdsworth, and A. J. Berlinsky, [Phys. Rev. Lett. **70**, 3812 \(1993\)](#).
- [79] P. Chandra, P. Coleman, and I. Ritchey, [J. Phys. I France **3**, 591 \(1993\)](#).
- [80] A. W. Sandvik and D. J. Scalapino, [Phys. Rev. Lett. **72**, 2777 \(1994\)](#).

- [81] D. Bergman, J. Alicea, E. Gull, S. Trebst, and L. Balents, *Nature Physics* **3**, 487–491 (2007).
- [82] J. a. C. Getelina, Z. Zhuang, P. Chandra, P. Coleman, P. P. Orth, and S. L. Sondhi, *Phys. Rev. B* **109**, 075137 (2024).
- [83] A. P. Ramirez, A. Hayashi, R. J. Cava, R. Siddharthan, and B. S. Shastry, *Nature* **399**, 333 (1999).
- [84] J. Lago, I. Živković, B. Z. Malkin, J. Rodriguez Fernandez, P. Ghigna, P. Dalmas de Réotier, A. Yaouanc, and T. Rojo, *Phys. Rev. Lett.* **104**, 247203 (2010).
- [85] E. Kermarrec, R. Kumar, G. Bernard, R. Hénaff, P. Mendels, F. Bert, P. L. Paulose, B. K. Hazra, and B. Koteswararao, *Phys. Rev. Lett.* **127**, 157202 (2021).
- [86] K. D. Kimura, S. Nakatsuji, S. Nakatsuji, J. Wen, C. L. Broholm, C. L. Broholm, C. L. Broholm, M. B. Stone, E. Nishibori, and H. Sawa, *Nature Communications* **4** (2013).
- [87] R. Sibille, N. Gauthier, H. Yan, M. Ciomaga Hatnean, J. Ollivier, B. Winn, U. Filges, G. Balakrishnan, M. Kenzelmann, N. Shannon, and T. Fennell, *Nature Physics* **14**, 711–715 (2018).
- [88] J. Gaudet, E. M. Smith, J. Dudemaine, J. Beare, C. R. C. Buhariwalla, N. P. Butch, M. B. Stone, A. I. Kolesnikov, G. Xu, D. R. Yahne, K. A. Ross, C. A. Marjerrison, J. D. Garrett, G. M. Luke, A. D. Bianchi, and B. D. Gaulin, *Phys. Rev. Lett.* **122**, 187201 (2019).
- [89] L. A. S. Mól, A. R. Pereira, and W. A. Moura-Melo, *Phys. Rev. B* **85**, 184410 (2012).
- [90] Y. Li, P. Gegenwart, and A. A. Tsirlin, *Journal of Physics: Condensed Matter* **32**, 224004 (2020).
- [91] D. T. Liu, F. J. Burnell, L. D. C. Jaubert, and J. T. Chalker, *Phys. Rev. B* **94**, 224413 (2016).
- [92] Y. Iqbal, H. O. Jeschke, J. Reuther, R. Valentí, I. I. Mazin, M. Greiter, and R. Thomale, *Phys. Rev. B* **92**, 220404 (2015).
- [93] T. Mizoguchi, L. D. C. Jaubert, and M. Udagawa, *Phys. Rev. Lett.* **119**, 077207 (2017).
- [94] K. Essafi, O. Benton, and L. D. C. Jaubert, *Phys. Rev. B* **96**, 205126 (2017).
- [95] M. Fujihala, K. Morita, R. Mole, S. Mitsuda, T. Tohyama, S.-i. Yano, D. Yu, S. Sota, T. Kuwai, A. Koda, *et al.*, *Nat. Commun.* **11**, 3429 (2020).

-
- [96] O. V. Yakubovich, L. V. Shvanskaya, G. V. Kiriukhina, A. S. Volkov, O. V. Dimitrova, and A. N. Vasiliev, *Inorganic Chemistry* **60**, 11450 (2021), pMID: 34264636.
- [97] M. M. Markina, P. S. Berdonosov, T. M. Vasilchikova, K. V. Zakharov, A. F. Murtazoev, V. A. Dolgikh, A. V. Moskin, V. N. Glazkov, A. I. Smirnov, and A. N. Vasiliev, (2023), [arXiv:2212.11623 \[cond-mat.str-el\]](https://arxiv.org/abs/2212.11623) .

3

Emergent Glassiness in Disorder-free Kitaev model

The complete phase diagram of the Kitaev model with a magnetic field remains elusive, as do the experimental results in the candidate material α -RuCl₃. Here, this chapter discusses the study of the Kitaev model on a one-dimensional ladder setting within the density-matrix renormalization group (DMRG) method in the presence of a magnetic field at zero temperature. There are five distinct phases found with increasing magnetic field, which are characterized by a homogeneous flux phase, the Z_2 vortex gas, solid and emergent *glass* phase, and finally, a spin-polarized phase. The emergent glassiness is confirmed by calculating correlation functions showing quasi-long range behavior and ground state fidelity, showing a plethora of energetically accessible orthogonal saddle points corresponding to different flux configurations. This glassy behavior seems to arise from the slow dynamics of the Z_2 fluxes, which is a consequence of the local constraints present in the underlying Hilbert space. This phenomenon can also be explored in other spin-liquid systems where the corresponding low-energy excitations are similarly retarded due to constraints.¹

¹This chapter is a reproduction of our published work on 'Emergent Glassiness in disorder-free Kitaev Model' with reference [PHYSICAL REVIEW B 108, 165118 \(2023\)](#).

3.1 Introduction

Quantum magnetism in crystalline solids and the study of spin liquids is experiencing a resurgence. It is partly due to a remarkable exactly solvable quantum spin model on a honeycomb lattice by Kitaev [1], followed by an exciting proposal by Jackeli and Khaliullin [2] of experimental realization of Kitaev spin liquid in certain real materials. Several potential Kitaev proximity materials are appearing on the scene [3–11]. New experimental results in possible Kitaev systems, such as α -RuCl₃ [12–19], continue to surprise us. Beyond basic sciences, developments in quantum spin liquids give hope and pave the way for novel qubits, topological quantum computation, and quantum information science and technology.

The Kitaev model is studied extensively in the presence of the magnetic field in 2D honeycomb lattice [20–25], in ladder setups [26, 27], and combined with other interactions [28–30]. There has been a variety of results and proposals, some of which are ubiquitous while others remain active research topics. There is theoretical evidence of $U(1)$ quantum spin liquid (QSL) in the intermediate field regime, with gapless excitations whose nature is still debated (for reviews see [31–34]). Our understanding of the constituent gauge and matter excitations in the Kitaev model with other interactions [35–42] and external perturbations are gradually evolving [43–48]. In particular, the behaviour of the gauge fluxes is not explicitly investigated in the previous numerical studies at finite magnetic fields, and hence their role in the corresponding phases remained unknown. Moreover, given that the dynamics of the flux excitations are restricted by the constraints in the underlying theory, interesting features such as amorphous solid and glass phases can be expected here but remain unexplored in the literature.

The experimental situations similarly remained inconclusive. Experiments have observed half quantization in the thermal Hall effect [49], and quantum oscillations in in-plane longitudinal thermal conductivity without any observed quantization in the corresponding transverse conductivity [50] in α -RuCl₃ in the intermediate magnetic field region. Another experiment has indicated multiple phase transitions in the same field region based on the anomalies in thermal (both longitudinal and Hall) conductivity [51]. Evidence of magnetic excitations [52] and phonon anomalies [53] are also presented in experiments in the same field region (before polarized phase appears). More recently, this is roughly the same magnetic field region where an experiment finds a signature of significantly strong and unusual temperature dependence in non-linear susceptibilities (χ_2 and χ_3). [54] Generally, a negative divergence in χ_3 is taken as the signature of spin-glass. However, in α -RuCl₃ a *positive* (λ '-like) divergence in χ_3 , along with other unusual signals in $\chi_{1,2}$, indicates the possible presence of some glass phase and/or excitations with slow dynamics, but not a spin glass.

Emergent glassiness in disorder-free many-body systems is seen, sporadically or otherwise, in many earlier works, although the observed phase was not often associated with glassiness.

Intuitively, if the ground state is in proximity to a wealth of local minima due to (say frustration-induced or topological-) degeneracy [55], ‘emergent disorder’ arising from an excessive number of conserved quantities [56–58], or orthogonal catastrophe near a critical point [59, 60], or local constraints or local bath, [55, 61, 62] its dynamics are impeded. In modern calculations, it is also shown that if the Hilbert space is partitioned [63, 64] and/or disentangled [65] into (local) Hilbert space, then the ergodicity is hampered.

The presence of a glass phase in the Kitaev model is highly probable, thanks to its distinctive excitation spectrum. When a local spin flip occurs, it induces the non-local excitations of a pair of Z_2 fluxes and/or a flux coupled with a Majorana fermion. However, the mobility of these excitations is limited due to constraints within the underlying Hilbert space. Can these excitations eventually freeze into a glass phase? Furthermore, what role does the flux density play in the potential formation of the glass phase? What is the role of the parent spin-liquid phase in it? In this work, we delve into these questions.

Here, we carry out a DMRG study on the Kitaev model on the 1D ladder at a finite magnetic field and zero temperature. The problem has previously been studied using the DMRG, iDMRG, and exact diagonalization methods, with or without the so-called Γ interaction term.[26, 66, 67]. While the phase boundaries with the magnetic field strength are reproduced below, the identification of the phases, especially the amorphous and glass phases, remained undisclosed in the previous studies. We find that the phases are described by the flux operator on each plaquette, while interesting features are also observed in the local operators such as spin operator per site[67] and flux operator in half of the plaquette. We find a set of interesting phases with an increasing magnetic field. At low fields, the Z_2 gauge flux stabilizes in a spatially homogeneous phase before it tends to crystallize. In the intermediate field region, we spot a robust glass phase determined by random spatial distributions of the Z_2 gauge fluxes, with possible gapless excitations. The emergence of glass physics is corroborated by the signature results of the correlation functions and quantum Fidelity calculations of the ground state. The dynamics of the glass phase have not been studied in detail because they are computationally expensive to simulate using the DMRG method. The glass phase intervenes in the homogeneous flux phase on one side and a homogeneous polarised phase at a high field. The candidate mechanism for the intrinsic glass phase is that the dynamics of low-energy excitations are restricted by constraints within the underlying Hilbert space, not by the quintessential emergence of conserved charges. As the count of π -fluxes reaches the half-filling fraction of the plaquette number, the fluxes acquire a near-freezing behavior. We also conducted the same DMRG analysis on a 4-leg Honeycomb strip with cylindrical boundary conditions. The nature of the phases is the same as that of the 1D ladder except for

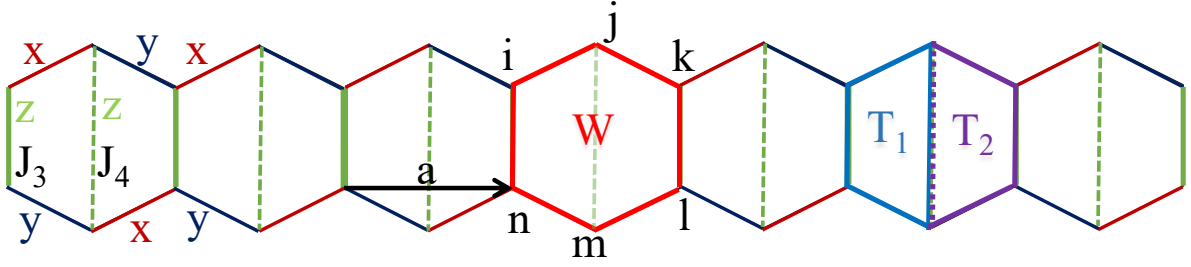


Fig. 3.1 A Kitaev ladder setup that we study here. At each site, we have three nearest neighbor bonds with exchange interactions, $J_{x,y,z}$, between $S^{x,y,z}$, respectively, as in a honeycomb analog. The J_z interactions (J_3, J_4) are kept to be the same as well as different for comparison. \mathbf{a} denotes the lattice constant, while W, T_i are flux operators defined in the text.

the quantitative values of phase boundaries. The glassy phase is observed for the range of fields where the U(1) spin liquid was proposed [20–25].

Our remaining article is organized as follows. We present our DMRG method and results in the Kitaev ladder at $T = 0$ as a function of the magnetic field and discuss the emergence of various phases with emphasis on the intrinsic glass phase.

3.2 Method

We consider the Kitaev model with the magnetic field (\mathbf{h}) along the [111]-direction as

$$H = \sum_{\langle ij \rangle_\alpha} J_\alpha S_i^\alpha S_j^\alpha - \sum_{i,\alpha} h_\alpha S_i^\alpha. \quad (3.1)$$

Here $J_\alpha > 0$ are bond dependent exchange couplings, $\alpha = x, y, z$. This model is set on the 1D Ladder as shown in Fig. 4.1). Each bond has three nearest-neighbor interactions, hence mimicking the setup proposed by Kitaev on a honeycomb lattice. The coupling along the z -bond (between the chains) is taken to be staggered, in general, as $J_z = J_3$ or J_4 in alternative rungs, see Fig. 4.1.

The spin operator S_i^α at each site i can be factorized into matter Majorana fermion (c_i) and gauge Majorana fermion (b_i^α) operators. Then the gauge Majorana operators in the nearest bonds can be combined into a bilinear operator $u_{ij}^\alpha = ib_i^\alpha b_j^\alpha$, which serves as a Z_2 gauge field. With this, we can define a flux operator at a six-bond plaquette p as

$$W_p = S_i^y S_j^z S_k^x S_l^y S_m^z S_n^x = \prod_{l_p} u_{l_p}^\alpha, \quad (3.2)$$

where $l_p = ij, jk, kl, lm, mn$, and ni are nearest neighbor bonds. The chosen spin component at a given site is the one present in the outward bond (normal to the plaquette). It turns out that W_p at each plaquette commutes with the Hamiltonian at $h = 0$, giving N conserved quantities in both 2D Honeycomb lattice as well as in the 1D ladder. In addition, in the present 1D ladder setting, there are two additional local conserved quantities, which are four-bond plaquette operators as defined by

$$\begin{aligned} T_{1p} &= S_i^y S_j^y S_k^x S_l^x = - \prod_{l_p} u_{l_p}^\alpha, \\ T_{2p} &= S_j^x S_m^x S_n^y S_k^y = - \prod_{l_p} u_{l_p}^\alpha, \end{aligned} \quad (3.3)$$

where $l_p = ij, jk, kl, li$ bonds in the $1p$ -plaquette, and so on. These operators are shown in Fig. 4.1. Consequently, $W_p = T_{1p} T_{2p}$ and $[T_{1p}, T_{2p}] = 0$ ¹. In the ground state, all these conserved quantities assume $W = +1$ and $T_{1p/2p} = +1$, (uniform flux-free phase),² giving us an extensive number of conserved quantities. Hence, the many-body Hilbert space is made of ‘trivial’ product states of gauge sectors and matter sectors [68]. This is a Z_2 - QSL state [69]. The phase diagram of the ladder Kitaev model with $J_{x,y,z}$ has been previously explored in Ref. [70]. The lines defined by $J_x - J_y = J_3$, $J_x - J_y = -J_3$ for $J_3 = J_4$ exhibit gapless phases characterized by linear dispersions. Furthermore, the $J_4 = 0$ line also features gapless excitations but with quadratic band touching. The rest of the phase diagram has gapped excitations.

We study Eq. 4.1 at $h \neq 0$ by using the DMRG method for $N = 200, 300, 400$ with cylindrical boundary conditions between the chains and open boundary conditions at the edge. The randomly initialized Matrix product state (MPS) is variationally tuned to the ground state by minimizing the expectation value of the matrix product operator of H in Eq. 4.1 (energy) with bond dimension up to $D \leq 2500$ and truncation error, $\varepsilon \sim 10^{-10}$. The DMRG algorithm is implemented using ITensors Library [72]. All the results of the main text are with $J_x = J_y = J_3 = J_4 = 1$; see Appendix. C.2 for results of other couplings. The expectation values of any gauge-invariant operators are calculated by contracting the MPO with DMRG-predicted ground state MPS.

We repeat some of the calculations on a four-leg 1D lattice with cylindrical boundary conditions along the armchair direction and open boundary conditions along the zig-zag direction. This geometry is closer to the 2D Honeycomb lattice; see Appendix. 3.6. The

¹These four-bond plaquette operators do not commute themselves or with the 2D Kitaev Hamiltonian but commute with the 1D ladder Hamiltonian in Eq. 1 at $h = 0$.

²Uniform flux free ground state is obtained by fixing the gauge: $u_{ij}^\alpha = +1$ on $\alpha = x, y$ bonds and on the legs, $u_{ij}^z = +1(-1)$ along J_3 (J_4)-couplings [69–71].

salient properties that are presented in the main text for the two-ladder are reproduced in the four-ladder settings.

3.3 Results

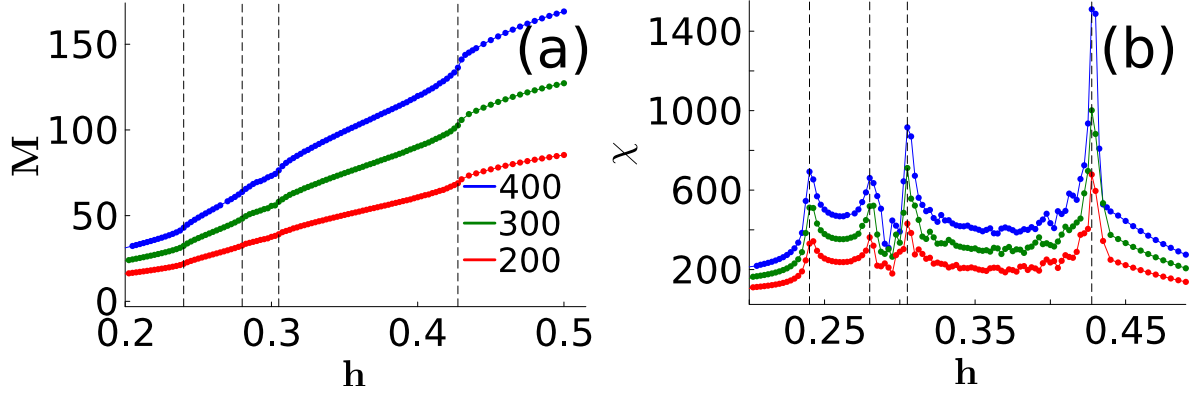


Fig. 3.2 (a) The spatial average value of the magnetization along the magnetic field direction is plotted as a function of field strength. (b) Corresponding values of the uniform spin susceptibility (χ) are plotted here. Three different colors denote the same calculated values but for three different system sizes $N = 400, 300, 200$. The vertical dashed lines mark the phase boundaries, which are located at $h \simeq 0.24, 0.28, 0.3$, and 0.43 . (The plots are magnified between $h = 0.2 - 0.5$ values for visualization.)

In gauge theories of the present kind, it is often difficult to find the right order parameter (s), especially when there are multiple phases that compete and/or coexist. As $h \rightarrow 0$, we have a non-local multi-linear operator, W_p , which acquires a fixed eigenvalue at each site as discussed above. At $h \rightarrow \infty$, the local linear (magnetization) operator $S_i^{\hat{h}}$ has a uniform average value in the polarised phase with the easy axis oriented along the field direction \hat{h} . There is no obvious way to smoothly interpolate between these two (quasi-) local operators, and a phase transition between them, if exists, evades the Landau theory and occasionally can be classified within the deconfined quantum critical paradigm. Non-local string operators arise as dynamics are introduced in the intermediate magnetic field strength. These string operators bind flux-flux, matter-matter, and/or flux-matter excitations. It is numerically expensive to evaluate their expectation values within DMRG. We will, however, occasionally comment on the possible role of such non-local string operators for the slow dynamics of the glassy phase we obtain here.

We present the spatial average values of the ground-state expectation value $\langle \mathcal{O} \rangle = \frac{1}{N} \sum_l \langle \mathcal{O}_l \rangle$, where $\mathcal{O}_l = S_i^{\hat{h}}$, $l = i$ site index as shown in Fig. 3.2, and $\mathcal{O}_l = W_p, T_{1p}, T_{1p}$; $l = p$ plaquette

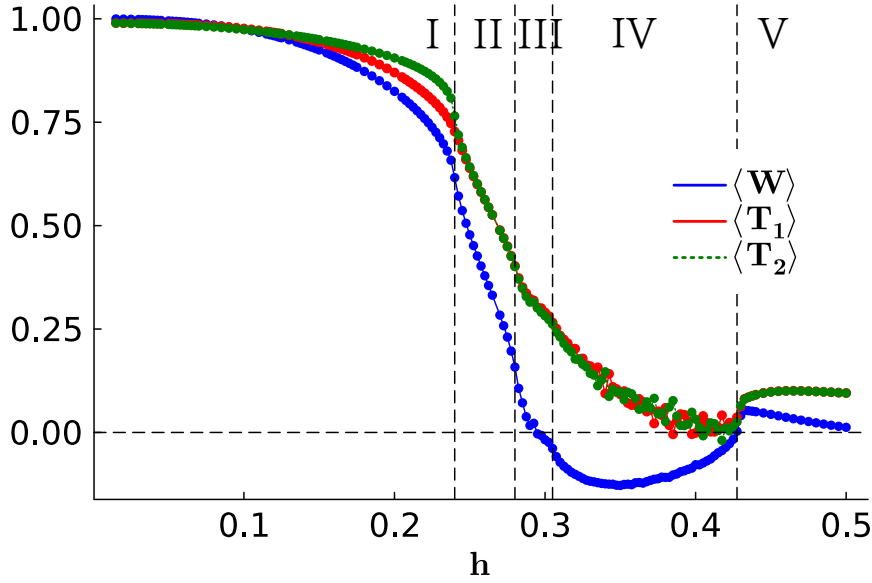


Fig. 3.3 Computed values of the spatial average of the three flux operators W , T_i are plotted as a function of field strength. The results are shown for a DMRG run on a 400 site lattice. The vertical dashed lines indicate the same phase boundaries as in Fig. 3.2. The horizontal dashed line marks the $\langle W \rangle = 0$ line.

index, as shown in Fig. 3.3. In both values of $M = \langle S \rangle$ and $\langle W \rangle$, we observe concurrence of kinks or jumps with increasing magnetic field strength h . We denote these finite-field phases by I, II, III, IV, and V. We see in Phase I, a uniform flux value at all plaquettes with the average value decreasing with h , and hence we dub it the uniform-flux phase, see Fig. 3.4. In Phase II, local flux (we will call them Z_2 vortex) values begin to deviate from their finite mean value at a few plaquettes. This is a result of the appearance of the low density of π fluxes in the ground state. Phase III appears in the region where the number of vortices is nearly half of the number of lattice sites (half-filling), and Z_2 vortices tend to crystallize. Phase IV corresponds to the glass phase with random fluctuations in the Z_2 vortices around a zero-mean value. Finally, Phase V corresponds to the uniform polarised phase.

The magnetization grows near-linearly at all field strengths except in the intermediate region. The uniform spin susceptibility, defined as $\chi = \frac{\partial M}{\partial h}$, shows divergence features at all phase boundaries. The divergence in χ is most sharp at $h = 0.43J$, at the phase boundary between the glass and the polarized phases, possibly indicating a phase transition caused by the long-wavelength collective excitations (magnons).

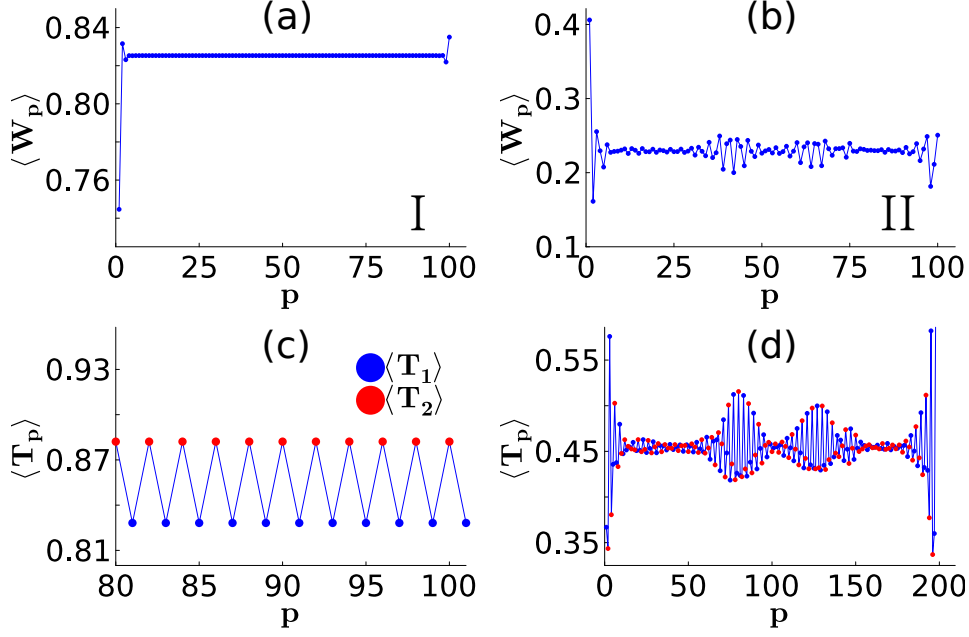


Fig. 3.4 The computed value of $\langle W_p \rangle$ are shown for each plaquette p for two different fields (a) $h = 0.2$ (b) $h = 0.275$, which correspond to Phase I and Phase II. (c),(d) The values of $\langle T_{\beta p} \rangle$ are shown in the corresponding bottom panel. The $T_{2p} > T_{1p}$ at a p corresponds to T_{1p} flux sitting at the boundaries, and vice versa

3.3.1 Uniform and Crystalline phases of fluxes

The expectation values of flux operators show an intriguing behavior, as shown in Fig. 3.3. Up to $h \approx 0.24J$, we observe a uniform value of $\langle W_p \rangle$, but $\langle T_{ip} \rangle$ obtain staggered mean values between the alternative four-bond plaquettes, as shown in Fig. 4(a) and 4(b), respectively. (The condition for $T_{1p} > T_{2p}$ versus $T_{1p} < T_{2p}$ at a given plaquette depends on the open boundary condition.) Moreover, the uniform value of $\langle W_p \rangle < 1$ at all plaquettes suggests that the gauge sector of the ground state can still be approximated to be a product state of local basis, but now the local states have changed from $|+\rangle_p$ at $h = 0$ to $\alpha_p |+\rangle_p + \beta_p |-\rangle_p$ for $h > 0$, where $W_p |\pm\rangle_p = \pm |\pm\rangle_p$, and $\alpha_p^2 - \beta_p^2 = \langle W_p \rangle$, $\forall p$. The normalization condition dictates $\alpha_p^2 = (1 + \langle W_p \rangle)/2$.

When the Kitaev model is perturbed, in general, one gets complicated multi-body interactions among Majorana Fermions and Z_2 gauge fluxes. Z_2 gauge fluxes become dynamic and acquire finite effective masses[45]. Further, open string operators carrying Majorana fermion modes (both $b_i^{x,y,z}$ and c_i) at their ends also have expectation values in the ground state. The study of open strings using DMRG at finite fields is cumbersome. Elaborated discussion on these string objects at finite fields and their role in dynamics is presented in Appendix. 3.7. There are excitations due to T_{ip} fluxes whose energy scale is $< 10^{-3}J$. But in the uniform $\langle W_p \rangle$ phase, we find that $\langle T_{1p} \rangle > \langle T_{2p} \rangle$ for T_{1p} sitting at the boundaries ($\langle T_{1p} \rangle < \langle T_{2p} \rangle$ for T_{2p}

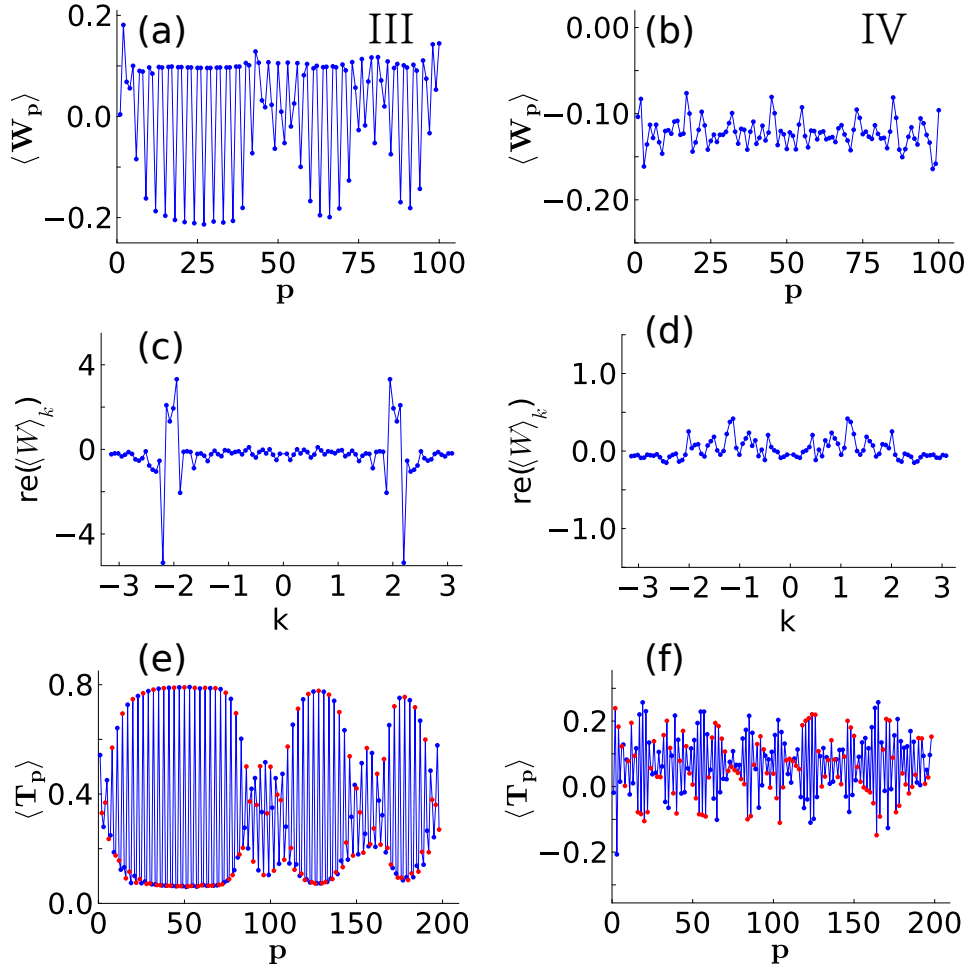


Fig. 3.5 Similar to Fig. 3.4, but here the results are shown at two representative fields of Phase III ($h = 0.2975$) and Phase IV ($h = 0.365$). In the middle panel ((c),(d)), we plot the real part of the Fourier transformation of $\langle W_p \rangle$ with wave vector k .

at boundaries). In addition, both the W and T flux pairs are also virtual excitations. These excitations induce further neighbor hopping to the matter fermions. The density of these excitations increases as a function of h , changing the magnitude of the $\langle W \rangle$. The energy gap to create flux-pair is $\leq 10^{-3}$. Similarly for T -flux pair, it is $\leq 10^{-5}$ (see, Appendix. C.1). There are long-wavelength collective excitations, in which α_p (i.e., $\langle W_p \rangle$) varies slowly across the lattice but with a gap that scales with the system size. Finally, single matter Majorana excitations appear at higher energy.

A single Z_2 vortex creation in the uniform flux case at a six-bond plaquette, i.e., changing W_p from $+1$ to -1 costs energy $E \sim 0.24J$. Therefore, for $h > 0.24J$, W_p vortex creation is energetically feasible. In the dilute limit, the vortices start to proliferate in the lattice like a vortex gas or liquid phase, which is Phase II in our phase diagram.

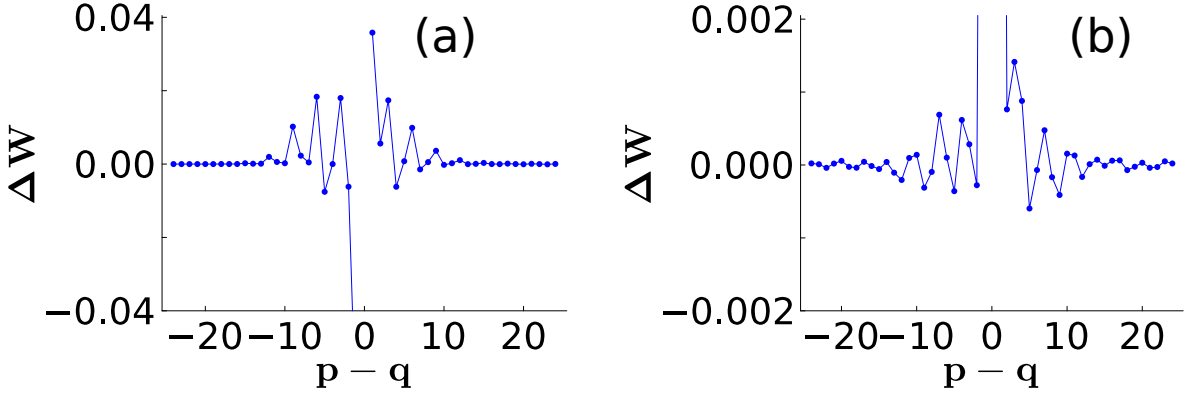


Fig. 3.6 We plot the correlation function of the flux operator ΔW_p with $p = 50$ for (a) $h = 0.295$, and (b) $h = 0.365$.

With further increase of the field strength, by $h \geq 0.28J$ there is a tendency for the vortices to crystallize, as shown in Fig. 3.5(a). This is Phase III. Here, $W_p = \pm 1$ plaquettes are nearly equal in number, giving $\langle W \rangle \rightarrow 0$, which is close to half-filling. In this case, the vortices are ‘frozen’ to the lattice site with alternating plaquettes having opposite W_p sites; see Fig. 3.5(a). This phase is analogous to a density wave order in a correlated fermionic insulator or hard-core bosonic insulator at half-filling. The vortex lattice formation is evident in the dominant value of the Fourier component of the flux operators at a single wavevector as shown in Fig. 3.5(c). Slightly away from the half-filling on both sides, we observe here a few wavevectors and quasi-long-range correlation functions. which suggests an amorphous behavior.

3.3.2 Emergent Glassiness

An amorphous crystal is a precursor to glassiness and may be at play in the present case as well. The energy to create a single W_p flux in the crystalline phase is $\sim 0.05J$ (assuming uniform crystal for this estimation; see Appendix C.1 for more details). Therefore, at $h > 0.3J$, we enter into the dense vortex region (Phase IV). The large value of the Z_2 vortex density is evident in the $\langle W \rangle \leq 0$ value shown in Fig. 3.3. Because of this high density, any small local fluctuation tends to impede the ordering of the entire lattice, and hence a *glassiness* arises.

We calculate the correlations of W_p , quantifying the fluctuations from its mean, as $\Delta W = \langle W_p W_q \rangle - \langle W_p \rangle \langle W_q \rangle$, where the expectation value is calculated with respect to the MPS ground state. The value of the correlation of the fluxes is $\sim 10\%$, and the correlation length extends up to 20-30 plaquette distance on both sides, as shown in Fig. 3.6(d). Furthermore, this quasi-long correlation length in the glass phase is larger than its precursor crystalline phase. This is in contrast to a solid-to-liquid phase transition where the correlation length decreases in a liquid

phase. This is one aspect of the glassiness that distinguishes phase IV from it being the liquid phase.

In this phase, the local spin operators exhibit an incommensurate order, as also reported earlier.[67] Different incommensurate orders in finite lattice give closely lying energy states but fail to become orthogonal to each other. On the other hand, as we will see below via the Fidelity calculation, different local minima states are completely orthogonal to each other, suggesting that the glass state is not governed by the incommensurate local spin but by the flux operators.

Furthermore, we have also checked that the phase has a non-zero central charge, signaling gapless excitations. Note that this is the approximate range of fields where gapless $U(1)$ QSL state is proposed in the 2D Honeycomb Kitaev model [20–25]. The convergence of DMRG minimization in this range of fields is slow compared to time scales for other phases (see the Fidelity result for the corresponding interpretation).

Referring to the definition of W_p in Eq. 3.2, it is easy to associate the fluctuation of $\langle W_p \rangle$ with the quantum fluctuation of the spins. This sets the present glass physics apart from the classical glassy phase of frozen spin configurations. Note that apart from single flux productions, there are also non-local flux pairs that are connected by Wilson operator $(W_p)^n$ - which in the spin operator form takes a string operator. This automatically generates n -point spin-spin correlations in this system. Define a n^{th} -order uniform susceptibility $\chi_n \sim \partial^n M / \partial h^n$, we have checked that the second and third-order susceptibilities in this region are large and more chaotic as a function of the magnetic field. Note that in a Gaussian fluctuation theory, the third and higher-order susceptibilities vanish, as we also find in the other phases. But in Phase IV, we find significant enhancement of the mean square values of the second and third-order susceptibilities in the range of $\mathcal{O}(10^2)$ to $\mathcal{O}(10^3)$.

For the high magnetic fields, Phase V is trivially polarised along the $[111]$ direction. The fluxes are half of the plaquettes with π - fluxes resulting in $\langle W_p \rangle = 0$ and $\langle T_{1p/2p} \rangle = 0$ in every plaquette uniformly.

There is no glassy phase observed for the ferromagnetic couplings, i.e. $J_x = J_y = J_3 = J_4 = -1$. Here, we find two phases: the uniform flux phase at a small magnetic field region and the polarised phase with uniform $\langle W_p \rangle = 0$ (and $\langle T_{1p/2p} \rangle = 0$).

3.3.3 Robustness of results with other Lattice Settings

We repeat the DMRG calculation in a 2D lattice strip via the four-leg Honeycomb lattice with cylindrical boundary conditions; see Appendix. 3.6 for more details. We find four phases (Fig. 3.8), where phase II and phase III are not distinguishable within the finite system size calculation. More importantly, the glass phase is reproduced here.

We also repeat the DMRG calculation in the 1D ladder for $J_4 = 0$ with other parameters fixed at 1. This creates open boundary conditions between the chains. The result is presented in Appendix C.2. We find two phases: at $h > 0$, we immediately find a crystalline phase (phase III) and the uniform polarized phase (phase V). The glass phase is absent here.

3.4 Phase transitions and Fidelity

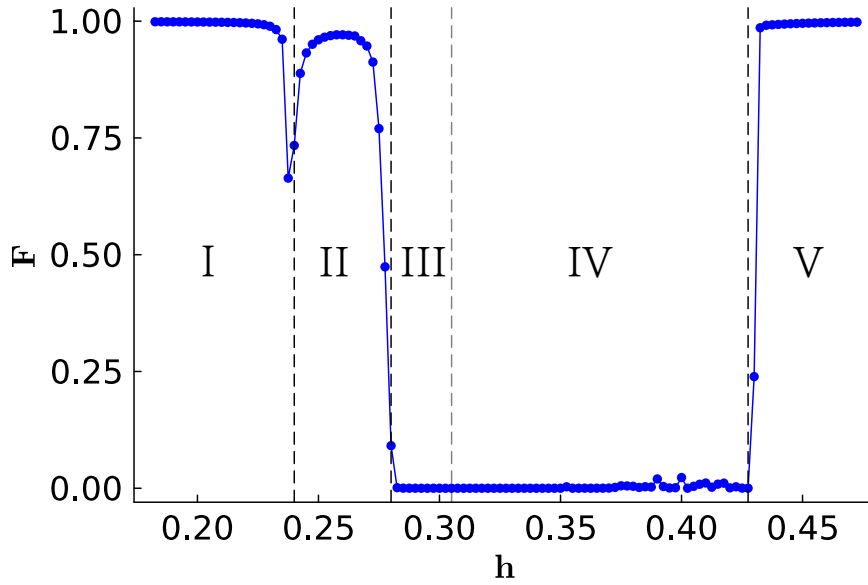


Fig. 3.7 I plot the quantum Fidelity (defined in the text) with magnetic field for $N = 400$ lattice sites. The vertical dashed lines indicate all five phase transition points, which coincides with Figs. 3.2 and 3.3.

In the absence of a well-defined local order parameter, characterizing phase boundaries and phase transitions becomes challenging. In such a scenario, we can study how different variational ground states are mutually orthogonal as a function of the control parameter. This information can be obtained by the quantum fidelity analysis.

The quantum Fidelity is defined as $F(h) = |\langle \psi_0(h) | \psi_0(h + \delta h) \rangle|$, where $|\psi_0(h)\rangle$ is the ground state vector obtained from the DMRG calculation at h [73–77]. It is now evident that if the states $|\psi(h)\rangle$ and $|\psi(h + \delta h)\rangle$ are linearly dependent, we have $F \rightarrow 1$, and if they are completely orthogonal, we get $F \rightarrow 0$, and any value between them measures the overlap between the two wavefunctions.[78] The fidelity F vanishes in two major scenarios: due to gapless excitations and emergent glassiness. As the system is tuned to a new configuration, and if the corresponding state is orthogonal to the preceding one, the fidelity between the two states vanishes. This phenomenon is known as the orthogonality catastrophe, as proposed

by Anderson in free Fermion systems. It is an infrared catastrophe that arises from gapless excitations. However, fidelity can also vanish due to emerging glassiness. In this case, the system becomes trapped in some metastable local minima whose states are mutually orthogonal to each other. We discuss below why the glass phase is the origin of the $F = 0$ value in our case.

As shown in Fig. 3.7, we see that $F \rightarrow 1$ in both the uniform phases of flux (Phase I) and of spin (Phase V), suggesting a unique ground state in these phases. F sharply decreases at the phase boundary between Phase I and II, implying that the vortex gas phase is separated from the uniform phase by a phase transition. Within the Phase II region, the Fidelity does not completely reach 1, suggesting the presence of configurations that partially overlap with the chosen ground state.

The most exciting feature is obtained in Phase III (amorphous vortex crystal) and Phase IV (vortex glass) where $F = 0$. This clearly indicates the presence of a plethora of local minima whose wavefunctions are orthogonal to the chosen ground states. These local minima are not degenerate, as in the case of an infrared catastrophe, but lie within the energy fluctuation scale provided by the magnetic field. Additionally, we repeated the DMRG runs with different random initial configurations at a fixed value of the magnetic field. In each iteration, the obtained ground states are orthogonal to each other. We have performed the ED calculations with system sizes 6, 10, and 14. And found that the results qualitatively agree with the DMRG; see Appendix 3.8 for the details. These findings strongly suggest that the orthogonality is unlikely to be driven by gapless excitations and rather points towards the stabilization of a glass phase.

The fidelity is consistently zero in both Phase III and Phase IV, which aligns with expectations since an amorphous solid serves as a precursor to a glass phase. In an amorphous solid, a domain of fluxes has a metastable ground state, while in the glass phase, the domain size reduces to a single flux. Orthogonal ground states obtained from different DMRG runs for phase-III have different domain wall structures. Since the flux configurations vary for different initial conditions in DMRG runs, the size of domains varies from one another. However, the size of the largest domain scales proportionately with the system size.

3.5 Discussion

A key feature of the QSLs, in general, and the Kitaev model, in particular, is the presence of constraints on the Hilbert space for low-energy excitations. The emergent matter excitations typically enjoy an enlarged Hilbert space than the physical Hilbert space of the spin operator provided by the Hamiltonian. This restriction on the available Hilbert space limits the dynamics of the excitations on the phase space.

In this DMRG study, we observed the glassy phase at the intermediate field range on the 1D ladder and then in a 4-leg Honeycomb strip with a cylindrical boundary. Previously, various numerical studies have suspected intrinsic glassiness or slow dynamics in general as a function of temperature and applied field. Localization features are observed for a range of different couplings in the Kitaev ladder model at low field [79], indicating that the localization behavior is beyond uniform flux approximations at low fields. A non-ergodic phase is also proposed in the 2D Kitaev model under quench with skew magnetic field [80] and without the field for anisotropic couplings [81]. Recall that the exact solution of the Kitaev model at the zero field is a result of N local conserved quantities (flux operators) in a honeycomb lattice of N plaquettes. As claimed in Refs. [63, 64], the local conservation constraint leads to the shattering of the full Hilbert space of dimension 2^{2N} into 2^N sectors of equal dimension. Each sector defines a 2^N dimensional Hilbert space of free neutral fermions. This perfect partitioning of Hilbert space and consequent superselection impairs ergodicity and favors many-body localization.

Any external perturbation that directly couples to the local spins generates excitations of flux pairs or flux-Majorana bonding. These topologically protected excitations have restricted dynamics in the lattices and are impervious to annihilation by temperature or local defects [82]. However, the emergence of a glass phase, specifically a flux glass rather than a spin glass, necessitates further fine-tuning. In our study, we observe that as the number of fluxes reaches half-filling, the disorder configurations of these fluxes form local energy minima with corresponding orthogonal quantum states. These local minima possess slightly different energies, comparable to the magnetic field's strength, and do not give rise to a degenerate manifold. Consequently, an infrared catastrophe does not occur; instead, the system freezes into one of these local minima configurations. Since the flux operators are products of spin operators within a plaquette, the flux correlation function corresponds to a many-spin correlation function. Measuring such a correlation function is currently infeasible using existing experimental techniques. However, indirect measurements can be achieved through experiments involving field quenching and non-equilibrium analyses. For instance, femtosecond laser pulses can be employed to probe the glassiness present in Kitaev spin liquid materials.

Extending these ideas to the RVB state, a few conjectures can be made for future studies. A local spin flip at a site produces two spinons, which separate away during time evolution. However, spinons as sources of emergent gauge fields, carry gauge fluxes [83]; sometimes both electric and magnetic charges, called Dyons [84, 85]. Net gauge fluxes created by the spin operators are zero, even though the spin operators are gauge invariant. Flux attachment endows spinons with fractional exchange statistics in 2 dimensions [86]. This is also transparent in Kalmeyer-Laughlin chiral spin liquid state [87, 88] and later works, where low energy spinon carries a Vison or Meron (half-Skyrmion) [85] or SU(2) gauge fluxes [89]. The restrictions on

the spinon dynamics lower its kinetic energy. Whether these spinons can freeze to form a glass phase in a U(1) spin liquid phase remains to be investigated in future studies.

3.6 Towards 2D: Results on 4 Leg model

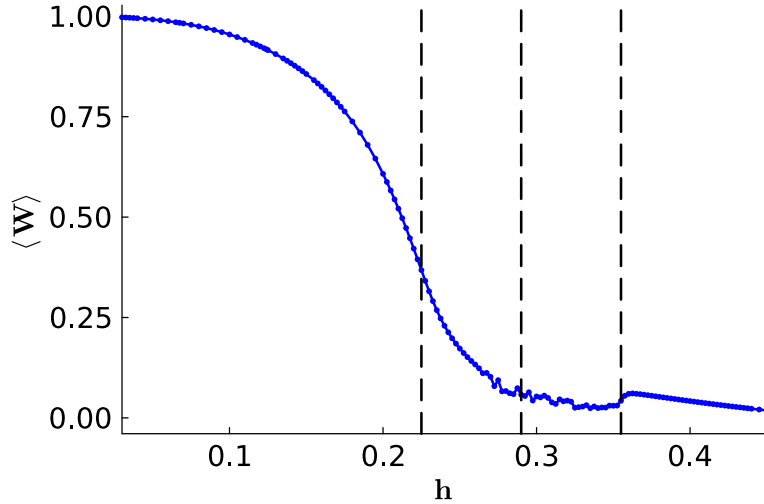


Fig. 3.8 The spatial average values of $\langle W_p \rangle$ as a function of the magnetic field for the four-leg Honeycomb lattice with system size $N = 52$ sites. The vertical dashed lines are pointing the fields of phase transitions identified from the magnetic susceptibility.

To find out the robustness of the phase diagram presented in the main text on a two-leg DMRG calculation, we repeat the calculation on a four-leg ladder with cylindrical boundary conditions of system size, $N = 52$ sites and with bond dimension $D \leq 1000$, truncation error, $\epsilon \approx 10^{-10}$. We reproduce four phases as presented in Fig. 3.8. Those four Phases are Phase I, Phase III, Phase IV, and Phase V of the 1D ladder results presented in the main text.

The different phase boundaries are identified from the magnetization values with smaller steps of the magnetic field than seen in previous studies; see, for example, Ref. [20]. The average expectation of the plaquette operators as a function of the magnetic field is shown in Fig. 3.8 agreeing with the previous findings [21].

Even though the system size is small and prone to boundary effects along the legs, we reproduce four phases, as seen in the 1D ladder. Here, the boundary between Phase- II to Phase- III is not explicit within the finite size calculations. The low field phase, Phase-I, for fields up to $0.23J$, has uniform flux configurations, as shown in Fig. 3.9(a). Then, in Phase III, for a range of fields $0.23 < h < 0.29$, the proliferation of the dynamically generated fluxes into the ordered configurations is observed, see Fig. 3.9(b). For fields above 0.29, the randomly distributed

fluxes without any order are observed up to 0.36 in the proposed U(1) spin liquid region. The flux configurations in the polarised phase are with $\langle W_p \rangle = 0$ in all the plaquettes uniformly.

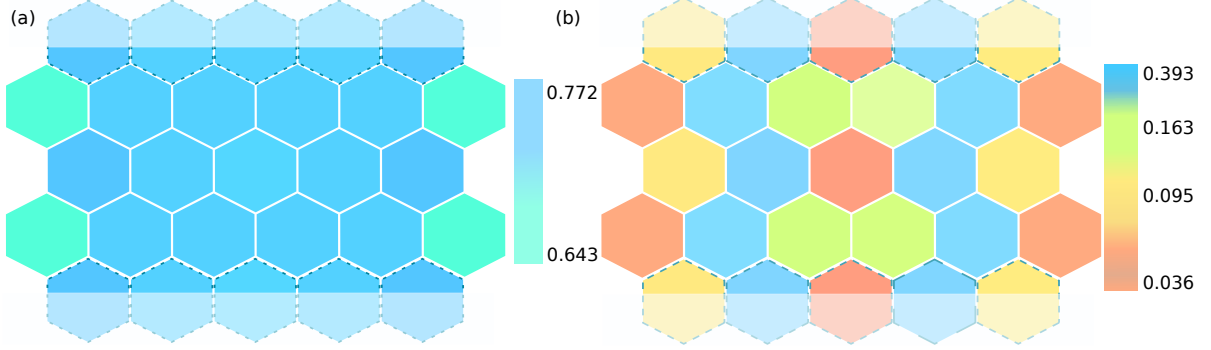


Fig. 3.9 $\langle W_p \rangle$ at (a) $h = 0.18$ and (b) $h = 0.26$, the emergence of periodic ordering in flux configurations is observed at this field. The color bar indicates the strength of the flux in a given plaquette. The shaded plaquettes are connected for the periodic boundary in the cylinder geometry.

3.7 Topological Overprotection, Non-local String Operators and Emergent glassiness at finite temperature in Disorder free Kitaev model

In this section, we elaborate on the discussion of the non-local string excitations in the Kitaev Honeycomb Lattice model and their constrained dynamics. The ground state of the uniform Kitaev model, a zero Fermion number sector, lies in the zero flux sector, as dictated by Lieb's theorem (2D analogue of discussions in Sec. 3.2 of main text). This sector has full translational invariance, and a graphene-like Dirac cone spectrum of positive energy Fermion excitations (Majorana fermion) in Bloch states in the Brillouin zone of the honeycomb lattice. Other flux sectors bring in new physics. The spatial distribution of conserved and static π -fluxes, selected randomly from among the 2^N sectors, is typically random. Consequently, one particle wave function of the positive energy Fermions will be non-Bloch-like and generically Anderson localized.

We demonstrate that the Kitaev model has features that encourage glassiness at finite temperatures in the absence of disorder. The notion of Topological overprotection [55] induced glassiness was introduced by Chamon using 3D toric code quantum spin models. At the heart of Chamon's work is the observation that coupling of the constituent spin degree of freedom at lattice sites to a dissipative Bosonic (model thermal) bath results in the creation of defect

(anyons) clusters. Because of topological protection, defect annihilation and propagation are severely constrained. It results in anomalous and slow relaxation - this is the beginning of glassiness.

To induce dynamics, following Chamon, we couple the constituent spin degrees of freedom at lattice sites to Bose oscillators (of some external heat bath) at every site: $a_i^\alpha, a_i^{\alpha\dagger}$ (this is analogous to applying site-dependent magnetic fields in Eq. 4.1. And this discussion also applies in case of homogeneous fields mentioned in the main text).

$$H_{spin/bath} = \sum_{i,\alpha} g_\alpha S_i^\alpha \left(a_i^\alpha + a_i^{\alpha\dagger} \right)$$

Where g_α is the coupling strength. It was shown [68, 90] that a spin operator at site i , when acting on the ground state, creates a pair of static π -flux excitations in two plaquettes that share a single bond (in α -direction) and a dynamical Majorana Fermion. During time evolution, the Majorana Fermion propagates away from the site i , while the two π -fluxes remain immobile. The dynamics of the two fluxes are restricted (topologically protected) in the following sense: They disappear only when a specific process takes place - when the nearest neighbor spin at a specific site creates/annihilates a (bath) boson and adds two more π -fluxes (thereby annihilating the two π -fluxes that are already present). If a different spin component at the same site i creates/annihilates a boson, then the π -flux pair does not get annihilated but reoriented. If a wrong nearest neighbor spin creates/annihilates a bath Boson, two fluxes split and separate into two next nearest neighbor π -fluxes.

Another extended operator arises from the liberated Majorana fermion. In terms of constituent spin operators, the Majorana fermion operator is a product of a string of spin operators. One end of the string is attached to the plaquette pair, and the other end carries the Majorana fermion. In other words, the Majorana fermion that has been created by coupling to bath Boson's degree of freedom is an extended object (strings). Strings of two Majorana Fermions can cross and get reconnected but never disappear. This feature of topological protection of strings is absent in models discussed in Ref. [55].

The above two types of non-local string operators from π -flux pairs and spin strings attached to Majorana fermions limit the disappearances of fluxes and discourage the proliferation of strings. Equilibration processes get slowed down, and glassiness may emerge. Thus, at any finite temperature, because of the production of π -flux excitations and strings, glassiness is induced via coupling to the bath.

From another point of view, the Quantum disentangled liquid [65] character at any finite temperature is manifest and exact in the Kitaev spin liquid. We have thermally produced infinitely massive Z_2 fluxes, in the background of which light Majorana Fermions hop and

attempt to delocalize. In the thermal ensemble, various superselected sectors with static fluxes appear and typically support Anderson localized positive energy neutral Fermions [91]. Thus we have overwhelming members of the thermal ensemble that form a quantum disentangled liquid with a high susceptibility for glassiness and non-thermalization.

3.8 Exact diagonalization calculations

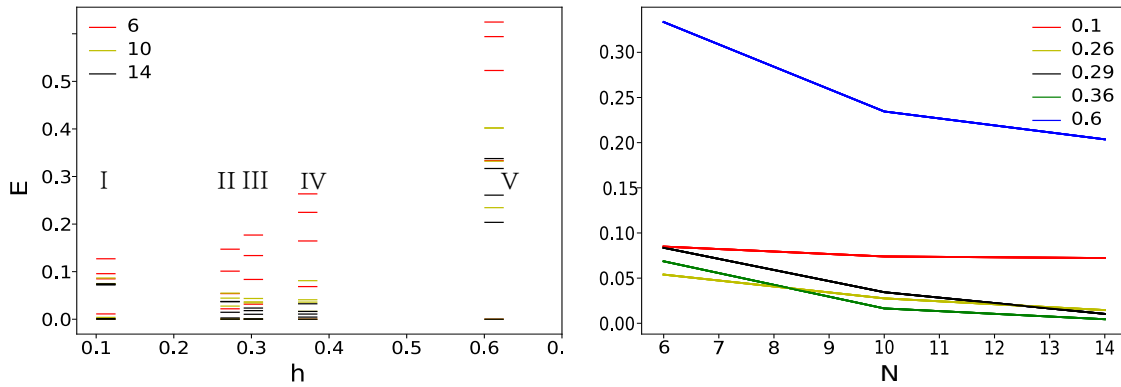


Fig. 3.10 (a) $E - E_0$ at the magnetic fields: $h= 0.1$ (Phase-I), 0.26 (Phase-II), 0.29 (Phase-III), 0.36 (Phase-IV) and 0.6 (Phase-V) for system sizes $N = 6, 10,$ and 14 are plotted. E_0 is the corresponding ground state energy. (b) The gap between the first excited state from the ground state at the above-mentioned magnetic fields is plotted as a function of system size (N).

We have performed the exact diagonalization (ED) calculations with the system sizes $N = 6, 10,$ and 14 . The results are shown in Fig. 3.10, where we have plotted the lowest five energy levels at five representative field values. A plot of the energy gap between the ground state and the first excited state is given in Fig. 3.10(b). We find that in Phases II, III, and IV, the energy gap decreases with increasing system size. The gap decreases much more slowly in the polarised phase (V), while that in the homogeneous phase (I) is nearly constant. There is a ground state degeneracy in Phases I and II, as also observed in the DMRG results. Within the numerically accessible system sizes, the ED results are consistent with our DMRG conclusions.

3.9 Conclusions

Our detailed DMRG study on the 1D Kitaev model with a magnetic field reveals an intriguing phase diagram with five phases, and among them, we discover a glass phase. All these five phases are also obtained in the Kitaev- Γ model in previous studies[26, 66, 67]. We have found

an intriguing intrinsic glassiness in a part of their phase diagram when $\Gamma = 0$. It is likely that glassiness is present in other regions of the phase diagram which remains to be investigated in the future. Furthermore, we are able to segregate between the vortex gas, crystal, and glass phases in the otherwise known $U(1)$ QSL phase, due to the detailed analysis of the vortex operators as well as the Fidelity calculation. We find evidence of gapless excitations in the vortex glass phase but not in the gas and crystal phases.

How robust is our phase diagram beyond a two-leg ladder geometry and beyond the limitations of the DMRG studies? A complete answer to this question is not known in the community. We have, however, repeated the DMRG calculation on a four-leg ladder geometry as given in the Appendix. Here, we find four Phases: Phase I, Phase III, Phase IV, and Phase V. This means the boundary between Phase II (vortex gas) and Phase III (vortex crystal) is not discernible. However, the vortex glass of present interest is well reproduced.

There are now numerical software available for finite temperature calculation within DMRG and Tensor network formalism. Future extension of our calculation to finite temperature will shed light on the possibility of a BKT-like physics for Z_2 vortex as well as the stability of the glass phase to thermal broadening.

C

Appendices for chapter 3

C.1 Estimation of Gaps

The gap to the excited state with π - fluxes from uniform flux phase at $h = 0$ is estimated by Exact Diagonalization. The ED calculations are done with matter Majorana fermions by fixing the gauge in accordance with uniform flux configuration. The Z_2 vortex gap for creating a single W or T is, in principle, calculated by keeping two W or T π - fluxes infinitely far apart. In finite-size calculations, that is approximately the y-axis intercept of the plot: gap versus $1/d$, where d is the distances between the two π - fluxes with systems sizes, $(2d)$. The π - flux pair can be created by changing the bond operator from $u_{\langle ij \rangle}^z = +1$ to -1 on z - bond common to the two adjacent plaquettes. Further creating a series of adjacent π -fluxes either to the right or left of already created flux-pair for separating those initially created π -fluxes accordingly. The gap to single W vortex is ≈ 0.24 and for W flux-pair, $\leq 10^{-3}$. In case of T plaquettes, it is $\leq 10^{-3}$ for single vortex and $\leq 10^{-5}$ for flux-pair.

The ordered superlattice flux configuration at the finite field strength is approximated to uniform crystal for estimation of the gap. Further, it is approximated as follows: the high $\langle W_p \rangle$ value in the plaquette p to $+1$, the lower one to -1 . With this approximated flux configuration, the estimated gap to the single vortex is calculated following the same approach as for the

uniform flux case. The gap to a single W vortex is ≈ 0.05 in this approximated uniform crystallized flux configuration. All the energy values mentioned in this article are per unit cell.

C.2 Phases for Different Couplings

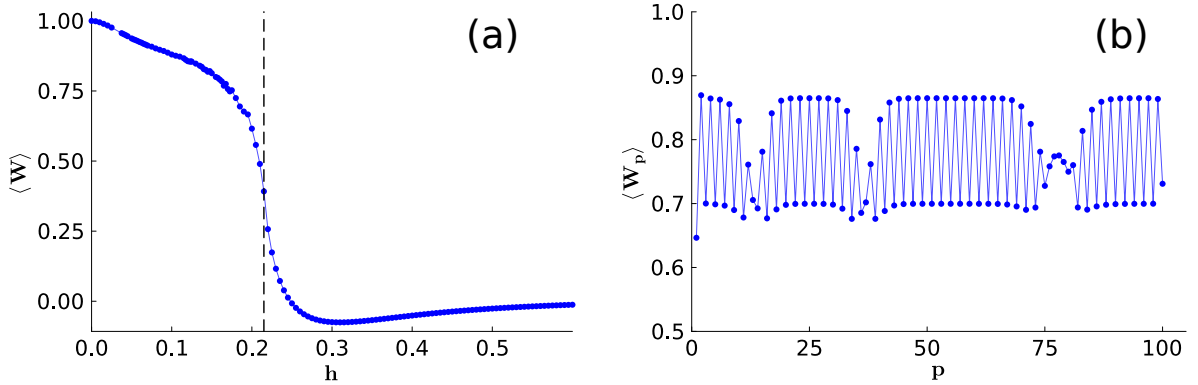


Fig. C.1 (a) Average of $\langle W_p \rangle$ for $N = 400$ as a function of magnetic field for the coupling $J_4 = 0$ with $J_x = J_y = J_3 = 1$. The phase boundary is indicated with a vertical dashed line. (b) $\langle W_p \rangle$ as function of plaquette number, p at field $h = 0.165$.

In the main text, we presented results for $J_x = J_y = J_3 = J_4 = 1$. $J_4 = 1$ imposed a cylindrical boundary condition perpendicular to the ladder, leaving no bond indices to be open. Now we set $J_4 = 0$, which gives alternating sites to have open bonds in the matrix product state. The energy dispersion of matter fermions in the ground state with $h = 0$ is gapless and quadratic. For $h > 0$, only two phases are present with a phase boundary at $h \approx 0.215$, which is distinguished by a cusp in the magnetization plot (not shown). The average value of the W_p operator as a function of the magnetic field is shown in Fig. C.1(a). The low field phase is a crystalline phase of $\langle W_p \rangle$, as shown in Fig. C.1(b). This phase is same as Phase-III for $J_4 = 1$ given in the main text. The high-field phase is a polarized phase with $\langle W_p \rangle = 0$ at all the plaquettes. There is no glass phase observed here.

Two phases with phase boundary around $h \approx 0.25$ as a function of the magnetic field are found with couplings $J_x = 2, J_y = J_3 = J_4 = 1$, where the ground state dispersion of matter fermions at $h = 0$ is gap-less and linear. No structural difference is observed in flux configurations in both phases, with $\langle W \rangle$ decreasing smoothly with increasing h .

References

- [1] A. Kitaev, [Annals of Physics](#) **321**, 2 (2006).
- [2] G. Jackeli and G. Khaliullin, [Phys. Rev. Lett.](#) **102**, 017205 (2009).
- [3] Y. Singh and P. Gegenwart, [Phys. Rev. B](#) **82**, 064412 (2010).
- [4] X. Liu, T. Berlijn, W.-G. Yin, W. Ku, A. Tsvelik, Y.-J. Kim, H. Gretarsson, Y. Singh, P. Gegenwart, and J. P. Hill, [Phys. Rev. B](#) **83**, 220403 (2011).
- [5] S. K. Choi, R. Coldea, A. N. Kolmogorov, T. Lancaster, I. I. Mazin, S. J. Blundell, P. G. Radaelli, Y. Singh, P. Gegenwart, K. R. Choi, S.-W. Cheong, P. J. Baker, C. Stock, and J. Taylor, [Phys. Rev. Lett.](#) **108**, 127204 (2012).
- [6] F. Ye, S. Chi, H. Cao, B. C. Chakoumakos, J. A. Fernandez-Baca, R. Custelcean, T. F. Qi, O. B. Korneta, and G. Cao, [Phys. Rev. B](#) **85**, 180403 (2012).
- [7] R. Comin, G. Levy, B. Ludbrook, Z.-H. Zhu, C. N. Veenstra, J. A. Rosen, Y. Singh, P. Gegenwart, D. Stricker, J. N. Hancock, D. van der Marel, I. S. Elfimov, and A. Damascelli, [Phys. Rev. Lett.](#) **109**, 266406 (2012).
- [8] S. Hwan Chun, J.-W. Kim, J. Kim, H. Zheng, C. C. Stoumpos, C. Malliakas, J. Mitchell, K. Mehlawat, Y. Singh, Y. Choi, *et al.*, [Nat. Phys.](#) **11**, 462 (2015).
- [9] Y. Kubota, H. Tanaka, T. Ono, Y. Narumi, and K. Kindo, [Phys. Rev. B](#) **91**, 094422 (2015).
- [10] S. C. Williams, R. D. Johnson, F. Freund, S. Choi, A. Jesche, I. Kimchi, S. Manni, A. Bombardi, P. Manuel, P. Gegenwart, and R. Coldea, [Phys. Rev. B](#) **93**, 195158 (2016).
- [11] K. Kitagawa, T. Takayama, Y. Matsumoto, A. Kato, R. Takano, Y. Kishimoto, S. Bette, R. Dinnebier, G. Jackeli, and H. Takagi, [Nature](#) **554**, 341 (2018).

- [12] K. W. Plumb, J. P. Clancy, L. J. Sandilands, V. V. Shankar, Y. F. Hu, K. S. Burch, H.-Y. Kee, and Y.-J. Kim, [Phys. Rev. B **90**, 041112 \(2014\)](#).
- [13] L. J. Sandilands, Y. Tian, K. W. Plumb, Y.-J. Kim, and K. S. Burch, [Phys. Rev. Lett. **114**, 147201 \(2015\)](#).
- [14] J. A. Sears, M. Songvilay, K. W. Plumb, J. P. Clancy, Y. Qiu, Y. Zhao, D. Parshall, and Y.-J. Kim, [Phys. Rev. B **91**, 144420 \(2015\)](#).
- [15] M. Majumder, M. Schmidt, H. Rosner, A. A. Tsirlin, H. Yasuoka, and M. Baenitz, [Phys. Rev. B **91**, 180401 \(2015\)](#).
- [16] R. D. Johnson, S. C. Williams, A. A. Haghighirad, J. Singleton, V. Zapf, P. Manuel, I. I. Mazin, Y. Li, H. O. Jeschke, R. Valentí, and R. Coldea, [Phys. Rev. B **92**, 235119 \(2015\)](#).
- [17] A. Banerjee, C. Bridges, J.-Q. Yan, A. Aczel, L. Li, M. Stone, G. Granroth, M. Lumsden, Y. Yiu, J. Knolle, *et al.*, [Nat. Mater. **15**, 733 \(2016\)](#).
- [18] S.-H. Do, S.-Y. Park, J. Yoshitake, J. Nasu, Y. Motome, Y. S. Kwon, D. Adroja, D. Voneshen, K. Kim, T.-H. Jang, *et al.*, [Nature Physics **13**, 1079 \(2017\)](#).
- [19] J. Wagner, A. Sahasrabudhe, R. B. Versteeg, L. Wysocki, Z. Wang, V. Tsurkan, A. Loidl, D. I. Khomskii, H. Hedayat, and P. H. van Loosdrecht, [npj Quantum Materials **7**, 1 \(2022\)](#).
- [20] N. D. Patel and N. Trivedi, [Proc. Natl. Acad. Sci. U.S.A. **116**, 12199 \(2019\)](#).
- [21] M. Gohlke, R. Moessner, and F. Pollmann, [Phys. Rev. B **98**, 014418 \(2018\)](#).
- [22] Z. Zhu, I. Kimchi, D. N. Sheng, and L. Fu, [Phys. Rev. B **97**, 241110 \(2018\)](#).
- [23] H.-C. Jiang, C.-Y. Wang, B. Huang, and Y.-M. Lu, [arXiv **10.48550/ARXIV.1809.08247** \(2018\)](#).
- [24] C. Hickey and S. Trebst, [Nat. Commun. **10**, 1 \(2019\)](#).
- [25] D. A. S. Kaib, S. M. Winter, and R. Valentí, [Phys. Rev. B **100**, 144445 \(2019\)](#).
- [26] J. S. Gordon, A. Catuneanu, E. S. Sørensen, and H.-Y. Kee, [Nat. Commun. **10**, 1 \(2019\)](#).
- [27] W. Yang, A. Nocera, T. Tummuru, H.-Y. Kee, and I. Affleck, [Phys. Rev. Lett. **124**, 147205 \(2020\)](#).
- [28] R. Yadav, N. A. Bogdanov, V. M. Katukuri, S. Nishimoto, J. Van Den Brink, and L. Hozoi, [Sci. Rep. **6**, 1 \(2016\)](#).

- [29] Y.-F. Jiang, T. P. Devereaux, and H.-C. Jiang, [Phys. Rev. B **100**, 165123 \(2019\)](#).
- [30] H.-Y. Lee, R. Kaneko, L. E. Chern, T. Okubo, Y. Yamaji, N. Kawashima, and Y. B. Kim, [Nat. Commun. **11**, 1 \(2020\)](#).
- [31] J. G. Rau, E. K.-H. Lee, and H.-Y. Kee, [Annu. Rev. Condens. Matter Phys. **7**, 195 \(2016\)](#).
- [32] M. Hermanns, I. Kimchi, and J. Knolle, [Annu. Rev. Condens. Matter Phys. **9**, 17 \(2018\)](#).
- [33] H. Takagi, T. Takayama, G. Jackeli, G. Khaliullin, and S. E. Nagler, [Nat. Rev. Phys. **1**, 264 \(2019\)](#).
- [34] S. Trebst and C. Hickey, [Phys. Rep. **950**, 1 \(2022\)](#).
- [35] R. Schaffer, S. Bhattacharjee, and Y. B. Kim, [Phys. Rev. B **86**, 224417 \(2012\)](#).
- [36] C. C. Price and N. B. Perkins, [Phys. Rev. Lett. **109**, 187201 \(2012\)](#).
- [37] J. Oitmaa, [Phys. Rev. B **92**, 020405 \(2015\)](#).
- [38] L. Janssen and M. Vojta, [J. Phys. Condens. Matter **31**, 423002 \(2019\)](#).
- [39] M. Gohlke, G. Wachtel, Y. Yamaji, F. Pollmann, and Y. B. Kim, [Phys. Rev. B **97**, 075126 \(2018\)](#).
- [40] S.-S. Zhang, G. B. Halász, W. Zhu, and C. D. Batista, [Phys. Rev. B **104**, 014411 \(2021\)](#).
- [41] K. Feng, N. B. Perkins, and F. J. Burnell, [Phys. Rev. B **102**, 224402 \(2020\)](#).
- [42] S. Pradhan, M. Laad, A. Ray, T. Maitra, and A. Taraphder, [Solid State Commun. **332**, 114308 \(2021\)](#).
- [43] C. Berke, S. Trebst, and C. Hickey, [Phys. Rev. B **101**, 214442 \(2020\)](#).
- [44] S.-S. Zhang, G. B. Halász, and C. D. Batista, [Nat. Commun. **13**, 1 \(2022\)](#).
- [45] A. P. Joy and A. Rosch, [Phys. Rev. X **12**, 041004 \(2022\)](#).
- [46] C. Chen, P. Rao, and I. Sodemann, [Phys. Rev. Research **4**, 043003 \(2022\)](#).
- [47] L. Zou and Y.-C. He, [Phys. Rev. Research **2**, 013072 \(2020\)](#).
- [48] A. Nanda, K. Dhochak, and S. Bhattacharjee, [Phys. Rev. B **102**, 235124 \(2020\)](#).
- [49] Y. Kasahara, T. Ohnishi, Y. Mizukami, O. Tanaka, S. Ma, K. Sugii, N. Kurita, H. Tanaka, J. Nasu, Y. Motome, *et al.*, [Nature **559**, 227 \(2018\)](#).

- [50] P. Czajka, T. Gao, M. Hirschberger, P. Lampen-Kelley, A. Banerjee, J. Yan, D. G. Mandrus, S. E. Nagler, and N. P. Ong, *Nat. Phys.* **17**, 915 (2021).
- [51] J. A. N. Bruin, R. R. Claus, Y. Matsumoto, N. Kurita, H. Tanaka, and H. Takagi, *Nat. Phys.* **18**, 401 (2022).
- [52] A. Banerjee, P. Lampen-Kelley, J. Knolle, C. Balz, A. A. Aczel, B. Winn, Y. Liu, D. Pajerowski, J. Yan, C. A. Bridges, *et al.*, *npj Quantum Mater.* **3**, 1 (2018).
- [53] H. Li, T. T. Zhang, A. Said, G. Fabbris, D. G. Mazzone, J. Q. Yan, D. Mandrus, G. B. Halász, S. Okamoto, S. Murakami, M. P. M. Dean, H. N. Lee, and H. Miao, *Nature Commun.* **12**, 10.1038/s41467-021-23826-1 (2021).
- [54] L. Holleis, J. C. Prestigiacomo, Z. Fan, S. Nishimoto, M. Osofsky, G.-W. Chern, J. van den Brink, and B. Shivaram, *npj Quantum Mater.* **6**, 1 (2021).
- [55] C. Chamon, *Phys. Rev. Lett.* **94**, 040402 (2005).
- [56] A. Smith, J. Knolle, D. L. Kovrizhin, and R. Moessner, *Phys. Rev. Lett.* **118**, 266601 (2017).
- [57] A. Prem, J. Haah, and R. Nandkishore, *Phys. Rev. B* **95**, 155133 (2017).
- [58] O. Hart, S. Gopalakrishnan, and C. Castelnovo, *Phys. Rev. Lett.* **126**, 227202 (2021).
- [59] P. W. Anderson, *Phys. Rev. Lett.* **18**, 1049 (1967).
- [60] S. Sachdev, *Physics World* **12**, 33 (1999).
- [61] P. Karpov, R. Verdel, Y.-P. Huang, M. Schmitt, and M. Heyl, *Phys. Rev. Lett.* **126**, 130401 (2021).
- [62] J. Feldmeier, F. Pollmann, and M. Knap, *Phys. Rev. Lett.* **123**, 040601 (2019).
- [63] V. Khemani, M. Hermele, and R. Nandkishore, *Phys. Rev. B* **101**, 174204 (2020).
- [64] K. Lee, A. Pal, and H. J. Changlani, *Phys. Rev. B* **103**, 235133 (2021).
- [65] T. Grover and M. P. Fisher, *J. Stat. Mech. Theory Exp.* **2014**, P10010 (2014).
- [66] A. Catuneanu, E. S. Sørensen, and H.-Y. Kee, *Phys. Rev. B* **99**, 195112 (2019).
- [67] E. S. Sørensen, A. Catuneanu, J. S. Gordon, and H.-Y. Kee, *Phys. Rev. X* **11**, 011013 (2021).

-
- [68] G. Baskaran, S. Mandal, and R. Shankar, *Phys. Rev. Lett.* **98**, 247201 (2007).
- [69] A. Metavitsiadis and W. Brenig, *Phys. Rev. B* **96**, 041115 (2017).
- [70] X.-Y. Feng, G.-M. Zhang, and T. Xiang, *Phys. Rev. Lett.* **98**, 087204 (2007).
- [71] C. E. Agrapidis, J. van den Brink, and S. Nishimoto, *Phys. Rev. B* **99**, 224418 (2019).
- [72] M. Fishman, S. R. White, and E. M. Stoudenmire, arXiv [10.48550/ARXIV.2007.14822](https://arxiv.org/abs/10.48550/ARXIV.2007.14822) (2020).
- [73] P. Zanardi and N. Paunković, *Phys. Rev. E* **74**, 031123 (2006).
- [74] H.-Q. Zhou, R. Orús, and G. Vidal, *Phys. Rev. Lett.* **100**, 080601 (2008).
- [75] H.-Q. Zhou, J.-H. Zhao, and B. Li, *J. Phys. A Math. Theor.* **41**, 492002 (2008).
- [76] S. Yang, S.-J. Gu, C.-P. Sun, and H.-Q. Lin, *Phys. Rev. A* **78**, 012304 (2008).
- [77] V. Mukherjee, A. Dutta, and D. Sen, *Phys. Rev. B* **85**, 024301 (2012).
- [78] C. Castelnovo, C. Chamon, and D. Sherrington, *Phys. Rev. B* **81**, 184303 (2010).
- [79] A. Metavitsiadis and W. Brenig, *Phys. Rev. B* **103**, 195102 (2021).
- [80] G.-Y. Zhu and M. Heyl, *Phys. Rev. Research* **3**, L032069 (2021).
- [81] L. Rademaker, *SciPost Phys.* **7**, 071 (2019).
- [82] O. Hart, Y. Wan, and C. Castelnovo, *Nature Commun.* **12**, 1 (2021).
- [83] G. Baskaran and R. Shankar, *Mod. Phys. Lett. B* **2**, 1211 (1988).
- [84] I. Affleck, *Phys. Rev. Lett.* **57**, 1048 (1986).
- [85] G. Baskaran, *Phys. Rev. B* **68**, 212409 (2003).
- [86] N. Read and B. Chakraborty, *Phys. Rev. B* **40**, 7133 (1989).
- [87] V. Kalmeyer and R. B. Laughlin, *Phys. Rev. Lett.* **59**, 2095 (1987).
- [88] R. B. Laughlin and Z. Zou, *Phys. Rev. B* **41**, 664 (1990).
- [89] D.-H. Lee, *Phys. Rev. Lett.* **84**, 2694 (2000).
- [90] J. Knolle, D. L. Kovrizhin, J. T. Chalker, and R. Moessner, *Phys. Rev. Lett.* **112**, 207203 (2014).
- [91] M. Giordano and T. G. Kovács, *Universe* **7**, [10.3390/universe7060194](https://arxiv.org/abs/10.3390/universe7060194) (2021).

4

Fractional Wannier Orbitals and Tight-Binding Gauge Fields in Kitaev Honeycomb Superlattices with Flat Majorana Bands

Fractional excitations offer vast potential for both fundamental physics and quantum technologies. However, their dynamics under the influence of gauge fields pose a significant challenge to conventional models. Here, we present a systematic approach for constructing low-energy lattice models for fractional Wannier orbitals traversing via tight-binding gauge fields. The method transcends the geometric approach for eliminating high-energy states by systematically removing these states through virtual hopping, thereby deriving the gauge potential via a superexchange-like mechanism. We apply this method to investigate the evolution of low-energy Majorana dispersions across various crystalline phases of the π -flux in the Kitaev spin model on a honeycomb lattice. Our study reveals an intriguing phase transition between two non-trivial topological phases characterized by gapless flat-band (extensive) degeneracy. Additionally, to analytically model the interaction effects of fractional particles, we introduce

a gauge-invariant mean-field theory for Majorana flat bands, resulting in correlation-induced fractional Chern insulators. Our work opens doors for future exploration of $U(1)$, $SU(N)$ gauge-mediated tight-binding approach to other fractional or entangled Wannier excitations.¹

4.1 Introduction

The key to harnessing quantum materials for quantum technologies lies in engineering and controlling emergent excitations that obey unique statistics. [1–7] The sought-after excitations such as anyons, Majorana-, and para-fermions living on the enlarged (fractionalized/entangled) states embedded in a physical many-body Hilbert space of electrons or quantum spins. In the effective field theories for these emergent excitations, the influence of the remaining system degrees of freedom is incorporated through a geometric term.[8–15]. This couples the particle-like excitations with the emergent gauge fields to commence exotic statistics that enjoy constrained, protected, and slow dynamics of various characteristics.[16–19]

Within a lattice, how are the orbital states of fractional particles characterized when they undergo hopping under tight-binding gauge fields? Standard methods such as maximally localized Wannier orbitals (MLWOs),[20–22] the perturbation theory,[23–26, 26–29], renormalized Hamiltonian,[30], rotating-wave approximation, [31, 32], Hubbard-Stratonovich transformation,[33, 34] produce effective low-energy models for conventional quasiparticles hopping in a lattice potential. In contrast, entangled or fractional particles traverse a lattice under a lattice gauge potential. Symmetry arguments and dualities are often employed to postulate such lattice-gauge theory coupled with particle-like excitations [9, 35–38]. Wegner realized that the high-temperature disorder phase of the Ising model is dual to a \mathbb{Z}_2 lattice gauge theory.[39]. Kitaev introduced the first exactly solvable low-energy spin model exhibiting a spin-liquid ground state, which directly translates to a \mathbb{Z}_2 lattice gauge theory.[40–43] However, a systematic derivation of an effective \mathbb{Z}_2 gauge field-mediated TB model for the low-energy states for fractional particles that are embedded in a larger Hilbert space is missing in the literature.

This work presents a systematic derivation for a TB model describing Wannier Majorana orbitals traversing a lattice via a \mathbb{Z}_2 gauge potential. The method generalizes to any lattice $U(1)$ gauge field for anyons, incorporating an additional particle-hole symmetry constraint specifically tailored for Majorana fermions and \mathbb{Z}_2 gauge fields. Conventional approaches for quasiparticles utilize projection operators on derived Wannier orbitals to eliminate high-energy states and subsequently acquire gauge fields through the pullback operation on the manifold.

¹This chapter is a reproduction of the preprint on our work titled 'Fractional Wannier Orbitals and Tight-Binding Gauge Fields for Kitaev Honeycomb Superlattices with Flat Majorana Bands' with reference [arXiv:2407.12559](https://arxiv.org/abs/2407.12559).

We propose an alternative approach, introducing a variational potential within the effective Hamiltonian. This potential acts as a superexchange-like interaction, mediated by virtual hopping processes to the eliminated states. Through analysis, we determine the conditions under which this potential manifests as a gauge potential. Additionally, the method facilitates the imposition of a flux-preservation constraint, ensuring consistency between the derived low-energy lattice theory and the parent full model.

The Kitaev spin model on the honeycomb lattice [40] is an exactly solvable model exhibiting uniform \mathbb{Z}_2 fluxes in the ground state and \mathbb{Z}_2 vortices and Majorana fermions as excitations. With an applied magnetic field, the Majorana excitations - confined to \mathbb{Z}_2 vortices - can be proliferated, leading to flux crystallization and an exotic quantum glass phase [19], before turning into other possible $U(1)$ phases.[44–50]. Alternatively, manipulating the \mathbb{Z}_2 flux distributions from uniform to staggered in the parameter regime of the flux crystalline phase can provide a versatile platform for controlling the dispersion relation of the Majorana fermions.[51–56] The present work focuses on exploring various superlattices of \mathbb{Z}_2 flux pairs and the corresponding evolution of the Majorana dispersions, with a particular emphasis on cases where flat bands emerge. We then construct an effective lattice \mathbb{Z}_2 gauge theory for these flat bands to investigate Majorana Wannier orbitals. The gauge potential is introduced in the Hamiltonian via a superexchange-like interaction with the eliminated states that act as TB parameters between Majorana Wannier orbitals. The effective model facilitates the determination of the Chern number and the criterion for vortexibility through quantum metric. We find an interesting case where the flat band with extensive degeneracy underlies a novel critical point between two topologically non-trivial phases. Finally, we introduce a mean-field theory for the gauge-invariant Majorana density-wave state in the flat bands to obtain an analytically tractable description of a fractional Chern insulator state.

4.2 The Kitaev model with staggered fluxes

The Kitaev model is a particular lattice model of the spin-1/2 operator \mathbf{S}_i sitting at the i^{th} site on a honeycomb lattice and interacting with the nearest neighboring sites with bond-dependent exchange coupling J . In the Majorana fermion c_i representations of the spin-1/2 operators, the model reduces to a model of nearest-neighbor Majorana hoppings mediated by a bond-dependent \mathbb{Z}_2 gauge field $u_{ij} = \pm 1$. For a small magnetic field, h applied along the [111] - direction, the lowest-order perturbation term produces a next nearest-neighbor hopping with the coupling constant $K = h^3/J^2$ (from the term $\sum_{\langle\langle ik \rangle\rangle} S_i^y S_j^z S_k^x$).[40, 57–63] The model is

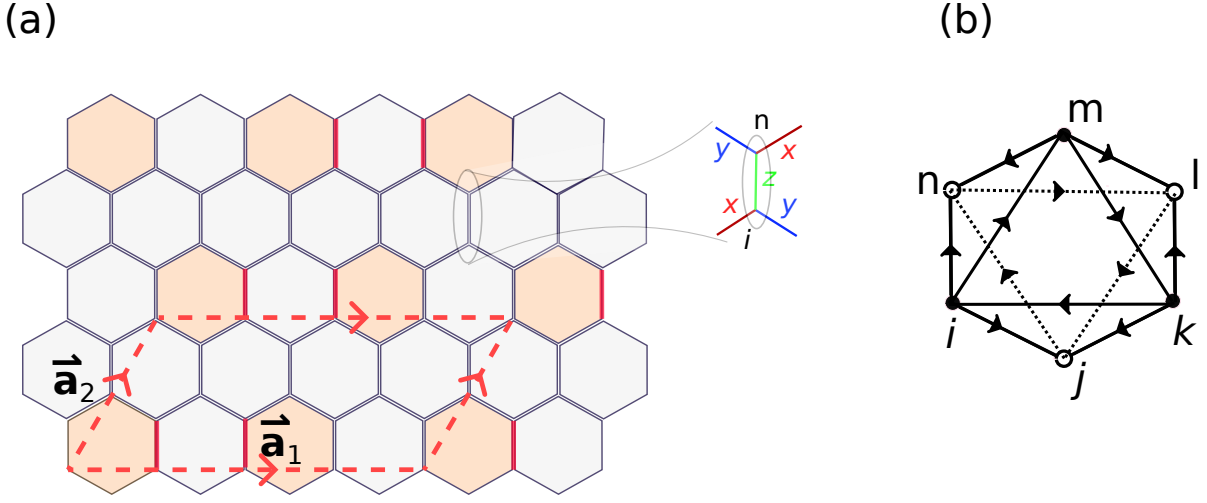


Fig. 4.1 \mathbb{Z}_2 flux crystal structure and the supercell formation in the Kitaev model. (a) We show a 2×2 supercell of honeycomb lattice containing a π -flux ($W_p = -1$) pair (orange plaquette) separated by two vertical bonds having $u_{ij} = -1$, while the rest of the plaquettes (white) have zero flux and bond have $u_{ij} = +1$. $\mathbf{a}_1 = (4a\sqrt{3}, 0)$ and $\mathbf{a}_2 = a(\sqrt{3}, 3)$, where a is the nearest neighbor distance in the honeycomb lattice. *Inset*: Three different exchange interactions J along the three nearest neighbors at each site are highlighted in different colors. (b) The chosen gauge convention for the u operators in the Kitaev model is shown as $u_{ij} = +1$ if an arrow points from site i to j , or -1 otherwise. The same is shown for the next nearest neighbors by dashed lines where two u operators for the intervening nearest neighbor bonds are multiplied. For example, the bond from the site, i to k term has $u_{ij}u_{jk}$ is -1 . This convention is for the uniform flux sector, where each plaquette has zero flux.

expressed as

$$H = iJ \sum_{\langle ij \rangle} u_{ij} c_i c_j + iK \sum_{\langle\langle ik \rangle\rangle} u_{ij} u_{jk} c_i c_k. \quad (4.1)$$

The candidacy of the gauge field u_{ij} demands it to be an antisymmetric tensor: $u_{ij} = -u_{ji}$, living on the bond between the i and j sites. And, the gauge field for the next-nearest neighbor u_{ik} is a path-ordered product of two subsequent nearest-neighbor gauge fields $u_{ik} = u_{ij}u_{jk}$, where j is the intermediate site between i and k . This is reflected in the second term in Eq. (4.1). A gauge choice of u_{ij} is shown in Fig. 4.1(b). A \mathbb{Z}_2 operator, defined on six consecutive links forming a loop on a plaquette p , is defined as $W_p = u_{ij}u_{jk}u_{kl}u_{lm}u_{mn}u_{ni}$. W_p gives the \mathbb{Z}_2 flux monopole charge with $W_p = \pm 1$ for zero (π) flux. Another flux operator of importance is defined at the i^{th} site (called a vertex) as $X_i = u_{ij}u_{ik}u_{il}$, which acts as a \mathbb{Z}_2 electric charge, which introduces quartic interaction between Majoranas (see Sec. 4.4.4).

The Hamiltonian's gauge redundancy manifests in gauge-dependent Majorana dispersions. However, the essential properties of these dispersions, such as the presence of gapless point

(point degeneracy), flat band (extensive degeneracy), or topological features (band inversions), are gauge-invariant. The specific location of these gapless or band inversion points depends on the chosen gauge. In uniform flux configuration with all $W_p = +1$ and a gauge fixing of all $u = +1$ gives a graphene-like gapless Dirac node for $K = 0$. $K \neq 0$ breaks the time-reversal symmetry, opening a band gap at the Dirac cone to topological Chern bands for Majorana fermions. This topological phase has Majorana zero modes (MZMs) at the boundary. Bound states of MZM with π -flux excitations can be created in bulk by thermal energy or vacancies. MZMs are topologically protected Ising anyons, which can be detected by electrical probes [64] and by scanning tunneling microscopic techniques [65].

The focus of this work is to study different supercell formations of staggered W_p fluxes and their impact on low-energy Majorana dispersions. [52–56]. Analogous to the $U(1)$ magnetic monopole, the creation of a \mathbb{Z}_2 monopole W_p is topologically protected. A \mathbb{Z}_2 flux pair is defined by two π fluxes separated by d number of plaquettes with $u = -1$ in the intermediate links, as shown in Fig 4.1(a). There is gauge redundancy in defining the same supercell, and we fix the gauge for all considered supercells in the same way, as shown in the figure in Fig. 4.1(b). This produces a $d \times d$ supercell of honeycomb lattice containing $2N = 4d^2$ number of Majorana sublattices. A \mathbb{Z}_2 flux pair (ZFP) for $d > 1$ naturally breaks the C_6 symmetry of the honeycomb lattice; however, the alignments of the \mathbb{Z}_2 flux pair along, say, \mathbf{a}_1 or \mathbf{a}_2 primitive lattice vectors, are gauge equivalent.

We chose a Majorana spinor $C_I = (c_1 c_2 \dots c_{2N})^T$ at the I^{th} supercell site. Then, the matrix-valued Hamiltonian in this spinor can be written from Eq. (4.1) as

$$H = i \sum_I C_I^T \mathcal{T}_{II} C_I + i \sum_{\langle IJ \rangle} C_I^T \mathcal{T}_{IJ} C_J. \quad (4.2)$$

Here, the \mathcal{T}_{IJ} is an (anti-symmetric) rank-2 tensor, with each element being a $2N \times 2N$ matrix. Their explicit forms are given in the Appendix D.1. The basis vectors of the supercell are $\mathbf{a}_1 = 2da(\sqrt{3}, 0)$, $\mathbf{a}_2 = \frac{da}{2}(\sqrt{3}, 3)$, where a is the nearest neighbor distance of the honeycomb primitive unit cell. The corresponding reciprocal vectors are $\mathbf{G}_1 = \frac{2\pi}{a} \left(\frac{\sqrt{3}}{6d}, \frac{-1}{6d} \right)$, $\mathbf{G}_2 = \frac{2\pi}{a} \left(0, \frac{2}{3d} \right)$. \mathbf{a}_2 vector of these supercells is half compared to the C_6 symmetric honeycomb lattice; see Fig. 4.1(a). Hence, the first Brillouin zone has two graphene-like BZs along the \mathbf{G}_2 vector.

The (virtual) Majorana spinor state in the momentum space is $C(\mathbf{k}) = \frac{1}{\sqrt{L}} \sum_I e^{-i\mathbf{k} \cdot \mathbf{R}_I} C_I$, where $\mathbf{R}_{I \in \mathbb{Z}} = \sum_i I_i \mathbf{a}_i$ are the lattice sites of the supercell, and correspondingly, \mathbf{k} is defined in the reciprocal space of $\mathbf{G}_{1,2}$. The corresponding Hamiltonian in the momentum space is obtained from Eq. 4.2: $H = \frac{1}{\sqrt{N}} \sum_{\mathbf{k} \in \text{BZ}_+} C^\dagger(\mathbf{k}) \mathcal{H}(\mathbf{k}) C(\mathbf{k})$, where the matrix-elements of \mathcal{H} are given in Appendix D.1. The physical Majorana fermions $c_i = c_i^\dagger$ turn into particle-hole symmetric virtual Majorana fermions in the \mathbf{k} -space $c^\dagger(\mathbf{k}) = c(-\mathbf{k})$, leading to $\mathbf{k} \geq \mathbf{0}$ being restricted to the

positive quadrant in the first Brillouin zone (BZ_+). The (anti-unitary) particle-hole symmetry C relates the Hamiltonian between different BZ quadrants as $C\mathcal{H}(\mathbf{k})C^{-1} = -\mathcal{H}^T(\mathbf{k})$. The final task is to diagonalize the $2N \times 2N$ particle-hole symmetric matrix $\mathcal{H}(\mathbf{k})$. We denote the eigenvector states as $|n, \pm, \mathbf{k}\rangle$ corresponding to the eigenvalues of $\pm E_n(\mathbf{k})$, where $n = 1, 2, \dots, N$. In this eigenbasis, the matter fields are the complex fermions (particles and holes), defined by the creation operators $|n, \pm, \mathbf{k}\rangle = \gamma_{n, \pm}^\dagger(\mathbf{k})|0\rangle$, and related to the virtual Majoranas by a unitary transformation (Γ) as $\gamma_{n, \pm}^\dagger(\mathbf{k}) = \sum_\alpha \Gamma_{n, \pm, \alpha}(\mathbf{k})c_\alpha(\mathbf{k})$, for $\Gamma_{n, \pm, \alpha}(\mathbf{k}) \in \mathbb{C}$. The corresponding results are presented in Sec. 4.4 for several representative $d \times d$ supercell configurations.

4.3 Tight-binding Gauge-field model for Majorana orbitals

Our task now is to obtain an effective TB model for a few low-energy eigenstates $|n, \pm, \mathbf{k}\rangle$. Since $|n, \pm, \mathbf{k}\rangle$ states are for complex fermions, we may treat the corresponding Wannier orbitals to be of the usual complex fermionic nature. However, owing to the underlying physics of Majorana Wannier orbitals hopping under lattice \mathbb{Z}_2 gauge field in real space, the TB model construction becomes non-trivial. In essence, we need to construct ‘Wannier’ fields for both Majorana matter fields and the \mathbb{Z}_2 gauge fields while keeping all the symmetries and flux-preservation constraints intact.

To avoid overloading with many new symbols, for the TB model, we adopt the same set of symbols, such as \mathcal{H} , \mathcal{T} , c , C and others used in the above Sec. 4.2 with the same meanings. Should confusion arise, we explicitly mention the corresponding definition.

We are interested in modeling the $P < N$ number of low-energy Majorana pair states $|p, \pm, \mathbf{k}\rangle \equiv |p, \mathbf{k}\rangle$, where we combine the indices $p \equiv (p, \pm)$ for $p = 1, \dots, P$ with eigenvalues $\pm E_p(\mathbf{k})$. These states are obtained from the full Hilbert space $|\mathbf{n}\rangle \equiv (n, \pm), \mathbf{k}$ by the projector $\mathcal{P} = \mathcal{P}_+ + \mathcal{P}_- = \sum_{p < N} (|p, +\rangle\langle p, +| + |p, -\rangle\langle p, -|)$, where \mathbf{k} dependence in each term is kept implicit for simplicity in notation. $\mathcal{Q} = I - \mathcal{P}$ is the projection outside the low-energy states of our interest. $|p, \mathbf{k}\rangle$ states are incomplete, so its Fourier transformation to the Wannier orbitals states would not be useful.

Our aim is to obtain complete, orthogonal states denoted by $|\tilde{p}, \mathbf{k}\rangle$ with corresponding eigenenergies $\tilde{E}_p(\mathbf{k}) \approx E_p(\mathbf{k})$. One typically defines a complex quantum geometric tensor from the \mathcal{Q} projector and affix it with the $|p, \mathbf{k}\rangle$ states to obtain corresponding complete, orthogonal states (with a quantum metric) $|\tilde{p}, \mathbf{k}\rangle$. [20, 66–71] Here, we devise an alternative bottom-up approach to construct a (variational) effective Hamiltonian H_{eff} with eigenstates $|\tilde{p}, \mathbf{k}\rangle$, and eigenenergies $\pm \tilde{E}_p(\mathbf{k})$. We introduce a superexchange interaction that produces tunneling between $|p, \mathbf{k}\rangle$ and $|p', \mathbf{k}\rangle$ states with intermediate hopping to the \mathcal{Q} states,

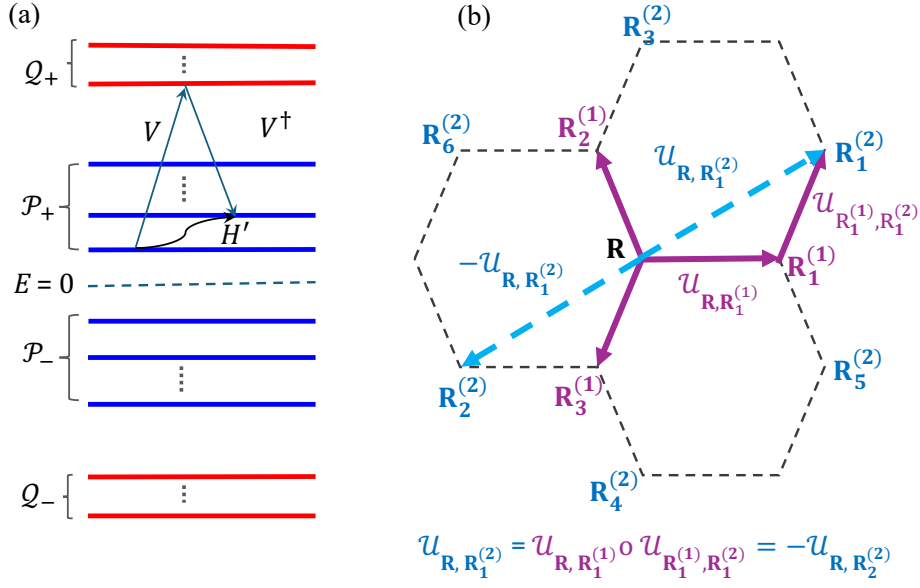


Fig. 4.2 (a) Schematic plots of the superexchange mechanism of gauge potential H' in the low-energy spectrum (blue lines) due to virtual hopping to the eliminated high-energy states (red lines). Note that the virtual hopping potential V is a fitting parameter in the TB model. (b) The gauge fields in the effective theory in a honeycomb lattice. The sets of first and second nearest neighbor sites are denoted by $\mathbf{R}^{(1)} = \{\mathbf{R}_{1-3}^{(1)}\}$ and $\mathbf{R}^{(2)} = \{\mathbf{R}_{1-6}^{(2)}\}$. The gauge field for the second nearest neighbor across diagonally opposite directions must be opposite in sign to commence odd-parity hopping (superconducting term in Eq. (D.6), i.e., $u_{\mathbf{R}, \mathbf{R}_2^{(2)}} = -u_{\mathbf{R}, \mathbf{R}_1^{(2)}}$).

see Fig. 4.2. We call such a superexchange potential a ‘gauge’ potential, through which we can define the \mathbb{Z}_2 gauge fields and topology in a lattice.

In what follows, we seek an effective Majorana Hamiltonian of the form $H_{\text{eff}} = \mathcal{P}(H + H')\mathcal{P}$, $\forall \mathbf{k}$, where H is the full supercell Hamiltonian, and H' is an unknown superexchange/‘gauge’ potential to be evaluated self-consistently. H' gives off-diagonal terms in H_{eff} arising from the transitions between different Majorana states $|p = (p, \pm), \mathbf{k}\rangle$ via intermediate hopping to the Q states. In what follows, $|p, \mathbf{k}\rangle$ acts as Majorana orbital states for H_{eff} , except they are incomplete. We denote the corresponding complete Majorana orbital states by $|\alpha = (\alpha, \pm), \mathbf{k}\rangle$ for $\alpha = 1, \dots, P$. In the Majorana basis of $|\alpha, +, \mathbf{k}\rangle \oplus |\alpha, -, \mathbf{k}\rangle$, we denote the matrix elements of $H_{\text{eff}}(\mathbf{k})$ as

$$\mathcal{H}_{\text{eff}}(\mathbf{k}) = \begin{pmatrix} \Delta_R & \Delta_I + ih_S \\ \text{H.c.} & -\Delta_R \end{pmatrix}, \quad (4.3)$$

where \mathbf{k} dependence on R.H.S. is kept implicit. $h_S(\mathbf{k}) = h(\mathbf{k}) + h^T(-\mathbf{k})$, and $\Delta(\mathbf{k}) = \Delta_R(\mathbf{k}) + i\Delta_I(\mathbf{k})$. The diagonal and off-diagonal $P \times P$ matrices of \mathcal{H}_{eff} are relabelled in terms of h and Δ ,

so that the corresponding Hamiltonian in the complex fermion basis turns into a Bogolyubov-Gennes Hamiltonian with h and Δ being their dispersion and pairing terms.[40, 72] The block-off-diagonal term $(\Delta_I + ih_S)_{\alpha,\alpha'}$ couples different Majoranas $|\alpha, \pm, \mathbf{k}\rangle$ and $|\alpha', \mp, \mathbf{k}\rangle$, while the block-diagonal terms $\pm(\Delta_R)_{\alpha,\alpha'}$ give the dispersion for the same type of Majoranas $|\alpha, \pm, \mathbf{k}\rangle$ and $|\alpha', \pm, \mathbf{k}\rangle$. \mathcal{H}_{eff} follows all the symmetries of the original Hamiltonian; in addition, the fermion-odd-parity in the pairing term Δ is also imposed. Explicit expressions of h and Δ in terms of H and H' are derived in Appendix D.2.

Our next task is to Fourier transform H_{eff} to real space by converting h and Δ into \mathbb{Z}_2 gauge-field induced hoppings between Wannier Majorana orbitals in a lattice. We consider a lattice of \mathcal{N} unit cells at positions \mathbf{R} . The Fourier basis states are the Bloch phases at the \mathbf{R}^{th} cell as $z_{\mathbf{R}}(\mathbf{k}) = \langle \mathbf{R} | \mathbf{k} \rangle = e^{i\mathbf{k} \cdot \mathbf{R}}$. Then, we define the Majorana orbital states in real space as

$$|\alpha, \mathbf{R}\rangle = \frac{1}{\sqrt{\mathcal{N}}} \sum_{\mathbf{k}>0} \bar{z}_{\mathbf{R}}(\mathbf{k}) |\alpha, \mathbf{k}\rangle. \quad (4.4)$$

The physical Majorana operators are defined in real space as $|\alpha, \mathbf{R}\rangle = c_{\alpha, \mathbf{R}} |0\rangle$ where $c_{\alpha, \mathbf{R}} = c_{\alpha, \mathbf{R}}^\dagger$. The corresponding orthogonal Majorana wavefunctions at position $\mathbf{r} \in \mathbf{R}$ unit cell are called the Bloch states $\psi_{\alpha, \mathbf{k}}(\mathbf{r}) = e^{i\mathbf{k} \cdot \mathbf{r}} u_{\alpha, \mathbf{k}}(\mathbf{r}) = \langle \mathbf{r} | \alpha, \mathbf{k} \rangle$, and Wannier states $w_{\alpha, \mathbf{R}}(\mathbf{r}) = \langle \mathbf{r} | \alpha, \mathbf{R} \rangle$. In the TB orbital case, the real space wavefunctions are fully localized to $w_{\alpha, \mathbf{R}}(\mathbf{r}) \sim \delta(\mathbf{r} - \mathbf{R})$. In the Wannier orbital model $w_{\alpha, \mathbf{R}}$ is (exponentially) maximally localized at $\langle \mathbf{r} \rangle_\alpha = \int_{\mathbf{R}} d\mathbf{r} \mathbf{r} |w_{\alpha, \mathbf{R}}(\mathbf{r})|^2$, with its spread $\Delta \mathbf{r}_\alpha = \langle \mathbf{r}^2 \rangle_\alpha - \langle \mathbf{r} \rangle_\alpha^2$ also contained within the unit cell (see Appendix D.3). The two particle-hole Majorana pairs may have different Wannier centers $\langle \mathbf{r} \rangle_{\alpha,+} \neq \langle \mathbf{r} \rangle_{\alpha,-}$, generally connected by a string \mathbb{Z}_2 vortex. However, their linear combination particle-hole complex fermion wavefunctions must be at the same position such that the $U(1)$ charge is conserved in each unit cell.

It is convenient to represent the \mathbf{R} positions in terms of sets of 1st, 2nd, 3rd, and higher nearest neighbors rather than primitive lattice vectors. For the n^{th} nearest neighbor with d_n number of sites, we define a d_n -dimensional vector as $\mathbf{Z}_n := (z_1 \dots z_{d_n})^T, \forall \mathbf{k}$. We split the \mathcal{N} -dimensional vector of the Bloch phases as $\mathbf{Z}(\mathbf{k}) = \mathbf{Z}_1(\mathbf{k}) \oplus \mathbf{Z}_2(\mathbf{k}) \oplus \dots$ ²³

We now expand the dispersion relations in the Bloch basis $\mathbf{Z}(\mathbf{k})$ to obtain the TB hopping tensor as $\mathcal{T} = \mathbf{Z}(\mathbf{k}) \mathcal{H}_{\text{eff}}(\mathbf{k}) \mathbf{Z}^\dagger(\mathbf{k})$. \mathcal{T} is a rank-2 tensor with component $\mathcal{T}_{\mathbf{R}, \mathbf{R}'}$ corresponding to

²We make an approximation that the single-particle dispersion, many-body interaction, and superconducting order parameters are short-ranged, restricting to a few nearest neighbors only. (This truncation of the Fourier series to a polynomial of few sites gives a finite width of the single-particle states in both position and momentum space, and the number of nearest neighbors \mathcal{N} to be considered is determined within a numerical procedure by fitting to the band structure at all \mathbf{k} -points. This yields the so-called compact localized orbitals for the flat band in the Wannierization procedure).

³Note that in our procedure, it is easy to implement the lattice (point-/space-) group symmetry by doing the invariant rotation on the Bloch phase spinor $\mathbf{Z}_n(\mathbf{k})$.

Majorana hoppings between $\mathbf{R}, \mathbf{R}' \in \mathcal{N}$ sites. (Here, the symbol \mathcal{T} is redefined for the Wannier states and not to be confused with those in the supercell in Eq. (4.2).) Each component $\mathcal{T}_{\mathbf{R}, \mathbf{R}'}$ is a $2P \times 2P$ matrix in the $2P$ -dimensional Majorana basis present at the \mathbf{R}, \mathbf{R}' sites. We split the Hamiltonian into hoppings between different neighboring sites as

$$\mathcal{H}_{\text{eff}}(\mathbf{k}) = \sum_{n, n'} \mathbf{Z}_n^\dagger(\mathbf{k}) \mathcal{T}_{nn'} \mathbf{Z}_{n'}(\mathbf{k}) + \text{h.c.} \quad (4.5)$$

$\mathcal{T}_{nn'}$ gives a set of Majorana hopping tensors between the n and n' neighbors: $\mathcal{T}_{n, n'} = \{\mathcal{T}_{\mathbf{R}, \mathbf{R}'} | \mathbf{R} \in d_n, \mathbf{R}' \in d_{n'}\}$. Due to the translational invariance, only the difference between n and n' is relevant.

The intra-site hopping gives the onsite energy $\mathcal{T}_{nn} = i\mathcal{K}_0$ between $2P$ -Majoranas with the particle-hole symmetric constraint $\text{Tr}(\mathcal{T}_{nn}) = 0$.

Now, we consider the first nearest neighbor term $\mathcal{T}_{\mathbf{R}, \mathbf{R}'} \in \mathcal{T}_{n, n+1}$, where $\mathbf{R}' - \mathbf{R} \in d_1$ and $\mathbf{R} \neq \mathbf{R}'$. Using Taylor's expansion (assuming analyticity), we obtain the hopping tensor as

$$\mathcal{T}_{\mathbf{R}, \mathbf{R}'} = i\mathcal{K}_1^{-1} \left. \frac{\partial^2 \mathcal{H}_{\text{eff}}}{\partial \bar{z}_{\mathbf{R}} \partial z_{\mathbf{R}'}} \right|_{z_{\mathbf{R}} = z_{\mathbf{R}'} = 0}. \quad (4.6)$$

\mathcal{K}_1 is, in general, orbital dependent ($2P \times 2P$ non-singular matrices) as well as bond (i.e., \mathbf{R}, \mathbf{R}') dependent. (This expansion holds when \mathcal{H}_{eff} are polynomials in terms of $z_{\mathbf{R}}(\mathbf{k})$, which holds for most band structures, except for non-compact flat bands [73, 74].) \mathcal{K}_1 absorbs the energy dimension such that $\mathcal{T}_{\mathbf{R}, \mathbf{R}'}$ becomes dimensionless, which is now to be defined in terms of gauge fields. The crux of the gauge theory is that $\mathcal{T}_{\mathbf{R}, \mathbf{R}'} \neq \mathcal{T}_{\mathbf{R}', \mathbf{R}}$ in general. We separate the symmetric and anti-symmetric parts as

$$\mathcal{G}_{\mathbf{R}, \mathbf{R}'} = \frac{1}{2}(\mathcal{T}_{\mathbf{R}, \mathbf{R}'} + \mathcal{T}_{\mathbf{R}', \mathbf{R}}), \quad \text{and} \quad \mathcal{U}_{\mathbf{R}, \mathbf{R}'} = -\frac{i}{2}(\mathcal{T}_{\mathbf{R}, \mathbf{R}'} - \mathcal{T}_{\mathbf{R}', \mathbf{R}}). \quad (4.7)$$

Roughly speaking, \mathcal{G} and \mathcal{U} produce the amplitude and phase variation of the hopping term in the effective Hamiltonian between unit cells. In the momentum space, these are precisely what the Fubini-Study metric ($\mathcal{G}_{\mu\nu}$) and the curvature ($\mathcal{U}_{\mu\nu}$) terms constitute the symmetric and anti-symmetric components of the quantum geometric tensor.[67, 68, 75, 76] Their expressions in terms of the projectors $\mathcal{P}(\mathbf{k})$ are as follows

$$\mathcal{G}_{\mu\nu}(\mathbf{k}) = \frac{1}{2} \mathcal{P}(\mathbf{k}) \{ \partial_\mu \mathcal{P}(\mathbf{k}), \partial_\nu \mathcal{P}(\mathbf{k}) \}, \quad (4.8)$$

$$\mathcal{U}_{\mu\nu}(\mathbf{k}) = -\frac{i}{2} \mathcal{P}(\mathbf{k}) [\partial_\mu \mathcal{P}(\mathbf{k}), \partial_\nu \mathcal{P}(\mathbf{k})], \quad (4.9)$$

where $\partial_\mu = \frac{\partial}{\partial k_\mu}$ with $\mu = 1, 2$ for \mathbf{k}_μ spanned along the reciprocal lattice vector \mathbf{G}_μ . $\{\}$ and $[\]$ are the anti-commutator and commutator. It is now obvious that \mathcal{U} acts as parallel transport or Wilson line, which is \mathbb{Z}_2 -valued in this particular case. In their present forms, \mathcal{G} and \mathcal{U} are not gauge invariant in both real and momentum space formalism. Then, matter fields are attached at the two ends to commence gauge invariance. Otherwise, we take a trace over the matrix components and their product in a loop/plaquette in real/momentum space, giving topological invariants such as flux (W), Chern number (C) and similar quantum metric invariants as defined in Sec. 4.4.3

The diagonal term of \mathcal{G} tensor is zero as the $\mathbf{R} = \mathbf{R}'$ terms are separated into the onsite energy matrix \mathcal{K}_0 . The off-diagonal components $\mathcal{G}_{\mathbf{R},\mathbf{R}'}$ give the symmetric hopping matrix element between the orbitals localized at \mathbf{R} and \mathbf{R}' sites. Such symmetric hoppings are mediated by periodic lattice potential (e.g., potential due to nucleus in solid state systems) and depend on the symmetries of the two orbitals (e.g., it's present if the two orbitals have the same parity or absent if the parity of the two orbitals is opposite such as for the s and p orbitals). In our particular example below, we will seek a fully gauge-field mediated hopping between the two sites and set $\mathcal{G} = 0$ in the effective theory.

We identify $\mathcal{U}_{\mathbf{R},\mathbf{R}'}$ as an anti-symmetric tensor that mediates tunneling between the Majoranas at the \mathbf{R} and \mathbf{R}' sites. For the gauge invariance of the theory for Majorana, the gauge fields must be \mathbb{Z}_2 , which puts the constraints that $\mathcal{U}_{\mathbf{R},\mathbf{R}'}^2 = \mathbb{I}$. So we interpret $\mathcal{U}_{\mathbf{R},\mathbf{R}'}$ as the non-Abelian ($2P$ -dimensional matrix-valued) \mathbb{Z}_2 Wilson line operator, which can be written as (path-ordered) exponentials of a (non-Abelian) gauge field \mathcal{A} .

Next, we consider the second nearest neighbor term $\mathcal{T}_{\mathbf{R},\mathbf{R}''} \in \mathcal{T}_{n,n+2}$, where $\mathbf{R}'' - \mathbf{R} \in d_2$ and $\mathbf{R} \neq \mathbf{R}''$. Proceeding similarly, we define we define the \mathbb{Z}_2 gauge field as the second nearest neighbor as $\mathcal{U}_{\mathbf{R},\mathbf{R}''}^{(2)}$. All gauge fields \mathcal{U} are localized at the link/bond between the two sites. So we can smoothly deform the path to pass through a site \mathbf{R}' corresponding to the 1st nearest neighbor to both \mathbf{R} and \mathbf{R}'' sites, as shown in Fig. 4.2. In other words, we can write $\mathcal{U}_{\mathbf{R},\mathbf{R}''} = \mathcal{U}_{\mathbf{R},\mathbf{R}'} \circ \mathcal{U}_{\mathbf{R}',\mathbf{R}''}$, where the composition operation \circ reflects a matrix product for the tensor components. Therefore, for the n^{th} -nearest neighbor gauge field, we have

$$\mathcal{U}_{\mathbf{R},\mathbf{R}^{(n)}} = \prod_{\mathbf{R}^{(m)} \in d_{n-1}} \mathcal{U}_{\mathbf{R},\mathbf{R}^{(m)}} \circ \mathcal{U}_{\mathbf{R}^{(m)},\mathbf{R}^{(n)}}, \quad (4.10)$$

where $\mathbf{R}^{(m)}$ runs over the $n - 1$ intermediate sites that minimize the distance between the \mathbf{R} and $\mathbf{R}^{(n)}$ sites. Substituting these considerations in

$$\begin{aligned} \mathcal{H}_{\text{eff}}(\mathbf{k}) = & i\mathcal{K}_0 + i\mathcal{K}_1 \sum_{\{\mathbf{R}, \mathbf{R}^{(1)}\} \in d_1} \mathcal{U}_{\mathbf{R}, \mathbf{R}^{(1)}} \bar{z}_{\mathbf{R}}(\mathbf{k}) z_{\mathbf{R}'}(\mathbf{k}) \\ & + i\mathcal{K}_2 \sum_{\{\mathbf{R}, \mathbf{R}^{(2)}\} \in d_2} \mathcal{U}_{\mathbf{R}, \mathbf{R}^{(2)}} \bar{z}_{\mathbf{R}}(\mathbf{k}) z_{\mathbf{R}^{(2)}}(\mathbf{k}) + \dots \end{aligned} \quad (4.11)$$

The above Hamiltonian can be expressed in terms of physical Majorana orbitals $c_{\alpha, \mathbf{R}}$ in real space up to any number of nearest neighbor hoppings as

$$H_{\text{eff}} = i \sum_{n=0}^{\mathcal{N}} \mathcal{K}_n \sum_{\{\mathbf{R}, \mathbf{R}^{(n)}\} \in d_n} \sum_{\alpha, \alpha'} (\mathcal{U}_{\mathbf{R}, \mathbf{R}^{(n)}})_{\alpha, \alpha'} c_{\alpha, \mathbf{R}} c_{\alpha', \mathbf{R}^{(n)}}. \quad (4.12)$$

Summation over n corresponds to a different nearest neighbors. The gauge fields $\mathcal{U}_{\mathbf{R}, \mathbf{R}^{(n)}}$ sit on the link between the $\mathbf{R}, \mathbf{R}^{(n)}$ sites, and hence, there is no gauge field for the $n = 0$ term, while $n = 1$ term has one gauge field, $n = 2$ has two gauge fields, and so on. Here, we have assumed the coupling constants \mathcal{K}_n to be independent of the orbital and bond-independent and only depending on the n^{th} nearest neighbor distance. This is a reasonable assumption as at the n^{th} nearest neighbor site, only one type of orbital is placed.

4.3.1 Gauge fixing and topological invariants

An important property of the gauge theory is the gauge constraint, which restricts gauge redundancy to the physical states. Although the gauge operators $\mathcal{U}_{\mathbf{R}, \mathbf{R}^{(n)}}$ are gauge-dependent, the flux is a gauge-invariant physical operator. Therefore, the total flux in the supercell must be preserved in both the effective model and the supercell model.

The total flux in a supercell is defined as $W_S = \prod_{p \in S} W_p$, where S is the supercell index containing S number of original unit cells. The W_S , written in terms of the effective \mathbb{Z}_2 gauge field, is

$$W_S = \text{Tr} \left(\prod_{\{\mathbf{R}, \mathbf{R}^{(n)}\} \in S} \mathcal{U}_{\mathbf{R}, \mathbf{R}^{(n)}} \right). \quad (4.13)$$

In the effective theory, we can define a similar invariant for the symmetric tensor \mathcal{G} as $G_S = \text{Tr} \left(\prod_{\{\mathbf{R}, \mathbf{R}^{(n)}\} \in S} \mathcal{G}_{\mathbf{R}, \mathbf{R}^{(n)}} \right)$.

Their counterparts in the momentum space are called the quantum metric invariant and the Chern number as defined to be [67, 68, 75, 76]:

$$G = \frac{1}{(2\pi)^2} \int_{\text{BZ}} \sqrt{\det(\eta)} \eta_{\mu\nu} dk_\mu dk_\nu \text{Tr} \mathcal{G}_{\mu\nu}(\mathbf{k}), \quad (4.14)$$

$$C = \frac{1}{2\pi} \int_{\text{BZ}} dk_1 dk_2 \text{Tr} \mathcal{U}_{12}(\mathbf{k}), \quad (4.15)$$

where $\eta_{\mu\nu} = \hat{\mathbf{G}}_\mu \cdot \hat{\mathbf{G}}_\nu$ is a symmetric tensor that measures the curvature of the torus geometry and depends on the lattice under consideration. W_S and G_S can describe both local and global topological properties in real space, depending on the size of the 2-loop S . In contrast, C and G in the momentum space only capture the global topology on the torus. Do they correspond to the same topological invariant? Indeed, this is the case. Because the flux crystal in the original lattice is taken into account in the formation of the supercell, the total flux is uniform among all the supercells. This is reflected in the effective theory, as well, in that each band corresponds to uniform flux values $W_S = \pm 1$, $\forall S$, corresponding to Chern numbers $C = \pm 1$ for the two respective bands.

Both $\mathcal{G}_{\mu\nu}(\mathbf{k})$ and $\mathcal{U}_{\mu\nu}(\mathbf{k})$ can also be calculated directly from the effective Hamiltonian $\mathcal{H}_{\text{eff}}(\mathbf{k})$. The corresponding formulas appear similar by replacing $\mathcal{P}(\mathbf{k})$ with $\mathcal{H}_{\text{eff}}(\mathbf{k})$. For the Chern number, the formula coincides with the Kubo formula for Hall conductivity, while the same formula for G has no analog in any previous analysis. We compute them in Sec. (4.4.3).

We consider \mathcal{K}_n to be the TB hopping parameters related to the gauge potential H' in a self-consistent way. We consider \mathcal{K}_n to fit the low-energy band structure of our interest under an additional constraint of flux preservation. The values of the \mathcal{K}_n parameters are the same as those obtained on the Wannier orbital basis, as shown below.

4.3.2 Examples of two Majorana bands in a honeycomb lattice

As an example, appropriate for the Kitaev model of present interest, we consider a honeycomb lattice with one ($P = 1$) pair of Majorana bands, see Fig. 4.2(b). Here we have $d_1 = 3$ first nearest neighbors $\mathbf{R}^{(1)} - \mathbf{R} = \delta \mathbf{R}^{(1)} = \{\frac{1}{2}(1, \pm\sqrt{3}), (-1, 0)\}$ and $d_2 = 6$ second nearest neighbors $\mathbf{R}^{(2)} - \mathbf{R} = \delta \mathbf{R}^{(2)} = \{\pm\frac{1}{2}(3, \sqrt{3}), \pm\frac{1}{2}(3, -\sqrt{3}), \pm(0, -\sqrt{3})\}$, and so on.

Since only one type of Majorana orbital is positioned at each site, we can split the position and orbital indices from the gauge field as $\mathcal{U}_{\mathbf{R}, \mathbf{R}'} = u_{\mathbf{R}, \mathbf{R}'} \sigma$. Here $u_{\mathbf{R}, \mathbf{R}'} = \pm 1$, and $u_{\mathbf{R}, \mathbf{R}'} = -u_{\mathbf{R}', \mathbf{R}}$ are the \mathbb{Z}_2 gauge fields for two orbitals positions at \mathbf{R} , and \mathbf{R}' sites, and σ are the Pauli matrices in two ($a = \pm$) Majorana basis. In this bipartite lattice, the same (different) Majorana orbitals are positioned at the first (second) nearest neighbor sites. Hence, the first nearest neighbor gauge field is off-diagonal: $\mathcal{U}_{\mathbf{R}, \mathbf{R}^{(1)}} = u_{\mathbf{R}, \mathbf{R}^{(1)}} \sigma^x$. The second nearest neighbor is diagonal

$\mathcal{U}_{\mathbf{R},\mathbf{R}^{(2)}} = u_{\mathbf{R},\mathbf{R}^{(1)}} u_{\mathbf{R}^{(1)},\mathbf{R}^{(2)}} \sigma^z$, where $\mathbf{R}^{(1)}$ is the 1st nearest neighbor that connects \mathbf{R} and $\mathbf{R}^{(2)}$ sites in the shortest distance. In all the diagonal terms, $a = \pm$ orbitals must have opposite gauge fields for the Hamiltonian to be particle-hole symmetric, and hence, we have σ^z here.

Taking into account the above properties, we have the TB Majorana orbital Hamiltonian (up to the second nearest neighbors):

$$\begin{aligned} H_{\text{eff}} = & K_0 \sum_{\mathbf{R}} \sum_{a=\pm} c_{a,\mathbf{R}} \sigma_{aa'}^z c_{a',\mathbf{R}} + iK_1 \sum_{\mathbf{R},\mathbf{R}_i^{(1)} \in d_1} u_{\mathbf{R},\mathbf{R}_i^{(1)}} \sum_{a=\pm} c_{a,\mathbf{R}} \sigma_{aa'}^x c_{a',\mathbf{R}_i^{(1)}} \\ & + iK_2 \sum_{\mathbf{R},\mathbf{R}_j^{(2)} \in d_2} u_{\mathbf{R},\mathbf{R}_j^{(2)}} u_{\mathbf{R}_j^{(2)},\mathbf{R}} \sum_{a=\pm} c_{a,\mathbf{R}} \sigma_{aa'}^z c_{a',\mathbf{R}_j^{(2)}}. \end{aligned} \quad (4.16)$$

$u_{\mathbf{R},\mathbf{R}^{(1)}} = \pm 1$ can take any value in a link, provided the total flux in a unit cell is conserved to the value in the full Hamiltonian. $\mathcal{K}_i = K_i \mathbb{1}$ are set to be orbital-independent coupling constants for simplicity in notation in this example, however, in the fitting procedure in Sec. 4.4.2 they are considered orbital dependent. Going to the momentum space, we obtain the diagonal and off-diagonal terms as

$$\begin{aligned} \Delta_I(\mathbf{k}) + ih_S(\mathbf{k}) &= iK_1 \sum_{\mathbf{R},\mathbf{R}_i^{(1)} \in d_1} u_{\mathbf{R},\mathbf{R}_i^{(1)}} e^{i\mathbf{k} \cdot \delta \mathbf{R}_i^{(1)}}, \\ \Delta_R(\mathbf{k}) &= K_0 + iK_2 \sum_{\mathbf{R},\mathbf{R}_j^{(2)} \in d_2} u_{\mathbf{R},\mathbf{R}_j^{(2)}} u_{\mathbf{R}_j^{(2)},\mathbf{R}} e^{i\mathbf{k} \cdot \delta \mathbf{R}_j^{(2)}}. \end{aligned} \quad (4.17)$$

It is interesting to notice here that the imaginary and real parts of the superconducting (complex-fermion) pairing gaps arise from the first and second nearest neighbor Majorana hoppings, respectively.

Note that $h_S, \Delta_{R,I}$ are real. We set K_i to be real and $K_0 = 0$. This makes $\Delta_I = -2K_1 \sum_{i=1}^3 \times \sin(\mathbf{k} \cdot \delta \mathbf{R}_i^{(1)})$, $h_S = -2K_1 \sum_{i=1}^3 \cos(\mathbf{k} \cdot \delta \mathbf{R}_i^{(1)})$. Δ_R arises from the second next-nearest neighbor, which gives $-2K_2 \sum_{j=1,3,5} \sin(\mathbf{k} \cdot \delta \mathbf{R}_j^{(2)})$. This reduces the gauge choices for nearest neighbors to be $u_{\mathbf{R},\mathbf{R}_1^{(2)}} = -u_{\mathbf{R},\mathbf{R}_2^{(2)}}$, $u_{\mathbf{R},\mathbf{R}_3^{(2)}} = -u_{\mathbf{R},\mathbf{R}_4^{(2)}}$, and $u_{\mathbf{R},\mathbf{R}_5^{(2)}} = -u_{\mathbf{R},\mathbf{R}_6^{(2)}}$. This affects the gauge choices for the nearest neighbors and also the flux-modulation-induced supercell constructions, shown in Fig. 4.1. Both $\Delta_{R,I}$ are odd under spatial parity and are consistent with odd-fermion parity for the fermionic odd-parity for complex fermion pairing for the same spin states. This gives the well-known $p + ip$ pairing state for the corresponding complex fermion state.

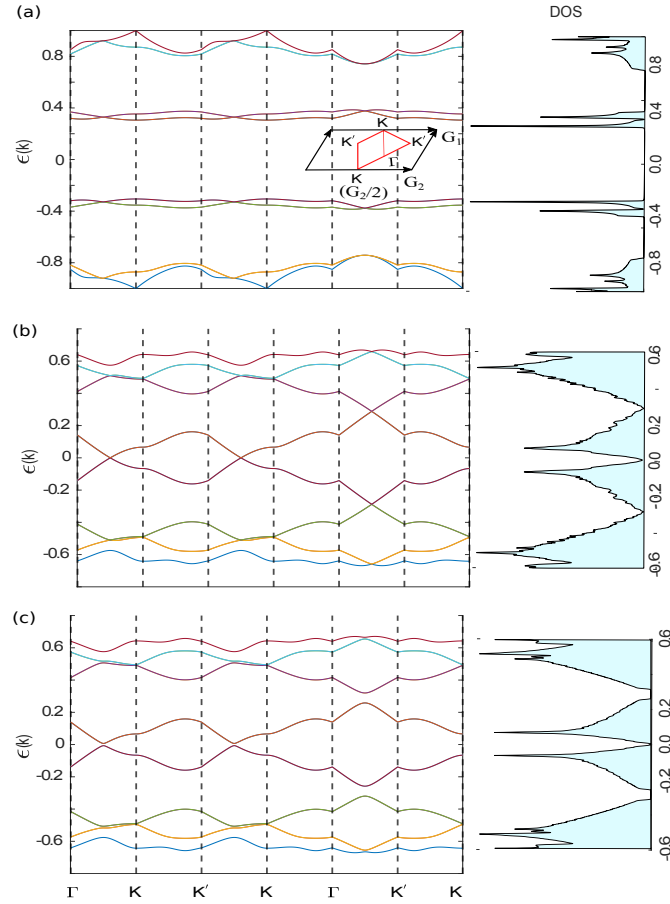


Fig. 4.3 The dispersions of the Majorana fermions for two representative flux configurations. (a) The dispersions for the 3×3 are shown here along the \mathbf{k} - directions as given in the inset. Here, we set $K/J = 0$, which shows a gapped dispersion. (b–c) The Majorana dispersions for 4×4 supercell are shown for $K/J = 0.0$ in (b) and $K/J = 0.01$ in (c). $K/J > 0$ opens a band gap across the zero energy. The adjacent right-hand panel shows the density of states for all three cases.

4.4 Results

4.4.1 Majorana band structure of the full supercell Hamiltonian

We consider here several representative superlattices of dimension $d \times d$ containing a single \mathbb{Z}_2 flux pair of length d , i.e., the number of $u = -1$ gauge fields flipped between the two \mathbb{Z}_2 fluxes, while $u = +1$ in the rest of the bonds in the supercell. This makes the supercell Hamiltonian dimension to be $2N = 4d^2$. A typical superlattice for $d = 2$ is shown in Fig. 4.1(a). It turns out the band structure properties are characteristically similar for all $3d \times 3d$ supercells, which differ from the characteristically similar band structure for other supercells. Therefore, we present the numerical results for two representative values of $d = 3, 4$ in Fig. 4.3 by

diagonalizing the supercell Hamiltonian given in Eq. (4.2). We remind the reader that although the band dispersion depends on the gauge choice, but different gauge choices give equivalent dispersion along different momentum directions. Moreover, the salient properties such as gapless (degeneracy), gap, flat bands, Chern number, and quantum metric indices are gauge invariant. We show the gauge choice and the orientation of the \mathbb{Z}_2 flux pair for one example case of $d = 4$ in Fig. 4.4.

Interestingly, we find that only for the $d = 3$ (and its integer multiples) flux configuration, the Majorana dispersions are gapped even for $K = 0$, and render nearly flat-band, see Fig. 4.3(a). The reason for the gapped behavior is the broken sublattice symmetry that protects the degeneracy at energy $E = 0$, although the particle-hole symmetry remains intact.

For other flux configurations, the Majorana bands show a gapless feature at energy $E = 0$ at the high-symmetric momenta for $K = 0$, a representative result of which is shown in Fig. 4.3(b). The low-energy particle-hole symmetric bands have linear dispersions around the gapless point, as in graphene, and also show linearly dispersing gap-closing points with high-energy bands. All these gapless points acquire mass term for $K \neq 0$ value, 4.3(c). The gap to the higher energy bands is larger than that at $E = 0$. We denote the gap at $E = 0$ by Δ , while the bandwidth of the corresponding two low-energy bands is denoted by δ . The ratio δ/Δ , called the fitness ratio, measures the flatness of the low-energy bands, with $\delta/\Delta \rightarrow 0$ corresponding to complete flatness (i.e., all \mathbf{k} points are degenerate), while $\delta/\Delta \rightarrow \infty$ corresponds to point degeneracy. K controls the band gap $\Delta(K)$, while the larger the length (d) of the \mathbb{Z}_2 flux pair, the smaller is δ , and typically δ scales allegorically as $\delta \sim 1/d^2$.

Increasing d while holding all other parameters constant elevates the sublattice dimension. In other words, it expands the dimension of the local Hilbert space C_l . This, in turn, enhances the level-repulsion from the eliminated high-energy bands to the target low-energy bands. This repulsion is captured by the quantum metric \mathcal{G} in the wavefunction description or by the superexchange or gauge potential (H^l) within our effective theory, see Fig. 4.3(c).

As K increases, we observe a fascinating topological phase transition, depicted in Figs. 4.5. Initially, the gap scales as $\Delta \sim K$ for $K \rightarrow 0$, before it reaches a maximum around $K \approx 0.06J$. This is an interesting point where the band gap varies minimally with K . With a further increase of K , Δ reduces and eventually vanishes entirely around $K \approx 0.175J$. Notably, the bandwidth (δ) also vanishes at this critical point, suggesting the formation of a completely flat band where both bands become degenerate across all \mathbf{k} -points. This results in an extensive degeneracy in the Hamiltonian. It is noteworthy that on either side of this flat band degeneracy, the system exhibits well-defined Chern bands with $C = \pm 1$. This observation suggests a unique type of topological phase transition characterized by the emergence of an extensive band degeneracy,

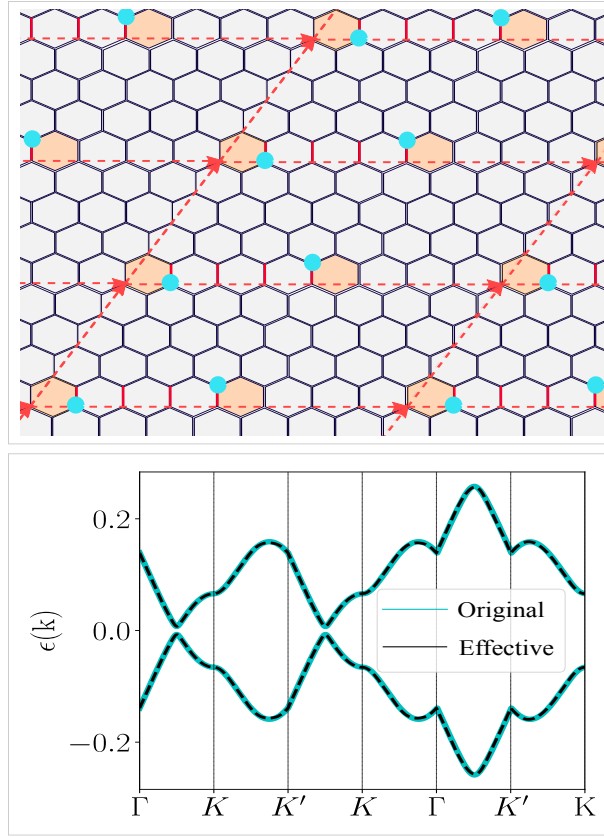


Fig. 4.4 (a) The locations of the Wannier centers (magenta color) are shown to be adjacent to the π flux plaquettes for the 4×4 supercell. (bottom) (b) The band structures from the original band structure and the effective Hamiltonian are shown for $K/J = 0.01$ on 4×4 configuration.

which is different from the quintessential Dirac cone degeneracy at other topological phase transitions; see Sec. 4.4.3.

4.4.2 Effective model and Majorana Wannier centers

We proceed by constructing an effective Hamiltonian H_{eff} to capture the behavior of the two low-energy bands ($\alpha = 1$, and $a = \pm$) and the localization of the corresponding Wannier orbitals $|\pm, \mathbf{R}\rangle$. Here, we focus on the supercell results for the $d = 4$ case for $K \neq 0$, i.e., a gapped system. The construction of the effective band mirrors the example provided in Sec. 4.3.2, utilizing the same sets of nearest neighbors, except the $\mathbf{G}_{1,2}$ are different here. We expand the Hamiltonian up to several nearest neighbors, incorporating the coupling constants, and the specific values of the TB parameters are given in Appendix D.3.4. The fitting yields a near-perfect fit of the energy dispersions $\pm E(\mathbf{k})$ to the original supercell results, see Fig. 4.4(b). For the fitting procedure, we use the Wannier90 code [77]. A key advantage of using the

Wannier90 code is its ability to provide the real-space projection of the $w_{\pm, \mathbf{R}}(\mathbf{r})$, and their corresponding spread functions $\Delta \mathbf{r}_{\pm}$. Due to the non-zero Chern numbers of these flat bands, identifying their Wannier centers presents a challenge due to global gauge obstruction. In the effective theory, this gauge obstruction is evaded by choosing uniform flux W_S at all unit cells. The flux condition deduced in the effective Hamiltonian in Eq. (4.16) gives constraints on the fitting parameters. This method is discussed in Appendix D.3

As anticipated, the Majorana Wannier orbitals $w_{\pm, \mathbf{R}}(\mathbf{r})$ are localized at the \mathbb{Z}_2 flux sites, as shown in Fig. 4.4(a). Within the original supercell, these two states were linked by the string operator that connects the \mathbb{Z}_2 flux pair. However, in the effective theory, $w_{\pm, \mathbf{R}}(\mathbf{r})$ represents the two basis states of a unit cell. Since the effective gauge fields reside on the links connecting lattice sites, there is no gauge field directly coupling the two Majorana orbitals within a unit cell. Their coupling is not parametrized by the anti-symmetric onsite interaction term $i\mathcal{K}_0 = K_0\sigma^z + K_0^I\sigma^y$, where σ^μ matrices are defined in the $a = \pm$ Wannier orbital basis, as in the example case given in Sec. 4.3.2. Here, K_0 captures the onsite energy difference of the two orbitals, while K_0^I describes the intra-unit cell coupling between them. The remaining terms in Eq. (4.16) remain the same.

4.4.3 Chern number and Quantum metric

This work suggests that the \mathbb{Z}_2 flux quantization condition within the supercell leads to similar properties as in the integer $U(1)$ flux quantization condition in a magnetic Brillouin zone in the TKNN theory for $U(1)$ quantum Hall insulators.[78] Both mechanisms lead to a finite Chern number for each Majorana band, a characteristic that persists in both the full supercell Hamiltonian and the resulting effective theory.

Alternatively, we can interpret this behavior by parametrizing the eliminated states either as a geometry term in the wave function or as gauge fields within the Hamiltonian. A trivial topological space would correspond to a product state between the low-energy names and the eliminated states. Conversely, a non-trivial topology signifies entangled states between them. In the case of flat band geometry encountered here, a non-trivial topology necessarily arises.

To ensure consistency, we compute the Chern number for both cases. In the supercell case, we employ the projector $\mathcal{P}(\mathbf{k})$ to compute the Chern number (C) using Eq. (4.15). Similarly, for the effective Hamiltonian, C is obtained using it projector $\tilde{\mathcal{P}}(\mathbf{k}) = |\tilde{\mathbf{p}}, \mathbf{k}\rangle\langle\tilde{\mathbf{p}}, \mathbf{k}|$, where $|\tilde{\mathbf{p}}, \mathbf{k}\rangle$ are the eigenstates of $\mathcal{H}_{\text{eff}}(\mathbf{k})$. We present the results for the $d = 4$ case and compare them with the zero-flux ($d = 0$) scenario. Our calculations consistently reveal that the $K \neq 0$ case exhibits a Chern number of $C = +1$ for both $d = 0$ and $d = 4$ cases (for the $-E(\mathbf{k})$ band). However, in the $d = 4$ supercell, a sharp transition from $C = +1$ to -1 occurs at the critical point $K = 0.175J$, where the band gap (δ) closes and reopens. The underlying physics governing the Chern

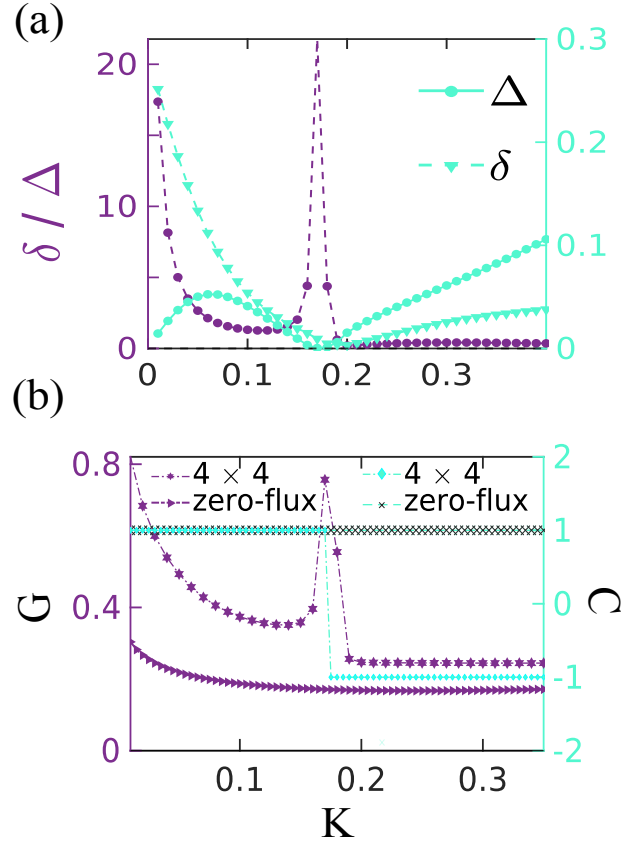


Fig. 4.5 (a) Band gap (Δ), bandwidth (δ), and the fitness ratio (δ/Δ) are plotted as a function of K (from Eq. (4.2)) for the 4×4 supercell. (b) Computed values of the quantum metric invariant (G) and Chern number (C) are plotted as a function of K , and compared with zero-flux configuration. Two topological phase transitions are located here: at $K=0$, we have a topological phase transition from trivial to non-trivial phase with Dirac cone degeneracy, and another one at $K \approx 0.175J$ between two non-trivial topologies with a flat-band degeneracy.

number transition obtained from the effective Hamiltonian $\mathcal{H}_{\text{eff}}(\mathbf{k})$ is analogous in which the uniform flux sector changes from $W_s = +1$ to $W_s = -1$. The transition is different from the gap closing and reopening at a single Dirac point; the involvement of the flat band at this transition point to a novel topological phase transition.

The influence of flat band physics and the geometry effect introduced by the eliminated high-energy states are effectively captured by the quantum metric ($\mathcal{G}(\mathbf{k})$) term in Eq. (4.8). The corresponding invariant (G) is defined in Eq. (4.14) and is plotted in Fig. (4.5)(b) as a function of K .⁴ As expected, the G value for the zero-flux configuration exhibits no distinguishing features, reinforcing the notion that G captures a distinct topological invariant arising from

⁴The symmetric tensor $\eta_{\mu\nu}$ for the hexagonal lattice becomes $\eta_{\mu\nu} = \hat{\mathbf{G}}_\mu \cdot \hat{\mathbf{G}}_\nu = \begin{pmatrix} 1 & -1/2 \\ -1/2 & 1 \end{pmatrix}$.

the projector, separate from the Chern number. In the supercell case, however, G displays an additional singularity at the gap-closing point of $K = 0.175J$. Interestingly, both G and the fitness ratio, δ/Δ , exhibit similar behavior. This suggests that the singularity in G is sensitive to the characteristics of the flat band, particularly the presence of extensive band degeneracy.

It's important to distinguish between the phase transition properties of interacting and non-interacting systems. In interacting theories, a second-order phase transition is characterized by the appearance of gapless collective modes and singular correlation functions. In contrast, in this non-interacting theory, an extensive degeneracy emerges at the flat bands. Here, the flat bands exhibit maximal entanglement with the eliminated high-energy bands, and consequently, we expect this unique phase transition feature to be reflected in the topological entanglement entropy.[79–82]

A non-zero Chern number C signifies an obstacle in smoothly changing the wavefunction's phase ($\arg(w_{a,\mathbf{R}})$) throughout the material.[83, 84] In contrast, a non-zero quantum metric G directly affects how "spread out" ($\Delta_{\mathbf{r}_a}$) the wavefunction is[85, 86]. More generally, \mathcal{G} puts constraints on how different parts of the wavefunction are correlated, and $\Delta_{\mathbf{r}_a}$ is a type of correlation function. In the effective Hamiltonian $\mathcal{H}_{\text{eff}}(\mathbf{k})$, the winding number of the wavefunction is determined by the complex phase of the off-diagonal term $\Delta_I(\mathbf{k}) + ih_S(\mathbf{k})$. $\Delta_R(\mathbf{k})$ acts like a Dirac mass term, which gives the inverse correlation length of the wavefunction, essentially defining its spread. At discrete Dirac points, all these terms simultaneously vanish at a single \mathbf{k} -point, while for the degenerate flat bands, they vanish at all \mathbf{k} -points. In our effective theory, $\Delta_{I,R}$, and h_S are assumed to be polynomials of Bloch phases $z_{\mathbf{R}}(\mathbf{k})$, which are a set of linearly independent basis functions. Consequently, a flat band arises when all the coefficients in these polynomials, i.e., the TB parameters \mathcal{K}_i , become zero.

4.4.4 Gauge invariant Mean-field theory for Fractional Chern insulator

The interplay between \mathcal{U} and \mathcal{G} creates a promising platform for realizing fractional Chern insulating states through interactions [87–89]. The current understanding of fractional Chern insulating state primarily relies on numerical results. [87–98] In this section, we propose a mean-field theory that predicts the emergence of a fractional Chern number in Majorana bands.

We introduce a mean-field theory to split the Majorana flat bands by forming a density wave order state. A density wave state effectively folds the BZ into a reduced BZ, with the ordering vector \mathbf{Q} defining the new reciprocal lattice vectors. The original Chern bands transform into a main band and folded (or shadow) bands within the reduced BZ. These bands share partial occupation density. This process leads to a fascinating consequence: a single, split Chern band becomes partially filled with a finite interacting gap separating it from another partially filled Chern band. [87–89, 99]

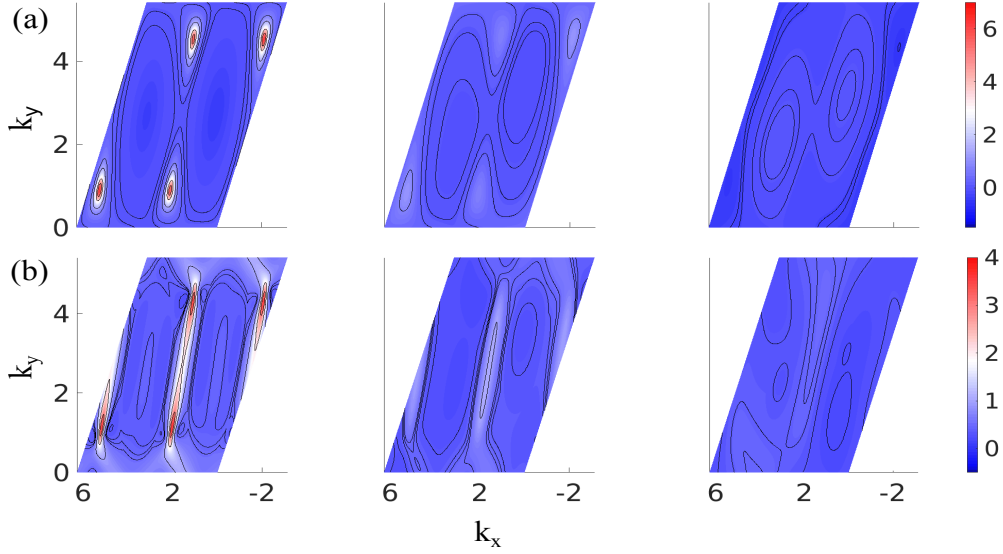


Fig. 4.6 We plot (a) the Berry curvature $G(\mathbf{k})$ and (b) the difference $G(\mathbf{k}) - U(\mathbf{k})$ from the trace condition (ii) in the first Brillouin zone. The plots in each column correspond to different K values of 0.035, 0.12, and 0.22, from left to right.

Here, we begin by verifying if the bands fulfill the essential criteria for an ideal ‘vortexable’ band, a prerequisite for realizing a fractional Chern phase. [93, 100–102] Interestingly, the low-energy Majorana bands in the supercell configurations fulfill those conditions: i) uniform-in- \mathbf{k} Berry curvature $U(\mathbf{k}) = \text{Tr}\mathcal{U}_{\mu\nu}(\mathbf{k})$ and ii) the trace condition $G(\mathbf{k}) = \frac{1}{2} \sum_{\mu} \text{Tr}\mathcal{G}_{\mu\mu}(\mathbf{k}) \simeq U(\mathbf{k})$, $\forall \mathbf{k}$ -point. Another quantity that measures how good is a flat band is called the flatness ratio (δ/Δ), where δ is the bandwidth of each flat band, and Δ is the band gap between the two flat bands under consideration. When δ/Δ is less, as shown in Fig. 4.5(a) for the 4×4 supercell, the conditions for ideal Chern bands are satisfied more accurately. Fig. 4.6(a) shows $U(\mathbf{k})$ and Fig. 4.6 (b) gives the difference $G(\mathbf{k}) - U(\mathbf{k})$ in ii) at three different K values, 0.035, 0.12, and 0.22 from left to right. δ/Δ decreases with increasing K , and $U(\mathbf{k})$ becomes more uniform. The same is true for the trace condition in (ii), i.e., the difference $G(\mathbf{k}) - U(\mathbf{k})$ is much less with increasing K .

Having established that the Chern Majorana bands in the supercell settings are prone to fractionalization, we now include an interaction term within the effective Hamiltonian H_{eff} in Eq. (4.12), or more specifically in Eq. (4.16) for the case of 2×2 Honeycomb lattice. Interestingly, a \mathbb{Z}_2 ‘electric field’ operator introduced below Eq. (4.1) mediates a quartic Majorana interaction in the honeycomb lattice with three nearest neighbors.[35, 103] The corresponding operator for the Wannier orbitals, in general, reads as $X_{\mathbf{R}} = \prod_{\{\mathbf{R}, \mathbf{R}^{(1)}\} \in d_1} \mathcal{U}_{\mathbf{R}, \mathbf{R}^{(1)}}$, where it is reminded that $\mathbf{R}^{(1)}$ is a set of first nearest neighbor sites containing d_1 elements with

respect to the \mathbf{R} site. $X_{\mathbf{R}}$ is a gauge-dependent operator, and it couples to all the Majoranas sitting at \mathbf{R} and $\mathbf{R}^{(1)}$, which then becomes gauge invariant. In the original Kitaev model with the small magnetic field, it was shown that such a term arises in the same third-order perturbation term as in Eq. (4.1) and has the same coupling constant of iK . Here, we consider a general coupling term of $i\mathcal{K}'_1$ and write the interaction term on a honeycomb lattice an $a = \pm$ particle-hole Majorana pair in a single $\alpha = 1$ orbital state as

$$H_{\text{int}} = -i\mathcal{K}'_1 \sum_{\mathbf{R}, a, a' = \pm} iu_{\mathbf{R}, \mathbf{R}_1^{(1)}} u_{\mathbf{R}, \mathbf{R}_2^{(1)}} u_{\mathbf{R}, \mathbf{R}_3^{(1)}} c_{a, \mathbf{R}} c_{a', \mathbf{R}_1^{(1)}} c_{a', \mathbf{R}_2^{(1)}} c_{a', \mathbf{R}_3^{(1)}}. \quad (4.18)$$

Consistent with Elitzur's theorem [104], we can write down two gauge invariant mean-field order parameters, defined as follows:

$$\Omega_1 = \frac{i\mathcal{K}'_1}{3} \sum_{i=1}^3 \langle u_{\mathbf{R}, \mathbf{R}_i^{(1)}} c_{a, \mathbf{R}} c_{a', \mathbf{R}_i^{(i)}} \rangle, \text{ and } \Omega_2 = -\frac{i\mathcal{K}'_1}{3} \sum_{i \neq j=1}^3 \langle u_{\mathbf{R}_i^{(1)}, \mathbf{R}_j^{(1)}} c_{a', \mathbf{R}_i^{(1)}} c_{a', \mathbf{R}_j^{(1)}} \rangle. \quad (4.19)$$

Here, the expectation value is self-consistently evaluated within the mean-field ground state. We have also assumed the order parameters $\Omega_{1,2}$ to be independent of \mathbf{R} (uniform phase), and hence, it is dropped or from the L.H.S. of the above equation. Both order parameters involve two Majorana operators, and the gauge field links them so that the order parameter remains gauge invariant. The resultant mean-field interaction (gauge-invariant) Hamiltonian becomes

$$H_{\text{int}}^{(\text{MF})} = i\Omega_2 \sum_{\mathbf{R}, i, a'} u_{\mathbf{R}, \mathbf{R}_i^{(1)}} c_{a, \mathbf{R}} c_{a', \mathbf{R}_i^{(1)}} + i\Omega_1 \sum_{\mathbf{R}, i \neq j, a \neq a'} u_{\mathbf{R}_i^{(1)}, \mathbf{R}_j^{(1)}} c_{a', \mathbf{R}_i^{(1)}} c_{a', \mathbf{R}_j^{(1)}}, \quad (4.20)$$

In the second term in Eq.(4.19) and the first term in Eq. (4.20), we have implemented the relation: $u_{\mathbf{R}_i^{(1)}, \mathbf{R}_j^{(1)}} = -u_{\mathbf{R}, \mathbf{R}_i^{(1)}} u_{\mathbf{R}, \mathbf{R}_j^{(1)}}$. In the Fourier space, we assume $\Omega_{1,2}$ breaks the translational symmetry to a staggered density wave state at a fixed wavevector \mathbf{Q} such that $\Omega_1(\mathbf{Q}) = \sum_{\mathbf{R}_i - \mathbf{R}_j^{(1)}} \Omega_1 e^{i\mathbf{Q} \cdot (\mathbf{R}_i - \mathbf{R}_j^{(1)})}$, and $\Omega_2(\mathbf{Q}) = \sum_{\mathbf{R} - \mathbf{R}_j^{(1)}} \Omega_2 e^{i\mathbf{Q} \cdot (\mathbf{R} - \mathbf{R}_j^{(1)})}$. While the above gauge-invariant mean-field theory admits various generalizations, we focus on a simpler case here to illustrate the emergence of partially filled Chern bands within this framework.

Adding $H_{\text{int}}^{(\text{MF})}$ to the effective Hamiltonian H_{eff} in Eq. (4.16), we can express the matrix form of the Hamiltonian in the spinor $(c_+(\mathbf{k}) \ c_-(\mathbf{k}) \ c_+(\mathbf{k} + \mathbf{Q}) \ c_-(\mathbf{k} + \mathbf{Q}))^T$ for the $\alpha = 1$ band as

$$\mathcal{H}_{\text{MF}}(\mathbf{k}) = \begin{pmatrix} \mathcal{H}_{\text{eff}}(\mathbf{k}) & i\Omega(\mathbf{Q}) \\ \text{H.c.} & \mathcal{H}_{\text{eff}}(\mathbf{k} + \mathbf{Q}) \end{pmatrix}, \Omega(\mathbf{Q}) = \begin{pmatrix} \Omega_1(\mathbf{Q}) & \Omega_2(\mathbf{Q}) \\ \Omega_2^*(\mathbf{Q}) & \Omega_1^*(\mathbf{Q}) \end{pmatrix}. \quad (4.21)$$

The above form of $\Omega(\mathbf{Q})$ maintains the particle-hole symmetry of the Hamiltonian. The eigenvectors of the mean-field Hamiltonian in Eq. (4.21) is used in Eq. (4.19) to calculate these order -parameter self-consistently.

We test out results for a simpler commensurate density wave order for $\mathbf{Q} = \mathbf{G}_2/2$, and $\Omega_1 = 0.01, \Omega_2 = 0.015$ with $K = 0.12$. The corresponding energy eigenvalues of $\mathcal{H}_{\text{MF}}(\mathbf{k})$ split the particle-hole symmetric eigenvalues $\pm E_{\mathbf{k}}$ into four bands with a finite gap between all of them. The Chern number of each band now corresponds to $C_n = \sum_{\mathbf{k} \in \text{RBZ}} \sum_a \mathcal{V}_{na}^\dagger(\mathbf{k}) \mathcal{V}_{na}(\mathbf{k}) \text{Tr}_a \mathcal{U}_{12}(\mathbf{k})$, where \mathcal{V} corresponds to the eigenvectors of \mathcal{H}_{MF} , and Tr_a corresponds to the trace operation with the $a = \pm$ eigenvector on the Berry curvature given in Eq. (4.9). RBZ corresponds to the reduced BZ in the density wave state. The obtained values of the Chern number for all four bands are $C = -0.4, -0.94, 0.6$, and 0.136 .

4.5 Summary and outlook

In summary, our work revealed the following key results. (i) We examined how the \mathbb{Z}_2 flux pairs with variable length d lead to superlattice formation. These superlattices introduce low-energy Majorana bands with intriguing topological properties, including Dirac-like excitations or flat-band degeneracy. (ii) We constructed a novel \mathbb{Z}_2 gauge-mediated tight-binding model for Majorana Wannier orbitals. This involved introducing a gauge potential in the low-energy Hamiltonian through a superexchange-like potential arising from virtual hopping to the eliminated high-energy energy levels. Conditions are deduced under which the superexchange potential acts as a TB gauge field for Majorana hoppings within the lattice. Importantly, it satisfies a flux-presentation constraint that matches the original supercell Hamiltonian. This method of introducing gauge fields directly in the Hamiltonian offers several advantages over traditional geometric terms introduced in the wavefunction description. (iii) We analyzed how the Berry curvature and quantum metric of the effective theory evolve as flat bands form with increasing nearest-neighbor hopping. Notably, we discovered a novel critical point where the quantum metric diverges, suggesting a phase transition between $C = \pm 1$ phases within the same band. This behavior is a hallmark of flat bands with extensive degeneracy. Since this transition occurs in the non-interacting theory, we propose that it signifies a state of maximal entanglement between low-energy and high-energy bands. (iv) Finally, we leveraged the existence of flat bands with a divergent quantum metric to develop a mean-field theory for a gauge-invariant Majorana density wave order. The resulting split Chern bands enable us to achieve partial filling with a gapped spectrum relative to other Majorana bands.

The experimental proposals for attaining control over the creation/annihilation of \mathbb{Z}_2 fluxes are reviewed first. It is shown in Ref. [105] that the local modulation of the exchange in-

teractions by introducing Dzyaloshinskii-Moriya interactions flips the sign of local bond interactions. That produces a \mathbb{Z}_2 flux pair. Further desired configurations are obtained by creating/annihilating the sequence of pairs in neighboring plaquettes. In general, Superconducting quantum interference device (SQUID) microscopy is helpful in experimentally visualizing these vortex networks.[106]

This work centers on constructing a gauge-field mediated TB model for fractional particles. Since fractional/entangled excitations do not exist by themselves, their combinations must produce electronic states. Alternatively, one can view these fractional particles as residing within a medium of gauge fields, either confined or deconfined. Our focus is twofold: understanding the origin of these gauge fields and establishing a systematic framework for their parameterization within a TB model. The emergence of such gauge fields stems from the projection operation used to eliminate high-energy states. This operation effectively imposes constraints, leading to restricted dynamics and correlation functions pertaining to the fractional particles. These constrained dynamics can give rise to more phenomena such as a distinct type of quantum glass,[19] or deconfined critically,[107, 108] or extensive degeneracy in the formation of flat bands, leading to novel topological criticality in the non-interacting theory as observed here.

Our approach deviates from conventional methods by introducing a gauge potential directly within the Hamiltonian through a superexchange mechanism. This mechanism gives rise to gauge-mediated tight-binding (TB) hoppings arising from the anti-symmetric part of the superexchange potential. Notably, an additional constraint can be readily incorporated to ensure flux preservation and topology without worrying about the maximal localization of the Wannier orbitals. The detailed constructions are provided in Sec. 4.3 applies to a general $SU(N)$ gauge field, \mathcal{U} , and its corresponding fractional particle. In this specific work, we have inserted the \mathbb{Z}_2 valuedness of the \mathcal{U} operators towards the end and in the particle-hole symmetry of \mathcal{H}_{eff} , which ensures real Majorana states in real space. Therefore, it will be rather straightforward to generalize the TB theory to the $SU(N)$ gauge field coupled to other fractional particles.

Our analysis reveals an interacting critical point within the theory as a function of the second nearest-neighbor hopping strength (K). At this critical point, the quantum metric diverges, and the Chern number exhibits a transition between +1 and -1. This signifies a potential singularity in the entanglement entropy spectrum where the entanglement is maximal between the low-energy and the eliminated high-energy states. Quantifying this entanglement spectrum in terms of the gauge-mediated TB parameters remains an intriguing challenge for future investigations.

Finally, leveraging the insights from the effective Hamiltonian, we propose a mean-field theory for a gauge-invariant Majorana density wave order. In conventional gauge theories, the mean-field order parameter is subject to an additional constraint arising from the requirement of gauge invariance. This constraint often presents significant challenges within the geometric

framework, leading to a reliance on numerical methods for studying fractional Chern insulator states. Our effective Hamiltonian, however, allows us to derive a self-consistent mean-field theory for Majorana fermions. This method paves the way for future investigations into more exotic interaction effects within both \mathbb{Z}_2 and $SU(N)$ gauge theories.

D

Appendices for chapter 4

D.1 Matrix Elements of the Supercell Hamiltonian

Here, we explicitly give the matrix elements of the $2N \times 2N$ matrices \mathcal{H}_{IJ} as

$$\mathcal{T}_{II} = \begin{pmatrix} 0 & Ju_{1,2} & Ku_{1,2}u_{2,3} & 0 & \dots & 0 & 0 \\ -Ju_{1,2} & 0 & Ju_{2,3} & Ku_{2,3}u_{3,4} & \dots & 0 & 0 \\ -Ku_{1,2}u_{2,3} & -Ju_{2,3} & 0 & Ju_{3,4} & \dots & 0 & 0 \\ 0 & -Ku_{2,3}u_{3,4} & -Ju_{3,4} & 0 & \dots & 0 & 0 \\ \vdots & \vdots & \vdots & \vdots & \ddots & 0 & Ju_{2N-1,2N} \\ 0 & 0 & 0 & 0 & 0 & -Ju_{2N-1,2N} & 0 \end{pmatrix} \quad (\text{D.1})$$

and

$$\mathcal{T}_{IJ} = \begin{pmatrix} 0 & 0 & 0 & \dots & 0 \\ \vdots & \vdots & \vdots & \ddots & \vdots \\ 0 & 0 & 0 & \dots & 0 \\ Ku_{2N-1,2N}u_{2N,1} & 0 & 0 & \dots & 0 \\ Ju_{2N,1} & Ku_{2N,1}u_{12} & 0 & \dots & 0 \end{pmatrix}. \quad (\text{D.2})$$

The matrix elements in the momentum space become

$$\mathcal{H}(\mathbf{k}) = i\mathcal{T}_{II} + \begin{pmatrix} 0 & 0 & 0 & \dots & 0 & \mathcal{K}_{1,2N-1}(\mathbf{k}) & \mathcal{J}_{1,2N}(\mathbf{k}) \\ 0 & 0 & 0 & \dots & 0 & 0 & \mathcal{K}_{2,2N}(\mathbf{k}) \\ 0 & 0 & 0 & \dots & 0 & 0 & 0 \\ \vdots & \vdots & \vdots & \ddots & \vdots & \vdots & \vdots \\ 0 & 0 & 0 & \dots & 0 & 0 & 0 \\ \mathcal{K}_{1,2N-1}^*(\mathbf{k}) & 0 & 0 & \dots & 0 & 0 & 0 \\ \mathcal{J}_{1,2N}^*(\mathbf{k}) & \mathcal{K}_{2,2N}^*(\mathbf{k}) & 0 & \dots & 0 & 0 & 0 \end{pmatrix}, \quad (\text{D.3})$$

where $\mathcal{K}_{1,2N-1}(\mathbf{k}) = iKu_{2N-1,2N}u_{2N,1}e^{-i\mathbf{k}\cdot(\mathbf{R}_1-\mathbf{R}_{2N-1})}$, $\mathcal{J}_{1,2N}(\mathbf{k}) = iJu_{2N,1}e^{i\mathbf{k}\cdot(\mathbf{R}_1-\mathbf{R}_{2N})}$, $\mathcal{K}_{2,2N}(\mathbf{k}) = iKu_{2N,1}u_{1,2}e^{-i\mathbf{k}\cdot(\mathbf{R}_2-\mathbf{R}_{2N})}$.

D.2 Matrix-Elements of the Tight-Binding Model

To ensure the Majorana operators are well defined and the corresponding complex fermion operators recover the $U(1)$ gauge fields, we transform the Hamiltonian on a complex fermion basis. For each α -orbital, the two Majorana orbitals pair, $a = \pm$ constitute a complex fermion particle-hole pair states at different momenta as

$$|\alpha, a, \mathbf{k}\rangle = +e^{i\phi_{\alpha,a}}|\alpha, -, -\mathbf{k}\rangle_F + e^{-i\phi_{\alpha,a}}|\alpha, +, \mathbf{k}\rangle_F. \quad (\text{D.4})$$

where $\phi_{\alpha,+} = 0$ and $\phi_{\alpha,-} = \pi/2$. $|\alpha, \pm, \mathbf{k}\rangle_F$ are the complex fermionic hole and particle excitation states defined as $|\alpha, +, \mathbf{k}\rangle_F = f_{\alpha,\mathbf{k}}|G\rangle$ and $|\alpha, -, \mathbf{k}\rangle_F = f_{\alpha,\mathbf{k}}^\dagger|G\rangle$ with $f_{\alpha,\mathbf{k}}$, and $f_{\alpha,\mathbf{k}}^\dagger$ corresponding annihilation and creation operators of complex fermions from some grand canonical ensemble state $|G\rangle$. It is easy to see that the corresponding Majorana and complex fermion operators are local in real space as $|\alpha, a, \mathbf{R}\rangle = e^{i\phi_{\alpha,a}}|\alpha, -, \mathbf{R}\rangle_c + e^{-i\phi_{\alpha,a}}|\alpha, +, \mathbf{R}\rangle_c$. Note that $|\alpha, a, \mathbf{R}\rangle$ are the physical Majorana states in real space, whereas complex fermions correspond to physical states in both real and momentum spaces. There is an inherent gauge obstruction between the two Majorana orbitals by a phase difference of $\phi_\alpha = \phi_{\alpha,+} - \phi_{\alpha,-}$. We have kept this phase difference to orbital independent, but it can be generalized to be orbital dependent, which may commence interesting properties.

We construct a $2P$ dimensional Majorana spinor as $|\alpha, +, \mathbf{k}\rangle \oplus |\alpha, -, \mathbf{k}\rangle$ and complex fermionic particle-hole symmetric Nambu spinor $|\alpha, +, \mathbf{k}\rangle_F \oplus |\alpha, -, -\mathbf{k}\rangle_F$. The transformation

between them is defined by the unitary operator:

$$S = \frac{1}{2} \begin{pmatrix} 1 & i \\ 1 & -i \end{pmatrix} \otimes I_{P \times P}. \quad (\text{D.5})$$

The Majorana Hamiltonian given in the main text is written generally as

$$H_{\text{eff}} = h_A \otimes \mathcal{I}_{2 \times 2} + \begin{pmatrix} \Delta_R & \Delta_I + ih_S \\ \text{H.c} & -\Delta_R \end{pmatrix}, \quad (\text{D.6})$$

where \mathbf{k} dependence in all variables is kept implicit. Here $h_{S/A}(\mathbf{k}) = h(\mathbf{k}) \pm h^T(-\mathbf{k})$, and $\Delta(\mathbf{k}) = \Delta_R(\mathbf{k}) + i\Delta_I(\mathbf{k})$. Then, by transforming this Hamiltonian to the complex fermion basis gives

$$H_{\text{eff}}^{(\text{F})} = \frac{1}{4} S H_{\text{eff}}(\mathbf{k}) S^\dagger = \begin{pmatrix} h(\mathbf{k}) & \Delta(\mathbf{k}) \\ \Delta^\dagger(\mathbf{k}) & -h^T(-\mathbf{k}) \end{pmatrix}. \quad (\text{D.7})$$

This is a typical Bogolyubov-de-Gennes Hamiltonian in the particle-hole basis, where $h_{\mathbf{k}}$ is a $P \times P$ Hamiltonian for complex-fermions hopping, and $\Delta(\mathbf{k})$ is the $P \times P$ matrix consisting of superconducting pairings of the complex fermions.

The explicit form of the matrix elements of eq. (D.6) can be written as

$$(\Delta_R)_{\alpha, \alpha'}(\mathbf{k}) = \sum_{p, p'=1}^P \langle \alpha, +, \mathbf{k} | p, +, \mathbf{k} \rangle \langle p, +, \mathbf{k} | (H + H') | p', +, \mathbf{k} \rangle \langle p', +, \mathbf{k} | \alpha', +, \mathbf{k} \rangle, \quad (\text{D.8})$$

$$(\Delta_I + iH_S)_{\alpha, \alpha'}(\mathbf{k}) = \sum_{p, p'=1}^P \langle \alpha, +, \mathbf{k} | p, +, \mathbf{k} \rangle \langle p, +, \mathbf{k} | (H + H') | p', -, \mathbf{k} \rangle \langle p', -, \mathbf{k} | \alpha', -, \mathbf{k} \rangle, \quad (\text{D.9})$$

Due to particle-hole symmetry, $|p, +, \mathbf{k}\rangle$ states give $|\alpha, +, \mathbf{k}\rangle$ Majorana orbital, while $|p, -, \mathbf{k}\rangle$ states give $|\alpha, -, \mathbf{k}\rangle$ orbital, respectively. We define $(U_{\pm})_{\alpha, p} = \langle \alpha, \pm, \mathbf{k} | p, \pm, \mathbf{k} \rangle$ a $P \times P$ overlap matrix which consists of the probability amplitudes of the particle-hole symmetric eigenstates of the full Hamiltonian $|p, \pm, \mathbf{k}\rangle$ to the effective Majorana orbital states. Note that U is not a unitary operator as $|p, \pm, \mathbf{k}\rangle$ states are incomplete. We denote the matrix elements of H is $(\mathcal{D}_{\pm})_{p, p'}(\mathbf{k}) = \langle p, \pm, \mathbf{k} | H | p', \pm, \mathbf{k} \rangle = \pm E_p(\mathbf{k}) \delta_{p, p'}$. The matrix elements H' can be written in second-order perturbation theory with respect to some gauge interaction/superexchange

potential V that makes the transition from the \mathcal{P} to the \mathcal{Q} states as

$$\begin{aligned} (\mathcal{H}'_{aa'})_{p,p'} &= \langle p, a, \mathbf{k} | H' | p', a', \mathbf{k} \rangle \\ &= \frac{1}{2} \sum_{q, q' \in \mathcal{Q}} (V_a)_{pq} (V_{a'})_{q'p'} \left[\frac{\text{sgn}(a)}{E_p - E_q} - \frac{\text{sgn}(a')}{E_{q'} - E_{p'}} \right] + \dots \end{aligned} \quad (\text{D.10})$$

Here $q \in \mathcal{Q}_{\pm} = \mathcal{I} - \mathcal{P}_{\pm}$ states are the particle-hole pairs outside the subspace of our interest. $(V_{\pm})_{pq} = \langle p, \pm, \mathbf{k} | V | q, \pm, \mathbf{k} \rangle$ is the tunneling amplitude between the two eigenstates, our fitting parameters. $|p, \pm, \mathbf{k}\rangle$ are the eigenstates of H and hence are particle-hole symmetric. Interestingly, H' is not particle hole-symmetric in the $|p, \pm, \mathbf{k}\rangle$ as it allows for transition between the particle-hole symmetric states in Eq. (D.9), but its matrix elements must be particle-hole symmetric in the $|\alpha, \pm, \mathbf{k}\rangle$ states, by construction. If C is the particle-hole symmetric operator in the $|\alpha, \pm, \mathbf{k}\rangle$ basis, defined as $|\alpha, +, \mathbf{k}\rangle = C|\alpha, -, \mathbf{k}\rangle$, the matrix elements transform as: $CD_+(\mathbf{k})C^{-1} = -D_-(\mathbf{k})$, $C\mathcal{H}'_{++}(\mathbf{k})C^{-1} = -\mathcal{H}'_{--}(\mathbf{k})$, and $C\mathcal{H}'_{+-}(\mathbf{k})C^{-1} = -\mathcal{H}'_{-+}(\mathbf{k})$. Substituting them in Eqs. (D.8),(D.9) we get $\Delta_R = -U_+(\mathcal{D}_+ + \mathcal{H}'_{++})U_+^{-1} = -U_-(\mathcal{D}_- + \mathcal{H}'_{--})U_-^{-1}$, and $(\Delta_I + i\mathcal{H}_S) = U_+\mathcal{H}'_{+-}U_-^{-1} = -U_-\mathcal{H}'_{-+}U_+^{-1}$, $\forall \mathbf{k}$.

D.3 Numerical fitting procedure

D.3.1 Gauge Obstruction and spread function of Wannier Majorana states

Here, we address the issue of the gauge obstruction for Wannier orbitals of the electrons and how they transcend into the Wannier orbitals of fractional particles. Fixing a smooth global gauge for all Wannier orbitals of electrons within a unit cell can be hindered by several factors. Below, we discuss several such cases and their corresponding remedies.

(a) Topological Insulators: In topological insulators, band inversion between two Wannier orbitals obstructs a global momentum-space gauge. Here, the Wannier orbitals differ by a well-defined local gauge connection, reflecting the non-trivial topology. For example, while a Chern number of 1 requires a band inversion within the Brillouin zone (BZ), its specific location can be shifted without affecting the overall topology (movable gauge obstruction). As discussed in [20, 109–115], this can be addressed by defining an appropriate gauge-fixing matrix.

(b) Gapless Points: If a gapless point arises from a symmetry-protected degeneracy between two bands, it may not be readily movable (unless it is a gauge theory). [73, 116, 117] This can

be tackled by expressing the Wannier orbital states as superpositions within the degenerate manifold and carefully handling the singular point in the expansion coefficient (unitary matrix).

(c) Flat Bands.: Constructing Wannier orbitals becomes challenging for specific flat bands, particularly when they exhibit degeneracy with another band. In such cases, a complete set of localized compact Wannier orbitals may not be achievable. Instead, a combination of compact localized states and extended states might be necessary to form a complete basis set.[66, 67, 118–124]

(d) Atomically Obstructed Insulators: This recently discovered class of (trivial or fragile) topological insulators presents a unique challenge. [125–128] Here, each of the multiple Wannier orbitals must individually possess a sufficiently small spread function ($\Delta\mathbf{r}$) such that their combined spread stays confined within a unit cell.

Can the aforementioned challenges be entirely overcome using Wannier orbitals for fractional particles within a gauge theory framework? The fractional particles of interest here arise from the superposition states of the original complex matter fermions. The fractional particles exhibit a physical separation in real space due to emergent local gauge fields and/or topology. Their physical separation is linked by the gauge fields such as W_p , X_v , and \mathcal{U}_{ij} . For example, in the present case, the two Majorana orbitals are pinned at the two π -flux pairs that are separated by a distance d . Therefore, in analogy with the atomically obstructed orbitals, the spread function ($\Delta\mathbf{r}$) associated with each Majorana Wannier orbital must be less than $d/2$ if there exists a finite trivial gap between the two Majorana bands. For the gapless case, $\Delta\mathbf{r} \sim d/2$, whereas in a topologically non-trivial case, $\Delta\mathbf{r} > d/2$ such that the two Majorana Wannier orbitals overlap within the unit cell, and an intra-unit-cell gauge field between the two orbitals contains a winding or knot to produce the topological invariant.

The gauge obstruction is incorporated within the eigenstates of the full Hamiltonian $|\mathbf{p}, \mathbf{k}\rangle$ before fractionalizing them in the orbital states. This is done as in the standard method outlined in Ref. [21]. The procedure has two steps. First, we allow a unitary transformation $B(\mathbf{k})$ to the eigenstates as $|\tilde{\mathbf{p}}, \mathbf{k}\rangle = \sum_p B_{\tilde{\mathbf{p}}, \mathbf{p}}(\mathbf{k})|\mathbf{p}, \mathbf{k}\rangle$ - which incorporates the singular gauge that needs to be added/subtracted from the global gauge. Next, we perform a smooth gauge fixing on the rotated states $|\tilde{\mathbf{p}}, \mathbf{k}\rangle$ between the two nearest momenta differ by the grid size of $\delta\mathbf{k} = 2\pi/L$, where L is the sample length. It turns out the spread function $\Delta\mathbf{r} = \sum_{\tilde{\mathbf{p}}} \langle \mathbf{r}^2 \rangle_{\tilde{\mathbf{p}}} - \langle \mathbf{r} \rangle_{\tilde{\mathbf{p}}}^2$ is related to the overall matrix

$$M_{\tilde{\mathbf{p}}, \tilde{\mathbf{p}}'}(\mathbf{k}, \mathbf{k} + \delta\mathbf{k}) = \frac{1}{\sqrt{2N}} \sum_i \sum_{\mathbf{p}, \mathbf{p}'} B_{\mathbf{p}, \tilde{\mathbf{p}}}^\dagger(\mathbf{k}) \Gamma_{i, \mathbf{p}}^\dagger(\mathbf{k}) \bar{z}_{\mathbf{t}_i}(\delta\mathbf{k}) \Gamma_{\mathbf{p}', i}(\mathbf{k} + \delta\mathbf{k}) B_{\tilde{\mathbf{p}}', \mathbf{p}'}(\mathbf{k} + \delta\mathbf{k}), \quad (\text{D.11})$$

where \mathbf{t}_i are the positions of the original $2N$ Majorana sublattices in the full Hamiltonian within the \mathbf{R} supercell. Γ is the unitary matrix consisting of the eigenvector of the full Hamiltonian

defined in Sec. 4.2. \mathbf{R}_α is the position of the α -sublattice within the supercell, and we sum over all \mathbf{R} in the entire lattice. In the main text, we work with the $|\tilde{\mathbf{p}}, \mathbf{k}\rangle$ after the gauge fixing, which we continue to denote by $|\mathbf{p}, \mathbf{k}\rangle$ for simplicity in notation.

D.3.2 Completeness of the Wannier Majorana states

In the above description, the $|\alpha, \pm, \mathbf{k}\rangle$ are defined to be the orthonormal complete Wannier states for the effective $2P \times 2P$ Hamiltonian, while $|p, \pm, \mathbf{k}\rangle$ are the low-energy eigenstates of our interests of the full Hamiltonian which orthonormal but not complete. Our numerical procedure follows two steps. First, we construct $|\alpha, \pm, \mathbf{k}\rangle$ states iteratively and then use \mathcal{K}_n as fitting parameters to find the corresponding energies $\pm E_p(\mathbf{k})$ subject to the flux conservation constraint. The procedure followed is the same as [20] and implemented in the Wannier90 package.

We assume $|\alpha, \pm, \mathbf{k}\rangle_t$ as some trial non-orthogonal complete Wannier states related to the $|p, \pm, \mathbf{k}\rangle$ states by an overall matrix $(U_\pm^{(t)})_{p,\alpha}(\mathbf{k}) = \langle p, \pm, \mathbf{k} | \alpha, \pm, \mathbf{k} \rangle_t$. Note that $U_\pm^{(t)}$ are not the same as the desired overlap matrix U_\pm defined below Eq. (D.9) and we want to find a relation between them. To orthonormalize $|\alpha, \pm, \mathbf{k}\rangle_t$ we define their overlap matrix

$$(S_\pm)_{\alpha\alpha'}(\mathbf{k}) = \sum_{pp'} (U_\pm^{(t)\dagger})_{\alpha,p}(\mathbf{k})(U_\pm^{(t)})_{p',\alpha'}(\mathbf{k}) \langle p, \pm, \mathbf{k} | p', \pm, \mathbf{k} \rangle = (U_\pm^{(t)\dagger} U_\pm^{(t)})_{\alpha\alpha'} \quad (\text{D.12})$$

Then the orthonormal Wannier states are defined as $|\alpha, \pm, \mathbf{k}\rangle = \sum_{\alpha'} (S_\pm^{-1/2})_{\alpha\alpha'}(\mathbf{k}) |\alpha', \pm, \mathbf{k}\rangle$. Then it is easy to show that the overlap matrix is defined as $U_\pm = U_\pm^{(t)} S_\pm^{-1/2}$, $\forall \mathbf{k}$. For the method to work, i.e., the Wannier orbitals to be smooth in the momentum space, the overall matrix $U_\pm^{(t)}$ must be non-singular. This is often not the case for topological insulators, atomically obstructed insulators, or flat bands with singular compact orbitals. For removable singularity, the procedure works well as described in [66, 73, 109, 111]. Note that we do not need separate trial functions for the \pm states as they are related by the particle-hole symmetry \mathcal{C} .

D.3.3 Choosing the trial wavefunction

How do we efficiently guess the trial Wannier states $|\alpha, \pm, \mathbf{k}\rangle_t$? We follow the procedure outlined in [111] for complex fermions and make necessary modifications. Because we have the eigenvalues and eigenvectors of the full Hamiltonian H in the supercell, we study first where our interested eigenvectors are localized in the supercell. This gives hints on the location of the Wannier centers for the trial states.

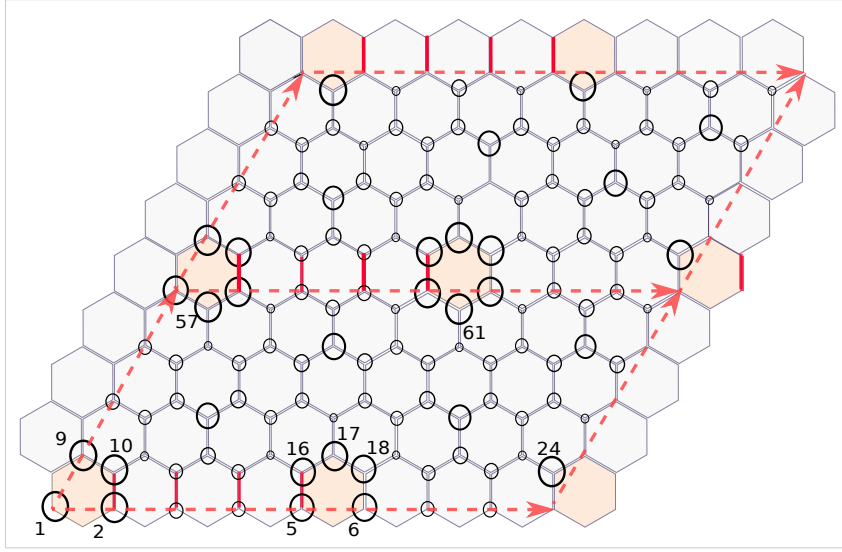


Fig. D.1 We plot the orbital weight of the two lowest energy ($p = 1$) particle-hole states $\sum_{\mathbf{k}} \chi_{p,i}(\mathbf{k})$ at different sites i , defined in Eq. D.13. The results are shown for the 4×4 - flux configuration. The size of the open circles denotes the orbital weight strength. We notice that the weight is largest around the π - fluxes.

The trial functions are considered as follows: following the procedure mentioned in Ref. [111], we can expect the sites close to the π -fluxes to be the most probable regions for Majorana wave functions. We confirm this by plotting the probability amplitude of each Majorana sublattice of the Full supercell Hamiltonian:

$$\chi_{p,i}(\mathbf{k}) = \sum_{a=\pm} |\Gamma_{p,a,i}(\mathbf{k})|^2. \quad (\text{D.13})$$

This signifies the occupation probability of the targeted bands for each sublattice index, α for a \mathbf{k} -point. The highest probability indeed coincides at sites close to the π - fluxes, as shown in Fig. D.1. Based on this, we construct the trial functions for the α -Wannier Majorana orbital

$$|\alpha, \pm, \mathbf{R}\rangle_t = \frac{1}{\sqrt{2N}} \sum_i^{2N} \delta(\mathbf{r} - \mathbf{R} - \mathbf{t}_i) |\mathbf{r}\rangle, \quad (\text{D.14})$$

where \mathbf{t}_i are the positions of the original Majorana sublattices in the full Hamiltonian within the \mathbf{R} supercell. For example, for the 4×4 - configuration shown in Fig. D.1, the sublattice indices for the trial function with $(\alpha, +) \in \{1, 9, 10\}$; and $(\alpha, -) \in \{5, 16, 17, 18\}$. There is no unique definition for these trial functions. The good choice is the functions that give 10 – 20% change in the spread function, from the initial spread function to the final spreads after the minimization procedure. In the \mathbf{k} - space, we obtained $|\alpha, \pm, \mathbf{k}\rangle_t$ by the Fourier transformation

given in Eq. (4.4). With these trial functions, the Wannier centers are shown in Fig. 4.4(a) for 4×4 - configurations. In Fig. 4.4(b), we plot the dispersions of Majorana fermions from Wannierised orbitals, and it fits ED results well with distances, $\mathbf{R} \leq |9\mathbf{a}_1 + 9\mathbf{a}_2|$.

D.3.4 Values of tight-binding parameters

The lattice vectors are given below in terms of the Miller indices and $\mathbf{R} = (0, 0)$. The rest of the parameters are nearly zero and hence ignored in this table. The 2×2 matrices for each tensor

component are in the two particle-hole Majorana basis of $a = \pm$.

$$\begin{aligned}
\mathcal{T}_{\mathbf{R},\mathbf{R}} &= i \begin{pmatrix} 0 & -0.036 \\ 0.036 & 0 \end{pmatrix}, \\
\mathcal{T}_{\mathbf{R},\mathbf{R}^{(1)=(1,0)}} &= i \begin{pmatrix} 0.000 & 0.005 \\ -0.023 & -0.000 \end{pmatrix} = \mathcal{T}_{\mathbf{R},-\mathbf{R}^{(1)}}^\dagger, \\
\mathcal{T}_{\mathbf{R},\mathbf{R}^{(2)=(0,1)}} &= i \begin{pmatrix} 0.028 & -0.05 \\ -0.05 & -0.028 \end{pmatrix} = \mathcal{T}_{\mathbf{R},-\mathbf{R}^{(2)}}^\dagger, \\
\mathcal{T}_{\mathbf{R},\mathbf{R}^{(3)=(1,1)}} &= i \begin{pmatrix} -0.004 & 0.005 \\ -0.008 & -0.004 \end{pmatrix} = \mathcal{T}_{\mathbf{R},-\mathbf{R}^{(3)}}^\dagger, \\
\mathcal{T}_{\mathbf{R},\mathbf{R}^{(4)=(1,-1)}} &= i \begin{pmatrix} 0.018 & -0.008 \\ -0.038 & -0.018 \end{pmatrix} = \mathcal{T}_{\mathbf{R},-\mathbf{R}^{(4)}}^\dagger, \\
\mathcal{T}_{\mathbf{R},\mathbf{R}^{(5)=(2,0)}} &= i \begin{pmatrix} 0.025 & -0.002 \\ 0.012 & -0.25 \end{pmatrix} = \mathcal{T}_{\mathbf{R},-\mathbf{R}^{(5)}}^\dagger, \\
\mathcal{T}_{\mathbf{R},\mathbf{R}^{(6)=(0,2)}} &= i \begin{pmatrix} 0.005 & 0.006 \\ -0.029 & 0.005 \end{pmatrix} = \mathcal{T}_{\mathbf{R},-\mathbf{R}^{(6)}}^\dagger, \\
\mathcal{T}_{\mathbf{R},\mathbf{R}^{(7)=(1,2)}} &= i \begin{pmatrix} 0.003 & -0.002 \\ 0.011 & -0.003 \end{pmatrix} = -\mathcal{T}_{\mathbf{R},-\mathbf{R}^{(7)}}, \\
\mathcal{T}_{\mathbf{R},\mathbf{R}^{(8)=(1,-2)}} &= i \begin{pmatrix} -0.011 & -0.004 \\ -0.014 & 0.011 \end{pmatrix} = -\mathcal{T}_{\mathbf{R},-\mathbf{R}^{(8)}}, \\
\mathcal{T}_{\mathbf{R},\mathbf{R}^{(9)=(2,-1)}} &= i \begin{pmatrix} -0.006 & 0.003 \\ -0.026 & 0.006 \end{pmatrix} = \mathcal{T}_{\mathbf{R},-\mathbf{R}^{(9)}}^\dagger, \\
\mathcal{T}_{\mathbf{R},\mathbf{R}^{(10)=(2,1)}} &= i \begin{pmatrix} 0.001 & -0.001 \\ 0.001 & -0.001 \end{pmatrix} = \mathcal{T}_{\mathbf{R},-\mathbf{R}^{(10)}}^\dagger, \\
\mathcal{T}_{\mathbf{R},\mathbf{R}^{(11)=(2,2)}} &= i \begin{pmatrix} -0.017 & 0.001 \\ -0.004 & 0.017 \end{pmatrix} = \mathcal{T}_{\mathbf{R},-\mathbf{R}^{(11)}}^\dagger, \\
\mathcal{T}_{\mathbf{R},\mathbf{R}^{(12)=(2,-2)}} &= i \begin{pmatrix} 0.003 & 0.001 \\ 0.025 & -0.003 \end{pmatrix} = \mathcal{T}_{\mathbf{R},-\mathbf{R}^{(12)}}^\dagger, \\
\mathcal{T}_{\mathbf{R},\mathbf{R}^{(13)=(2,3)}} &= i \begin{pmatrix} 0.00 & 0.000 \\ 0.002 & 0.00 \end{pmatrix} = \mathcal{T}_{\mathbf{R},-\mathbf{R}^{(13)}}^\dagger, \\
\mathcal{T}_{\mathbf{R},\mathbf{R}^{(14)=(2,-3)}} &= i \begin{pmatrix} 0.003 & -0.003 \\ -0.010 & -0.003 \end{pmatrix} = \mathcal{T}_{\mathbf{R},-\mathbf{R}^{(14)}}^\dagger,
\end{aligned}$$

$$\begin{aligned}\mathcal{T}_{\mathbf{R},\mathbf{R}^{(15)}=(1,3)} &= i \begin{pmatrix} 0.000 & 0.00 \\ -0.004 & 0.00 \end{pmatrix} = \mathcal{T}_{\mathbf{R},-\mathbf{R}^{(15)}}^\dagger, \\ \mathcal{T}_{\mathbf{R},\mathbf{R}^{(16)}=(1,-3)} &= i \begin{pmatrix} -0.002 & 0.005 \\ 0.013 & 0.002 \end{pmatrix} = \mathcal{T}_{\mathbf{R},-\mathbf{R}^{(16)}}^\dagger, \\ \mathcal{T}_{\mathbf{R},\mathbf{R}^{(17)}=(3,2)} &= i \begin{pmatrix} 0.00 & 0.000 \\ 0.002 & 0.00 \end{pmatrix} = \mathcal{T}_{\mathbf{R},-\mathbf{R}^{(17)}}^\dagger, \\ \mathcal{T}_{\mathbf{R},\mathbf{R}^{(18)}=(3,-2)} &= i \begin{pmatrix} 0.00 & 0.000 \\ -0.006 & 0.00 \end{pmatrix} = \mathcal{T}_{\mathbf{R},-\mathbf{R}^{(18)}}^\dagger, \\ \mathcal{T}_{\mathbf{R},\mathbf{R}^{(19)}=(3,3)} &= i \begin{pmatrix} 0.000 & 0.000 \\ -0.001 & 0.000 \end{pmatrix} = \mathcal{T}_{\mathbf{R},-\mathbf{R}^{(19)}}^\dagger, \\ \mathcal{T}_{\mathbf{R},\mathbf{R}^{(20)}=(3,-3)} &= i \begin{pmatrix} -0.002 & 0.001 \\ -0.002 & 0.003 \end{pmatrix} = \mathcal{T}_{\mathbf{R},-\mathbf{R}^{(20)}}^\dagger,\end{aligned}$$

(D.15)

References

- [1] M. Greiter and F. Wilczek, [Annual Review of Condensed Matter Physics](#) **15**, 131 (2024).
- [2] R. Aguado and L. P. Kouwenhoven, [Physics Today](#) **73**, 44 (2020).
- [3] B. Keimer and J. E. Moore, [Nature Physics](#) **13**, 1045 (2017).
- [4] D. N. Basov, R. D. Averitt, and D. Hsieh, [Nature Materials](#) **16**, 1077 (2017).
- [5] Y. Tokura, M. Kawasaki, and N. Nagaosa, [Nature Physics](#) **13**, 1056 (2017).
- [6] D. Aasen, M. Hell, R. V. Mishmash, A. Higginbotham, J. Danon, M. Leijnse, T. S. Jespersen, J. A. Folk, C. M. Marcus, K. Flensberg, and J. Alicea, [Phys. Rev. X](#) **6**, 031016 (2016).
- [7] S. D. Sarma, M. Freedman, and C. Nayak, [npj Quantum Information](#) **1**, 10.1038/npjqi.2015.1 (2015).
- [8] X.-G. Wen, *Quantum Field Theory of Many-Body Systems: From the Origin of Sound to an Origin of Light and Electrons* (Oxford University Press, 2007).
- [9] E. Fradkin, *Field Theories of Condensed Matter Physics*, 2nd ed. (Cambridge University Press, 2013).
- [10] S. Sachdev, *Quantum Phase Transitions*, 2nd ed. (Cambridge University Press, 2011).
- [11] S. Gay and I. Mackie, eds., *Semantic Techniques in Quantum Computation* (Cambridge University Press, 2009).
- [12] C. W. J. Beenakker, [Rev. Mod. Phys.](#) **87**, 1037 (2015).
- [13] A. Rahmani and M. Franz, [Reports on Progress in Physics](#) **82**, 084501 (2019).

-
- [14] S. C. Zhang, T. H. Hansson, and S. Kivelson, *Phys. Rev. Lett.* **62**, 82 (1989).
- [15] V. E. TARASOV, *International Journal of Modern Physics B* **27**, 1330005 (2013).
- [16] C. Chamon, *Phys. Rev. Lett.* **94**, 040402 (2005).
- [17] A. Prem, J. Haah, and R. Nandkishore, *Phys. Rev. B* **95**, 155133 (2017).
- [18] O. Hart, S. Gopalakrishnan, and C. Castelnovo, *Phys. Rev. Lett.* **126**, 227202 (2021).
- [19] K. B. Yogendra, T. Das, and G. Baskaran, *Phys. Rev. B* **108**, 165118 (2023).
- [20] N. Marzari, A. A. Mostofi, J. R. Yates, I. Souza, and D. Vanderbilt, *Rev. Mod. Phys.* **84**, 1419 (2012).
- [21] N. Marzari and D. Vanderbilt, *Phys. Rev. B* **56**, 12847 (1997).
- [22] I. Souza, N. Marzari, and D. Vanderbilt, *Phys. Rev. B* **65**, 035109 (2001).
- [23] D. J. Klein, *The Journal of Chemical Physics* **61**, 786 (1974).
- [24] I. Shavitt and L. T. Redmon, *The Journal of Chemical Physics* **73**, 5711 (1980).
- [25] C. Cohen-Tannoudji, B. Diu, and F. Laloë, *Quantum Mechanics*, A Wiley - Interscience publication No. v. 1 (Wiley, 1977).
- [26] P. W. Anderson, G. Baskaran, Z. Zou, and T. Hsu, *Phys. Rev. Lett.* **58**, 2790 (1987).
- [27] P. Fazekas and P. W. Anderson, *Philosophical Magazine* **30**, 423 (1974).
- [28] J. R. Schrieffer and P. A. Wolff, *Phys. Rev.* **149**, 491 (1966).
- [29] S. Bravyi, D. P. DiVincenzo, and D. Loss, *Annals of Physics* **326**, 2793 (2011).
- [30] G. Giuliani and G. Vignale, *Quantum Theory of the Electron Liquid, Chapter 8.6* (Cambridge University Press, 2005).
- [31] Y. Wu and X. Yang, *Phys. Rev. Lett.* **98**, 013601 (2007).
- [32] R. K. Nesbet, *Rev. Mod. Phys.* **33**, 28 (1961).
- [33] R. L. Stratonovich, *Soviet Physics Doklady* **2**, 416 (1957).
- [34] J. Hubbard, *Phys. Rev. Lett.* **3**, 77 (1959).
- [35] A. Kitaev, *Annals of Physics* **303**, 2 (2003).

- [36] J. B. Kogut, [Rev. Mod. Phys. **51**, 659 \(1979\)](#).
- [37] T. B. Wahl, H.-H. Tu, N. Schuch, and J. I. Cirac, [Phys. Rev. Lett. **111**, 236805 \(2013\)](#).
- [38] J. Haegeman, K. Van Acoleyen, N. Schuch, J. I. Cirac, and F. Verstraete, [Phys. Rev. X **5**, 011024 \(2015\)](#).
- [39] F. J. Wegner, [Journal of Mathematical Physics **12**, 2259 \(1971\)](#).
- [40] A. Kitaev, [Annals of Physics **321**, 2 \(2006\)](#).
- [41] G. Baskaran, S. Mandal, and R. Shankar, [Phys. Rev. Lett. **98**, 247201 \(2007\)](#).
- [42] I. S. Tupitsyn, A. Kitaev, N. V. Prokof'ev, and P. C. E. Stamp, [Phys. Rev. B **82**, 085114 \(2010\)](#).
- [43] Z.-C. Gu and X.-G. Wen, [Phys. Rev. B **90**, 115141 \(2014\)](#).
- [44] N. D. Patel and N. Trivedi, [Proc. Natl. Acad. Sci. U.S.A. **116**, 12199 \(2019\)](#).
- [45] M. Gohlke, R. Moessner, and F. Pollmann, [Phys. Rev. B **98**, 014418 \(2018\)](#).
- [46] Z. Zhu, I. Kimchi, D. N. Sheng, and L. Fu, [Phys. Rev. B **97**, 241110 \(2018\)](#).
- [47] H.-C. Jiang, C.-Y. Wang, B. Huang, and Y.-M. Lu, [arXiv 10.48550/ARXIV.1809.08247 \(2018\)](#).
- [48] C. Hickey and S. Trebst, [Nat. Commun. **10**, 1 \(2019\)](#).
- [49] D. A. S. Kaib, S. M. Winter, and R. Valentí, [Phys. Rev. B **100**, 144445 \(2019\)](#).
- [50] E. S. Sørensen, A. Catuneanu, J. S. Gordon, and H.-Y. Kee, [Phys. Rev. X **11**, 011013 \(2021\)](#).
- [51] R. R. Biswas, [Phys. Rev. Lett. **111**, 136401 \(2013\)](#).
- [52] A. Koga, Y. Murakami, and J. Nasu, [Phys. Rev. B **103**, 214421 \(2021\)](#).
- [53] A. Hashimoto, Y. Murakami, and A. Koga, Majorana gap formation in the anisotropic kitaev model with ordered flux configuration (2023), [arXiv:2303.04295 \[cond-mat.str-el\]](#)
- [54] S.-S. Zhang, Z. Wang, G. B. Halász, and C. D. Batista, [Phys. Rev. Lett. **123**, 057201 \(2019\)](#).

- [55] S. Chulliparambil, L. Janssen, M. Vojta, H.-H. Tu, and U. F. P. Seifert, *Phys. Rev. B* **103**, 075144 (2021).
- [56] D. J. Alspaugh, J.-N. Fuchs, A. Ritz-Zwilling, and J. Vidal, *Phys. Rev. B* **109**, 115107 (2024).
- [57] J. Nasu, J. Yoshitake, and Y. Motome, *Phys. Rev. Lett.* **119**, 127204 (2017).
- [58] D. Otten, A. Roy, and F. Hassler, *Phys. Rev. B* **99**, 035137 (2019).
- [59] K. Feng, N. B. Perkins, and F. J. Burnell, *Phys. Rev. B* **102**, 224402 (2020).
- [60] A. Metavitsiadis and W. Brenig, *Phys. Rev. B* **103**, 195102 (2021).
- [61] G.-Y. Zhu and M. Heyl, *Phys. Rev. Research* **3**, L032069 (2021).
- [62] W.-H. Kao, J. Knolle, G. B. Halász, R. Moessner, and N. B. Perkins, *Phys. Rev. X* **11**, 011034 (2021).
- [63] W.-H. Kao and N. B. Perkins, *Annals of Physics* **435**, 168506 (2021), special issue on Philip W. Anderson.
- [64] R. G. Pereira and R. Egger, *Phys. Rev. Lett.* **125**, 227202 (2020).
- [65] M. Udagawa, S. Takayoshi, and T. Oka, *Phys. Rev. Lett.* **126**, 127201 (2021).
- [66] J. Kang and O. Vafek, *Phys. Rev. X* **8**, 031088 (2018).
- [67] S. Peotta and P. Törmä, *Nature Communications* **6**, 8944 (2015).
- [68] J. Herzog-Arbeitman, V. Peri, F. Schindler, S. D. Huber, and B. A. Bernevig, *Phys. Rev. Lett.* **128**, 087002 (2022).
- [69] L. Zou, H. C. Po, A. Vishwanath, and T. Senthil, *Phys. Rev. B* **98**, 085435 (2018).
- [70] A. Kruchkov, *Phys. Rev. B* **105**, L241102 (2022).
- [71] M. Koshino, N. F. Q. Yuan, T. Koretsune, M. Ochi, K. Kuroki, and L. Fu, *Phys. Rev. X* **8**, 031087 (2018).
- [72] F. Schindler, B. Bradlyn, M. H. Fischer, and T. Neupert, *Phys. Rev. Lett.* **124**, 247001 (2020).
- [73] J.-W. Rhim and B.-J. Yang, *Phys. Rev. B* **99**, 045107 (2019).

- [74] S. M. Zhang and L. Jin, *Phys. Rev. B* **102**, 054301 (2020).
- [75] Y. Onishi and L. Fu, *Physical Review X* **14**, 011052 (2024), [arXiv:2306.00078 \[cond-mat.mes-hall\]](#) .
- [76] A. Bouhon, A. Timmel, and R.-J. Slager, *Quantum geometry beyond projective single bands* (2023), [arXiv:2303.02180 \[cond-mat.mes-hall\]](#) .
- [77] A. A. Mostofi, J. R. Yates, G. Pizzi, Y.-S. Lee, I. Souza, D. Vanderbilt, and N. Marzari, *Computer Physics Communications* **185**, 2309 (2014).
- [78] D. J. Thouless, M. Kohmoto, M. P. Nightingale, and M. den Nijs, *Phys. Rev. Lett.* **49**, 405 (1982).
- [79] A. Kitaev and J. Preskill, *Phys. Rev. Lett.* **96**, 110404 (2006).
- [80] M. Levin and X.-G. Wen, *Phys. Rev. Lett.* **96**, 110405 (2006).
- [81] R. Nehra, D. S. Bhakuni, A. Ramachandran, and A. Sharma, *Phys. Rev. Res.* **2**, 013175 (2020).
- [82] Y. Kuno, *Phys. Rev. B* **101**, 184112 (2020).
- [83] C. Brouder, G. Panati, M. Calandra, C. Mourougane, and N. Marzari, *Phys. Rev. Lett.* **98**, 046402 (2007).
- [84] D. Monaco, G. Panati, A. Pisante, and S. Teufel, *Communications in Mathematical Physics* **359**, 61 (2018).
- [85] S. Peotta and P. Törmä, *Nature Communications* **6**, [10.1038/ncomms9944](#) (2015).
- [86] P. Törmä, S. Peotta, and B. A. Bernevig, *Nature Reviews Physics* **4**, 528 (2022).
- [87] T. Neupert, L. Santos, C. Chamon, and C. Mudry, *Phys. Rev. Lett.* **106**, 236804 (2011).
- [88] E. Tang, J.-W. Mei, and X.-G. Wen, *Phys. Rev. Lett.* **106**, 236802 (2011).
- [89] K. Sun, Z. Gu, H. Katsura, and S. Das Sarma, *Phys. Rev. Lett.* **106**, 236803 (2011).
- [90] T. Neupert, C. Chamon, T. Iadecola, L. H. Santos, and C. Mudry, *Physica Scripta* **2015**, 014005 (2015).
- [91] N. Regnault and B. A. Bernevig, *Phys. Rev. X* **1**, 021014 (2011).

- [92] Z. Liu, E. J. Bergholtz, H. Fan, and A. M. Läuchli, *Phys. Rev. Lett.* **109**, 186805 (2012).
- [93] S. A. Parameswaran, R. Roy, and S. L. Sondhi, *Comptes Rendus Physique* **14**, 816 (2013), topological insulators / Isolants topologiques.
- [94] M. Barkeshli, N. Y. Yao, and C. R. Laumann, *Phys. Rev. Lett.* **115**, 026802 (2015).
- [95] G. Möller and N. R. Cooper, *Phys. Rev. Lett.* **115**, 126401 (2015).
- [96] J. Behrmann, Z. Liu, and E. J. Bergholtz, *Phys. Rev. Lett.* **116**, 216802 (2016).
- [97] C. H. Lee, M. Claassen, and R. Thomale, *Phys. Rev. B* **96**, 165150 (2017).
- [98] Z. Liu and E. J. Bergholtz, in *Encyclopedia of Condensed Matter Physics (Second Edition)*, edited by T. Chakraborty (Academic Press, Oxford, 2024) second edition ed., pp. 515–538.
- [99] G. K. Gupta and T. Das, *Phys. Rev. B* **95**, 161109 (2017).
- [100] R. Roy, *Phys. Rev. B* **90**, 165139 (2014).
- [101] S. H. Simon and M. S. Rudner, *Phys. Rev. B* **102**, 165148 (2020).
- [102] P. J. Ledwith, A. Vishwanath, and D. E. Parker, *Phys. Rev. B* **108**, 205144 (2023).
- [103] S.-S. Zhang, C. D. Batista, and G. B. Halász, *Phys. Rev. Res.* **2**, 023334 (2020).
- [104] S. Elitzur, *Phys. Rev. D* **12**, 3978 (1975).
- [105] S.-H. Jang, Y. Kato, and Y. Motome, *Phys. Rev. B* **104**, 085142 (2021).
- [106] X. Wang, M. Laav, I. Volotsenko, A. Frydman, and B. Kalisky, *Phys. Rev. Appl.* **17**, 024073 (2022).
- [107] T. Senthil, A. Vishwanath, L. Balents, S. Sachdev, and M. P. A. Fisher, *Science* **303**, 1490 (2004).
- [108] T. Senthil, *arXiv e-prints*, arXiv:2306.12638 (2023), arXiv:2306.12638 [cond-mat.str-el]
- [109] M. Kohmoto, *Annals of Physics* **160**, 343 (1985).
- [110] T. Thonhauser and D. Vanderbilt, *Phys. Rev. B* **74**, 235111 (2006).
- [111] A. A. Soluyanov and D. Vanderbilt, *Phys. Rev. B* **83**, 035108 (2011).

- [112] R. Yu, X. L. Qi, A. Bernevig, Z. Fang, and X. Dai, *Phys. Rev. B* **84**, 075119 (2011).
- [113] X.-L. Qi, *Phys. Rev. Lett.* **107**, 126803 (2011).
- [114] T. M. Gunawardana, A. M. Turner, and R. Barnett, *Phys. Rev. Res.* **6**, 023046 (2024).
- [115] F. Xie, Y. Fang, L. Chen, J. Cano, and Q. Si, *arXiv* (2024), arXiv:2407.08920 [cond-mat.mes-hall] .
- [116] G. Strinati, *Phys. Rev. B* **18**, 4104 (1978).
- [117] D. L. Bergman, C. Wu, and L. Balents, *Phys. Rev. B* **78**, 125104 (2008).
- [118] J. Herzog-Arbeitman, V. Peri, F. Schindler, S. D. Huber, and B. A. Bernevig, *Phys. Rev. Lett.* **128**, 087002 (2022).
- [119] S. Flach, D. Leykam, J. D. Bodyfelt, P. Matthies, and A. S. Desyatnikov, *Europhysics Letters* **105**, 30001 (2014).
- [120] J. Dubail and N. Read, *Phys. Rev. B* **92**, 205307 (2015).
- [121] L. Morales-Inostroza and R. A. Vicencio, *Phys. Rev. A* **94**, 043831 (2016).
- [122] W. Maimaiti, A. Andreev, H. C. Park, O. Gendelman, and S. Flach, *Phys. Rev. B* **95**, 115135 (2017).
- [123] N. Read, *Phys. Rev. B* **95**, 115309 (2017).
- [124] S. M. Zhang and L. Jin, *Phys. Rev. B* **102**, 054301 (2020).
- [125] B. Bradlyn, L. Elcoro, J. Cano, M. G. Vergniory, Z. Wang, C. Felser, M. I. Aroyo, and B. A. Bernevig, *Nature* **547**, 298–305 (2017).
- [126] H. C. Po, A. Vishwanath, and H. Watanabe, *Nature Communications* **8** (2017).
- [127] F. Schindler and B. A. Bernevig, *Phys. Rev. B* **104**, L201114 (2021).
- [128] Y.-C. Chen, Y.-P. Lin, and Y.-J. Kao, *Phys. Rev. B* **107**, 075126 (2023).

5

Symmetry, Superposition, and Fragmentation in Classical Spin Models

Classical magnets exhibit exotic ground state properties such as spin liquids and fractionalization, promising a manifestation of superposition and projective symmetry construction in classical theory. While system-specific spin-ice or soft-spin models exist, a formal theory for general classical magnets remains elusive. Here, we introduce a generic symmetry group construction built from a vector field in a plaquette of classical spins, demonstrating how classical spins superpose in irreducible representations (irreps) of the symmetry group. The corresponding probability amplitudes serve as order parameters and local spins as fragmented excitations. The formalism offers a many-body vector field representation of diverse ground states, including spin liquids and fragmented phases described as degenerate ensembles of irreps. We apply the theory to a frustrated square Kagome lattice, where spin-ice or soft spin rules are inapt, to describe spin liquids and fragmented phases, all validated through irreps ensembles and unbiased Monte Carlo simulation. Our generic theory sheds light on previously

unknown aspects of spin-liquid phases and fragmentation and broadens their applications to other branches of field theory.¹

5.1 Introduction

Classical spin models can potentially capture exotic phenomena like spin liquid [1–6], spin ice [7–9], and fragmentation [2, 10–13], order by disorder [14–19], prethermal discrete time crystals[20], and exciting progress lies in designing novel and generic frameworks [6, 21–29]. While quantum theory allows the ground state of a spin liquid to be a superposition state, this concept does not have a classical analog. Classically, two main approaches so far describe the spin liquid phase. The spin-ice model applies to specific spin Hamiltonians that can be expressed in terms of $|\mathbf{S}_c|^2$, where \mathbf{S}_c is the total spin in a cluster, such that the $\mathbf{S}_c = 0$ configuration describes degenerate ground states.[2, 6, 11, 23, 24] However, this rule doesn't hold for models with Dzyaloshinskii-Moriya (DM) interactions. Recently, a Luttinger-Tisza approximation, also known as the spherical or soft-spin approximation, has been employed to analyze the degenerate energy state in momentum space in terms of extended states of classical spin.[23–27] A flat band in this model indicates the degeneracy characteristic of spin liquids. The drawback of this model is that it relaxes the local $|\mathbf{S}_i| = 1$ constraint, imposing it at the global spin value. Both approaches are suited for specific Hamiltonians and have so far been applied only to spin-ice models.

Magnetic fragmentation is another exotic phenomenon in the classical spin systems that draws recent attention.[10–13, 30, 31] In this phase, a local classical field (such as spin or magnetization) fragments into components with one (or more) components exhibiting order while others remain disordered or liquid-like. This phenomenon has so far been studied using Landau's coarse-grained magnetization fields, with or without local spin constraints. Despite progress in understanding specific models with ground state degeneracy or fragmentation, a comprehensive analytical framework, which would ideally encompass all lattice symmetries, frustration, DM interactions, local spin constraints, and hence do not necessarily follow the spin-ice rule, remains elusive.

Research on frustrated lattices, like pyrochlore,[6, 32–35] triangular,[36–38] Kagome,[39–41] and others[4, 15, 18, 42] has been a major focus in exploring spin liquids and related phenomena. Recently, the square Kagome lattice has sparked excitement due to experimental hints of spin liquid phases[43–45] and supporting theoretical investigations [46–50]. However,

¹This chapter is a reproduction of our published work on 'Symmetry, Superposition and Fragmentation in Classical Spin Liquids: A General Framework and Applications to Square Kagome Magnets' with reference [Phys. Rev. B 110, L060401 \(2024\)](#).

these materials likely possess a strong DM interaction[43–45] which the spin-ice and soft-spin models do not incorporate. Additionally, the square Kagome lattice boasts multiple sublattices, offering a richer platform with potentially larger degenerate manifolds and more fragmentation possibilities.

Here, we introduce a generic framework for studying ground state degeneracy and fragmentation in classical spin systems using a group theory approach. We apply this theory to a two-dimensional square Kagome lattice. Our approach transcends a prior approach[35, 41], used primarily for ordered phases, to encompass spin liquids and fragmented phases. We define a vector space representing the spins within a lattice plaquette, designed to be invariant under the lattice’s point-group symmetry. The plaquette spin vector can be expressed as a superposition of the irreducible representations (irreps) of the symmetry group. The expansion parameters of this superposition vector act as Landau-like order parameters. However, unlike traditional order parameters, they transform under ‘discrete’ spatial rotations and acquire continuous symmetry through degeneracy and irreps multiplets. Interestingly, these order parameters serve as spin’s ‘probability amplitudes’ and ‘occupation densities’ to irreps state and energy levels, respectively. This approach, with its resemblance to quantum concepts, paves the way for a novel construction of classical spin liquids and fragmentation states.

We apply the theory to a model consisting of XXZ and DM interactions in a 2D square Kagome lattice. We also employ unbiased classical Monte Carlo (MC) simulation to validate our group theory approach and reproduce the phase diagram. We find that DM interaction promotes a uniform or staggered ordering of specific irrep, containing vortex or anti-vortex. Near the critical boundaries between these ordered phases, we observe the emergence of classical spin liquid (CSL) states. Within the CSL phase, local spins remain fully disordered if the ground state consists of a randomly distributed irrep ensemble. Alternatively, the ground state can scramble ordered and disordered irreps to fragment the local spin vector into coexisting extended/collective and point-like excitations. Additionally, the spin-spin correlation function is analyzed in each phase to distinguish between magnetic Bragg peaks for the collective excitations in the ordered phase and the ‘pinch-point’ excitations in the liquid phases.

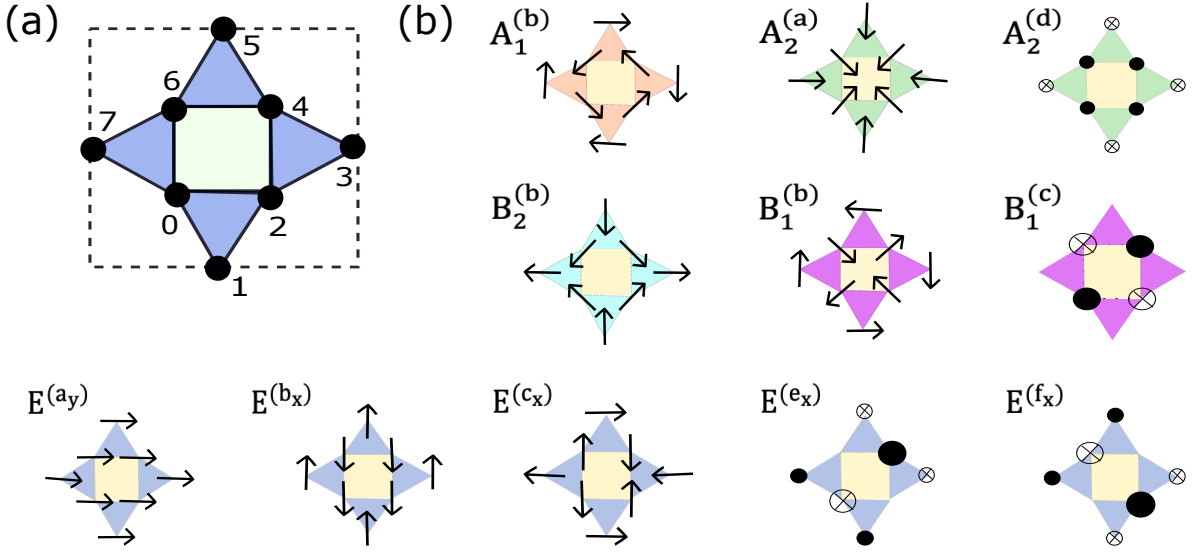


Fig. 5.1 (a) A plaquette of a 2D square-Kagome lattice, belonging to the D_4 group, is shown with sublattices enumerated as $i = 0 - 7$. (b) Among five irreps with different multiplets, we show a few representative irreps here, while others are shown in *SM*[51]. Each irrep consists of either S_i^\perp (horizontal arrow) or S_i^z (open and filled dots for up and down spins) components, with the sizes of the arrows or dots dictate their magnitudes.

5.2 Mathematical foundation:

We define a local vector field in a plaquette network p to be invariant under the lattice's point-group symmetry G :

$$\mathcal{S}_p = \bigoplus_{i \in p} S_i. \quad (5.1)$$

$S_i = (S_i^x \ S_i^y \ S_i^z)^T \in O_i(3)$ at the i^{th} site, and $\mathcal{S}_p \in O_p(3n)$ where n is the number of sublattices in p . ($O_i(n)$, $O_p(n)$ distinguish the orthogonal symmetry of the vector at the i -site and p -plaquette, respectively). Each plaquette, like a conventional unit cell, includes redundant sites than the primitive unit cell. This is adjusted by introducing a normalization factor in the dual vector definition to fix the length of \mathcal{S}_p . [52]

The transformation from the spin space to the irreps space of group G involves an orthogonal matrix, whose column vectors \mathcal{V}_α form the orthonormal basis of the irreps representation. Expressing \mathcal{S}_p in this irreps space yields

$$\mathcal{S}_p = \sum_{\alpha=1}^{3n} m_\alpha \mathcal{V}_\alpha. \quad (5.2)$$

Here $m_\alpha \in \mathbb{R}$ is the coefficient of the expansions. We keep the plaquette index in m and \mathcal{V} implicit for simplicity in notation. Interestingly, m_α conforms to Landau's order parameter as the coarse-grain average of local fields, except, here, it is invariant under a discrete symmetry group in a plaquette and is interpreted as the probability amplitude of vector field: $m_\alpha = \mathcal{V}_\alpha^\top \mathcal{S}_p$. [52] The local spins are defined by a rectangular projection matrix $\mathcal{P}_{i \in p}$ as $\mathbf{S}_{i \in p} = \mathcal{P}_{i \in p} \mathcal{S}_p = \sum_\alpha m_\alpha \mathcal{P}_{i \in p} \mathcal{V}_\alpha$.

Reformulating the order parameters in terms of the irreps conveniently decouples them in a symmetry invariant Hamiltonian, albeit the irreps' multiples can mix among themselves. To account for the multiplets' submanifold and emergent symmetry, it is convenient to introduce an $O_p(d_\alpha)$ 'spinor'-like field $m_\alpha := (m_\alpha^{(1)} \dots m_\alpha^{(d_\alpha)})^T$ for the α irrep with d_α multiplet. Then, the eigenmodes are obtained by orthogonal rotation $\tilde{m}_\alpha = e^{i\mathcal{L}_\alpha \cdot \phi_\alpha} m_\alpha$, where \mathcal{L}_α are the corresponding generators for the angle ϕ_α . ϕ_α lives on the Hamiltonian's parameter space and assumes fixed values for the energy eigenmodes. The orthonormal basis states ensure the constraint $|\mathcal{S}_p|^2 = \mathcal{S}_p^\top \mathcal{S}_p = \sum_\alpha d_\alpha |m_\alpha|^2 = nS^2$, $\forall p$, where $|S_i| = S$, $\forall i$ is an additional hardcore constraint on the classical spins [52]. Not all irreps necessarily adhere to the local constraint, requiring them to collaborate with others for existence. Such irreps ensembles may lead to non-analyticity and fragmentation into an order-disorder mixed phase. Additionally, the collapse of the eigenmodes \tilde{m}_α into its constituent irrep m_α causes distinct fragmented excitation.

We have a $3nN$ -dimensional vector space $\mathcal{S} = \bigoplus_p' \mathcal{S}_p$ for a generic N -unit cell lattice, commencing a $3nN \times 3nN$ -matrix valued quadratic-in-spin Hamiltonian (see SM [51] for further details. Lets call this Direct Sum as constrained direct sum with a prime sign over it. While a Direct Sum means different sectors are decoupled, but the definition of the constrained sum is that different sectors are related by the local constraint on the spin shared between the different plaquettes. This introduces a new type of frustration as well as correlation.). However, thanks to nearest-neighbor interaction and discrete-translation-invariance of the lattice, the Hamiltonian can be brought to a block-diagonal form in terms of the plaquette Hamiltonian H_p :

$$H_p = \frac{1}{2} \mathcal{S}_p^\top \mathcal{H}_p \mathcal{S}_p. \quad (5.3)$$

Here \mathcal{H}_p is an orthogonal matrix-valued Hamiltonian, analogous to the second quantized Hamiltonian, whose components consist of all possible interactions between \mathbf{S}_i and \mathbf{S}_j for $\langle ij \rangle \in p$. However, lattice symmetries restrict the allowed finite components in \mathcal{H}_p , which we now consider for a square kagome lattice.

5.2.1 Realizations in a square-Kagome lattice

The square-Kagome lattice belongs to the Dihedral (D_4) group with $n = 8$ sublattice spins, giving a 24-dimensional vector representation. Denoting the group element $g \in D_4$ in the \mathcal{S}_p -representation by the matrix-valued operators $\mathcal{D}(g)$, we impose the symmetry criterion that under a local symmetry transformation $\mathcal{S}_p \rightarrow \mathcal{D}(g)\mathcal{S}_p$, the local Hamiltonian H_p is invariant if $[\mathcal{D}(g), \mathcal{H}_p] = 0, \forall p, g$. Since local $O_i(3)$ and sublattice symmetries are abandoned, the plaquette symmetry allows us to have bond- and spin-dependent interactions $J_{ij}^{\mu\nu}$ with six exchange and three DM interactions (see *SM* for the details), leading to a bond-dependent XYZ-Heisenberg model with XY-DM interaction. However, imposing bond-independent interactions, we consider an XXZ model with DM interaction as more appropriate for realistic materials [43–45], $H = \sum_{\langle ij \rangle, \mu\nu} J^{\mu\nu} S_i^\mu S_j^\nu$. This can, for future convenience, be expressed as:

$$H = J \sum_{\langle ij \rangle, \tau=\pm} \left(D^\tau e^{i\tau(\Theta_i + \Theta_j)} S_i^\perp S_j^\perp + \Delta S_i^z S_j^z \right). \quad (5.4)$$

Here $J^{\mu\nu} = J\delta_{\mu\nu} + JD\varepsilon_{\mu\nu}$ for $\mu = x, y$, and $J^{zz} = J\Delta$, $\delta_{\mu\nu}$ is the Kronecker delta and $\varepsilon_{\mu\nu}$ is the Levi-Civita tensor. J is the exchange term, Δ is the z -axis anisotropy ratio, and JD is the XY DM interaction strength. By diagonalizing the tensor $J^{\mu\nu}$, we define two ‘circularly polarized’ fields: $S_i^\tau = |S_i^\perp| e^{i\tau\Theta_i} \in O_i(2) \cong U_i(1)$, where $S_i^\perp = \sqrt{S^2 - (S_i^z)^2}$ is the coplanar spin magnitude and Θ_i is the azimuthal angle in the spin space, which interact via a complex (dimensionless) interaction $D^\tau = 1 + i\tau D$.

5.2.2 Irreps in square-Kagome lattice

There are five conjugacy classes in this non-Abelian group, giving five irreps: $m_\alpha \equiv A_{1,2}^{(d_\alpha)}$, $B_{1,2}^{(d_\alpha)}$, and one two-dimensional irrep $E^{(d_\alpha)}$, where the superscript denotes their multiplicity $(d_\alpha) = (2, 4, 3, 3, 6)$, respectively. Representative irreps configurations are shown in Fig. 5.1(b). We organize these irreps into a coplanar set $m_\perp := \{A_{1,2}^{(a,b)}, B_{1,2}^{(a,b)}, E^{(a_{x,x}, b_{x,y}, c_{x,y}, d_{x,y})}\}$, and an out-of-plane/colinear set $m_\parallel := \{A_2^{(c,d)}, B_{1,2}^{(c)}, E^{(e_{x,y}, f_{x,y})}\}$.

In the coplanar irreps basis $A_{1,2}^{(a,b)}, B_{1,2}^{(a,b)}$, even/odd under C_4 , the local spins S_i^τ are arranged in a topological texture following $\Theta_{i \in p} = Q_p \theta_i + \gamma_p$, where Θ_i and θ_i are the azimuthal angles in the spin and position manifolds, respectively. $\gamma_p \in [0, \pi)$ is the helicity angle, and $Q_p \in \pi_1(\mathbb{S}^1) \cong \mathbb{Z}$ is the topological charge. As shown in Fig. 5.1(b), this leads to (anti-) vortices for $A_{1,2}^{(a,b)}, B_{1,2}^{(a,b)}$ irreps. In fact, each (anti-) vortex consists of two concentric (anti-) vortices in the outer and inner squares, which are not related by symmetry but interact with each other by the interaction term D^τ . $A_1^{(a,b)}$ consist of concentric vortices with the same/opposite

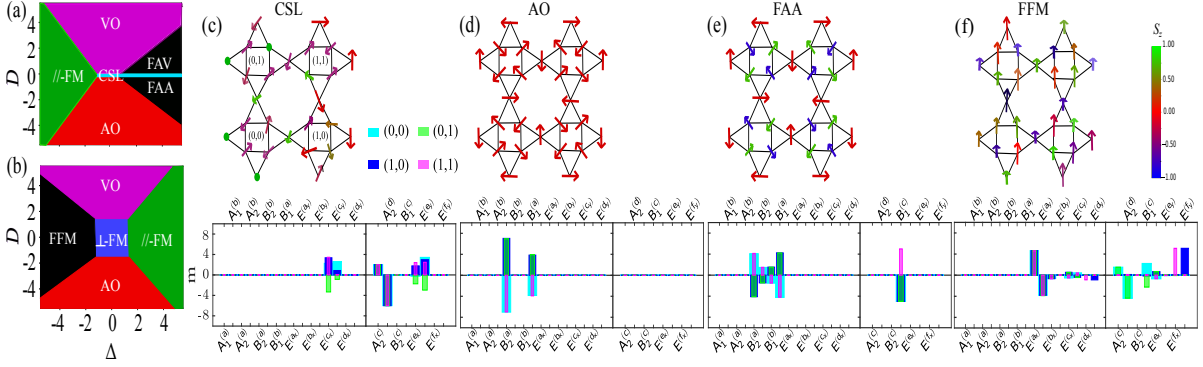


Fig. 5.2 Computed phase diagrams within the MC simulation (also group theory analysis) are shown for (a) for AFM ($J = +1$) and (b) for the FM ($J = -1$) couplings. We highlight spin textures in a randomly chosen four-plaquette setting for representative phases (upper panel) and respective ensembles of irreps in four plaquettes (lower panel). (c) CSL at $(J, \Delta, D) = (1, 1, 0)$ showing disordered values of m_v from both in-plane and out-of-plane ensembles. (d) AO at $(1, 0, -3)$ with degenerate irreps $B_{1,2}^{(a)}$ are staggered. (e) FAA phase at $(1, 4, -1)$ where $B_{1,2}^{(a)}$ being ordered but $B_1^{(c)}$ is disordered. (f) FFM phase at $(-1, -2.5, 0)$ where 2D irrep $E^{(a)}$ is ferromagnetically ordered in-plane, but out-of-plane irreps are disordered. Note that all disordered values take random numbers between different plaquettes, while we display only four representative plaquettes here.

helicities ($\gamma_p = \pm\pi/2$), while $A_2^{(a,b)}$, odd under reflection, have $\gamma_p = \pm\pi$. $B_{1,2}^{(a,b)}$ irreps (odd under C_4) are similar, except they contain anti-vortices. The out-of-plane $A_2^{(c,d)}$ are colinear FM/AFM irreps, while $B_{1,2}^{(c)}$ are colinear AFM irreps. Finally, among the six-fold multiplets of 2D E irreps, $E^{(a-d)}$ are coplaner FM/ nematic/AFM order parameters, while $E^{(e,f)}$ are colinear irreps. Notably, the colinear irreps $B_{1,2}^{(c)}$ and $E^{(e,f)}$ violate the local constraints, and hence their low-energy configurations vitiate any long-range order.

5.2.3 Eigen energies:

The final task is to diagonalize the multiples of the irreps. In our case, the irreps' multiplets split as either $O_p(d_\alpha) = O_p(2) \oplus O_p(2) \oplus \dots$, or $O_p(d_\alpha) = O_p(2) \oplus Z_2 \oplus \dots$, in which all $O_p(2)$ operators have the same generator $\mathcal{L}_\alpha = i\sigma_y$. ϕ_α depends only on $\arg(D^\tau)$ in the eigenstates of \mathcal{H}_p . The resultant diagonal Hamiltonian per plaquette is

$$H_p = \sum_{v=1}^{3n} E_v |\tilde{\mathbf{m}}_v|^2. \quad (5.5)$$

Phase	Acronym	Irreps $\{v_p\}$	Parameters	Color code
Classical Spin Liquid	CSL	$m_{\perp} \cup m_{\parallel}$	$J = 1, \Delta > 0, D = 0$	Cyan
Vortex Order	VO	$\bar{A}_{1,2}^{(a)}$	$J = 1, \Delta < 2D, D > 0$	Magenta
Anti-vortex Order	AO	$\bar{B}_{1,2}^{(a)}$	$J = 1, \Delta < 2D, D < 0$	Red
Fragmented AFM-vortex	FAV	$\bar{A}_{1,2}^{(a)} \cup B_1^{(c)}$	$J = 1, \Delta > 2D, D > 0$	Black
Fragmented AFM-Anti-vortex	FAA	$\bar{B}_{1,2}^{(a)} \cup B_1^{(c)}$	$J = 1, \Delta > 2D, D < 0$	Black
Fragmented Ferromagnet	FFM	$\bar{E}^{(a)} \cup m_{\parallel}$	$J = -1, \Delta > 2 D , \pm D$	Black
Collinear Ferromagnet Order	-FM	$\bar{A}_2^{(c)}$	$\Delta J < 0, \Delta > 2 D $	Green
Coplanar Ferromagnet Order	\perp -FM	$\bar{E}^{(a)}$	$J = -1, \Delta < 2 D $	Blue

Table 5.1 We tabulate all the phases and the contributing irreps obtained consistently with the MC simulation and the group theory analysis. The irrep with a bar in the third column reflects it to be ordered; otherwise, it's a disorder irrep.

Here $|\tilde{\mathbf{m}}_v|^2$ serves as ‘occupation density’ to the v^{th} energy level E_v . Henceforth, we omit the tilde symbol for simplicity, and all irreps are considered eigenmodes unless mentioned otherwise. The functional form of E_v in terms of J, D , and Δ is given in the SM[51]. Constrained by symmetry, $E_{v \in m_{\perp}}$ depends solely on D^{τ} , while $E_{v \in m_{\parallel}}$ is proportional to Δ^2 . One or more irrep (s) can form an ordered phase with a global energy minimum at NE_v if they satisfy the constraint and frustration; otherwise, they blend with other irreps to form a degenerate ensemble, giving disorder, liquid, and mixed phases. A zero-temperature phase transition occurs at the $E_v = 0$ line.

5.3 Phase diagrams and correlation functions

We solve the Hamiltonian in Eq. (5.4) both numerically using classical MC simulations and the group theory analysis. The details of the MC simulation are given in the SM[51]. The corresponding phase diagram is summarized in Table 1 and shown in Fig. 5.2. Note that the same phase diagram is also reproduced by the lowest energy eigenvalue E_v , and the values of m_v are obtained from the MC result as shown in the lower panel in Fig. (5.2) agrees with the group theory result.

²Specifically, the (anti-) vortex irreps $B_{1,2}^{(a,b)}, A_{1,2}^{(a,b)}$ are promoted by $\mp D$, while $E^{(a,b)}$ do not depend on D .

Remarkably, we find that all the phases can be understood in terms of an analytical definition of the many-body ground state vector field as:

$$\mathcal{S}_{\text{GS}} = \bigoplus_p \sum_{\{\mathbf{v}_p\}} m_{\mathbf{v}_p} \mathcal{V}_{\mathbf{v}_p}. \quad (5.6)$$

The ordered phase harbors a summated state of a fixed irrep $\bar{\mathbf{v}} \in \{\mathbf{v}_p\}$ (with $m_{\bar{\mathbf{v}}} = \bar{m}$, $m_{\mathbf{v} \neq \bar{\mathbf{v}}} = 0$, $\forall p$); while the staggered phase features two alternating but fixed irreps $\bar{\mathbf{v}}_p$ and $\bar{\mathbf{v}}_q$ in neighboring plaquettes. The CSL state, on the other hand, combines an ensemble of irreps $\{\mathbf{v}_p\}$ within each plaquette p . Within this ensemble, the probability amplitude $m_{\mathbf{v}_p}$ may vary randomly, subject to local constraints, corresponding to the same plaquette energy. The random distribution of $m_{\mathbf{v}_p}$ differs between plaquettes, resulting in an extensively degenerate ground state.

In addition, we also compare our results with a soft-spin approximation in the Fourier space [4, 6, 34, 53–55], and the resulting dispersion relation is shown in *SM*[51]. Given that we have experimental access to the correlation function of local spins $\mathbf{S}_{i \in p}$, we report its correlation function. We project the structure factor $\chi(\mathbf{k}) = 1/\mathcal{N} \sum_{i,j} \langle \mathbf{S}_i \cdot \mathbf{S}_j \rangle \exp\{i(\mathbf{k} \cdot (\mathbf{r}_i - \mathbf{r}_j))\}$ to the irreps space as

$$\langle \mathbf{S}_i \cdot \mathbf{S}_j \rangle = \sum_{\mathbf{v}_p \mathbf{v}_q} m_{\mathbf{v}_p} m_{\mathbf{v}_q} \langle \mathcal{V}_{\mathbf{v}_p}^T \mathcal{P}_i^T \mathcal{P}_j \mathcal{V}_{\mathbf{v}_q} \rangle, \quad (5.7)$$

with \mathbf{r}_i is the i^{th} spin's position in p and $j \in q$ plaquette.

The phase diagram in Fig. 5.2 reveals a predominance of (uniform or staggered) order phases in both $J < 0$ (frustration inactive) and $J > 0$ (frustration active) regions. A CSL phase emerges only at the critical line of $D \rightarrow 0$, which turns into distinct mixed/fragmented phases for $2|D|/\Delta < 1$. For $D \rightarrow 0$, $J > 0$, three distinct CSL phases emerge with increasing Δ in Fig. 5.2(a) (cyan color). As $\Delta \rightarrow 0$, we have an XX model in Eq. (5.4), and the contributing irreps arise from the degenerate manifold of the coplanar irrep ensemble $\{m_{\mathbf{v}_p}\} \subseteq \mathfrak{m}_{\perp}$. This gives a CSL phase of $S_i^{\tau} \in O_i(2)$ spins. The structure factor $\chi(\mathbf{k})$ displays a characteristic disorder pattern without any magnetic Bragg peak but with a prominent pinch-point around $\mathbf{k} = (\pm\pi, \pm3\pi)$. The pinch-point characterizes an algebraic correlation between the topological charges. At $\Delta = 1$, the Hamiltonian is subject to a full $O_i(3)$ symmetry constraint per site, resulting in symmetry-allowed access to the entire ensemble $\{m_{\mathbf{v}_p}\} \subseteq \mathfrak{m}_{\perp} \cup \mathfrak{m}_{\parallel}$. For example, $\{m_{\mathbf{v}}\} \in \{m_{\mathbf{A}_{1,2}^{(a,b,c,d)}}, m_{\mathbf{B}_{1,2}^{(a,b)}}\}$ are degenerate at $E_{\mathbf{v}} = -2J$ and $\{m_{\mathbf{v}'}\} \in \{m_{\mathbf{B}_{1,2}^{(c)}}, m_{\mathbf{E}^{(c,d)}}\}$ at $E_{\mathbf{v}'} = -4J$, making a larger CSL ensemble degenerate at energy $E_p = m_{\mathbf{v}}^2 E_{\mathbf{v}} + m_{\mathbf{v}'}^2 E_{\mathbf{v}'} = -4J$ for $m_{\mathbf{v}} = \sqrt{2} m_{\mathbf{v}'}$. Consequently, $\chi(\mathbf{k})$ displays pinch-point correlations among both S_i^{τ} and S_i^z . Finally, as $\Delta \rightarrow \infty$, the Hamiltonian (last term in Eq. (5.4)) retains a residual local Z_2 symmetry

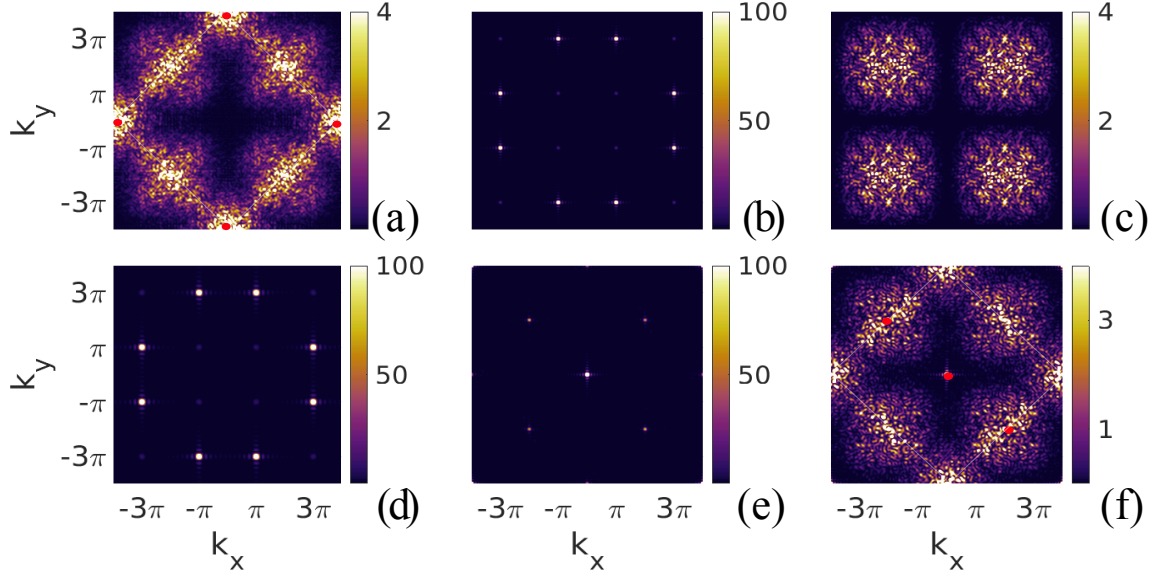


Fig. 5.3 Simulated $\chi(\mathbf{k})$ is plotted in the momentum space for the four phases discussed in Fig. 2. (a) CSL at $(J, \Delta, D) = (1, 1, 0)$, where red dots are plotted separately to signify additional strong magnetic Bragg-like peaks that overwhelm the spectral density of the disordered pattern. (b-c) FFA at $(1, 4, -1)$ where the plots for the ordered S_i^\perp and disordered S_i^z components are separated in (b) and (c), respectively. (d) AO at $(1, 0, -3)$ showing Bragg peaks similar to S_i^\perp components in (b). (e-f) FFM phase at $(-1, -2.5, 0)$ with FM ordered S_i^\perp and disorder S_i^z are separated in (e) and (f). Panels (a) and (f) host pinch-points around $(\pi, 3\pi)$ and its equivalent points.

constraint, and the disorder ground state solely stems from the $\{m_{v_p}\} \in m_{||}$ ensemble. $\chi(\mathbf{k})$ is contributed solely by S_i^z with pinch-points at $\mathbf{k} = (\pm\pi, \pm 3\pi)$. Based on their distinct local constraints, it is convenient to refer to these phases as $O(2)$, $O(3)$, and Z_2 CSLs, respectively, without implying a Landau-type phase boundary between them.

Any finite D steers the CSL phase into either order or fragmented (mixed) phases. Note that vortex irreps $A_1^{(a,b)}$ and $A_2^{(a,b)}$ are degenerate at $E_v = 2D \pm 2\sqrt{D^2 + (1+D)^2}$, while the anti-vortex irreps $B_1^{(a,b)}$ and $B_2^{(a,b)}$ are degenerate at $E_v = -2D \pm 2\sqrt{D^2 + (1-D)^2}$. This makes all the phases in Fig. 5.2(a),(b) symmetric for $D \leftrightarrow -D$ with vortices \leftrightarrow anti-vortices. Hence, we mainly focus on the $-D$ region with anti-vortices for the discussions.

For weak out-of-plane anisotropy $\Delta < 2|D|$, we have ordered phases of (anti-)vortices for $\mp D$, which we call (Anti-)Vortex Order (AO/VO) phases (red/magenta regions in Fig. 5.2). In AO phase, the degenerate irreps $B_{1,2}^{(a)}$ are mixed in an $O(2)$ order parameter and are staggered between the neighboring plaquettes with a $\gamma_p = \pi$ phase shift. The extracted values of the order parameter m from the MC data confirm the only finite and uniform weight of the $\bar{m}_{B_{1,2}^{(a)}}$ irreps in

the AO phase, as shown in Fig. 5.2(d) (lower panel). Interestingly, the CSL lies at the phase transition line between the VO and AO phases. The ordering is also evident in $\chi(\mathbf{k})$ with a magnetic Bragg peak at $\mathbf{k} = (\pi, \pi)$.

However, for strong $\Delta > 2|D|$ (with AFM anisotropy $J\Delta > 0$), the coplanar ordered irreps become scrambled with disordered out-of-plane irreps: $\{m_{v_p}\}_{\text{mix}} \subseteq \bar{m}_{A/B} \cup m_{||}$, in black region Fig. 5.2(a). In particular, the outer (anti-) vortex maintains co-planarity, while the inner (anti-) vortex mixes with the $m_{B_1^{(c)}} \in m_{||}$ irrep. The combination produces a novel *AFM-vortex/AFM-anti-vortex* texture within the inner square where neighboring spins possess opposite easy axes³. Consequently, \mathbf{S}_i spin fragments into its S_i^z components become non-interacting and fail to order or exhibit any significant correlation, while the S_i^x fields exhibit long-range order with magnetic Bragg peaks in the structure factor, see Figs. 5.3(b,c). We denote these phases as fragmented AFM-vortex (FAV) and fragmented AFM-Anti-vortex (FAA) for $\pm D$ regions and confirm the same the extracted values of m_v from the MC result.

For strong $\Delta > 2|D|$ with FM anisotropy $\Delta < 0$ and $J > 0$ naturally select colinear FM order of the $A_2^{(c)}$ irrep (green region Fig. 5.2(a)). We denote this phase as $||$ -FM. The same phase reemerges for $\Delta > 0$ and $J < 0$ in Fig. 5.2(b).

The interplay between the FM interaction, $J = -1$, and strong AFM anisotropy $\Delta > 2|D|$ generates a distinct fragmented phase, see Fig. 5.1(b) (black region). The extracted values of m from the MC data show that the in-plane FM 2D irrep $\bar{m}_{E^{(a)}}$ is ordered while the out-of-plane AFM irreps $\in m_{||}$ are disordered, see Fig. 5.1(f). These out-of-plane irreps violate the local constraint, leading to an intriguing fragmented structure in $\chi(\mathbf{k})$, resulting in an in-plane FM order in S_i^x , but a pinch-point disorder in S_i^z , see Fig. 5.3(e-f). We dub this a Fragmented FM (FFM) phase.

Any finite D disfavors this mixed phase, causing a phase transition at $D > 2\Delta$ to in-plane VO or AO orders for $\pm D$, as observed in the $J = 1$ phase diagram. The remaining two phases are readily identifiable: a uniform coplanar FM (namely, \perp -FM) order with $\bar{m}_{E^{(a)}}$ irrep at $\Delta \rightarrow 0$ (blue region in Fig. 5.2(b)), and an out-of-plane $||$ -FM order with $\bar{m}_{A_2^{(c)}}$ for $J\Delta \rightarrow \infty$ (green region in Fig. 5.2(b)).

5.4 Conclusions and outlook

Discussions on their excitations and phase transition are merited. The VO/AO order phases (red and magenta) exhibit novel collective excitations. Gapless collective excitations emerge from the long-wavelength fluctuation of the helicity angle γ_p across the lattice, protected by

³This AFM-vortex topology is homotopically distinct from the known AFM skyrmion[56], and has not been predicted previously

the topology of the irreps space through the charge $Q_p \in \mathbb{Z}$. These modes, termed helicity phase modes or phasons, possess novel characteristics. The two concentric vortices per plaquette are coupled by interaction but not symmetry. Frustration affects only the outer vortex, resulting in the fragmentation of the excitation spectrum into a collective mode for the ordered fields and local excitations for the disordered components. The Mermin-Wagner theorem dictates the instability of ordered states to gapless magnons or phason modes, while disorder phases tend to order via thermal fluctuations according to the order-by-disorder paradigm [14, 16–18]. Moreover, the VO/AO phases for $\pm D$ consist of different irreps, i.e., distinct conjugacy classes, that do not couple in the Hamiltonian. Hence, their phase boundary at $D = 0$ signifies a topological phase transition associated with a spin liquid phase at the critical point, reminiscence of the deconfined critical point [57]. The CSL critical point can be extended by applying a magnetic field in the z -direction (see *SM*[51]). Finally, transitions between ordered and fragmented phases, or within fragmented phases, offer intriguing avenues for studying non-Landau-type phase transitions.

E

Appendices for chapter 5

E.1 Detailed derivation of the Symmetry properties

Here, we provide further details of the relevant mathematical constructions that are used in the main text. We start with a system of \mathcal{N} spins. Much like how one starts in the quantum case with a direct product state basis to construct exotic entangled states, here we can also start with a many-body $3\mathcal{N}$ -dimensional vector field as a direct sum basis: $\mathcal{S} = \oplus_i^{\mathcal{N}} \mathbf{S}_i$, where $\mathbf{S}_{i=1} \in O(3)$. Then, the most general two-spin interaction Hamiltonian is written as $H = \mathcal{S}^T \mathcal{H} \mathcal{S}$, where \mathcal{H} is the $3\mathcal{N} \times 3\mathcal{N}$ matrix-valued Hamiltonian. Short-range interaction and (discrete) translational symmetry drastically simplifies this Hamiltonian, giving a block-diagonal one.

We assume that there exists a (conventional) unit cell with sublattices that are invariant under a point group symmetry G . The spins sitting at the cell coordinates interact with the spins from the neighboring cells. This interaction term is translated back to a periodically equivalent interaction between the spins within the cell. This allows us to define a plaquette containing n sublattices (counting the sites fully that are shared with the neighboring cells, and hence, the number of sublattices in a plaquette is larger than that in the primitive cell). In this prescription, the Hamiltonian \mathcal{H} becomes block diagonal into a $3n \times 3n$ plaquette Hamiltonian \mathcal{H}_p , and the many-body spin vector field splits as $\mathcal{S} = \oplus_{p=1}^{N=\mathcal{N}/n} \mathcal{S}_p$, where \mathcal{S}_p the vector field in the plaquette.

Here, we focus on the square Kagome lattice, which has $n = 8$ sites in a plaquette, giving a 24-dimensional reducible representation \mathcal{S}_p , as shown in Fig.1 (a), while the primitive unit cell has 6 spins. Therefore, the 'completeness' property of the plaquette spin turns out to be $\sum_{p=1}^N \mathcal{S}_p^T \mathcal{S}_p = 8N$, whereas $\mathcal{N} = 6N$ is the total number of spin in the lattice of N unit cell. To deal with this, we introduce a local weight factor η_p in the definition of the dual vector, say, $\mathcal{S}_p^T = \mathcal{S}_p^T \eta_p$, where T corresponds to the transpose operator. Then, the length of the vector is defined as $\mathcal{S}_p^T \mathcal{S}_{p'} = \mathcal{S}_p^T \eta_p \mathcal{S}_{p'} = \eta_p \delta_{pp'}$. We approximate $\eta_p = 6/8\mathcal{I}$ in each plaquette. The Monte Carlo result confirms that the obtained order parameters for phase phases are scaled with the group theory result by $6/8$.

Our first job is to find the irreducible representation of the Dihedral group D_4 group in this vector field representation. The group elements are denoted by $D_4 = \{e, C_4, C_4^2, C_4^3, \sigma_v^x, \sigma_v^y = C_4^{-1} \sigma_v^x C_4, \sigma_v^{xy}, \sigma_v^{yx} = C_4^{-1} \sigma_v^{xy} C_4\}$, where C_4 is the four-fold rotation, σ_v are the reflection with respect to the verticle plane passing through the x, y - axis, or diagonal (xy/yx), as shown in Fig. 1(a). In this \mathcal{S}_p -representation, we can split each of the D_4 group elements as successive transformations on how the onsite spin $\mathbf{S}_i \in O(3)$ undergoes an internal spin rotation, followed by how each component $S_{i=1-8}^\mu$ of the 8 sublattices reorders in the plaquette vector \mathcal{S}_p . Noticeably further, the inner and outer squares of the square kagome lattice are decoupled from each other in terms of the D_4 symmetries and give a trivial transformation between the two concentric squares of four sublattices. In what follows, if we denote the \mathcal{S}_p -representation of the group elements $g \in D_4$ as $\mathcal{D}(g)$, then it can be decomposed into a direct product of three symmetries: $\mathcal{D}(g) = \mathcal{R}_I(g) \otimes \mathcal{R}_L(g) \otimes \mathcal{R}_S(g)$, where $\mathcal{R}_S(g)$ are the 3×3 rotational matrices of the local $O_i(3)$ spin, $\mathcal{R}_L(g)$ are the 4×4 rotational matrices of the four sublattices, and $\mathcal{R}_I(g)$ is the 2×2 transformation between the inner and outer squares.

$$\begin{aligned}
\mathcal{D}(C_4) &= \left[\tau_0 \otimes \mathcal{R}_L^{(1)}(C_4) + \tau_x \otimes \mathcal{R}_L^{(2)}(C_4) \right] \otimes \mathcal{R}_S(C_4), \\
\mathcal{D}(C_4^2) &= \tau_x \otimes \mathcal{I}_{4 \times 4} \otimes \mathcal{R}_S(C_4^2), \\
\mathcal{D}(C_4^3) &= \left[\tau_0 \otimes \mathcal{R}_L^{(2)}(C_4) + \tau_x \otimes \mathcal{R}_L^{(1)}(C_4) \right] \otimes \mathcal{R}_S(C_4^3), \\
\mathcal{D}(\sigma_v^x) &= \left[\tau_0 \otimes \mathcal{R}_L^{(1)}(\sigma_v^x) + \tau_x \otimes \mathcal{R}_L^{(2)}(\sigma_v^x) \right] \otimes \mathcal{R}_S(\sigma_v^x), \\
\mathcal{D}(\sigma_v^y) &= \left[\tau_0 \otimes \mathcal{R}_L^{(2)}(\sigma_v^x) + \tau_x \otimes \mathcal{R}_L^{(1)}(\sigma_v^x) \right] \otimes \mathcal{R}_S(\sigma_v^y), \\
\mathcal{D}(\sigma_v^{xy}) &= \left[\tau_0 \otimes \mathcal{R}_L^{(1)}(\sigma_v^{xy}) + \tau_x \otimes \mathcal{R}_L^{(2)}(\sigma_v^{xy}) \right] \otimes \mathcal{R}_S(\sigma_v^{xy}), \\
\mathcal{D}(\sigma_v^{yx}) &= \left[\tau_0 \otimes \mathcal{R}_L^{(2)}(\sigma_v^{xy}) + \tau_x \otimes \mathcal{R}_L^{(1)}(\sigma_v^{xy}) \right] \otimes \mathcal{R}_S(\sigma_v^{yx}).
\end{aligned} \tag{E.1}$$

Here τ_0, τ_x are Pauli matrices defining the internal symmetry $\mathcal{D}_4(\mathbf{g})$, and

$$\begin{aligned} \mathcal{R}_L^{(1)}(C_4) &= \begin{pmatrix} 0 & 0 & 0 & 0 \\ 0 & 0 & 0 & 0 \\ 1 & 0 & 0 & 0 \\ 0 & 1 & 0 & 0 \end{pmatrix}, \mathcal{R}_L^{(2)}(C_4) = \begin{pmatrix} 0 & 0 & 1 & 0 \\ 0 & 0 & 0 & 1 \\ 0 & 0 & 0 & 0 \\ 0 & 0 & 0 & 0 \end{pmatrix}, \\ \mathcal{R}_L^{(1)}(\sigma_v^x) &= \begin{pmatrix} 0 & 0 & 0 & 0 \\ 0 & 0 & 0 & 0 \\ 0 & 0 & 0 & 0 \\ 0 & 0 & 0 & 1 \end{pmatrix}, \mathcal{R}_L^{(2)}(\sigma_v^x) = \begin{pmatrix} 0 & 0 & 1 & 0 \\ 0 & 1 & 0 & 0 \\ 1 & 0 & 0 & 0 \\ 0 & 0 & 0 & 0 \end{pmatrix}, \\ \mathcal{R}_L^{(1)}(\sigma_v^{xy}) &= \begin{pmatrix} 1 & 0 & 0 & 0 \\ 0 & 0 & 0 & 0 \\ 0 & 0 & 0 & 0 \\ 0 & 0 & 0 & 0 \end{pmatrix}, \mathcal{R}_L^{(2)}(\sigma_v^{xy}) = \begin{pmatrix} 0 & 0 & 0 & 0 \\ 0 & 0 & 0 & 1 \\ 0 & 0 & 1 & 0 \\ 0 & 1 & 0 & 0 \end{pmatrix}. \end{aligned}$$

Under C_4 , the continuous $O_i(3)$ symmetry simply becomes a discrete angle of rotation by $2\pi/4$ with L_z being the angular momentum, while under the mirror, spin is rotated as an axial vector. This gives

$$\mathcal{R}_S(C_4) = \begin{pmatrix} 0 & -1 & 0 \\ 1 & 0 & 0 \\ 0 & 0 & 1 \end{pmatrix}, \quad \mathcal{R}_S(\sigma_v^x) = \begin{pmatrix} 1 & 0 & 0 \\ 0 & -1 & 0 \\ 0 & 0 & -1 \end{pmatrix}, \quad \mathcal{R}_S(\sigma_v^{xy}) = \begin{pmatrix} 0 & -1 & 0 \\ -1 & 0 & 0 \\ 0 & 0 & -1 \end{pmatrix} \quad (\text{E.2})$$

and $\mathcal{R}_S(C_4^2) = (\mathcal{R}_S(C_4))^2$, $\mathcal{R}_S(C_4^3) = (\mathcal{R}_S(C_4))^3$, $\mathcal{R}_S(\sigma_v^y) = \mathcal{R}_S(C_4)^{-1} \mathcal{R}_S(\sigma_v^x) \mathcal{R}_S(C_4)$, and $\mathcal{R}_S(\sigma_v^{yx}) = \mathcal{R}_S(C_4)^{-1} \mathcal{R}_S(\sigma_v^{xy}) \mathcal{R}_S(C_4)$.

E.1.1 Symmetry of the Hamiltonian

The generic plaquette Hamiltonian is expressed in the main text as $H_p = \frac{1}{2} \mathcal{S}_p^T \mathcal{H}_p \mathcal{S}_p$, where \mathcal{H}_p is the 24×24 symmetric matrix containing all possible nearest neighbor interactions. The symmetry constraints make many terms vanish or be identical to other terms. Under a symmetry, the vector field transforms to $\mathcal{S}_p^I = \mathcal{D}(\mathbf{g}) \mathcal{S}$, $\forall \mathbf{g} \in \mathcal{D}_4$, and if the Hamiltonian to H_p is invariant, then the Hamiltonian matrix transforms as $\mathcal{D}^T(\mathbf{g}) \mathcal{H}_p \mathcal{D}(\mathbf{g}) = \mathcal{H}_p$, $\forall p$.

Under these conditions, we find that the interaction terms among the four triangles are related to each other by symmetry, while those within a triangle are independent of each other; see Fig. 1 (a). Consider the one independent triangle at sites $i = \{0, 1, 2\}$ in Fig. 1 (a), and we

D_4	d_α	E	$2C_4$	$2C_2''$	C_2	$2C_2'$
A_1	2	1	1	1	1	1
A_2	4	1	1	-1	1	-1
B_1	3	1	-1	1	1	-1
B_2	3	1	-1	-1	1	1
E	6	2	0	0	-2	0
S_p		24	0	-2	0	-2

Table E.1 Character table of the group D_4 . The last row corresponds to the characters of the reducible representation S_p for each class. $N_k C_k$ notion is used in the first row. N_k is the number of elements in each conjugacy class, C_k .

obtain three distinct 3×3 matrices between sites i and j :

$$\begin{aligned}
 (\mathcal{H}_p)_{01} &= \begin{pmatrix} J^{xx} & D^{xy} & 0 \\ D^{yx} & J^{yy} & 0 \\ 0 & 0 & J^{zz} \end{pmatrix}, (\mathcal{H}_p)_{12} = \begin{pmatrix} J^{xx} & -D^{yx} & 0 \\ -D^{xy} & J^{yy} & 0 \\ 0 & 0 & J^{zz} \end{pmatrix}, \text{ and} \\
 (\mathcal{H}_p)_{20} &= \begin{pmatrix} J^{lx} & D^{ly} & 0 \\ -D^{ly} & J^{ly} & 0 \\ 0 & 0 & J^{zz} \end{pmatrix}. \tag{E.3}
 \end{aligned}$$

Therefore, we have nine independent parameters: three exchange interactions $J^{\mu\mu}$, $J^{l\mu\mu}$. and three DM interactions D^{xy} , D^{yx} , and D^{lx} . Due to in-plane inversion symmetry, no in-plane DM interaction is allowed. We take a simpler XXZ + DM interaction model in which $J^{\mu\mu} = J^{l\mu\mu}$, $J^{xx} = J^{yy} = J^{zz} / \Delta = J$, and $D^{xy} = -D^{yx} = D^{lx} = JD$. This gives us three independent parameters, among which the global energy scaling by J is removed, except its sign \pm is considered in the main text.

E.1.2 Irreducible spin configurations

Finally, we find the irreducible representation of the S_p vector. There are five classes in the group D_4 denoted by $E = \{e\}$, $C_4 = \{C_4, C_4^3\}$, $C_2 = \{C_4^2\}$, $C_2' = \{\sigma_v^{xy}, \sigma_v^{yx}\}$, $C_2'' = \{\sigma_v^x, \sigma_v^y\}$. The character table for this symmetry group is given in Table E.1.

We have five irreps, which we denote by m_α for $\alpha = 1 - 5$. Then the vector representation of the irreps is a direct sum of the irreps $\mathcal{M} = \bigoplus_\alpha d_\alpha m_\alpha$ with d_α giving the number of times the α -th irrep appears in the sum. d_α is calculated from orthogonality relation with the characters: $\chi_{m_\alpha}(C_k)$, $\chi_{\mathcal{M}}(C_k)$ of the 24-dimensional representations $m_\alpha(C_k)$, $\mathcal{M}(C_k)$ respectively, for each

conjugacy class C_k , where k runs over the five conjugacy classes:

$$d_\alpha = \frac{1}{h} \sum_k N_k \chi_{m_\alpha}(C_k) \bar{\chi}_{\mathcal{M}}(C_k) \quad (\text{E.4})$$

where $h = 8$ is the order of the group \mathbf{D}_4 , and N_k is the number of elements in C_k conjugacy class. The values of d_α are given in the second column in Table E.1.

The final task in this section is to find the basis functions \mathcal{V}_α of each irrep. We denote the basis vectors as $|\mathcal{V}_\alpha^\mu\rangle$, where $\alpha = 1$ for one-dimensional irreps, and $\mu = 1, 2$ (which are relabelled as x, y in Fig. E.1) for the two-dimensional irrep E. The basis vectors follow a relation: $\mathcal{D}(g)|\mathcal{V}_\alpha^\mu\rangle = \sum_{\mu'} (U_\alpha(g))_{\mu\mu'} |\mathcal{V}_\alpha^{\mu'}\rangle$, $\forall g$. $(U_\alpha(g))_{\mu\mu'}$ are the $\mu \times \mu$ -matrix for the μ -dimensional irrep α defined for the group element g . For the one-dimensional irreps $A_{1,2}$ and $B_{1,2}$, $U_\alpha(g)$ simply gives the character of the group, and then $|\mathcal{V}_\alpha^\mu\rangle$ are the simultaneous eigenvectors of the group elements with the character being the eigenvalue. They can be solved easily and the corresponding basis functions for the one-dimensional irreps are shown in Fig. E.1(a-d). For the two-dimensional E irrep, the orthogonal condition of the basis vector simplifies the above equation to $(U_\alpha(g))_{\mu\mu'} = \langle \mathcal{V}_\alpha^\mu | \mathcal{D}(g) | \mathcal{V}_\alpha^{\mu'} \rangle$. We solve this matrix for the E irrep for each group elements, which comes out to be $U_E(\mathbf{e}) = \mathbb{I}_{2 \times 2}$, $U_E(C_4) = -i\tau_y$, $U_E(C_4^2) = -\mathbb{I}_{2 \times 2}$, $U_E(C_4^3) = i\tau_y$, $U_E(\sigma_v^x) = \tau_z$, $U_E(\sigma_v^y) = -tau_z$, $U_E(\sigma_v^{xy}) = \tau_x$, $U_E(\sigma_v^{yx}) = -\tau_x$. τ_μ are the 2×2 Pauli matrices.

We have the multiplets as $d_\alpha = 2, 4, 3, 3$ for the four one-dimensional irreps A_1, A_2, B_1, B_2 , giving 12 basis vectors, while the two-dimensional irrep with multiplicity $d_E = 6$ gives another 12 basis vectors, as shown in Fig. E.1(e). Among them, sixteen are in-plane, defined in the set m_\perp , and eight are out-of-plane, defined in the set m_z in the main text. Among them, six out-of-plane irreps do not satisfy the local constraint of $S = 1$ per site.

E.1.3 XXZ and DM interactions

In the plaquette Hamiltonian, after substituting $\mathcal{S}_p = \sum_{\alpha=1}^{3n} m_\alpha \mathcal{V}_\alpha$, we obtain a Hamiltonian that is block diagonal between the irreps but contains cross-terms along the multiplicity within an irrep. So we define a d_α -dimensional spinor field for each irrep as $m_\alpha := (m_\alpha^{(1)} \dots m_\alpha^{(d_\alpha)})^T \in \mathcal{O}_p(d_\alpha)$, in which the plaquette Hamiltonian splits as

$$H_p = \sum_{\alpha=1}^5 m_\alpha^T \mathcal{H}_\alpha m_\alpha, \quad (\text{E.5})$$

where we have suppressed the plaquette index on the right-hand side. \mathcal{H}_α is a $d_\alpha \times d_\alpha$ matrix. The $\mathcal{O}_p(d_\alpha)$ symmetry of each irrep breaks into $\mathcal{O}_p(2)$ and Z_2 symmetry as follows.

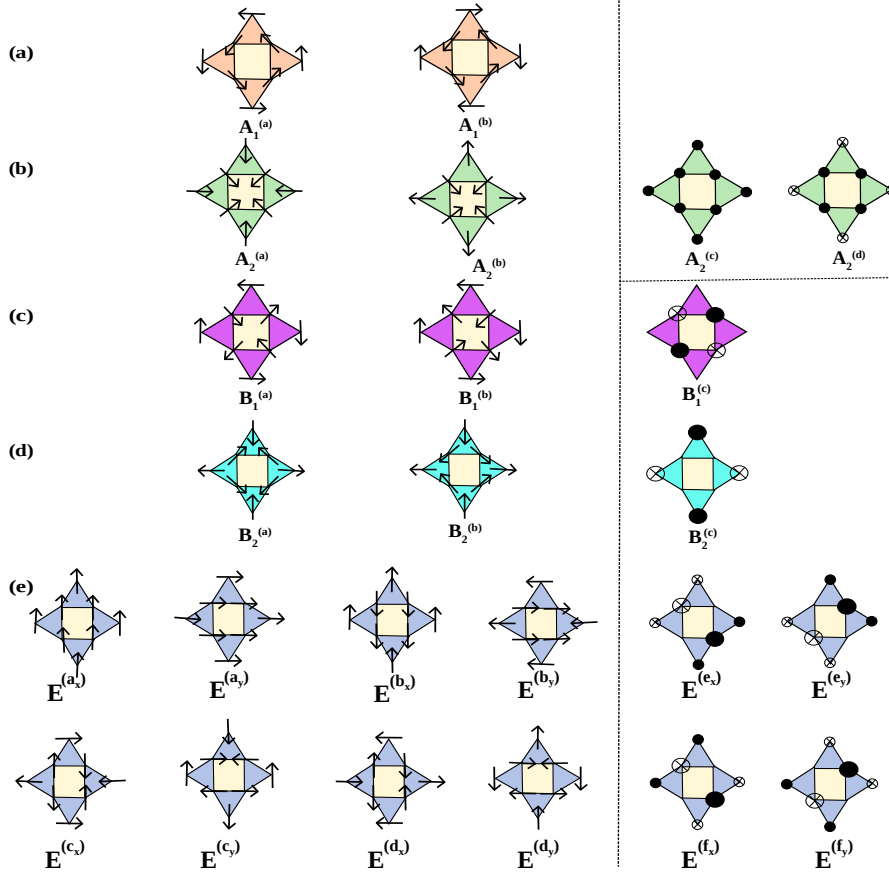


Fig. E.1 We plot all the irreps' basis functions. The vertical dashed line demarcates the out-of-plane irreps m_z on the right-hand side, among which only the top row satisfies the local constraint while the others do not. The horizontal arrows give the spin direction for S_i^\perp , while the filled and open dots correspond to S_i^z . The size of the dots corresponds to $|S_i^z|$. For $A_2^{(c,d)}$, the size of the dots is adjusted for $|S_i^z| = 1$, while for $B_{1,2}^{(c)}$, sites with symbols give $|S_i^z| = \sqrt{2}$, while sites without symbols have $|S_i^z| = 1$. Similar consideration is used for the E irreps that do not meet the local constraint.

For $\alpha = 1$, the A_1 irrep with $d_1 = 2$ multiplets follows an $O_p(2)$ symmetry.

For $\alpha = 2$, the A_2 irrep with $d_2 = 4$, we have an emergent $O_p(2) \times O_p(2)$ symmetry among the multiplets, giving $\mathcal{H}_{A_2} = \mathcal{H}_{A_2^{(a,b)}} \oplus \mathcal{H}_{A_2^{(c,d)}}$. This is obvious because $A_2^{(a,b)}$ consists of coplanar spins while $A_2^{(c,d)}$ are the two out-of-plane spins.

For both $\alpha = 3, d$, the $B_{1,2}$ irreps with $d_{3,4} = 3$, we have an emergent $O_p(2) \times Z_2$ symmetry with $\mathcal{H}_{B_{1,2}} = \mathcal{H}_{B_{1,2}^{(a,b)}} \oplus \mathcal{H}_{B_{1,2}^{(c)}}$. Here, the $B_{1,2}^{(a,b)}$ multiplets are coplanar spins forming $O(2)$ symmetry, while $B_{1,2}^{(c)}$ consists of out-of-plane spins that do not obey local constraints.

For $\alpha = 5$, the two-dimensional E irrep with $d_5 = 6$, each component of each multiplicity gives emergent $O_p(2)$ rotation as $\mathcal{H}_E = \mathcal{H}_{E(a,b)} \oplus \mathcal{H}_{E(c,d)} \oplus \mathcal{H}_{E(e,f)}$.

All the $O_p(2)$ invariant 2×2 Hamiltonian matrices for all irreps have this general form

$$(\mathcal{H}_\alpha)_{k,k'} = \varepsilon_\alpha^{(k+)} \sigma_0 + \varepsilon_\alpha^{(k-)} \sigma_z + \lambda_\alpha^{(kk')} \sigma_x, \quad (\text{E.6})$$

where $k, k' = 1, 2 \in (a,b)$ or (c,d) or (e,f) , and $\varepsilon_\alpha^{k\pm} = [\varepsilon_\alpha^{(k)} \pm \varepsilon_\alpha^{(k')}] / 2$ and $\varepsilon_\alpha^{(k)}$ is the onsite energy for the k^{th} multiplet of the α -irrep, and $\lambda_\alpha^{(kk')}$ is the ‘hopping energy’ between the k and k' multiples. The onsite energies of the two vortices with different helicities are $\varepsilon_{A_1^{(a)}} = \varepsilon_{A_2^{(a)}} = 2\sqrt{2} + 2(\sqrt{2} - 1)D$, $\varepsilon_{A_1^{(b)}} = \varepsilon_{A_2^{(b)}} = -2\sqrt{2} - 2(\sqrt{2} + 1)D$, while the energy cost to change the helicity angle is $\lambda_{A_1^{(a,b)}} = \lambda_{A_2^{(a,b)}} = -4D$. The same for the two anti-vortices are: $\varepsilon_{B_1^{(a)}} = \varepsilon_{B_2^{(a)}} = -2\sqrt{2} + 2(\sqrt{2} + 1)D$, $\varepsilon_{B_1^{(b)}} = \varepsilon_{B_2^{(b)}} = 2\sqrt{2} - 2(\sqrt{2} - 1)D$, $\lambda_{B_1^{(a,b)}} = \lambda_{B_2^{(a,b)}} = -4D$. The out-of-plane irreps with parallel and anti-parallel spins and spin-flip energies between them as $\varepsilon_{A_2^{(c)}} = 6\Delta$, $\varepsilon_{A_2^{(d)}} = -2\Delta$, $\lambda_{A_2^{(c,d)}} = 4\Delta$. The two irreps with only inner and out-square out-of-plane spins have the onsite energy: $\varepsilon_{B_1^{(c)}} = \varepsilon_{B_2^{(c)}} = -4\Delta$. Each two-dimensional irreps is degenerate. The in-plane FM E irreps have the energies $\varepsilon_{E^{(a)}} = 6$, $\varepsilon_{E^{(b)}} = -2$, and their hopping energy $\varepsilon_{E^{(a,b)}} = 4$. The in-plane AFM E irreps have the energies $\varepsilon_{E^{(c)}} = 4D - 2$, $\varepsilon_{E^{(d)}} = -4D - 2$, and $\varepsilon_{E^{(c,d)}} = -4$. The two out-of-plane E irreps that do not mix have the energies $\varepsilon_{E^{(e)}} = 2\sqrt{2}$, $\varepsilon_{E^{(b)}} = -2\sqrt{2}$. All energies are multiplied with J .

The explicit form of Hamiltonian in terms of the matrix elements in the basis of the irrep order parameter is

$$H_p = \sum_{\alpha=A_{1,2}, B_{1,2}} \sum_{k,k'} (\mathcal{H}_\alpha)_{k,k'} m_\alpha^{(k)} m_\alpha^{(k')} + \sum_{k,k'} (\mathcal{H}_E)_{k,k'} \mathbf{m}_E^{(k)} \cdot \mathbf{m}_E^{(k')} + \sum_{\alpha=B_{1,2}, k=c} (\mathcal{H}_E)_{k,k} (m_\alpha^k)^2. \quad (\text{E.7})$$

where $k, k' = a, b$ for all irreps, and in addition, we have $k, k' = c, d$ for A_2 and $k, k' = c, d$, and $k, k' = e, f$ for E.

Then, for all $O_p(2)$ order parameters, diagonalize the corresponding 2×2 \mathcal{H}_α matrices by the orthogonal transformation:

$$\begin{pmatrix} \tilde{m}_\alpha^{(k)} \\ \tilde{m}_\alpha^{(k')} \end{pmatrix} = \begin{bmatrix} \sigma_0 \cos \phi_\alpha^{(k,k')} & -i\sigma_y \sin \phi_\alpha^{(k,k')} \end{bmatrix} \begin{pmatrix} m_\alpha^{(k)} \\ m_\alpha^{(k')} \end{pmatrix}$$

where $\phi_\alpha^{(k,k')}$ is a fixed angle of rotation that diagonalizes the corresponding irrep multiplets. Eventually, we obtain a fully diagonal Hamiltonian as

$$H_p = \sum_{v=(\alpha,k=1,d_\alpha)} E_v |\tilde{m}_v|^2. \quad (\text{E.8})$$

We have abandoned the α and k symbols for the irreps and multiplicity and combined them into a single symbol v which runs from 1 to $3n$ in the eigenmodes, for simplicity. Here $E_v = \varepsilon_\alpha^+ \pm \sqrt{(\varepsilon_\alpha^-)^2 + \lambda_\alpha^2}$ for each $O_p(2)$ multiplets of α -irreps. Their explicit forms are

$$\begin{aligned} E_{v=1,2} &= -2D \pm 2\sqrt{D^2 + (1+D)^2}, & \text{for } \alpha = A_1^{(a,b)}, \\ E_{v=3,4} &= E_{v=1,2}, & \text{for } \alpha = A_2^{(a,b)}, \\ E_{v=5,6} &= 2\Delta(1 \pm \sqrt{5}), & \text{for } \alpha = A_2^{(c,d)}, \\ E_{v=7,8} &= 2D \pm 2\sqrt{D^2 + 2(1-D)^2}, & \text{for } \alpha = B_1^{(a,b)}, \\ E_{v=9} &= -4\Delta, & \text{for } \alpha = B_1^{(c)}, \\ E_{v=10-12} &= E_{v=7-9} & \text{for } \alpha = B_2^{(a,b,c)}, \\ E_{v=13,14} &= 2 \pm 2\sqrt{5}, & \text{for } \alpha = E^{(a,b)}, \\ E_{v=15,16} &= -2 \pm 2\sqrt{1+4D^2}, & \text{for } \alpha = E^{(c,d)}, \\ E_{v=17,18} &= \pm 2\sqrt{2}\Delta & \text{for } \alpha = E^{(e,f)}. \end{aligned} \quad (\text{E.9})$$

All the energies are defined with respect to J . The values of the angle ϕ are:

$$\begin{aligned} \phi_{A_1^{(a,b)}} &= \frac{1}{2} \tan^{-1} \left(\frac{D}{\sqrt{2}(1+D)} \right), & \phi_{A_2^{(a,b)}} &= \phi_{A_1^{(a,b)}}, & \phi_{A_1^{(c,d)}} &= -\frac{1}{2} \tan^{-1} \left(\frac{1}{2} \right), \\ \phi_{B_1^{(a,b)}} &= \frac{1}{2} \tan^{-1} \left(\frac{D}{\sqrt{2}(1-D)} \right), & \phi_{B_2^{(a,b)}} &= \frac{1}{2} \tan^{-1} \left(\frac{-D}{\sqrt{2}(1-D)} \right), \\ \phi_{E^{(a,b)}} &= -\frac{1}{2} \tan^{-1} \left(\frac{1}{2} \right), & \phi_{E^{(c,d)}} &= \frac{1}{2} \tan^{-1} \left(\frac{1}{2D} \right). \end{aligned} \quad (\text{E.10})$$

E.2 Details of Classical Monte Carlo

In the classical Monte Carlo calculation, the final temperature is achieved by annealing from the high temperature at each step with 8×10^5 Monte Carlo steps. The expectation values of the observables are calculated by taking the average over the last 7×10^5 configurations of a total 8×10^5 Monte Carlo steps with system size $N = 6L^2$ considering periodic boundary conditions,

with L number of unit cells. All the static structure factor averages are performed over system size, $L = 20$ at temperature 10^{-3} . The position vectors of each sublattice (denoted with indices 0,1, ... in Fig. 1(a) of main text) are taken as considering the origin at the center of the square,

$$\delta_0 = \left(\frac{-1}{4}, \frac{-1}{4}\right), \delta_1 = \left(\frac{1}{4}, \frac{-1}{4}\right), \delta_2 = \left(\frac{1}{4}, \frac{1}{4}\right), \delta_3 = \left(\frac{-1}{4}, \frac{1}{4}\right), \delta_4 = \left(0, \frac{-1}{2}\right), \delta_5 = \left(\frac{1}{2}, 0\right) \quad (\text{E.11})$$

E.3 Structure Factor Plots

In this section, we list the real space spin configurations of all the phases and their respective structure factors. As defined in the main text, the different structure factors are

$$\begin{aligned} \chi(\mathbf{k}) &= 1/\mathcal{N} \sum_{i,j} \langle \mathbf{S}_i \cdot \mathbf{S}_j \rangle \exp\{i\mathbf{k} \cdot (\mathbf{r}_i - \mathbf{r}_j)\} \\ \chi^\perp(\mathbf{k}) &= 1/\mathcal{N} \sum_{i,j} \langle \mathbf{S}_i^\perp \mathbf{S}_j^\perp \rangle \exp\{i\mathbf{k} \cdot (\mathbf{r}_i - \mathbf{r}_j)\} \\ \chi^z(\mathbf{k}) &= 1/\mathcal{N} \sum_{i,j} \langle \mathbf{S}_i^z \mathbf{S}_j^z \rangle \exp\{i\mathbf{k} \cdot (\mathbf{r}_i - \mathbf{r}_j)\} \end{aligned} \quad (\text{E.12})$$

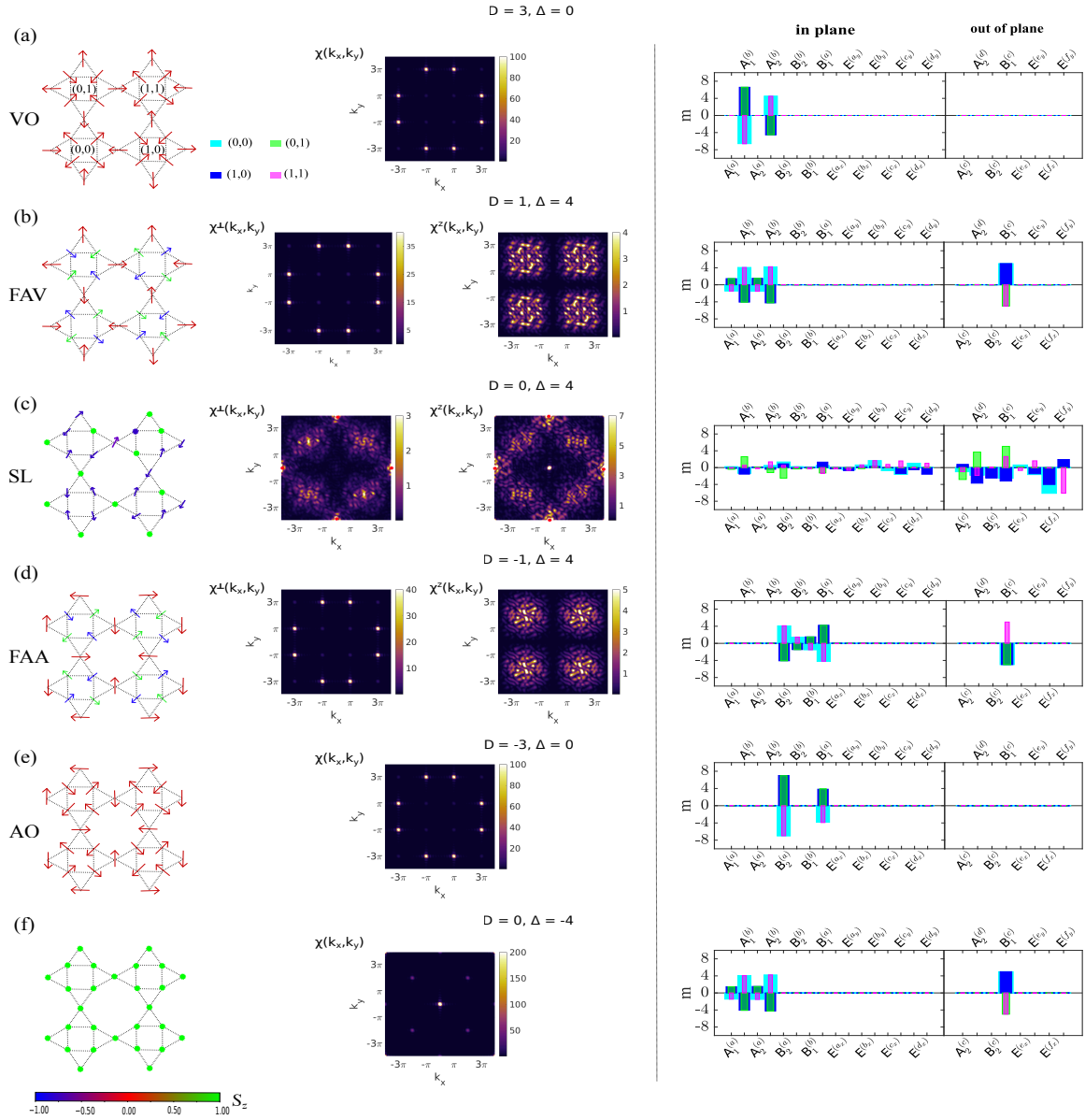


Fig. E.2 The real spin configurations (left panel) and the corresponding structure factor (middle panel) are plotted for various phases for the AFM coupling $J = +1$. The ensemble of order parameters, which are mentioned in the main text, for each phase is presented in the right panel. (a) Order phase (red region in the phase diagram) with staggered anti-vortices between the neighboring sites, showing Bragg-like peaks at a finite but preferential wavevector. (b) Mixed or fragmented phase where the inner anti-vortices turn into an AFM-anti-vortex with opposite S_i^z components, while $S_i^z = 0$ for the outer anti-vortex. The S_i^z values, however, take random values and show disorder features in the corresponding structure factor without any pinch-point correlation. This is expected as the inner vortices become decoupled from each other, lacking any significant correlation between them. (c) A CSL phase (close to the Z_2 CSL phase) showing larger spectral weight the S_i^z correlation function with pinch-points. (d) The mixed or fragmented phase for $D < 0$ is similar to the mixed phase for $D > 0$, except here, vortices replace the anti-vortices. (e) Orderd phase for $D < 0$, similar to the $D > 0$ case in (a), with vortices replacing anti-vortices. (f) A collinear out-of-plane FM phase arising in the limit of strong our-of-plane anisotropy term $\Delta \rightarrow -\infty$.

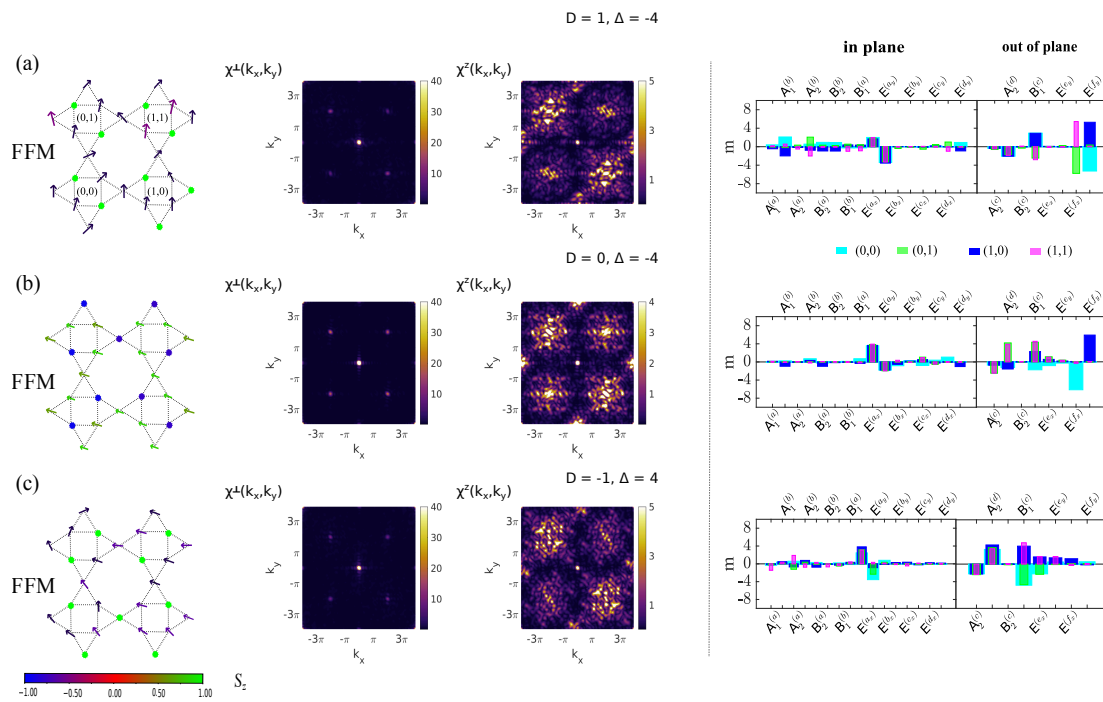


Fig. E.3 Similar to Fig. S2, but for the FM interaction $J = -1$. All three phases shown here are the fragmented phases at different values of D and Δ , showing pinch-point in the S_i^z correlation function, but FM ordering in the in-plane component.

E.4 Soft-spin Approximation

In this section, we analyze the Hamiltonian in Eq. 5.4 with 'soft spin' approximation i.e. spin length constraint ($|\mathbf{S}_i|^2 = 1$) is softened from exact value of 1 per site to the global value of $\sum_i^N |\mathbf{S}_i|^2 = NS$. Because of the global constraint, we have a uniform (fixed) chemical potential (Lagrangian multiplier) in the theory. Then, following Ref. [26], we have diagonalized the Hamiltonian in the Fourier space of the spin. There, a spin vector is defined per unit cell, not in the plaquette, which means we have six sublattices as $\mathcal{S}_i = (S_0^x, S_0^y, S_0^z, S_1^x, \dots, S_5^z)$. We Fourier transform the spin vector as $\mathcal{S}(\mathbf{q}) = \frac{1}{\sqrt{N}} \sum_i \mathcal{S}_i e^{-i\mathbf{q} \cdot \mathbf{r}_i}$, where $\mathbf{r} = a\mathbf{n}_1 + b\mathbf{n}_2$ with integers a, b and unit vectors $\mathbf{n}_1 = (1, 0), \mathbf{n}_2 = (0, 1)$. The Hamiltonian is then diagonal in the momentum space as

$$H = \sum_{\mathbf{q}} \mathcal{S}(\mathbf{q})^T \mathcal{H}(\mathbf{q}) \mathcal{S}(\mathbf{q}), \quad (\text{E.13})$$

where $\mathcal{H}(\mathbf{q})$ is a 18×18 matrix. We can now diagonalize the $\mathcal{H}(\mathbf{q})$ matrix, which gives the energy eigenvalues $E_v(\mathbf{q})$. The lowest energy state is the ground state, and then we plot a few low-energy excited states in Fig. E.4.

We note that the analysis on the Fourier basis leads to a violation of the local constraint and hence, inconsistency is expected between the real-space model and the Fourier space one, especially in the spin liquid phase. In the CSL phase, we find an extremely flat band as the lowest energy state, suggesting extensive degeneracy as expected here. We see the flat band in all the mixed phases as well. In addition, the spectrum is gapless in both phases, with gapless points present at $(\pm\pi, \pm\pi), (\pm\pi, \pm 3\pi)$, and $(\pm 3\pi, \pm 3\pi)$, as shown in Fig. E.4. The band degeneracy, denoted with d in the spectrum at each region is different: $d=4(2)$ for $\Delta < 1(> 1)$, $d=6$ at $\Delta = 1$ in the CSL phase where $D=0$; and $d=2$ for mixed phases both for $J = +1$ and -1 . Hence, there is no simple positive sum of the constrainer rule here; the direct matching of singular/non-singular bands to emergent gauge fields/fragility is not possible.

As discussed rigorously in the main text, the spin liquids (cyan(/black) colored phase for $J=+1(/-1)$) phase has pinch points belonging to the algebraic class of CSLs with 'emergent' low-energy gauge field excitations. The mixed (black-colored phase for $J=+1$) phase has no pinch points and, hence, belongs to the fragile class of CSLs. All the other ordered phase regions have dispersive bands.

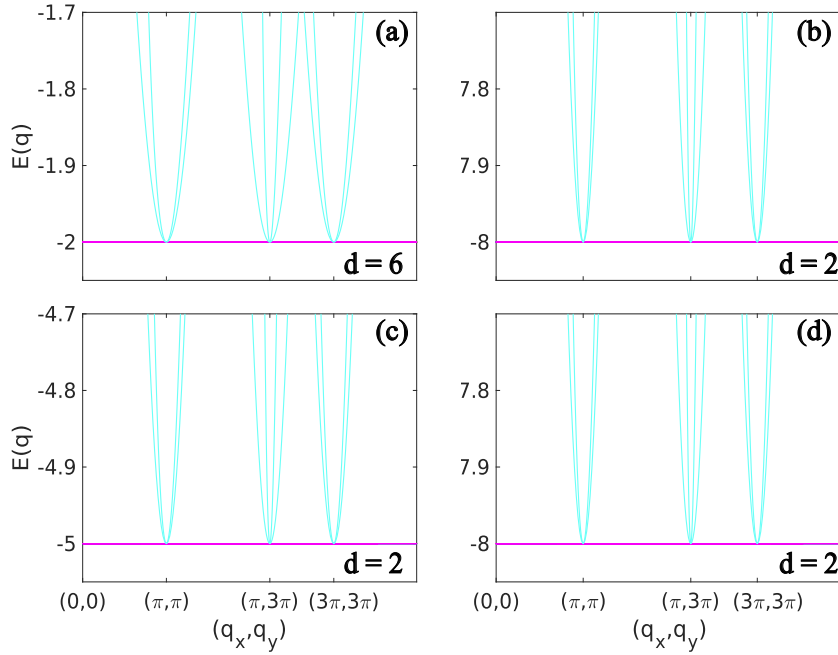


Fig. E.4 Energy dispersion of the Hamiltonian $\mathcal{H}(\mathbf{q})$ at four with re)spective degeneracy of flat bands d , for (a) $\Delta = 1.0, D = 0.0$ (CSL), (b) $\Delta = 4.0, D = 1.0$ (Mixed phase) for $J = +1$ and (c) $\Delta = -2.5, D = 0.0$ (d) $\Delta = 4.0, D = 1.0$ (Mixed phases) for $J = -1$

E.5 Finite Magnetic field

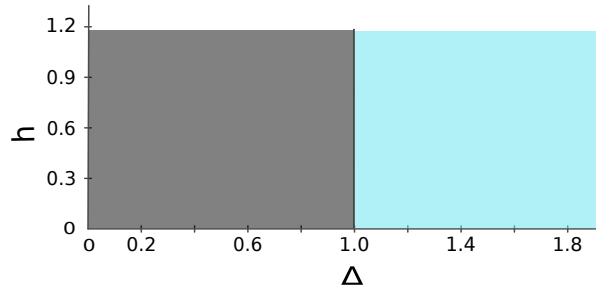


Fig. E.5 Phase diagram at $D=0$, as a function of h and Δ . For $\Delta < 1$, the phase is a mixed phase and spin liquid for another case. The mixed phase here is unstable for any finite value of D ; the phase becomes ordered in and out-of-plane for non-zero D value.

The external magnetic field is applied along the z -axis to the Hamiltonian, now written as

$$H_{mag} = H_{XXZ-DM} - h \sum_i S_i^z. \quad (\text{E.14})$$

The phase diagram as a function of h and Δ is presented in Fig. E.5 for $D = 0$. A mixed phase of disordered in-plane spins with ordered out-of-plane components is observed at $D = 0$ for $\Delta < 1$ with increasing h . The in-plane disordered spins exhibit a coexisting Bragg-like leak at $(0, 4\pi)$, and pinch points at $(\pm\pi, \pm 3\pi)$. The ordering along the z components is FM type. This phase is unstable for any finite value of D . A finite value of D gives an ordered phase depending on the sign of the D value, where the in-plane spins form an ordered supercell structure, and the out-of-plane spins are ferromagnetically ordered. As $\Delta > 1$, the spins become disordered both in in-plane and out-of-plane components. This phase also has pinch-points in the correlation function, indicating power-law correlations. This phase survives at finite values of D . Therefore, we conclude that, by applying the external magnetic field, the spin liquid phase can be stabilized in these materials.

References

- [1] L. Balents, *Nature* **464**, 199 (2010).
- [2] C. L. Henley, *Annual Review of Condensed Matter Physics* **1**, 179 (2010).
- [3] R. Moessner and J. T. Chalker, *Phys. Rev. Lett.* **80**, 2929 (1998).
- [4] J. Rehn, A. Sen, K. Damle, and R. Moessner, *Phys. Rev. Lett.* **117**, 167201 (2016).
- [5] O. Benton, L. Jaubert, H. Yan, and N. Shannon, *Nature Communications* **7**, [10.1038/ncomms11572](https://doi.org/10.1038/ncomms11572) (2016).
- [6] O. Benton and R. Moessner, *Phys. Rev. Lett.* **127**, 107202 (2021).
- [7] C. Castelnovo, R. Moessner, and S. Sondhi, *Annual Review of Condensed Matter Physics* **3**, 35–55 (2012).
- [8] C. Nisoli, R. Moessner, and P. Schiffer, *Rev. Mod. Phys.* **85**, 1473 (2013).
- [9] K. A. Ross, L. Savary, B. D. Gaulin, and L. Balents, *Phys. Rev. X* **1**, 021002 (2011).
- [10] M. E. Brooks-Bartlett, S. T. Banks, L. D. C. Jaubert, A. Harman-Clarke, and P. C. W. Holdsworth, *Phys. Rev. X* **4**, 011007 (2014).
- [11] S. Powell, *Phys. Rev. B* **91**, 094431 (2015).
- [12] S. Petit, E. Lhotel, B. Canals, M. Ciomaga-Hatnean, J. Ollivier, H. Mutka, E. Ressouche, A. R. Wildes, M. R. Lees, and G. Balakrishnan, Observation of magnetic fragmentation in spin ice (2016), [arXiv:1603.05008 \[cond-mat.str-el\]](https://arxiv.org/abs/1603.05008) .
- [13] B. Canals, I.-A. Chioar, V.-D. Nguyen, M. Hehn, D. Lacour, F. Montaigne, A. Locatelli, T. O. Menteş, B. S. Burgos, and N. Rougemaille, *Nature Communications* **7**, [10.1038/ncomms11446](https://doi.org/10.1038/ncomms11446) (2016).

- [14] Villain, J., Bidaux, R., Carton, J.-P., and Conte, R., *J. Phys. France* **41**, 1263 (1980).
- [15] C. L. Henley, *Phys. Rev. Lett.* **62**, 2056 (1989).
- [16] P. Chandra, P. Coleman, and A. I. Larkin, *Phys. Rev. Lett.* **64**, 88 (1990).
- [17] J. T. Chalker, P. C. W. Holdsworth, and E. F. Shender, *Phys. Rev. Lett.* **68**, 855 (1992).
- [18] E. F. Shender and P. C. W. Holdsworth, Order by disorder and topology in frustrated magnetic systems, in *Fluctuations and Order: The New Synthesis*, edited by M. Millonas (Springer US, New York, NY, 1996) pp. 259–279.
- [19] M. Biskup, L. Chayes, and S. A. Kivelson, *Annales Henri Poincaré* **5**, 1181–1205 (2004).
- [20] A. Pizzi, A. Nunnenkamp, and J. Knolle, *Phys. Rev. Lett.* **127**, 140602 (2021).
- [21] B. Placke, O. Benton, and R. Moessner, Ising fracton spin liquid on the honeycomb lattice (2023), [arXiv:2306.13151 \[cond-mat.str-el\]](https://arxiv.org/abs/2306.13151) .
- [22] D. Dahlbom, H. Zhang, Z. Laraib, D. M. Pajerowski, K. Barros, and C. Batista, Renormalized classical theory of quantum magnets (2023), [arXiv:2304.03874 \[cond-mat.str-el\]](https://arxiv.org/abs/2304.03874) .
- [23] R. P. Nutakki, L. D. C. Jaubert, and L. Pollet, *SciPost Phys.* **15**, 040 (2023).
- [24] N. Davier, F. A. Gómez Albarracín, H. D. Rosales, and P. Pujol, *Phys. Rev. B* **108**, 054408 (2023).
- [25] H. Yan, O. Benton, R. Moessner, and A. H. Nevidomskyy, Classification of classical spin liquids: Typology and resulting landscape (2023), [arXiv:2305.00155 \[cond-mat.str-el\]](https://arxiv.org/abs/2305.00155) .
- [26] H. Yan, O. Benton, A. H. Nevidomskyy, and R. Moessner, Classification of classical spin liquids: Detailed formalism and suite of examples (2023), [arXiv:2305.19189 \[cond-mat.str-el\]](https://arxiv.org/abs/2305.19189) .
- [27] Y. Fang, J. Cano, A. H. Nevidomskyy, and H. Yan, Classification of classical spin liquids: Topological quantum chemistry and crystalline symmetry (2023), [arXiv:2309.12652 \[cond-mat.str-el\]](https://arxiv.org/abs/2309.12652) .
- [28] Z. Nussinov, *Phys. Rev. B* **69**, 014208 (2004).
- [29] Z. Nussinov, Commensurate and incommensurate o(n) spin systems: Novel even-odd effects, a generalized mermin-wagner-coleman theorem, and ground states (2004), [arXiv:cond-mat/0105253 \[cond-mat.stat-mech\]](https://arxiv.org/abs/cond-mat/0105253) .

- [30] S. T. Bramwell, *Philosophical Transactions of the Royal Society A: Mathematical, Physical and Engineering Sciences* **370**, 5738 (2012).
- [31] L. Savary and L. Balents, *Phys. Rev. Lett.* **108**, 037202 (2012).
- [32] R. Siddharthan, B. S. Shastry, A. P. Ramirez, A. Hayashi, R. J. Cava, and S. Rosenkranz, *Phys. Rev. Lett.* **83**, 1854 (1999).
- [33] S. T. Bramwell and M. J. P. Gingras, *Science* **294**, 1495 (2001).
- [34] S. V. Isakov, K. Gregor, R. Moessner, and S. L. Sondhi, *Phys. Rev. Lett.* **93**, 167204 (2004).
- [35] H. Yan, O. Benton, L. Jaubert, and N. Shannon, *Phys. Rev. B* **95**, 094422 (2017).
- [36] L. A. S. Mól, A. R. Pereira, and W. A. Moura-Melo, *Phys. Rev. B* **85**, 184410 (2012).
- [37] Y. Li, P. Gegenwart, and A. A. Tsirlin, *Journal of Physics: Condensed Matter* **32**, 224004 (2020).
- [38] D. T. Liu, F. J. Burnell, L. D. C. Jaubert, and J. T. Chalker, *Phys. Rev. B* **94**, 224413 (2016).
- [39] Y. Iqbal, H. O. Jeschke, J. Reuther, R. Valentí, I. I. Mazin, M. Greiter, and R. Thomale, *Phys. Rev. B* **92**, 220404 (2015).
- [40] T. Mizoguchi, L. D. C. Jaubert, and M. Udagawa, *Phys. Rev. Lett.* **119**, 077207 (2017).
- [41] K. Essafi, O. Benton, and L. D. C. Jaubert, *Phys. Rev. B* **96**, 205126 (2017).
- [42] T. Yildirim, A. B. Harris, and E. F. Shender, *Phys. Rev. B* **58**, 3144 (1998).
- [43] M. Fujihala, K. Morita, R. Mole, S. Mitsuda, T. Tohyama, S.-i. Yano, D. Yu, S. Sota, T. Kuwai, A. Koda, *et al.*, *Nat. Commun.* **11**, 3429 (2020).
- [44] O. V. Yakubovich, L. V. Shvanskaya, G. V. Kiriukhina, A. S. Volkov, O. V. Dimitrova, and A. N. Vasiliev, *Inorganic Chemistry* **60**, 11450 (2021), PMID: 34264636.
- [45] M. M. Markina, P. S. Berdonosov, T. M. Vasilchikova, K. V. Zakharov, A. F. Murtazoev, V. A. Dolgikh, A. V. Moskin, V. N. Glazkov, A. I. Smirnov, and A. N. Vasiliev, (2023), [arXiv:2212.11623 \[cond-mat.str-el\]](https://arxiv.org/abs/2212.11623) .

- [46] N. Astrakhantsev, F. Ferrari, N. Niggemann, T. Müller, A. Chauhan, A. Kshetrimayum, P. Ghosh, N. Regnault, R. Thomale, J. Reuther, T. Neupert, and Y. Iqbal, [Phys. Rev. B **104**, L220408 \(2021\)](#).
- [47] J. Richter, O. Derzhko, and J. Schnack, [Phys. Rev. B **105**, 144427 \(2022\)](#).
- [48] N. Niggemann, N. Astrakhantsev, A. Ralko, F. Ferrari, A. Maity, T. Müller, J. Richter, R. Thomale, T. Neupert, J. Reuther, Y. Iqbal, and H. O. Jeschke, [Phys. Rev. B **108**, L241117 \(2023\)](#).
- [49] J. Richter and J. Schnack, [Phys. Rev. B **107**, 245115 \(2023\)](#).
- [50] M. Gembé, H.-J. Schmidt, C. Hickey, J. Richter, Y. Iqbal, and S. Trebst, [Phys. Rev. Res. **5**, 043204 \(2023\)](#).
- [51] See Supplementary Materials for the details of the calculations and results.
- [52] We define in the SM[51] the operation \mathcal{T} for the dual vector as transpose T followed by a normalization factor of $6/8$ to adjust the length of the plaquette spin to be $|\mathcal{S}_p| = 6$.
- [53] P. H. Conlon and J. T. Chalker, [Phys. Rev. Lett. **102**, 237206 \(2009\)](#).
- [54] P. H. Conlon and J. T. Chalker, [Phys. Rev. B **81**, 224413 \(2010\)](#).
- [55] J. Rehn, A. Sen, and R. Moessner, [Phys. Rev. Lett. **118**, 047201 \(2017\)](#).
- [56] X. Zhang, Y. Zhou, and M. Ezawa, [Scientific reports **6**, 24795 \(2016\)](#).
- [57] T. Senthil, A. Vishwanath, L. Balents, S. Sachdev, and M. P. A. Fisher, [Science **303**, 1490 \(2004\)](#).

6

Summary

The interplay between the interaction, lattice frustration, and quantum statistics in many-body systems are one of the main topics of interest in condensed matter physics. Both from the fundamental point of view in understanding the richness of existing materials in nature to the realization of a variety of new phases having diverse properties like fractionalization, emergent gauge fields, and entanglement. One of the phases that this thesis mainly focused on is spin liquids. Spin liquids have been actively studied for the last few decades, mainly with possible applications in quantum computing and quantum information processing. Yes many open questions await detailed theoretical investigations. In this thesis, I addressed several issues in the quantum regime, including the intricate relationship between gauge and matter degrees of freedom, the characteristics of gauge excitations under non-perturbative regimes, and their influence on the properties of matter sectors. The thesis is summarised below.

In Chapter 1, I have briefly summarised the existing methodologies for studying quantum spin liquids (QSLs) and their experimental signatures and realizations. One of the well-known approaches to studying QSLs is via the variational wavefunctions, such as resonating valence bond (RVB) states. The RVB states are effective in treating the QSLs numerically. Another approach is an analytical one using Parton representations of spins. Further, the resulting Hamiltonian is analyzed using mean-field theory to study effective low-energy physics. Parton

mean field analysis is effective in understanding the emergence of gauge theories at low energy and fractional statistics of quasi-particles. The states from Parton mean field theory may not always be the same as that of the RVB states. The subtle comparisons and similarities between these two approaches are also pointed out. For the gaped ground states, both descriptions give rise to the same states. Z_2 spin liquids are very well-studied examples to have a gaped spectrum. In this regard, the Kitaev 2D Honeycomb model is proposed to have Z_2 spin liquids in the ground state. It is one of the exactly solvable 2D models demonstrating all the subtleties of Parton theory. The ground state of the Kitaev model has excitations with both abelian and non-abelian statistics in different parameter regimes. The existence of topologically non-trivial quasi-particles with non-abelian statistics in this model and later in the various other models has opened a surge in activities related to spin liquids aimed at potential applications in fault-tolerant topological computing. Even though the model lacked any initial physical motivations, Jackeli-Khaliullin later proposed the possible realization of the Kitaev model in real strong spin-orbit materials. This proposal sparked a field of research of its own. The experimental evidence for the existence of the Kitaev physics in these candidate materials, for example, in $\alpha - RuCl_3$, is still open for debate. From the theoretical perspective, the ground state gauge sector of the model with other external perturbations is one of the primary interests and has not been studied previously. I have investigated this problem for the externally applied magnetic field along [111], which is discussed in Chapter Three in detail.

Chapter 2 introduces the classical spin liquids (CSLs). The topic of spin liquids in classical spin systems is relatively new compared to its quantum case. CSLs are cooperative paramagnetic states with non-zero entropy at zero temperature, having power-law correlations. These are discussed or started mainly from spin-ice pyrochlore materials. Starting with similarities or dissimilarities of CSLs with QSLs, I have tried to summarise briefly the aspects like the existence of power-law correlations, emergence gauge theories, and the low energy monopole excitations in pyrochlore spin ice models. Interestingly, the quantum spin-ice models possess low-energy photon excitations (from emergent Quantum electrodynamic theory at low energy) when tunneling events between the degenerate states of classical spin-ice configurations are considered. Hence, the classical spin ice materials are not only significant on their own but also a source of interest in generating quantum spin liquids. Later, the key ideas of spin-ice models are generalized further to construct models with more generalized higher-rank theories. One more approach to studying the CSLs is the Luttinger-Tisza (LT) approximation. In this approximation, the local unit-length constraint for classical spins is sacrificed to impose the same on the whole lattice. In the simple approximation, the spins are treated as scalars, and the low-energy is studied within the Fourier basis. This approximation provides a platform to make progress in classifying and constructing other new CSLs. One of the key problems in

CSLs is whether they exist in generic classical spin models that do not respect spin-ice rules or not. If yes, then how to study them? I have provided an answer to this question in the work with a unified group theoretical framework to treat them in generic classical spin models.

Chapter Three aims to address the ramifications of the coupling of gauge and matter sectors in the Kitaev model, especially in the case of strong coupling beyond the perturbative limit. In the pure Kitaev model, there is no term in the Hamiltonian that couples to gauge and matter sectors. The perfect decoupling of these sectors is the main simplification in solving the model exactly. But that is no longer the case with other terms. I have used the external magnetic field along [111], which couples both the sectors where the field strength tunes the coupling. This Hamiltonian is studied using the density matrix renormalization group (DMRG) method. DMRG is performed with different lattice settings, such as a 1D ladder and a finite-width cylindrical honeycomb strip with different system sizes. Since the plaquette operators, a product of spin operators, calculate the flux passing through the plaquette. The expectation values and correlation function of the plaquette operators in the ground state directly measure the ground state gauge sector at a given field strength¹. For the 1d ladder setting, with all the exchange couplings equal and anti-ferro, I found five distinct phases as a function of magnetic field strength. Each phase is classified/identified with the structure of flux operators in all the plaquettes of the lattice. The five phases are uniform-flux, vortex gas, amorphous phase, and *glassy* phases, and finally, the polarised phase. The uniform phase, as the name suggests, has uniform flux configurations throughout the lattice followed by the uniform configuration at zero field case. This phase persists up to a field value equal to the single flux gap. As the field increases, fluxes begin to emerge in the state, manifesting as ripples against a uniform background. So, this phase is called the vortex gas phase because of the dilute gas of π -fluxes. The corresponding flux configurations are amorphous in nature for the amorphous vortex phase and random in the glass phase. The glassy nature of both these phases is primarily characterized by an extensive number of local minima in the energy landscape. This is identified through the fidelity of the ground state and confirmed through exact diagonalization (ED) calculations. In the amorphous vortex phase, states stemming from each local minima, which are orthogonal to each other, correspond to states with different positions of domain walls. In the glassy phase, these states represent varying random configurations. The origin of the glassy phase, here, is mainly due to restricted dynamics of excitations present in the model due to constraints. The excitations in the Kitaev model are fluxes and matter Majorana fermions. These are not freely movable. They always move in pairs. The pairs are connected by strings forming flux-flux or flux-majorana excitation at their end. The constrained dynamics are also present in the generic

¹In the strong coupling limit, understanding the behavior of the gauge sector doesn't necessarily equate to solving the physics of the matter sector.

spin liquids where the spinon excitations also move in pairs. So, the QSLs are prone to show slow dynamics. This further reiterates the need for probing techniques to diagnose the time dynamics in these models. Such techniques, like tensor network methods, are often numerically expensive, and only very few analytical methods are available due to the complexity of the problem.

In Chapter 4, two main aspects are addressed: i) constructing the low-energy tight-binding models for the fractional Majorana fermions present in the Kitaev model in the presence of various background gauge fields. Furthermore, this includes the construction of Wannier orbitals for Majorana fermions. ii) studying the flat-band physics for Majorana fermions and the realization of the 'fractional Chern insulator' (FCI) phase for Majorana fermions. The FCI phase is analyzed using gauge-invariant mean-field theory. As I discussed in Chapter 3, various gauge sectors appear in the ground state as a function of magnetic fields. Crystallization of π - fluxes is one such interesting configuration. These crystallized fluxes/vortices provide a perfect avenue to modify the properties of the interacting Majorana fermions. Likewise, in other examples, like in type-II superconductors, the periodic arrangement of vortices also modifies the properties of other excitations, such as Bogoliubov quasi-particles. In the case of the Kitaev model, I have considered various periodic π - flux configurations, denoted by $d \times d$, where d is the distance between the two π -fluxes, and studied the modified Majorana fermions dispersions. This chapter provides a formal method to develop the low-energy tight-binding model for the Majorana fermions and the fractional particles in general, keeping the flux constraint intact in the effective model. Since the effective low-energy bands are not complete by themselves, a formal methodology is needed to make them complete. This is done by implementing self-consistent super-exchange-like potential, which allows virtual hoppings to higher energy bands and then projecting them back to the effective energy bands. This, in general, results in further neighbor hoppings in the effective model. This generic method is applied to modified Majorana bands in the Kitaev model. The unit cell in each case has 2π flux with Majorana fermions. The self-consistent procedure can be implemented by the Wannierization algorithm, but the Majorana particle-hole symmetry must be imposed throughout. The Wannier orbitals for Majorana fermions are constructed and further used to fit the band structure with hoppings up to 9- neighbors. This method, in general, can be used for general anyons with any 'exotic' statistics, at least abelian statistics. Interestingly, the Majorana Wannier orbitals are located near Z_2 - fluxes and resemble the Majorana zero modes at the low energies.

Further, these effective models for Majorana fermions are used to study other interesting flat-band physics for Majorana fermions. The bands for various configurations are nearly flat with gap and gapless points. The bandwidth of these bands can be tuned by changing the d value or by tuning the next-nearest neighbor hopping strength, K . These bands are topologically

non-trivial with a non-zero Chern number. Varying K value, the Chern number changes via topological phase transition where the bands become completely degenerate, which results in singularity in the quantum metric. Also, these bands possess non-trivial quantum metric values higher in magnitude than the flux-free case. Interestingly, these bands satisfy the criteria to be 'ideal' Chern insulators when the band flatness ratio is low. Hence, these flat bands incorporate the FCI phase in the presence of interactions. This phase is studied with gauge-invariant mean-field analysis. The mean-field method promises to be more general and is useful in getting an analytical handle on the FCI phase, where they are studied as of now numerically.

Chapter 5 discusses the group theoretical analysis for studying the CSLs in generic classical spin models, which do not respect spin ice rules or LT approximation, which is generally the scenario for models that are relevant experimentally. This analysis is used to study the generic spin models by constructing the vector space from the spins in the plaquette. Then, the general vector is decomposed into different irreducible representations (irreps) of the point group symmetry of the underlying lattice. This is utilized to study one of the symmetrically allowed Hamiltonian on the square-Kagome lattice, which is the XXZ Hamiltonian (with anisotropy Δ) with Dzyaloshinskii–Moriya interaction (denoted by D). The group theoretical calculations are further validated and endorsed with unbiased Monte-Carlo calculations. The exciting outcomes of the phase diagram as a function of (Δ, D) for both anti-ferro and ferro exchange interactions are the appearance of topologically non-trivial AFM-vortex and AFM-non-vortex excitations in the ordered phases. In addition, the mixed fragmented phases appear where the ordered and disordered phases coexist. Furthermore, a disordered CSL phase exists with algebraic correlations showing pinch points in the structure factor along the $D = 0$ line. This CSL phase becomes unstable for any finite value of D , but it can be stabilized using the applied magnetic field. In the general context of CSLs, the key results include that this analysis provides a unified understanding of the CSLs, fragmented phases, and various other ordered phases where the degenerate ensemble of irreps with varying weights of each irrep respecting the local spin length constraint. The degenerate ground state manifold for CSLs and fragmented phases comes from the degeneracy of irreps, which is not as direct as the spin-ice models. The weight factors of order and disordered components in the fragmented phase for the classical continuous spin case are calculated for the first time. The phase transitions between the fragmented phases and fragmented to ordered phases promise to be non-Landau-type transitions in classical spin models.

This work paves the way for delving into CSLs in the experimentally relevant classical spin models, extending beyond traditional ice-rule models. Highlighting the existence of numerous experimentally relevant spin models encourages the exploration of broader theoretical

frameworks, offering the potential for deeper insights into their behavior and applications in classical spin materials.

I hope this thesis inspires additional investigations into the diverse physics involved in different gauge sectors in QSLs. As of now, there is no precise handle over gauge degrees of freedom either experimentally or analytically. But there is certainly a potential chance that these will change, given the overwhelming activities in simulating the phases with emergent low-energy gauge theories in synthetic platforms like neutral Rydberg atoms or also with non-equilibrium techniques. One of the central questions of recent interest is the stability or the nature of the spin liquids (or any of the entangled phases) under open environmental settings and their relevance in practical applications. Also, non-equilibrium settings can induce interesting new characteristics to these phases, which the equilibrium counterpart may not offer.